Experimentelle Physik

Measurement of Direct Photons in pp and Pb–Pb Collisions with Conversion Pairs

Inauguraldissertation
zur Erlangung des Doktorgrades
der Naturwissenschaften im Fachbereich Physik
der Mathematisch-Naturwissenschaftlichen Fakultät
der Westfälischen Wilhelms-Universität Münster

vorgelegt von
Martin Rudolf Wilde
aus Herten

- 2015 -

Dekan: Prof. Dr. C. Weinheimer

Erster Gutachter: Prof. Dr. J. P. Wessels

Zweiter Gutachter: PD Dr. J. Heitger

Tag der Disputation:

Tag der Promotion:

Contents

II   Direct-Photon Analysis   73

6   Analyzed Data Samples and Monte Carlo Simulations   75

7   Photon Reconstruction Using the Conversion Method   95

8   Neutral Pion Reconstruction with Converted Photons   129

1 Introduction

Hadrons, the building blocks of matter, melt at appropriately large energy densities and temperatures. Using physical terms, the phase diagram of strongly interacting matter has phases separated by phase transitions. To understand this property of matter "A Large Ion Collider Experiment" (ALICE) analyzes ultrarelativistic lead-lead collisions at the Larger Hadron Collider (LHC) at CERN. In the overlap region of two colliding nuclei the hadrons should be dense and hot enough and the contained matter should cross the phase boundary separating the phases. The hadrons dissolve and its constituents, quarks and gluons, exist in a quasi-free plasma. This state of matter is, therefore, called quark-gluon plasma (QGP).

This new phase of matter exists only for a short amount of time. The overlap region expands, cools down rapidly, and the quarks and gluons condense back into their more familiar hadronic form. Since the life-time of the system is so short and the interactions of the constituents of the plasma so multitudinous, it is hard to get a handle on all aspects of the evolution. However, this understanding is crucial for interpreting the measurements, normally dealing with the remnants of the heavy-ion collisions.

The standard probes of particle physics, hadron spectra, will carry information determined at the end of the expansion. Low momentum hadrons are formed by low momentum quarks building the QGP. Due to their small momentum, they will be entrained by the medium and their properties evolve together with the expansion. Hard scattered quarks or gluons are produced during the initial interaction of the two nuclei. They thus carry information about the early times of the collision. Yet, they must traverse the medium. By their interaction with low momentum quarks and gluons in the medium their properties might be changed dramatically. The size of the effect depends on the length of the path through the medium, a quantity hard to access. The final-state observable, the jet, will lose a part of its energy to the medium.

A way out of this is provided by weak and electromagnetic probes. The main advantage of both types of probes is their insensibility to the strong force. The measurement of weak probes, the Z^0 and the $W^\pm$ bosons, is a fruitful field on

its own. But for the investigation of the properties of the evolving medium they provide no further insights. Their masses are too large to be produced at stages later than the initial collision. Moreover, their lifetime is too short to experience the evolving medium. Just like jets, they are strongly related to the physics of the early stages of the collision.

A better way of investigating the evolution of the QGP and the subsequent state of a hot gas of hadrons is given by electromagnetic probes. The kind of probe used in this thesis are photons. Photons are produced during all stages of a heavy-ion collisions. Their mean free path is much larger than the medium size. Therefore, they are decoupled from all further interactions.

If they are produced during the initial collision, during a hard interaction, their recoiled counter part will be a hard scattered quark or gluon with identical energy. Thus, such photons can be used as an energy calibration of the hard quark or gluon. The energy disbalance of the final-state jet and the photon is directly related to the in-medium energy loss of quarks and gluons due to the strong force.

However, not only hard scattered photons are important for the understanding of the properties of the QGP medium. The produced plasma is hot. All measurements seem to show that its constituents are interacting continuously, leading to a rapid thermalization. These interactions will also produce photons at all stages of the collision. The related photon momentum distribution is governed by the heat or the energy density at production time. Due to the thermalized medium, those photons are commonly called thermal photons. Since they do not interact strongly, their properties are fixed at their production.

Normally experiments are only able to measure total photon yields. Thus, a spectrum will contain any photon produced during the collision. The discussed set of photons are summarized under the name direct photons. The softer components are called thermal photons, the hard components, produced during initial collision, are referred to as prompt photons. More sources are expected for example photons which are produced by interactions of hard partons with the QGP medium and are thus related to both kinds of previously introduced sources.

The topic of this thesis is the measurement of direct photons produced in pp and Pb–Pb collisions recorded by the ALICE experiment. The pp results are used as a reference and a proof of concept. In the absence of a medium, only photons from hard scattering are expected. Thus, pp measurements can be understood as a baseline for Pb–Pb and as a test for prompt-photon predictions. For the Pb–Pb collisions, the additional contribution of thermal and jet-medium photons are expected. To draw solid conclusions from a measured total direct-photon spectrum the medium properties, a lot of additional theoretical effort is needed.

The whole evolution of the plasma and the hot hadronic gas phase has to be considered. Still, the baseline for all discussion is always a measurement provided by an experiment as discussed in this thesis.

The thesis is organized as follows: In the second chapter, the phase transition expected from basic thermodynamics considerations and from more recent QCD calculations is discussed. A second focus is on the evolution of a QGP medium produced in heavy-ion collisions. In the third chapter, some experimental signatures of the QGP and its thermalized nature are discussed. Only such signatures are introduced that are important for the presented direct-photon analysis. In the following chapter, the photon production in nucleon-nucleon and nucleus-nucleus is briefly described. The fifth chapter is dedicated to the Large Hadron Collider and a description of the ALICE experiment. Further, the software framework used for the analysis is introduced. In the sixth chapter, the analyzed data samples recorded by the experiment and the corresponding Monte Carlo event generation are described. Direct photons are produced along with a huge background of photons originating from particle decays. To estimate the amount of background photons, the neutral pion spectrum has to be measured in addition to the inclusive-photon spectrum. The extraction of those two spectra is discussed in chapters seven and eight, respectively. The subtraction of the decay photons from the inclusive photons is described in chapter nine. In the final chapter the direct-photon extraction is presented and the final results are shown.

Part I

Heavy-Ion Collisions, Direct-Photons and the LHC

2 From Hadrons to QGP − QCD Phase Transition

Quantum chromodynamics (QCD) describes the physics of quarks and gluons and is formulated as a quantum field theory. From perturbative QCD (pQCD) calculations, applicable for large momentum transfers (Q^2), it is known that the coupling depends strongly on Q^2 and vanishes at infinitely large values. However, quarks and gluons manifest confined in colorless hadrons. At sufficiently large temperatures or densities, still well below the perturbative regime, those bound states disintegrate and convert into a nearly ideal gas of quarks and gluons.

Before the theory of strongly interacting matter was understood on that level, a transition to free quarks (and gluons) had already been predicted. Hagedorn concluded in 1965 [1] from the exponential rising of the number of resonances in a hadron gas a limiting temperature T_C for hadronic matter on the basis of thermodynamics. At temperatures $T > T_C$ hadronic matter could not exist. In 1975 Cabibbo and Parisi [2] realized that this temperature, described by Hagedorn, is not necessarily a general upper limit. Instead, they found that the exponential rise could be avoided by a second phase separated by a second order phase transition. The new phase was suggested to consist of unconfined quarks.

Today it is fact that hadronic matter should undergo a phase transition at $T_C \sim 170\,\mathrm{MeV}$. A lot of effort is made to understand the nature and the properties of this transition. Also in laboratory, the transition is nowadays studied experimentally by heavy-ion collisions. Before details of the current understanding of the transition are reviewed, some important historical steps are summarized in the next section.

2.1 Historical Thermodynamic Approaches

First hints of the critical behavior were already found in the early 1960s, long before sufficiently high energies could be generated by collider experiments. QCD was also not yet established to study the phase diagram. During this time the

discovery of more and more resonance states (up to masses of $\sim 1000\,\mathrm{MeV}$) raised questions about the physics of hadronic matter at higher and higher energies. The first approaches to handle the experimentally found rise of the number of hadron states were based on thermodynamics.

The number of the resonances were found to grow exponentially with energy. In 1965, Hagedorn proposed [1] that hadronic matter should have a maximum temperature. In his ansatz he used a grand canonical ensemble, considering neutral scalar particles in a fixed volume with Boltzmann statistics. He assumed that the fireball created in a hadronic collisions is self-similar. Each fireball consists of fireballs, hadronic resonances, which consist again of hadronic resonances. The model is called the statistical bootstrap model. The experimentally found exponentially rising resonance spectrum is consequently described as a density of the self-similar resonances. It is given by [3]:

$$\rho(m, V_0) = \text{const.}\ m^{-3} \exp\left(m/T_H\right). \tag{2.1}$$

The quantity T_H, the so called Hagedorn temperature, can be derived from this density, which includes two parameters, the composition volume V_0 and T_H. Hagedorn assessed V_0 by the inverse pion mass as $V_0 \approx (4\pi/3)m_\pi^3$ and found T_H to be $\sim 150\,\mathrm{TeV}$. Anyhow, at T_H the partition function, corresponding to Eq. (2.1), diverges. Thus, T_H was considered as a limiting temperature for strong interactions and hadronic matter.

A second early approach leading to a critical temperature can be found in the bag model. It was first introduced in 1974 [4]. Within the model, hadrons are assumed as "bags", containing quarks. In general, the pressure of an ideal gas of pions is given by ($k_\mathrm{B} = 1$) [5]:

$$P_\pi = 3 \cdot \frac{\pi^2}{90} T^4 \tag{2.2}$$

A similar equation can be formulated for a quark-gluon plasma. If only two quark flavors are assumed its pressure is given by:

$$P_{QGP} = 37 \cdot \frac{\pi^2}{90} T^4 - B. \tag{2.3}$$

The two different constant pre-factors (3 and 37) of the two equations are given by the number of degrees of freedom. In the case of the pion gas, three different states exist (π^+, π^- and π^0). In the case of a QGP the corresponding number of the degrees of freedom is $[2 \cdot 8 + (7/8) \cdot (3 \cdot 2 \cdot 2 \cdot 2)]$ (eight gluons, two flavors). The constant B is the bag pressure. This pressure acts against the quarks and

gluons and confines them inside the hadron bags. Its value can be extracted from the proton radius and is on the order of 200 MeV. In thermodynamics, the system tends to the lowest free energy state and thus to the maximum possible pressure. By comparing (2.2) and (2.3), one gets a critical temperature $T_c \simeq 150$ MeV for equal pressures. For larger values of T, the maximum pressure is given by equation (2.3). The favorable state at temperatures above the critical value is a free gas of quarks and gluons instead of the hadronic pion gas.

Both models, bootstrap and bag model, predict a critical temperature. In both models very similar critical temperature values are found. A more precise analysis of the properties of the phase structure of strongly interacting matter can be provided by QCD calculations. The fundamental equations of QCD will be introduced in the next section.

2.2 QCD and the Running Coupling

Quantum Chromodynamics (QCD) is the theory of one of the four fundamental forces and describes strongly interacting matter. It is formulated as a quantum gauge field theory and was first introduced in the 1970s. The theory describes how quarks and gluons interact and why at low energy, those particles are confined in hadrons. The dynamics of the quarks and gluon fields are commonly described by a Lagrangian. The Lagrangian of Quantum Chromodynamics is given by:

$$\mathcal{L}_{QCD} = \mathcal{L}_{\text{classic}} + \mathcal{L}_{\text{gauge}} = \sum_f \bar{q}_f (i\gamma^\mu D_\mu - m_f) q_f - \frac{1}{4} F_{\mu\nu,a} F_a^{\mu\nu}. \qquad (2.4)$$

The classical part of the Lagrangian, $\mathcal{L}_{\text{classic}}$, describes the interaction of the fermionic quarks fields q_f with associated masses m_f. The index f refers to the different quarks species. Due to the large masses of the second and third quark family, it might be expedient to include only two (up, down) or three (up, down, strange) quark flavors in QCD calculations. The index a refers to the eight gluon field.

The gauge fields $A_{\mu,a}$, representing the gluons, are hidden in the covariant derivative

$$D_\mu = \partial_\mu - ig \sum_{a=1}^{8} \frac{\lambda_a}{2} A_{\mu,a} \qquad (2.5)$$

and in the field strength tensor

$$F_{\mu\nu,a} = \partial_\mu A_{\nu,a} - \partial_\nu A_{\mu,a} + g f_{abc} A_{\mu,b} A_{\nu,c}. \qquad (2.6)$$

The covariant derivative has to be introduced to guarantee the local gauge invariance of the quarks fields at every space point. In QCD, the corresponding gauge symmetry is given by the SU(3) group, defining the number of gauge fields and the number of charges. Thus, eight gluons carrying two out of six color charges (color and anti-color) exist. The last term in (2.4), containing the field strength tensor, describes the self-interactions of the gauge fields. The λ_a matrices are the generators of the QCD gauge group. They are the equivalents of the Pauli matrices used in the electromagnetic field theories. The most common choice of those generators are the eight Gell-Mann matrices. The structure constants f_{abc} define the commutator relations of the generators. The constant g describes the strength of the coupling between the fields.

One of the most interesting features of QCD is the momentum transfer (Q^2) dependent coupling $\alpha_s = g^2/4\pi$. Most simply, this can be explained as follows: A "free" quark will create quark-antiquark pairs and gluons. The quark-antiquark pairs will screen the color charge of the original quark. Since gluons carry two color charges, they will not screen the quark but create an additional cloud of net color charges. If the cloud is probed with higher and higher momentum transfers, more and more of the original smaller color charge in the center of the cloud is seen. At lower momenta, the additional gluons will amplify the probed charge. This results in a rising coupling strength towards low momentum transfers.

The dependence of α_s on the momentum transfer can be calculated analytically in leading order pQCD. The result describes the variation of the coupling constant with the momentum transfer, not the overall normalization of the coupling strength. The leading order result can be written as:

$$\alpha_s(Q^2) = \frac{12\pi}{(33 - 2n_f)\ln\left(Q^2/\Lambda_{\mathrm{QCD}}^2\right)}. \tag{2.7}$$

The formula depends on the number of considered quarks flavors n_f and on the QCD scale parameter Λ_{QCD}. This parameter cannot be derived from QCD calculations and has to be estimated by experiments. Normally, a value of $\Lambda_{\mathrm{QCD}} \sim 200\,\mathrm{MeV}$ is used. Alternatively, the measured coupling at the Z boson mass $Q = M_z = 91.188\,\mathrm{GeV}$ is used to normalize the coupling strength.

In Fig. 2.1 α_s, extracted by different measurements, is shown as a function of Q. In addition, the QCD result is shown as black lines. For small momentum transfers, the coupling becomes large and quarks are bound to hadrons. With these large couplings, pQCD becomes impossible. At large momentum transfers the coupling becomes weak, and the coupling strength tends to zero for $Q^2 \to \infty$. The tendency of quarks becoming free particles at large momentum transfers is
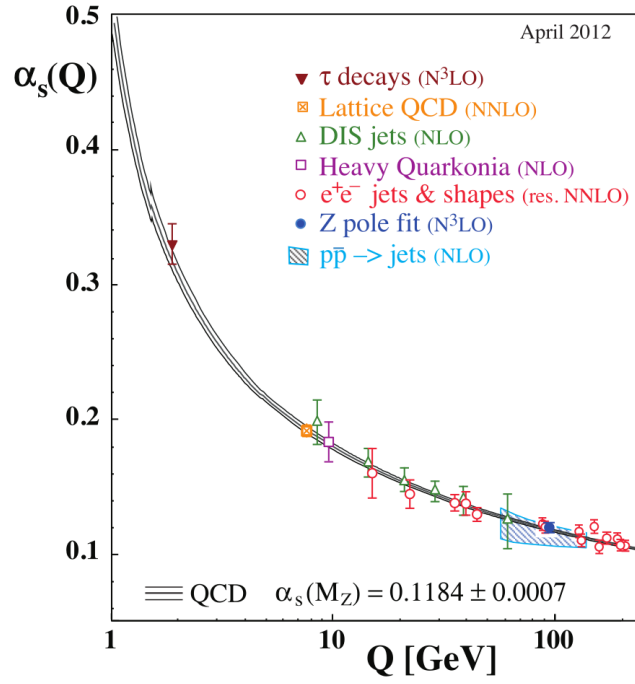
Figure 2.1: Various measurements of the strong coupling constant α_s. The lines correspond to a QCD prediction following Eq. (2.7). [6]

called asymptotic freedom. The opposite behavior at low momentum transfers is called confinement.

2.3 Phase Transitions in QCD and the QCD Phase Diagram

The critical behavior found in the thermodynamic consideration can be reproduced by more complex QCD calculations. An alternative is provided by finite-temperature lattice QCD.

The idea of lattice QCD is the substitution of the continuous space and time formulation of QCD, as it is used for example in equation (2.4), with a discrete space-time. The distance between the space and time points is given by the lattice parameter a. The continuum limes $a \rightarrow 0$ has to emerge the continuous QCD results. First approaches in lattice QCD were done by Wilson in 1974 [7]. To make predictions from finite-temperature lattice QCD, many further steps are needed. A short introduction is given in [8], a comprehensive overview in [9]. In the following, a zero baryochemical potential $\mu_B = 0$ is used. It is the amount of energy needed to add an extra baryon to the system. It is thus directly related to the baryon-anti-baryon number density. Simply, it can be considered as a net-baryon density.

In general, a phase transition is characterized by the change of its order parameter and by a simultaneous change of symmetry. In case of lattice QCD, the order parameter of (de-)confinement is the Polyakov loop [10]. It represents a closed Wilson loop in time direction for infinitely heavy quarks. In this case, only the gauge Yang-Mills part of the QCD Lagrangian enters the calculation (Eq. (2.4) last term).

The expectation value of the loop $\langle L \rangle$ is related to the free energy F_q of a free static quark. It depends on the temperature of the system and is given by:

$$\langle L \rangle = \exp\left(-F_q/T\right). \tag{2.8}$$

For an infinite space-time, it can be interpreted as the production of a single heavy quark at $t \rightarrow -\infty$ and its annihilation at $t \rightarrow +\infty$. In case of confinement, no free quarks exist. This implies that the probability of the creation of a free quark has to be zero ($\langle L \rangle = 0$) in the hadronic phase ($F_q \rightarrow \infty$). In the opposite case ($\langle L \rangle \neq 0$), free quarks exist and F_q has a finite value.

These basic considerations are valid for infinitely heavy quarks. In case of finite quark masses, the expectation value of the Polyakov loop is non-zero even in the confined phase. The static-quark potential, correlated with the free energy, will be finite. In this case, the growing potential energy will lead into quark-antiquark creation if the energy reaches the size of hadron masses.

From the study of QCD, a second phase transition emerges. It is related to the restoration of the chiral symmetries of QCD. The Lagrangian Eq. (2.4) is invariant under $SU_L(n_f) \times SU_R(n_f)$ for vanishing quarks masses. These two $SU(n_f)$ symmetries are the chiral symmetries. The indices L,R denote the left and right handed quark fields. For massive quarks, this symmetry is broken explicitly. The strength of the symmetry violation is given by the size of the quark masses. This can be directly seen from a very simple consideration. The QCD Lagrangian $\mathcal{L}_{\text{classic}}$, can be separated into a chiral symmetry conserving $\mathcal{L}_{\text{symm}}$ and a symmetry violating term $\mathcal{L}_{\text{break}}$. In case of two flavors, the Lagrangian is:

$$\mathcal{L}_{\text{classic}} = \mathcal{L}_{\text{symm}} + \mathcal{L}_{\text{break}} = \mathcal{L}_{\text{symm}} + m_u \bar{q}_u q_u + m_u \bar{q}_d q_d$$
$$= \mathcal{L}_{\text{symm}} + m_q \bar{q}q + \delta m_q \frac{\bar{q}_u q_u - \bar{q}_d q_d}{2}, \qquad (2.9)$$

where $m_q = m_u + m_d$, $\delta m_q = m_u - m_d$ and $\bar{q}q = (\bar{q}_u q_u + \bar{q}_d q_d)/2$. From this equation directly follows that the operator $\bar{q}q$ and its expectation value $\langle \bar{q}q \rangle$ characterize the magnitude of the symmetry breaking. This quantity is called the chiral quark condensate. A vanishing value would indicate a conserved chiral symmetry.

Related to the two order parameters $\langle L \rangle$ and $\langle \bar{q}q \rangle$ are the Polyakov loop susceptibility χ_L and chiral susceptibility χ_m, respectively. The susceptibilities represent the long distance correlations which are maximal at the phase transitions. In Fig. 2.2, the two order parameters and the related susceptibilities are shown as a function of the inverse temperature β. The figure is taken from [11] and shows calculations for two flavor QCD in the pure gauge limit. For the expectation values of the Polyakov loop, infinitely heavy quarks are used. The chiral condensate is calculated in the zero mass limit. Both transitions, chiral symmetry restoration and confinement-deconfinemet, occur at nearly the same temperature. This property of QCD is not evident at first sight. Various calculations with more quark flavors or a wide range of quark masses support the finding of an, at the least, very similar transition temperature.

It is important to mention that basic lattice QCD is only able to make predictions for zero baryochemical potential. For $\mu_B \neq 0$, more advanced techniques have to be considered. Calculations seem to show that for small μ_B, a cross-over is realized until a first order transition sets in [12]. The two different transition types are separated by a critical point. The critical temperatures of the transition decrease and come to zero at very high densities. In Fig. 2.3, the phase diagram of QCD is sketched. In addition to the previously discussed phases, the diagram shows an additional phase. A similar situation as in super-conducting materials,
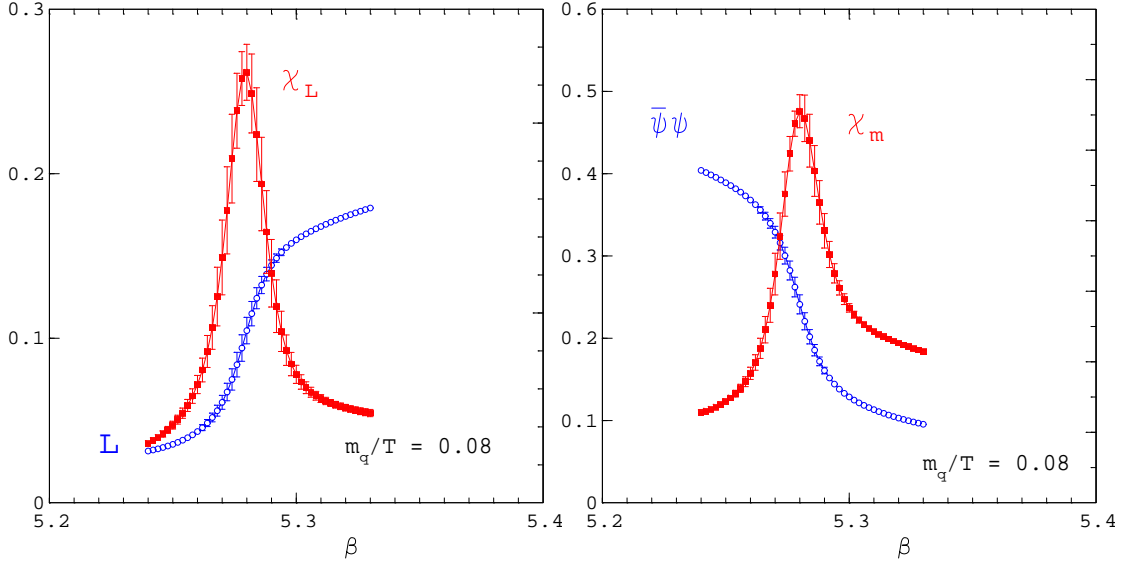
Figure 2.2: The two order parameters of the QCD phase transitions. Left: The Polyakov loop $\langle L \rangle$ and its susceptibility χ_L versus $\beta = 1/T$. The loop becomes non-zero, indicating a breaking of a symmetry, while χ_L reaches a maximum, indicating long range fluctuations. Right: The chiral quark condensate $\bar{\psi}\psi = \langle \bar{q}q \rangle$ becomes zero, indicating the restoration of chiral symmetry. As for the Polyakov loop, the susceptibility has its maximum at the phase transition. [11]
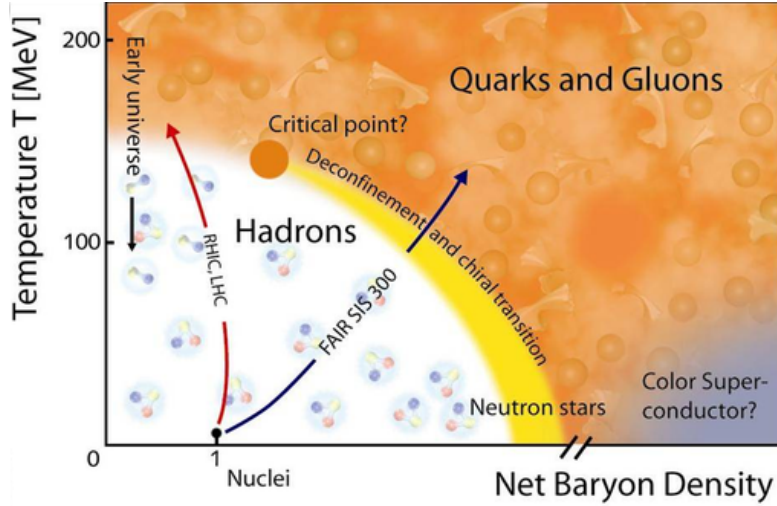
Figure 2.3: Current knowledge of the phase diagram of QCD. [13]

with quarks building Cooper-Pairs, is expected. The operation regions of various heavy-ion experiments are plotted additionally.

2.4 QCD Phase Transition in Heavy-Ion Collision

To study the QCD phase transition and the deconfined phase, a very hot and dense state of matter has to be created. These extreme conditions can be reached by the collision of two ultra-relativistic nuclei. The center-of-mass energy per nucleon pair, $\sqrt{s_{\mathrm{NN}}}$, should be at least on the order of $15\,\mathrm{GeV}$.

The history of heavy-ion collisions started in 1987 with the Alternating Gradient Synchrotron (AGS), at BNL and the Super Proton Synchrotron (SPS) at CERN. The AGS used silicon ions, the SPS sulfur ions. All of these experiments used fixed targets. The center-of-mass energy per nucleon pair $\sqrt{s_{\mathrm{NN}}}$ was still very small compared to current experiments. They were able to create maximum values of energy of $\sqrt{s_{\mathrm{NN}}} = 5\,\mathrm{GeV}$ and $20\,\mathrm{GeV}$, respectively. Nowadays, the nuclei are accelerated in opposite directions in large accelerator rings. By colliding two accelerated nuclei in collider experiments the center-of-mass energy was increased dramatically. The two experiments RHIC (Relativistic Heavy-Ion Collider) at BNL (since 2000) and the LHC (Large Hadron Collider) at CERN (since 2010) operate with $200\,\mathrm{GeV}$ and $2760\,\mathrm{GeV}$ per nucleon pair. The LHC has a design center-of-mass energy in heavy-ion collisions of $5500\,\mathrm{GeV}$ per nucleon pair. To create larger volumes of excited hadronic matter, larger ions like gold (at BNL) or lead (at CERN) are used.

Depending on the collision energy of the ions, two different scenarios are imaginable. At small energies ($\sqrt{s_{\mathrm{NN}}} < 10\,\mathrm{GeV}$), the two ions may stop each other and create a medium with a very high baryon density. In case of higher energy, the stopping-power will not be large enough and the ions will traverse each other. The overlap region will have very high temperatures but less baryon density compared to the first scenario. In Fig. 2.3, the operation areas of several experiments are sketched. Colliders with smaller energy, like the future SIS 300, create lower temperatures but higher values of μ_B. High energy colliders like the LHC operate at very low densities but create very large temperatures. All connected experiments should have the capability to explore different properties of the phase transitions [14].

Figure 2.4 shows a sketch of a heavy-ion collision at higher energies where the nuclei interpenetrate each other. The two Lorentz contracted ions collide with a certain impact parameter b. Every nucleon (grey pellets) involved in the collision is called a participant. Each nucleon not involved is called a spectator. The centrality of a heavy-ion collision is directly related to the impact parameter b and thus to the number of participants. In case of a head-on or so called central
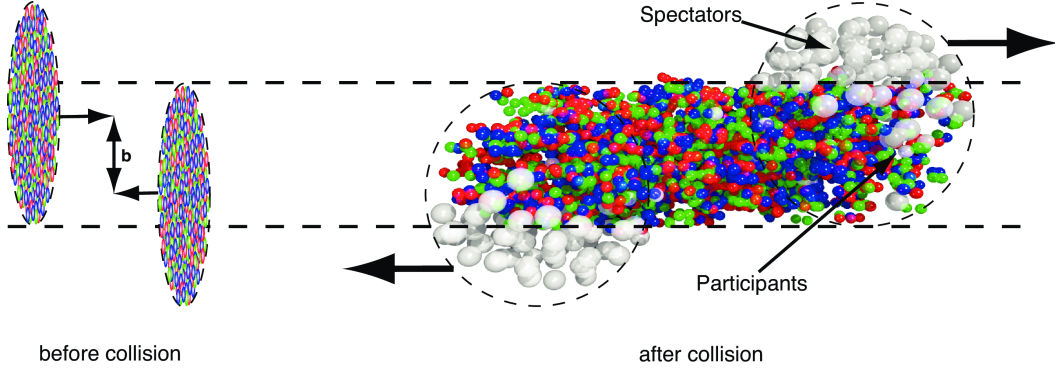
Figure 2.4: Sketch of a heavy-ion collision. On the left the situation before the collision is shown. The two nuclei are Lorentz contracted. After the collision with a certain impact parameter b, the transverse energy of the nucleons is converted into higher temperatures, and the quarks and gluons are liberated. [15]

collision, the impact parameter is zero and the number of participants is roughly the number of nucleons of the two ions. In case of a peripheral collision, the impact parameter is larger and the number of participants smaller.

The impact parameter or the number of participating nucleons is not directly accessible in a heavy-ion experiment. However, the centrality is also related to the number of produced particles in a given collision. By measuring the number of charged particles and comparing the results to models, the impact parameter as well as the number of binary collisions can be extracted. The measurement of the centrality in ALICE is described in Sec. 6.1.2.

The longitudinal energy of the nucleons building the nuclei is partially deposited by the collision in the overlap region, leading to very high temperatures. If the temperature is large enough, the nucleons will undergo the phase transition to the quark-gluon plasma. In Fig. 2.4, this is indicated by the colored pellets.

2.4.1 Time Evolution of a Heavy-Ion Collision

Figure 2.5 shows the space-time evolution for energy densities and temperatures large enough to produce a quark-gluon plasma ($\epsilon \sim 1\,\mathrm{GeV/fm^3}$, $T_C \sim 170\,\mathrm{MeV}$ [16]).

During the interpenetration of the two nuclei, the system is heated and the quarks and gluons are liberated. The longitudinal energy of the incoming particles is partially transferred to internal and transverse energy.
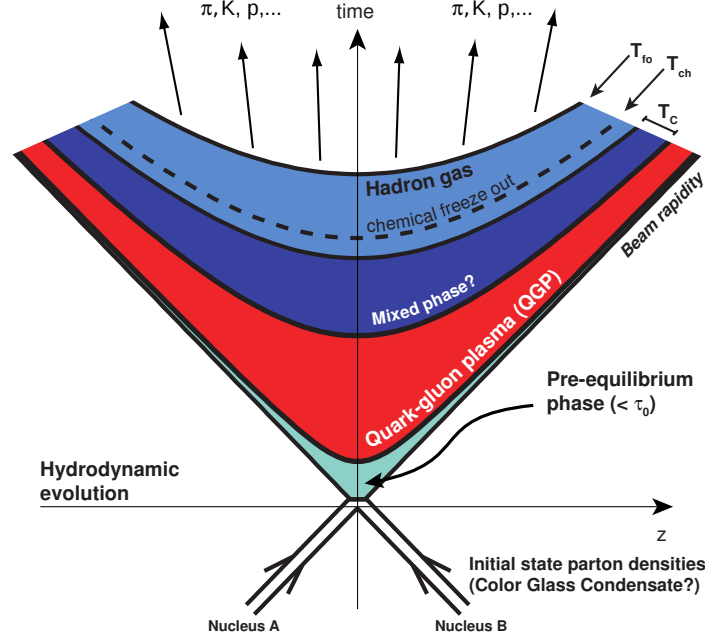
Figure 2.5: Space-Time evolution of a heavy-ion collision. The critical energy density $\epsilon_C \sim 1\,\text{GeV}$ and temperature $T_C \sim 170\,\text{MeV}$ are exceeded and a quark gluon plasma is produced after thermalization. The system expands, cools down and freezes out below T_C producing a wide spectrum of final-state particles. [17]

After the initial collision, the system is far from thermal equilibrium. It is still an open question how the energy is distributed in the overlap region. The time from the initial collision to the moment the equilibrium is reached is called thermalization time τ_0. At LHC energies it is on the order of $0.2\,\text{fm}/c$. Different models exist to describe the thermalization process. Most models have in common that the equilibrium is reached via multi (semi-hard and soft) interactions of quarks and gluons.

A standard approach to describe the evolution after thermalization is given by the description with relativistic hydrodynamics. Hydrodynamics are applicable if the mean free path of the constituents of the medium is much smaller than the size of the medium. The most simple approach is the Bjorken scenario [18] where only a longitudinal expansion is assumed. Each slice of the cylindrical volume, formed after the interpenetration, is boost invariant. All future states of the medium are fixed at thermalization, $\tau = \tau_0$. The related temperature is called initial temperature. The plasma can be approximated as a perfect fluid, and the dynamics are fully determined by the local energy density ϵ and the local pressure

P. For a more realistic description, beyond a perfect fluid, viscosity, shear stresses and head conductivity are to be taken into account. More advanced calculations use fluctuating initial conditions with more complex spatial temperature profiles.

During the expansion, the energy density reduces. At a certain volume it will be below the critical value, and the corresponding temperature becomes smaller than T_C. All quarks and gluons freeze out into hadrons. In case of a first order phase transition, there will be an intermediate mixed phase. In this phase, free quarks and gluons coexist with the hadrons until all quarks and gluons are confined. During this mixed phase, the temperature stays constant. Instead, the dropping of the energy density is converted from a larger number of partonic into a smaller number of hadronic degrees of freedom.

The composition of the different hadrons can still change via inelastic hadron-hadron interactions until the chemical freeze out at T_{ch} is reached. Below this value, the particle yields and thus their ratios are fixed. At even smaller energy densities, the elastic interactions will also stop, and the momentum distributions of each hadron species is additionally fixed. This freeze out is called the kinetic freeze out with the corresponding temperature T_{fo}.

3 Signatures of the QGP Phase Transition

It was discussed in the previous chapter that if a hadronic system is heated or compressed strong enough, it should undergo the chiral and the deconfinemet phase transitions. Both transitions seem to occur for small densities at very similar temperatures around $T_C \sim 170 \, \text{MeV}$. In an experiment, these extreme temperatures can be reached in the overlap region of two colliding ultra-relativistic heavy nuclei. This immediately leads to the question how these phase transitions can be confirmed and studied. If a quark-gluon plasma is created, what are its properties? In the following section, some of the wide selection of observables are introduced. The most important signature for this thesis is the production of photons from a QGP. In nucleon-nucleon collisions, no QGP is expected. The QGP photons should thus manifest as an enhanced photon production in heavy-ion collisions. The description of the photon prodcution in heavy-ion collisions has been shifted into the next chapter.

3.1 Particle Production in Heavy-Ion Collisions

All conclusions which can be drawn from a heavy-ion collision are related to the measurement of charged and neutral particles produced by the collision. Particles from hadronic collisions, proton-proton or heavy-ion (pp or AA) are produced via inelastic interactions of the two colliding hadrons or by their constituents. The two incoming projectiles lose a fraction of their energy. It is transformed in the production of new particles with the mass m_0 and the momentum $\vec{p}$.

The common observable describing the multiplicity of (charged) particles N_{ch} is the average multiplicity per unit of rapidity or pseudo-rapidity (y or η) $\text{d}N_{\text{ch}}/\text{d}\eta$. Figure 3.1 shows the $\sqrt{s}$ dependence of $\text{d}N_{\text{ch}}/\text{d}\eta$ for pp (p$\bar{\text{p}}$) and AA collisions. For LHC energies, the charged particle density is measured by ALICE, ATLAS and CMS. All agree within uncertainties and measure $\text{d}N_{\text{ch}}/\text{d}\eta \approx 1600$ in the 5% most central events [19–22].
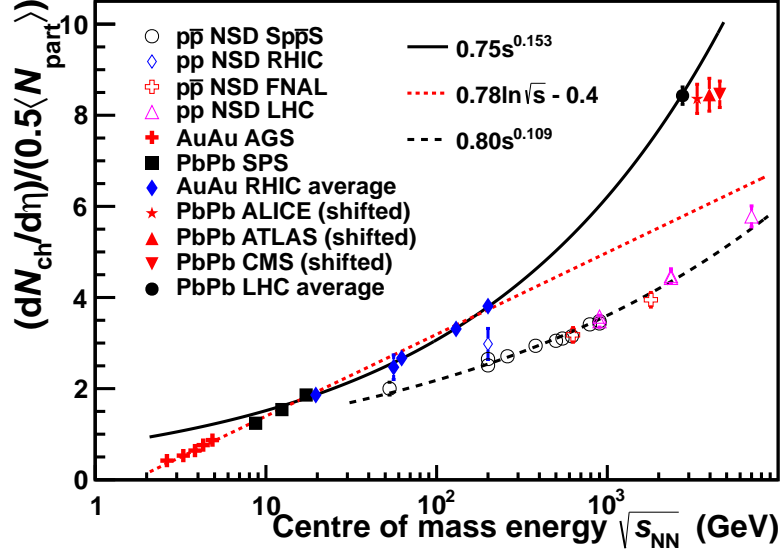
Figure 3.1: Charged particle multiplicity per unit of pseudo-rapidity per participant pair for pp (p$\bar{\text{p}}$) and heavy-ion collisions. [19]

The overall $\mathrm{d}N/\mathrm{d}y$ particle density can be directly related to the energy density at thermalization time τ_0 by using Bjorken's approach [18]. In the overlap area A of the two nuclei the energy density is, with the transverse mass m_T and energy E_T, given by:

$$\epsilon_\mathrm{Bj} = \frac{\langle E \rangle}{V} = \frac{\langle m_\mathrm{T} \rangle}{A\tau_0} \cdot \frac{\mathrm{d}N}{\mathrm{d}y} = \frac{1}{A\tau_0} \cdot \frac{\mathrm{d}E_\mathrm{T}}{\mathrm{d}y}. \tag{3.1}$$

This leads, with $t = 1\,\mathrm{fm}/c$, to an energy density of $14\,\mathrm{GeV/fm^3}$ at the LHC [23]. The value is approximately three times larger compared to energy densities found for RHIC energies [24]. The initial temperature, closely related, should be increase by approximately 30% corresponding to $T_\mathrm{init,LHC} \approx 300\,\mathrm{MeV}$ [19]. In both experiments, the temperature and energy density should be well within the deconfined phase ($\epsilon \sim 1\,\mathrm{GeV/fm^3}$, $T_C \sim 170\,\mathrm{MeV}$ [16]).

The energy density is proportional to the number of degrees of freedom and thus several times larger in a QGP than in a hadronic phase (bag model Eq. (2.2) and Eq. (2.3)). A lattice calculation for the energy density versus multiples of the critical temperature T_C is shown in Fig. 3.2. Around the critical temperature, the energy density rises rapidity. The saturation value depends on the number of considered quark flavors (QGP degrees of freedom). Thus, it is interpreted as a rise caused by the larger number of the degrees of freedom in the QGP. From the overall size of the energy density, conclusions can be drawn for the interaction of
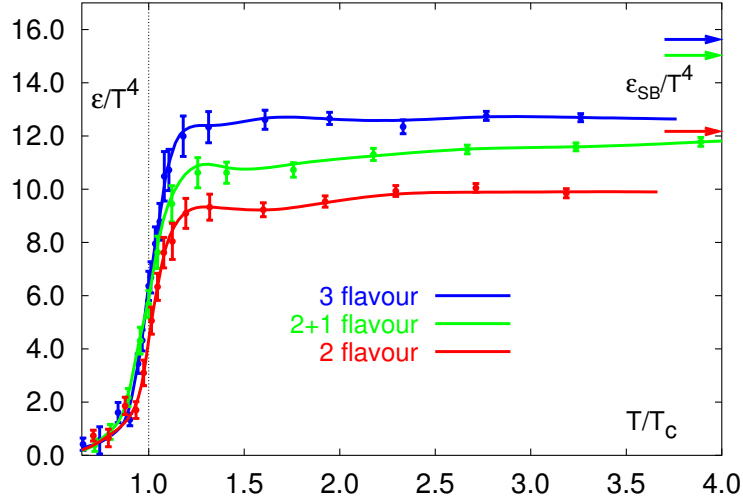
Figure 3.2: Lattice QCD energy density calculation for 3, 2+1 and 2 flavors. The arrows on the right hand side indicate the expected densities for an ideal gas of quarks and gluons. [11]

the constituents of the plasma phase. Comparisons with the ideal gas limit show that the QGP is clearly not free of interactions.

To gain information about the momentum transfer Q^2, normally the differential Lorentz invariant transverse momentum spectra (p_T) of the produced particles are measured. Two different mechanisms are distinguished by p_T. Large p_T ($> 2\,\mathrm{GeV}/c$) final state particles are produced by hard scatterings of quarks and gluons with large momentum transfers during the initial collision. Because of the large energy transfer, the two scattered partons normally belong to the two different projectiles. In a simplified picture, the two departing hard scattered color charged objects will form a color flux tube. The energy of the string rises and its breaking will produce a new quark-antiquark pair from the vacuum. The quarks will also radiate gluons, which will produce additional quark pairs. This production of more and more colored objects is called parton showering. In the process, the energy of the initially hard scattered parton is distributed to a large number of additionally produced quarks and gluons. Beyond the energy threshold, on the order of Λ_{QCD}, the string breaking will stop. All quarks and gluons will be confined into hadrons.

The remnants of the two nuclei after the interpenetration will also form color strings. These will result in particles with smaller (soft) transverse momenta. The hard interactions should scale with the number of binary (hard) parton col-

lisions (N_{coll}), the number of collisions of two partons of different nuclei. The soft interactions should in contrast scale with the number of participating nucleons (N_{part}). While the hard scattered partons will traverse the plasma, the soft particles are entrained by it.

It was already discovered in 1980, by colliding hadrons with different nuclei [25], that the overall particle production is proportional to the number of participants and is thus dominated by soft processes. While the soft particles p_{T} distribution follow an exponential, the high p_{T} particle spectra can be described by a power-law.

3.2 Collective Particle Flow

As it was discussed previously, the medium produced after a heavy-ion collision can be described by relativistic hydrodynamics. In this picture, a pressure gradient between the center of the medium and the surrounding vacuum, where the pressure is zero, exists. In case of a small mean free path of the particles in the medium, the gradient leads to a collective motion of all constituents. This motion will cause a momentum shift of all final state particles. The collective behavior of all constituents in the QGP and in the hadronic gas phase is referred to as flow.

3.2.1 Radial Flow

Hydrodynamics cannot describe the transition from the collective motion of a fluid to the momentum distribution of single hadrons, measured in a particle detector. Thus, it has to be assumed that the transverse momentum (or mass) distribution of the particles in the fluid at the end of the expansion is identical to the one of the outgoing hadrons (Cooper-Frye freeze-out picture [26]). As an approximation, a thermalized baryon-less fluid in rest with Boltzmann statistics can be assumed [27]:

$$\frac{\mathrm{d}N}{m_{\mathrm{T}}\mathrm{d}m_{\mathrm{T}}} \propto m_{\mathrm{T}}K_1\left(\frac{m_{\mathrm{T}}}{T}\right) \quad \xrightarrow{m_{\mathrm{T}}\gg T} \quad \sqrt{m_{\mathrm{T}}}\exp\left(-\frac{m_{\mathrm{T}}}{T}\right). \tag{3.2}$$

The modified Bessel function K_1 can be approximated with an exponential function for large values of m_{T}. This indicates, if the picture is correct, that all particle spectra, frozen out at the same value of T, should follow an exponential. The inverse slope of the exponential is given by the freeze-out temperature T_{fo}.

Since it is expected that the system is expanding in transverse and longitudinal direction, the thermal source has to be boosted for a more realistic description of the transverse mass spectra. Therefore, the transverse velocity profile $\beta_r(r) = \beta_s(r/R)^n$ is used between the center of the source $r = 0$ and its surface $r = R$. A prediction for the spectral shape is given by a superposition over all thermal spectra, in respect to r, boosted with $\rho = \tanh^{-1}(\beta_r(r))$:

$$\frac{1}{p_T}\frac{\mathrm{d}N}{\mathrm{d}p_T} \propto \int_0^R \mathrm{d}r\, m_T K_1\left(\frac{m_T \cosh(\rho)}{T}\right) I_0\left(\frac{p_T \sinh(\rho)}{T}\right). \tag{3.3}$$

The two functions K_1 and I_0 are two modified Bessel functions. For an unboosted thermalized volume with $\beta_r = 0$, the formula is identical to Eq. (3.2). The boosted spectra (3.3) therefore approximately follow an exponential with a slope $1/T_{\text{eff}}$. T_{eff} can be interpreted as the boosted temperature from the unboosted spectra given by Eq. (3.2). It is calculated as:

$$T_{\text{eff}} = T\sqrt{\frac{1+\beta_r}{1-\beta_r}}. \tag{3.4}$$

This description (3.3) of particle spectra is often called Blast-Wave Model. It is used to fit all available identified particle spectra (pion, kaons, protons, ...) with a common set of values of T, $\langle\beta_r\rangle$, the average radial flow and n, the exponent of the flow profile. These values should give the approximated values of the temperature T_{fo} (kinetic-freeze-out) and the average radial flow of the produced medium. An important remark at this point is that the inverse slope parameter of an exponential fit to a given p_T spectrum is not the temperature of the medium producing the particles. Depending on the production time and the corresponding drift velocity, the production temperature T is less and given by Eq. (3.4).

In Fig. 3.3, the results of such a common fit for ALICE and STAR (at RHIC) data are shown. In this figure, ellipses represent the bin-to-bin uncertainty while the dashed bars summarize all additional uncertainties, including the instability of the fit. The freeze-out temperature ($T_{\text{kin}} = T_{\text{fo}}$) decreases towards more central events, while the average transverse flow increases ($\langle\beta_T\rangle = \langle\beta_r\rangle$). This centrality dependence can be understood as a more rapid medium expansion in central events [29]. The larger values of T_{fo} for peripheral events indicate a shorter lived fireball with less time to build up radial flow. As a consequence, the decoupling of the particles from the medium occurs at higher densities and temperatures [30]. The STAR data is systematically below the ALICE data for a given centrality. In the better comparable observable, the particle multiplicity, both are aligned within uncertainties [28]. In central 0-5% ALICE events the resulting fit parameters are
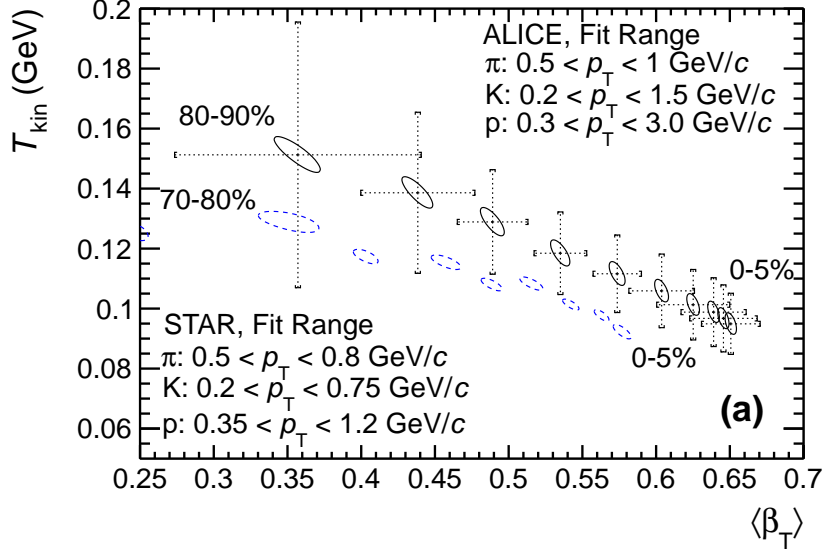
Figure 3.3: Combined Blast-Wave fit results for ALICE and STAR data. Both experiments use the same particle species but slightly different fit ranges. [28]

$\langle \beta_r \rangle = 0.651^{\pm 0.004 \pm 0.020}$, $T_{\text{fo}} = 0.095^{\pm 0.004 \pm 0.010}\,\text{GeV}/c$ and $n = 0.712^{\pm 0.019 \pm 0.086}$ [28]. The radial flow measured at the LHC is approximately 10% larger compared to RHIC. The extracted values of the kinetic freeze out temperature are similar [31].

3.2.2 Anisotropic Flow

As one can see from Fig. 3.4, the overlap region in the *x*-*y*-plane is non-spherical in non-central heavy-ion collisions. Instead, it has an almond shape. This asymmetry in the azimuth results in varying pressure gradients. They are strongest at the shorter half-axis and weakest at the longer axis. The plane, which is spanned by the trajectory of the nuclei and the shorter half-axis, the impact parameter *b* of the overlap region, is called the reaction plane Ψ_{RP}. The variation of the gradient in respect to the azimuth angle should lead to an isotropic distribution of dN/dφ and a collective momentum shift, depending of the size of the gradient. Low and intermediate p_{T} particles close to the reaction plane (in-plane direction) should have, on average, a larger momentum compared to particles which are emitted in out-of-plane direction. In contrast, hard particles should not show such a strong collective behavior. Due to other reasons, they may however also

show an anisotropy. This is not caused by collective behavior but is related to jet production discussed in Sec. 3.3.
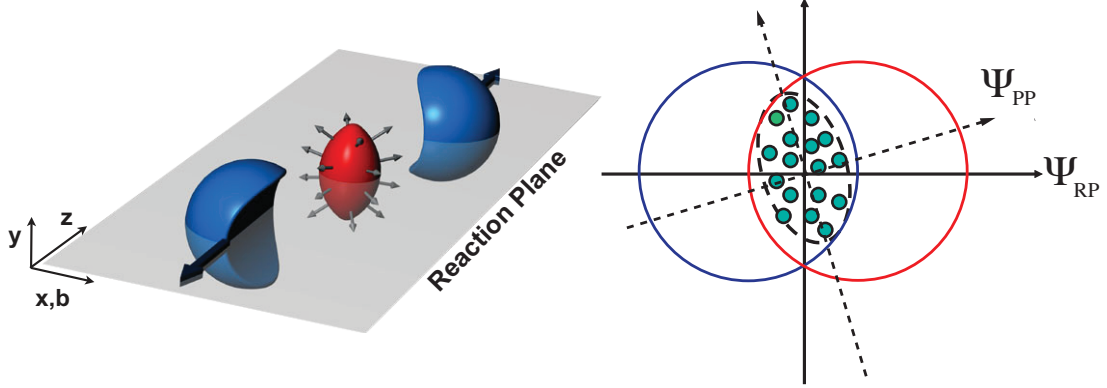
Figure 3.4: Left: Three-dimensional sketch of a semi-central heavy-ion collision with the typical almond shaped overlap region of the two nuclei. Right: Transverse plane of a heavy-ion collision. The participating nucleons are sketched as green points. Depending on the participant distribution, the reaction plane Ψ_{RP} may differ from the participant plane Ψ_{PP}. [15]

These general considerations should lead to the experimentally testable situation of the hydrodynamic picture. Particles should have an asymmetry in the azimuth depending on the centrality of the collision. This was first considered as a signal of collective flow in [32]. In the standard approach, the particle spectra are described with a Fourier expansion [33]:

$$E\frac{\mathrm{d}^3N}{\mathrm{d}^3p} = \frac{\mathrm{d}^2N}{2\pi p_{\mathrm{T}}\mathrm{d}p_{\mathrm{T}}\mathrm{d}y}\left(1 + 2\sum_{n=1}^{\infty} v_n \cos\left[n(\varphi - \Psi_n)\right]\right). \qquad (3.5)$$

The angle Ψ_n is the angle in respect to the maximum anisotropy for the n-th order of the Fourier series ($\Psi_2 \approx \Psi_{RP}$). The magnitude of the contribution of the order n is given by the flow coefficient v_n. It characterizes the size of the collective flow order by order. The Fourier coefficient v_n can be calculated as an event average over all particles with $\phi \equiv \varphi - \Psi_n$ and is defined as follows:

$$v_n(p_{\mathrm{T}}) = \frac{\int \mathrm{d}\phi \cos{(n\phi)}\frac{\mathrm{d}N}{\mathrm{d}\phi}}{\int \mathrm{d}\phi\frac{\mathrm{d}N}{\mathrm{d}\phi}} = \langle\cos{(n\phi)}\rangle. \qquad (3.6)$$

The angle Ψ_n has to be determined on event-by-event basis. With the most simple approach, it is directly extracted from the azimuthal asymmetry found in respect to the reaction plane. Alternatively, more advanced methods could be

used [34, 35]. Due to the finite number of particles used for the determination, the angle which defines the maximum anisotropy in a single event may fluctuate around the reaction plane angle Ψ_{RP}. This, on event basis defined plane, is called participant or event plane Ψ_{PP} and is additionally shown in Fig. 3.4.

The first harmonic v_1 of Eq. (3.5) is called directed flow. It represents the deflection from the beam direction of the two nuclei after the collision [36]. The v_1 component is small at mid-rapidity and will not be discussed. The second harmonic v_2 is called elliptic flow. It is caused by the previously described almond (elliptic) shape of the interaction volume of a non-central heavy-ion collision. It should be small for most central events where the elliptic shape of the overlap region vanishes and becomes spherical. It is the main observable in the anisotropic flow analysis. Higher harmonics like v_3 (triangular flow) should depend much less on centrality and are expected to be caused by fluctuations of the initial geometry and of local maxima of the energy density in the interaction volume. The same is true for even higher orders of flow coefficients. They should be only weakly correlated with the reaction plane and centrality [37, 38].

Not only the existence of a centrality dependent v_2 coefficient but also the size for different particle species is an important contribution to support the hydrodynamic picture of heavy-ion collisions. It is predicted that the size of v_n should depend on the particle mass with less flow for heavier particles at fixed p_T. In Fig. 3.5, the elliptic flow coefficient is shown for several particle species against p_T measured with ALICE [39]. The collective motion of the medium can be understood as a blast wave (3.3) leading to a similar flow velocity of all affected particles. Therefore, heavier particles will be shifted to higher momenta, clearly visible in Fig. 3.5. The plotted colored curves originate from viscous hydrodynamic calculations [40]. They are able to reproduce the measured flow within uncertainties.

The elliptic flow measured at the LHC is larger compared to RHIC results and seems to grow with collision energy [15, 34, 41]. RHIC data can be modeled with ideal hydrodynamics [42]. LHC data seems to suggest a less perfect fluid. A crucial quantity for the description of the ALICE data is the shear viscosity η normally quoted as η/s (entropy density s) of the medium [43]. This might be caused by the sensitivity at LHC energies to the the strong coupled plasma phase, while RHIC results are dominated by the hadronic phase closer to an ideal gas [44].

Most recent studies and advanced analysis techniques result in $1 < 4\pi(\eta/s)_{QGP} < 2.5$ [45] as upper and lower limits for ALICE data. It is very small if considering the theoretical quantum limit of $4\pi\eta/s \geq 1$ [46]. The shear viscosity over entropy
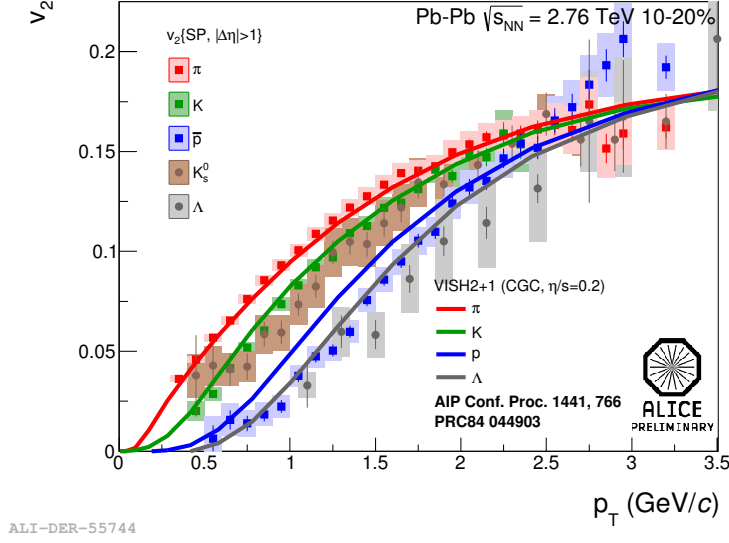
Figure 3.5: Elliptic flow measurements of identified particles with ALICE compared to hydrodynamic (viscous hydro) models. The model includes different particle masses as well as a non-perfect, viscous fluid. It is able to describe the data very precisely, strengthening the hydrodynamic picture. [39, 40]

density is normally extracted by fitting results of calculations with different η/s to the p_T and/or centrality dependent flow measurements.

Flow is developed during the whole time evolution of the expanding medium after thermalization. Therefore, the measured flow of hadrons, as shown in Fig. 3.5, reflects the size of the flow at freeze-out. As we will see in Sec. 4.2 photons are emitted during the whole evolution process and its flow carries information about its production time.

3.3 Nuclear Modification of Particle and Jet Spectra

In the absence of any medium effects in heavy-ion collisions, a nucleus-nucleus collision can be pictured as a superposition of multiple single nucleon-nucleon collisions. In general, this scaling can only hold for hard processes ($p_T \gtrsim 2\,\text{GeV}/c$) as discussed in Sec. 3.1. It is normally referred to as binary or point-like scaling.

In case of the presence of an interacting medium, observables like the p_T spectra of particles are modified. The quantity which quantifies the modification of spectra

is called the nuclear modification factor R_{AA}. It is defined as:

$$R_{\mathrm{AA}} = \frac{\mathrm{d}^2 N_{\mathrm{AA}}/\mathrm{d}p_{\mathrm{T}}\mathrm{d}y}{\langle T_{\mathrm{AA}}\rangle \mathrm{d}^2 \sigma_{\mathrm{pp}}/\mathrm{d}p_{\mathrm{T}}\mathrm{d}y}. \qquad (3.7)$$

In this formula, the numerator is the particle spectrum measured in heavy-ion collisions and the denominator the cross section of the same particle measured in pp collisions. For the point-like scaling, the pp cross section is weighted with the nuclear thickness function $\langle T_{AA}\rangle$. It can be calculated from a Glauber Model [47].

In the Glauber Model, two density functions for the two interpenetrating nucleons are assumed on a straight trajectory. From this, the number of binary collision N_{coll} can be deduced for any given impact parameter b. For the nuclear thickness function follows approximately:

$$\langle T_{\mathrm{AA}}(b)\rangle = \frac{\langle N_{\mathrm{coll}}\rangle_b}{\sigma_{\mathrm{NN}}}, \qquad (3.8)$$

with the inelastic cross section of nucleon-nucleon collisions σ_{NN}. Normally the calculation is done on Monte Carlo level [48] to include event-by-event fluctuations which will also occur in real collisions. The index b indicates that the number of binary collisions depends predominantly on the impact parameter of the collision.

If the binary scaling holds, then the R_{AA} is close to unity in the hard p_{T} region. Even simply considered it is not expected, even without any medium, that the scaling works perfectly. Nuclei are not built of protons exclusively but also have neutrons as constituents. Both nucleon types have a different quark substructure and are not isospin symmetric. It is also expected that nucleons bound in nuclei interact differently compared to free nucleons. The dominant modifying mechanisms are nuclear shadowing [49], gluon saturation [50] and the Cronin effect [51, 52].

The first two effects, connected with the initial properties of the two incoming projectiles, are called initial-state effects. The latter effect is caused by multiple parton scattering. All can be studied very precisely in nucleon-nucleus (pA) collisions where no hot medium is expected to be created [53].

If a medium is formed, the modification is expected to be significantly larger. From a QCD perspective, many possible sources of modification are suggested [54]. It is expected that partons traversing a strongly interacting quark-gluon plasma will lose energy by soft gluon radiation and by multiple scattering with partons in the medium. This loss should depend on the parton masses with heavy quarks losing less energy (dead-cone effect [55]). Also, gluons are expected to lose more energy due to their larger color charge [56].
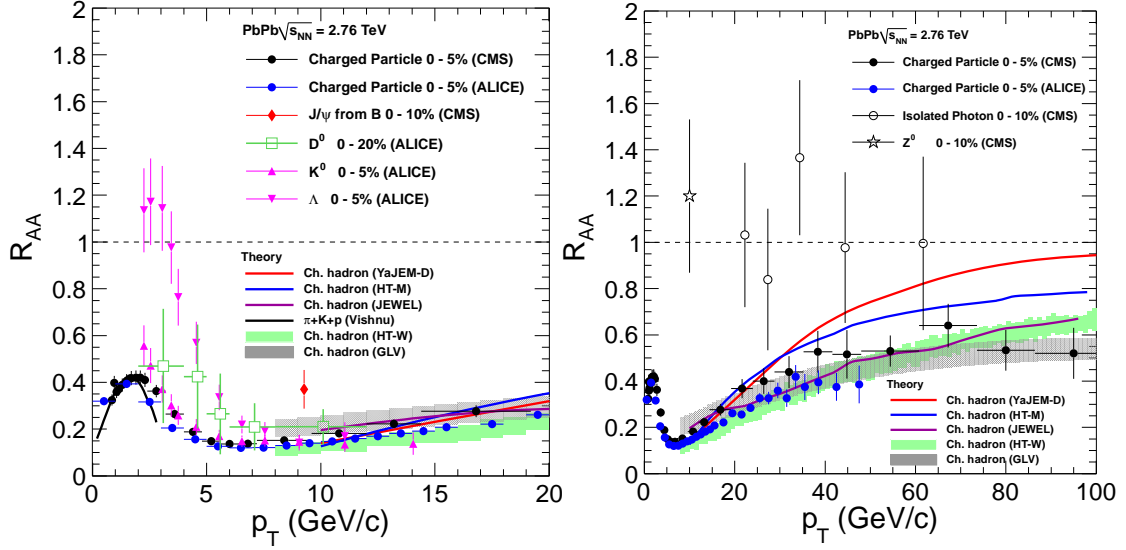
Figure 3.6: Particle nuclear modification factors R_{AA} for various particle species at $\sqrt{s_{\mathrm{NN}}} = 2.76\,\mathrm{TeV}$ measured by ALICE, ATLAS and CMS. The focus is on low (left) and high p_{T} (right), respectively. While hadrons show a strong suppression, weak Z^0 and electromagnetic probes are not modified. [58–62]

Not only hard scattered particles are modified by the strongly interacting medium. The low p_{T} part of the particle spectra, dominated by soft particles, will be modified by the collective motion discussed in the previous section (Sec. 3.2). As already mentioned in Sec. 3.1, the related production mechanisms are not expected to scale with the number of binary collision. The medium effects on soft and hard particles are referred to as final-state effects and take place after the initial collisions and the corresponding initial-state effects.

The large modification, visible in the N_{coll} scaled spectra, was first observed by the PHENIX collaboration at an energy of $\sqrt{s_{\mathrm{NN}}} = 130\,\mathrm{GeV}$ [57]. Fig. 3.6 shows more recent modification factors with respect to the low p_{T} (left) and high p_{T} part (right) measured at LHC. Heavier particles are less suppressed compared to lighter particles, as one can see from Λ and kaon measurements in comparison to the inclusive charged particle R_{AA}. State of the art hydrodynamic simulations at LHC collision energies are able to describe the effect very accurately [63]. It can be explained by the size of the radial flow. The large discrepancy between the meson and baryon (here Λ, but also seen for protons) suppression is not caused exclusively by the higher mass. The modification factor of the ϕ meson, which has a similar mass as a proton, is comparable to the modification factor of lighter mesons [64]. A possible explanation is that the baryons gain more p_{T} since they are built of three quarks.

The largest suppression is measured at $p_{\mathrm{T}} \sim 7\,\mathrm{GeV}/c$ with a factor of approximately ten. At this transverse momentum value, the spectra are dominated by particles produced in hard processes. The suppression is similar within the uncertainties in LHC [65–68] and RHIC [69–72] data with clear trend towards stronger suppression at LHC energies. The suppression at high p_{T} of particles containing heavy quarks like D^0 K^0 or J/Ψ [73, 74] is comparable to the suppression of lighter [75] particles.

At even higher momenta, the suppression is less pronounced. This feature was not seen at RHIC energies. Its appearance helps to test several energy-loss models which have to describe this rise rather than just a constant value. Some models are additionally plotted in Fig. 3.6 [58–62] but are not discussed in this context.

If the high energy-loss of particles is caused by a strongly interacting medium, weak and electromagnetic probes are not affected. Within uncertainties, this is the case for isolated photons [76, 77] and for the Z^0 boson [78] (Fig. 3.6 (right)). Thus, the measurement of high p_{T} electromagnetic and weak probes, where medium sources are not expected, is an important test of the assumed N_{coll} scaling.

The disadvantage of single particle R_{AA} is that it does not directly represent the energy loss of partons. Many particles can be produced from an initially hard scattered parton. Since the fragmentation process might also be affected by the medium, it is complicated to directly draw conclusions from single particle measurements. For that reason, experiments try to measure all particles originating from a single hard scattered parton.

From an experimental point of view it is not possible to identify all particles belonging to the fragmentation of one single quark or gluon. Nevertheless, many algorithms exist that try to reconstruct the initial parton energy. The resulting sum of particles is called jet. It is defined via a cone in the η-ϕ [79] direction or, in more modern approaches, by a sequential recombination [80, 81].

An important property of jets is that they are normally produced in pairs, back-to-back in azimuth with nearly the same transverse energy. By studying the energy disbalance of such jet pairs in heavy-ion collisions, the energy loss and the related medium characteristics can be extracted. A disadvantage of this method is caused by the unknown initial energy of the two scattered partons. A more direct approach to study the energy loss of hard partons is given by isolated- or direct-photon jet correlations [82, 83]. As discussed, photons are not affected by the strongly interacting medium. The energy difference between the photon and the jet is directly related to the energy loss. The production mechanisms of such photons, also called prompt photons, are discussed in the next chapter.

4 Photon Production in Hadronic Collisions

Particle production can be separated via momentum transfer into hard and soft mechanisms. The main reason for this separation is the Q^2 dependent coupling of QCD as introduced in Sec. 2.2. For large momentum transfers, the coupling becomes weak and the resulting hard process can be described in the context of perturbative QCD. In contrast, soft particle production can only be described by non-perturbative effective models [84, 85]. This kind of physics will not be discussed here. In heavy-ion collisions, soft particle production is governed by the evolution of the hot medium. Therefore, the production can be well described by hydrodynamic models combined with particle production rates. Additionally, microscopic approaches exist for the description of the radiation of heavy-ion collisions, like transport models.

In this chapter, the photon production in hadronic collisions is discussed. Many underlying concepts are identical for nucleon-nucleon and nucleus-nucleus collisions. Some are unique for heavy-ion collisions. In general, photons are separated in two groups. The first consists of decay photons, originating from the decays of hadronic particles. The second group, the direct photons, will be discussed in the following sections. In principle, every photon not produced via a particle decay is considered as a direct photon.

4.1 Hard Particle Production - Parton Distribution and Fragmentation Functions

Like all final state particles, photons can be produced during the initial collision. The theoretical description of the production is similar for photons and hadrons. Therefore, the general picture of particle production is introduced first. An important difference is that photon production is always based on an electromagnetic interaction.

The hard production of particles can be described by quark and gluon interactions in the pQCD framework. It is called the QCD improved parton model. In a general ansatz for the particle production, cross section $\sigma^{AB\to X}(P_1,P_2)$ of two colliding hadrons A and B with momentum P_1 and P_2 producing a particle X can be written under the assumptions of the factorization theorem [86]:

$$\sigma^{AB\to X}(P_1,P_2) = \sum_{a,b,c} \int \mathrm{d}x_1 \mathrm{d}x_2 \mathrm{d}z f_a(x_a,Q^2) f_b(x_b,Q^2) \hat{\sigma}_{ab}(p_1,p_2,\alpha_S,Q^2) \times D_c^X(z,Q^2).$$

$$(4.1)$$

The momentum fractions of the two interacting partons a,b in the two hadrons are $p_1 = x_1 P_1$ and $p_2 = x_2 P_2$. The cross section of the interaction of the two partons is given by $\hat{\sigma}_{ab}$ and can be calculated order-by-order in perturbative theory. It exclusively includes the short distance or equivalently the short time-scale interactions.

In this ansatz, the incoming hadrons and the contained quarks and gluons are characterized by Parton Distribution Functions (PDF). In Eq. (4.1) these functions are represented by f_a and f_b, for every parton type a,b. The PDFs describe the probability of being found in the hadron with the momentum fraction x for each parton species. An example set of proton PDFs are shown in Fig. 4.1. At large x the valence quarks defining the hadron can be found. Below $x \sim 10\times^{-2}$ gluons dominate. The second largest contribution at small x is given by the sea quarks.

The fragmentation of the scattered quark or gluon c to the final state hadron X is given by Fragmentation Functions (FF) $D_c^X(z,Q^2)$. These functions describe the probability of the scattered parton producing a final state particle X carrying the momentum fraction z of the parton momentum.

4.1.1 Prompt-Photon Production

In general, hard photon production can be described with Eq. (4.1). Such photons are commonly called prompt photons. The main difference to the general approach is that the production of photons does not require a Fragmentation Function in each case. A photon is already a final state object. On the other hand, photons can be produced during the fragmentation process of quarks and gluons. Such production again requires a FF. Hence, the total photon production cross section in next-to-leading order (NLO) can be written as [88]:

$$\sigma^\gamma = \sigma^{(F)} + \sigma^{(D)}.$$

$$(4.2)$$
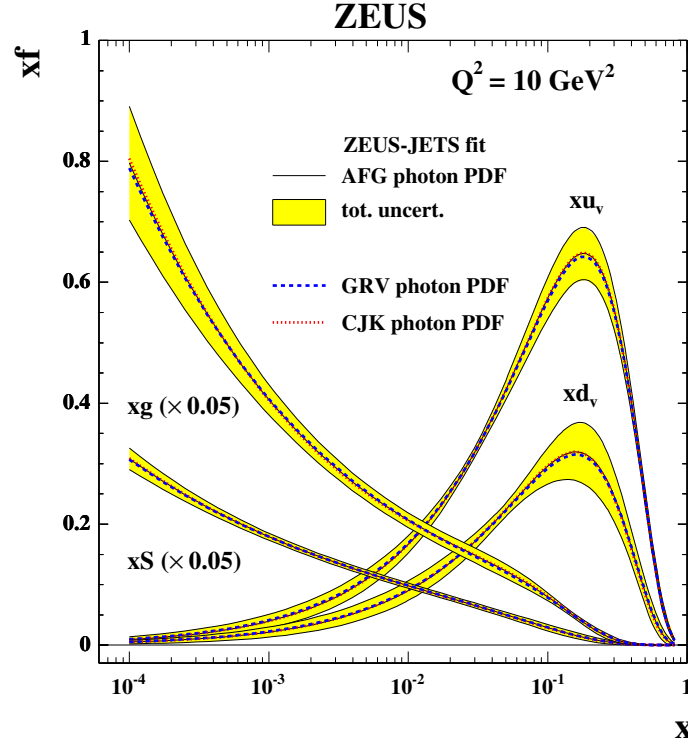
Figure 4.1: Proton PDFs measured by the ZEUS collaboration. Shown are the valence quarks u_v and d_v, the sea quarks S and the gluon distribution g. [87]

This summarizes the concept explained above: Like hadrons, photons can be produced via the fragmentation of scattered partons $\sigma^{(F)}$ or already during the initial hard scattering $\sigma^{(D)}$. The three dominating production processes are shown in Fig. 4.2 as Feynmann diagrams. The two graphs on the left hand side correspond
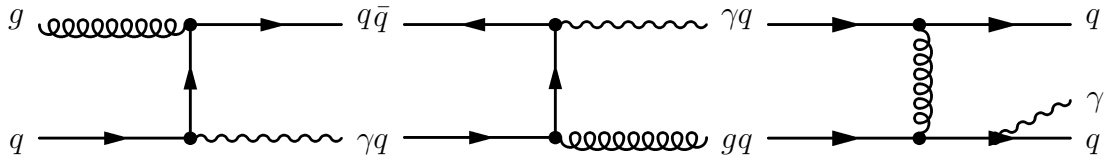
Figure 4.2: Leading order and next to leading order contribution to the prompt photons. (a) quark gluon Compton scattering (b) quark anti-quark annihilation (c) Bremsstrahlung or fragmentaion

to the two leading order production processes. These graphs are quark-gluon

Compton scattering ($q+g \rightarrow q+\gamma$) (left) and quark-antiquark annihilation ($q+\bar{q} \rightarrow g+\gamma$) (middle). Such processes produce photons without fragmentation. In NLO, many additional graphs contribute to the total production of prompt photons. One of those graphs is shown on the right hand side of Fig. 4.2. This graph represents fragmentation photons produced during the fragmentation of partons into hadrons. In addition, one-loop virtual contributions will enter and modify the first two graphs.

From the p_{T} distribution of prompt photons, the momentum fraction x of the initially scattered quarks or gluons can be estimated. In a collider experiment with the center-of-mass energy $\sqrt{s}$, each beam projectile carries $\sqrt{s}/2$. In a symmetric interaction of two partons, the momentum of each is consequently given by $p = x\sqrt{s}/2$. At mid rapidity ($\eta \approx 0$) with $p \approx p_{\mathrm{T}}$, the transverse momentum fraction x_{T} of the photon producing partons is:

$$x \sim x_{\mathrm{T}} = \frac{2p_{\mathrm{T}}}{\sqrt{s}}. \tag{4.3}$$

For LHC energies in the TeV regime, typical x values are on the order of 10^{-3} for photon momenta of several GeV/c. This result can be compared to the PDFs shown in Fig. 4.1. The photon production should be strongly dominated by gluons.

As a direct consequence, hard production mechanisms with gluons should dominate the prompt-photon production at LHC. Recent JETPHOX (pQCD NLO calculator [89]) studies for LHC energies [90], support the estimate of the previous paragraph. The resulting individual contributions to the total prompt-photon production are shown in Fig. 4.3. At high photon p_{T}, the quark-gluon Compton scattering clearly dominates the total production. At lower transverse momenta, photons are predominately produced in the fragmentation process of hard scattered gluons. As mentioned, Bremsstrahlung should be a sizable contribution at these low momenta.

With the current theoretical understanding of prompt-photon production in pp (or p$\bar{\text{p}}$) collisions, it is possible to describe the measured prompt-photon data over many orders of magnitude in p_{T} and x_{T}. A comparison between theoretical calculations and measured prompt-photon data is given in Fig. 4.4. The world data of prompt-photon invariant cross sections is in very good agreement with NLO pQCD calculations. On the right hand side, a ratio of measured over theory x_{T} values are presented. Only the E706 data differs clearly from the predicted x_{T} dependence.

It is notoriously difficult to measure prompt photons. Therefore, experiments often measure isolated photons instead. An isolated photon is defined as a photon
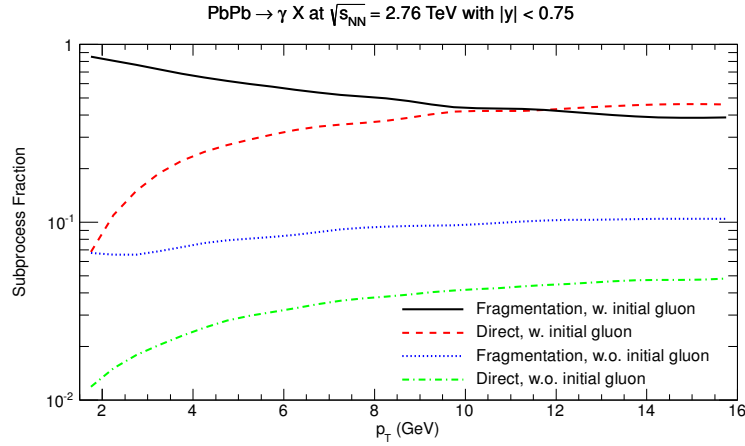
Figure 4.3: The single contributions to the total NLO prompt-photon cross section for Pb–Pb collisions at $\sqrt{s_{\mathrm{NN}}} = 2.76\,\mathrm{TeV}$. The fragmentation is the leading contribution for low transverse momenta. At the given center of mass energy processes with initial gluons (w. initial gluons) dominating the production. [90]
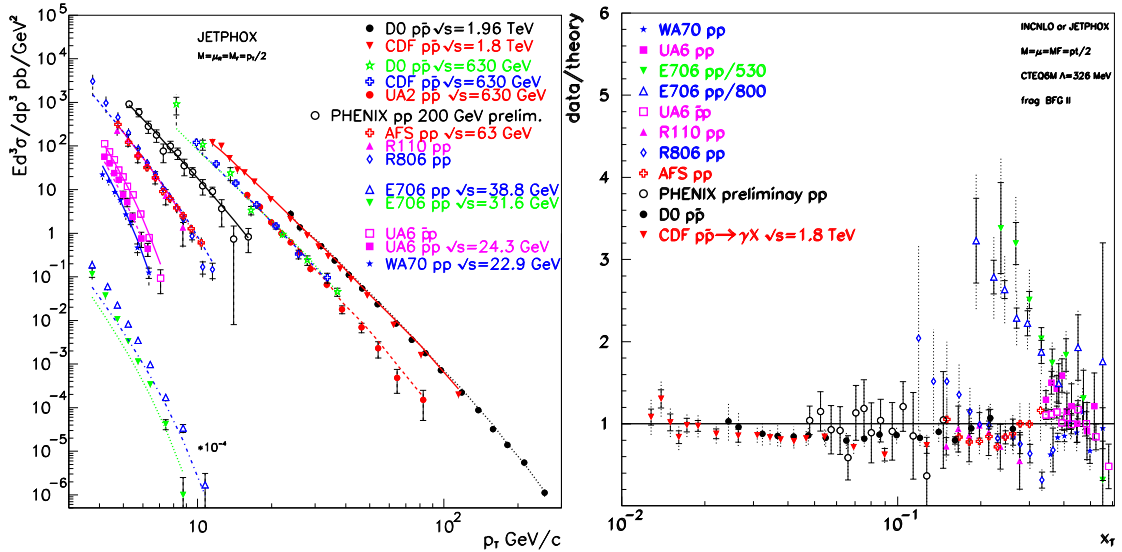
Figure 4.4: Comparison of x_{T} and p_{T} isolated prompt-photon data from pp and p$\bar{\mathrm{p}}$ collisions with JETPHOX predictions. A remarkable agreement between the theoretical calculations and the measured data over nine orders of magnitude is found. [88]

not surrounded by particles above a certain p_{T} threshold. At high p_{T}, the isolated photon spectrum should be very similar to the spectrum of prompt photons. This

is clearly expected for LO photons. They are produced as hard objects, just like a hard quark or gluon, but will not fragment into jets. In contrast, a high p_T decay photon will most likely be produced during the fragmentation of a jet and is thus surrounded by further particles. In addition, fragmentation photons (NLO) are normally produced in a hard fragmentation process. They carry a large fraction of the original parton momentum and only a minor part is transformed into hadronic particles surrounding the photon.

The production of prompt and fragmentation photons is comprehensively explained in [91]. In the next section, the modification of prompt-photon production in a heavy-ion environment is discussed.

4.1.2 Modification to the Prompt-Photon Production in Heavy-Ion Collisions

As stated in the end of the previous chapter (Sec. 3.3), photons do not interact with the QGP medium via the strong force. The electromagnetic interaction is weaker by more than one order of magnitude. The mean-free path of photons with an energy of $E_\gamma = 1\,\mathrm{GeV}/c$ in a QGP with $T = 200\,\mathrm{MeV}$ is approximately $\lambda = 430 - 480\,\mathrm{fm}$ [92, 93]. This is ~ 40 times larger than the medium size at its maximum extent at freeze-out. Thus, the medium is transparent for photons. Nevertheless, prompt-photon production is modified in the initial and final state of nucleus-nucleus collisions.

Initial State Effects
The initial state effects are introduced by a modified PDF, called nuclear Parton Distribution Function (nPDF). Two modifications exist. The first difference is dedicated to the composition of nuclei. In a nPDF, the different valence quark compositions of neutrons (udd) and protons (uud) have to be considered. In the standard approach, isospin symmetry is assumed [94]. No distinction is made between the PDFs of partons in a proton to partons in a neutron. The total nuclear PDF for each parton species is assumed as the weighted superposition of all individual parton contributions.

The second difference is related to the interplay of the nucleons building the nucleus. For that purpose, each individual nucleon PDF $f_i^p(x,Q^2)$ is modified. This modification is expressed by an extra factor $R_i^A(x,Q^2)$. The modified PDF is given by:

$$f_i^A(x,Q^2) = R_i^A(x,Q^2)f_i^p(x,Q^2). \tag{4.4}$$

A typical modification factor is shown in Fig. 4.5. It depends on the momentum
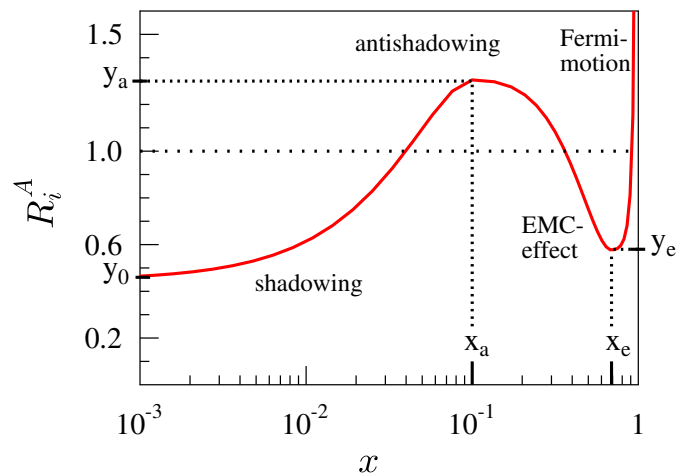
Figure 4.5: Parameterization of the free PDF nuclear modification factor for the EPS09 Nuclear Parton Distribution Function. [94]

fraction x of the partons and on the momentum transfer. The difference to the free PDF is found experimentally by comparing the obtained structure functions of pA or AA collisions with pp or pd (neutrons) results. The modification factor typically has four distinct regions separated in x. At small x, the probability of parton interactions is reduced. This region is called shadowing region, the effect Nuclear Shadowing [49, 50]. It is understood as a destructive interference effect within the nucleus. It is compensated by the anti-shadowing region at slightly larger x. The EMC-effect seems to have a complicated origin and is not yet fully understood. Due to Fermi-motion, the modification factor is strongly enhanced for large x values.

Final State Effects

The second modification of prompt-photon production in heavy-ion collision is expected in the final state, even though a photon is a color neutral object. Not the photon is modified by the medium, but the quarks traversing the hot partonic matter will be affected in their momentum. As discussed in Sec. 3.3, the parton will lose energy available for fragmentation by multi gluon-radiation or multiple scattering. This will also affect the momentum distribution of fragmentation photons. The missing parton energy can be considered in a simple approach by the rescaling of the parton energy fraction z of the fragmenting parton to a reduced value $z^\star$. This results in a modified in-medium Fragmentation Function which is

defined as [95]:

$$zD_{\gamma/i}(z) = \int_0^{k(1-z)} d\epsilon P_i(\epsilon,k) z^\star D_{\gamma/i}(z^\star) \qquad \text{with} \qquad z^\star = z/(1-\epsilon/k) \qquad (4.5)$$

The energy-loss fraction of the parton with momentum k is given by ϵ/k. The updated FF is deduced by integrating over all possible energy losses from zero to $k(1-z)$. The probability of a parton i losing the energy fraction ϵ/k is given by the probability distribution $P_i(\epsilon,k)$.

With the modifications described in this section, more precise prompt-photon predictions are expected. It must be mentioned that the magnitude of the modification is small, and the uncertainties of the measured spectra are large. Results on the isolated photon production in Pb–Pb collisions obtained by the CMS collaboration in 0-10% most central events are shown in Fig. 4.6 [76]. In the figure,
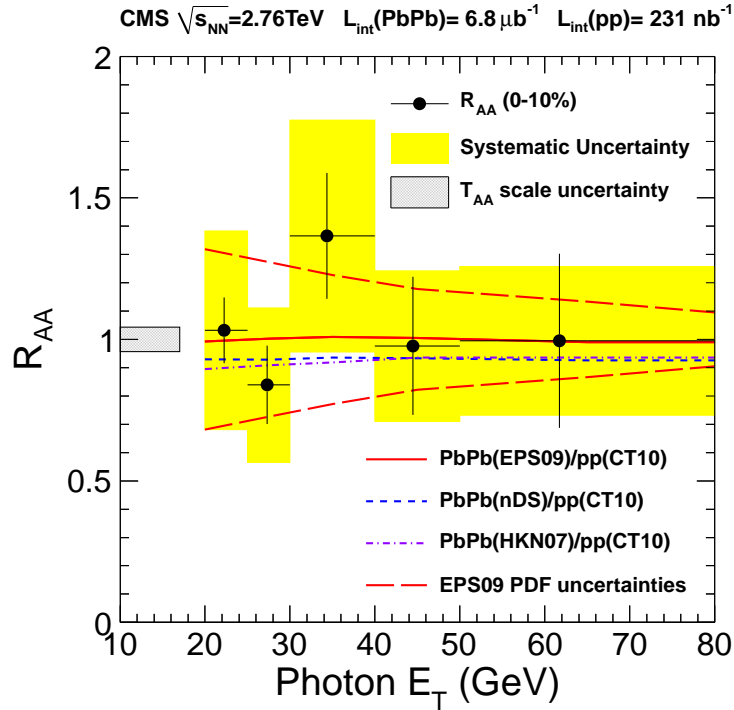
Figure 4.6: Nuclear modification factor R_{AA} of isolated photons measured by CMS in 0-10% most central events. For comparison, pQCD predictions using several (nuclear) PDFs are shown. [76]

the isolated-photon nuclear modification factor is shown. For comparison, various NLO pQCD predictions obtained with different (nuclear) PDFs are presented.

Within the large uncertainties, no deviation from the theory is found. Similar results are reported by ATLAS [96] and at lower energies at RHIC [97]. However, no large difference is expected.

4.2 Soft Production in Heavy-Ion Collisions - Medium Sources of Direct-Photons

The experimentally and theoretically more challenging part of direct-photon measurements in heavy-ion collisions is related to the medium [98–100]. In case of the creation of a QGP, the thermalized partons are expected to produce photons by similar reactions as shown in Fig. 4.2. These photons have been considered as an indication of the formation of a QGP state since 1975 [101].

Photons produced by the interaction of thermalized particles are called thermal photons. Not only the partonic stage produces thermal photons. The subsequent hot hadronic gas (HHG) will also emit thermal photons. The different contributions have to be well understood theoretically to distinguish partonic and hadronic sources and judge the existence of a QGP phase.

Several models exist which calculate the direct-photon production in heavy-ion collisions. The most direct approach is the microscopic Parton-Hadron-String-Dynamics (PHSD) model [102–104]. This off-shell transport model is able to describe all interactions starting directly after the initial scattering to the end after the hadronic freeze-out.

The most common approaches are macroscopic models. They use either a parameterized expanding fireball [105, 106], ideal [107, 108] or viscous [109, 110] hydrodynamics. In the fireball model, the medium has a single temperature, governed by conservation laws, for each time. The expansion of the medium is added externally by connecting the center of the fireball to its surface with an externally added flow velocity. The hydrodynamic models assume an ideal or viscous fluid. The temperature profile and, in contrast to the fireball model, the flow velocity are calculated by solving the relativistic equation of motion of the fluid. To get a more realistic description, event-by-event fluctuations are added in some models to the initial profile and are sampled via a Monte Carlo approach. All models have in common that the additional contributions from prompt photons produced during the initial collisions have to be estimated with other approaches. Normally, measured pp direct-photon spectra or pQCD NLO predictions are used.

With the known time evolution of the medium, the photon yield is calculated with photon rates. These rates depend on the medium temperature. In the kinetic

approach (PHSD), the rates are directly obtained by the integration over the full available phase space with partonic and hadronic matrix elements. The final rate is deduced by summing all individual processes. An alternative approach used by the hydrodynamic or fireball models are rates calculated with the photon self-energy $\Pi_\mu^{N,\mu}$. This non-perturbative approach relates the in-medium production rates of photons with the imaginary part of the self-energy polarization tensor [111, 112]. It has the advantage that it contains intrinsically all orders of photon productions. The full rate is given by [102]:

$$E\frac{\mathrm{d}N}{\mathrm{d}^3p} = -\frac{2}{(2\pi)^3}\frac{1}{\exp{(E/T)}-1}\operatorname{Im}\Pi_\mu^{N,\mu}. \qquad (4.6)$$

The photon self energy can be expanded in single diagrams and perturbatively expressed order-by-order. For the leading order production, given again by the first two diagrams in Fig. 4.2, the photon production rate is reduced to:

$$E\frac{\mathrm{d}N}{\mathrm{d}^3p} \propto \alpha\alpha_S T^2 \exp\left(-\frac{E}{T}\right)\ln\left(\frac{ET}{m_0^2}\right). \qquad (4.7)$$

The parameter m_0 represents the in-medium quark masses. The masses should be modified in the QGP due to the chiral symmetry restoration. Consequently, the rates as given by Eq. (4.7) additionally depend on the in-medium behavior of quarks. For the total photon yield, all temperature cells or profiles of the modeled medium are folded with the medium evolution. For large photon energies, E, compared to the medium temperature T, follows from Eq. (4.7) an exponential shape of the thermal-photon spectrum at LO:

$$E\frac{\mathrm{d}N}{\mathrm{d}^3p} \propto \exp\left(-\frac{E}{T}\right)\Bigg|_{E\gg T}. \qquad (4.8)$$

The partonic medium will additionally produce Bremsstrahlung photons. Bremsstrahlung is expected to be reduced by the Landau-Pomeranchuk-Migdal (LPM) effect [113]. The energy shift of the fragmentation photons was already discussed in Sec. 4.1.2. On the other hand, the fragmentation component could also be enhanced by medium-induced photon Bremsstrahlung. An additional source of photons with unknown magnitude are jet-photon-conversions [114–116].

The magnitude of the several contributions are under current theoretical discussion [117, 118]. Also not included in most models is the photon production of the early non-thermalized medium. Some argue that the early stage is highly gluon dominated. In the absence of electric charges, the LO contributions (Fig. 4.5)

should be suppressed accordingly [119]. In contrast, the high initial temperatures could level this effect [120].

The theoretical description of the HHG phase in the hydrodynamic models is based on the interaction of thermalized hadrons in a heat bath. Effective models have to be formulated for this phase [102]. Only pions and ρ mesons are often considered exclusively in the models. The ρ has an important role due to the vector meson dominance (VMD) [121]. In the lowest order, photons are produced by $\pi^+ + \pi^- \to \rho + \gamma$ (pion annihilation), $\pi^\pm + \rho \to \pi^\pm + \gamma$ (mesonic Compton Scattering) and the in medium decay of the $\rho \to \pi^+ + \pi^- + \gamma$. More advanced models also include η and ω mesons. Some calculations additionally consider K and $K^\star$ [105] or even the a_1 [122]. Future calculations will also have to include baryonic sources of thermal photons.

It can be concluded that the medium will produce additional direct photons. The energy of the photons is related to the energy density of the thermalized medium and thus to the photon producing particles. Thus, the transverse momentum differential yield of direct photons should be enhanced at low p_T compared to pp data or pQCD calculations. At intermediate p_T, additional photons from jet-medium conversion are expected. The size of this enhancement is under current theoretical discussion. At high p_T, the modification is caused by initial effects and by the in-medium modification of the FF. In ATLAS and CMS measurements, no significant deviation from calculated hard photon production is found (Fig. 4.6).

4.3 Production of Decay Photons

Direct photons are only a small fraction of all photons produced in hadronic collisions. The dominating source of photons are the decays of particles. The largest contribution to the total decay-photon spectrum is the decay $\pi^0 \to \gamma + \gamma$. The neutral pion is produced with a very high rate and the branching ratio (BR) of the decay is large (98.798%). The two photon decay of the η meson $\eta \to \gamma + \gamma$, with a BR of 39.30%, is the second largest contribution. The third largest contribution of decay photons is produced by the ω meson. It decays into a photon by $\omega \to \pi^0 + \gamma$ (BR: 8.28 %). All additional particles which have photon decay branches do not significantly contribute to the total decay-photon spectrum. The most important decays are listed in Tab. 4.7.

Heavier particles decay into lighter particles. This feed-down will produce particles which might decay into photons. One important contribution is the process $\eta \to \pi^0 + \pi^0 + \pi^0$ (32.56 %) or $\omega \to \pi^+ + \pi^- + \pi^0$ (89.2 %). The K_s^0 also contributes by $K_s^0 \to \pi^0 + \pi^0$ (30.69 %).

Particle	Mass (MeV)	Decay	Branching Ratio
π^0	134.98	$\gamma\gamma$	98.789%
		$e^+e^-\gamma$	1.198%
η	547.3	$\gamma\gamma$	39.21%
		$\pi^+\pi^-\gamma$	4.77%
		$e^+e^-\gamma$	$4.9 \cdot 10^{-3}$
ρ^0	770.0	$\pi^+\pi^-\gamma$	$9.9 \cdot 10^{-3}$
		$\pi^0\gamma$	$7.9 \cdot 10^{-4}$
ω	781.9	$\pi^0\gamma$	8.5%
		$\eta\gamma$	$6.5 \cdot 10^{-4}$
η'	957.8	$\rho^0\gamma$	30.2%
		$\omega\gamma$	3.01%
		$\gamma\gamma$	2.11%
ϕ	1019.5	$\eta\gamma$	1.3%
		$\pi^0\gamma$	$1.25 \cdot 10-3$
		$\omega\gamma$	$< 5\%$
Σ^0	1192.6	$\Lambda\gamma$	100%

Figure 4.7: Most important meson and baryon decays with photon decay branches. All values are taken from [6].

The final composition of all photons discussed in this section are sketched for central Au–Au collisions in Fig. 4.8. The figure is taken from [123]. Decay photons dominate for low and intermediate momenta. Only at very high p_T do the hard produced prompt photons exceed over all other contributions. The largest component of direct-photons at low momenta are thermal photons. Jet-medium conversions are not considered in the sketch. The momentum ranges quoted for the intersection of the individual components are for LHC energies at larger values of p_T. Due to higher temperatures and collision energies, the thermal and decay-photon spectra are harder.

Central Au+Au at RHIC
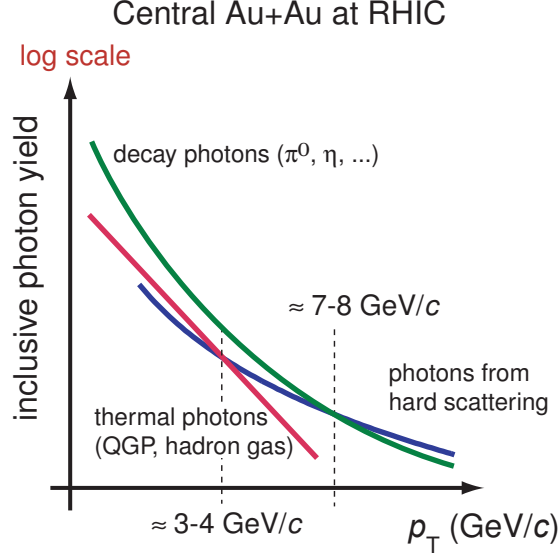
Figure 4.8: Different contribution to the total photon yield expected in Au–Au at $\sqrt{s_{\mathrm{NN}}} = 200\,\mathrm{GeV}$. [123]

4.4 Direct-Photon Spectra Measurements by PHENIX at RHIC

PHENIX has measured direct photon transverse momentum spectra in pp and Au–Au collisions at $\sqrt{s_{\mathrm{NN}}} = 200\,\mathrm{GeV}$. The results are shown in Fig. 4.9. The high p_{T} pp and Au–Au data points are measured via calorimeters [97, 124–126]. The low p_{T} data points are measured with two different methods. The older results, published in [127], are obtained by the measurement of virtual photons, e^+e^- pairs. The method is described later in this section. In addition, PHENIX has shown Au–Au direct-photon spectra obtained with real photons [128]. The method differs only slightly from the method applied in this thesis. It will not be discussed in this section. The two results (virtual, real) agree nicely within uncertainties (left: blue points and black open triangles). A clear enhancement in Au–Au is found by comparing to an extrapolated and N_{coll} scaled pp spectrum (left) or to pQCD calculations (right, black line) [129].

4.4.1 Internal Conversion Method

The measurement of direct photons with virtual photons is called the internal conversion method [127, 130]. It will be briefly introduced in the following: Every
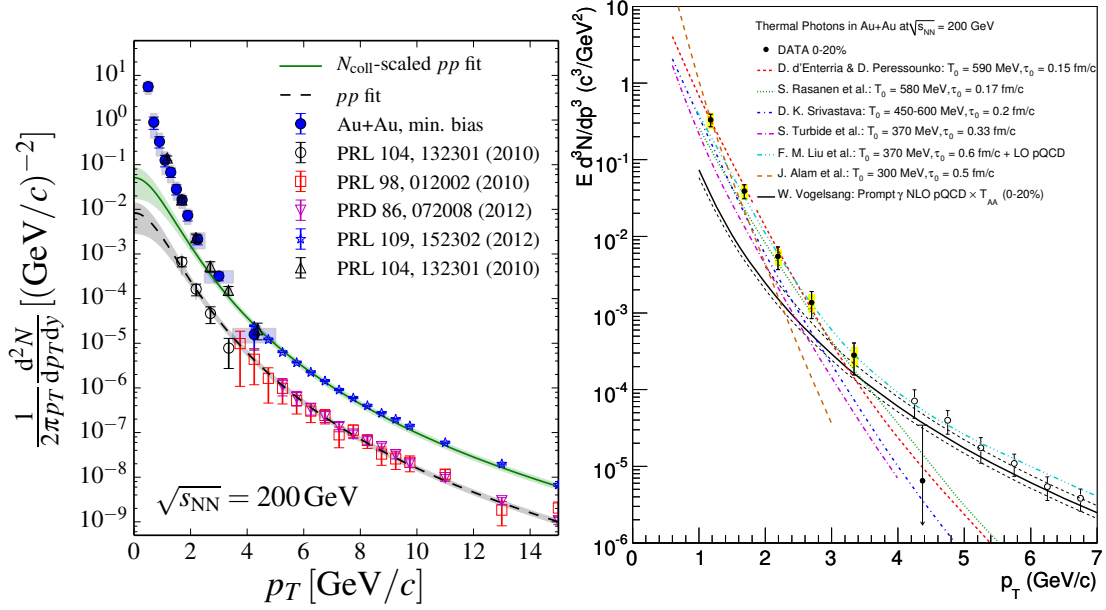
Figure 4.9: Left: PHENIX direct-photon spectra in pp and min. bias Au–Au collisions at $\sqrt{s_{\mathrm{NN}}} = 200\,\mathrm{GeV}$. [128] Right: Comparison of the Au–Au 0-20% centrality direct-photon spectrum [130] with several theory predictions [105, 108, 129, 131–133].

source of real photons will also produce virtual photons. These photons will convert if $m_{\gamma^{\star}} > 2m_e$ into a e^+e^- pairs, called di-electrons in this context.

The number of virtual photons and di-electrons is related. It can be expressed via a mass depended function $L(m_{ee})$. In addition, every process which produces real particles will also produce virtual particles. The difference in the yield between virtual and real particles is expressed by the mass and momentum dependent factor $S(m_{ee},q)$. In case of real di-electrons and virtual photons, the relation is given by the Kroll-Wada formula [134, 135]:

$$\frac{\mathrm{d}^2 N_{ee}}{\mathrm{d}m_{ee}\mathrm{d}p_{\mathrm{T}}} = \frac{2\alpha}{3\pi} \frac{L(m_{ee})}{m_{ee}} \frac{\mathrm{d}N_{\gamma^{\star}}}{\mathrm{d}p_{\mathrm{T}}} = \frac{2\alpha}{3\pi} \frac{L(m_{ee})}{m_{ee}} S(m_{ee},q) \frac{\mathrm{d}N_{\gamma}}{\mathrm{d}p_{\mathrm{T}}}. \qquad (4.9)$$

m_{ee} is the mass of the e^+e^- pair, and the di-electron yield is given by N_{ee}. The factor $S(m_{ee},q)$ generally depends on the form factors, phase space and spectral functions of particles producing photons. For the point-like direct-photon production with $m_{ee} \ll E_\gamma$, $S(m_{ee},q)$ becomes nearly unity. In addition, $L(m_{ee})$ is approximately one for "quasi-real" ($m_{ee} \to 0$) photons. This simplifies Eq. (4.9)

to:

$$\frac{\mathrm{d}^2 N_{ee}}{\mathrm{d}m_{ee}\mathrm{d}p_\mathrm{T}} \simeq \frac{2\alpha}{3\pi}\frac{1}{m_{ee}}\frac{\mathrm{d}N_\gamma}{\mathrm{d}p_\mathrm{T}}. \tag{4.10}$$

Fig. 4.10 shows the di-electron invariant mass spectrum for min. bias Au–Au collisions. Only pairs with $1\,\mathrm{GeV}/c < p_\mathrm{T} < 1.5\,\mathrm{GeV}/c$ are considered. The measured
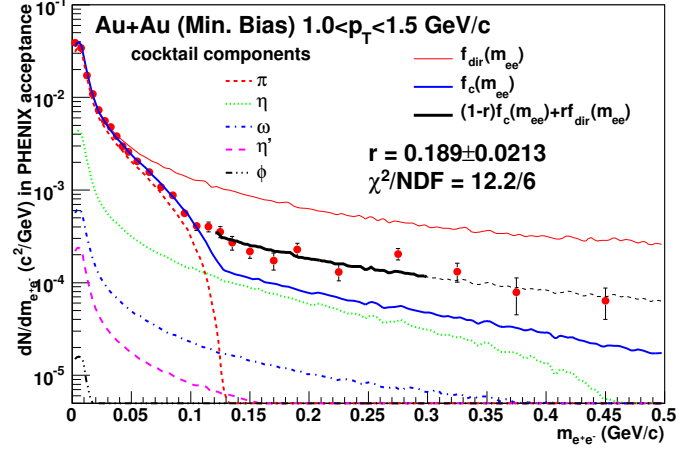
Figure 4.10: Minimum bias low mass di-electron spectrum from Au–Au collisions measured by PHENIX. [127]

di-electron spectrum is expressed by red dots. The dashed and dotted lines represent the calculated virtual decay-photon background contribution from π^0, η, ω, η' and ϕ Dalitz decays. The background is calculated with a similar method, as described in Chap. 9.

The direct-photon fraction r of virtual photons is obtained by a two component fit to the low mass di-electron spectrum. The fit is given by: $f_{\text{total}}(m_{ee}) = (1-r)f_c(m_{ee}) + rf_{\text{dir}}(m_{ee})$ and is additionally plotted in Fig. 4.10. It consists of a functional description of the background invariant mass spectrum $f_c(m_{ee})$ (blue line) and the expected $1/m_{ee}$ shape found in Eq. (4.10) of the direct-photon component $f_{\text{dir}}(m_{ee})$ (red line, arbitrary normalization). For a p_T differential direct-photon excess, the analysis is performed in various transverse momentum bins. The direct-photon spectrum is finally calculated from the excess $r(p_\mathrm{T})$ and the inclusive-photon spectrum by $r(p_\mathrm{T}) \times \gamma_{\text{inc}}(p_\mathrm{T})$.

5 The Large Hadron Collider and the LHC Experiments

In this chapter, the Large Hadron Collider (LHC) and the experiments installed at the LHC are introduced. After a brief description of the LHC and the other experiments, ALICE is presented in more detail. The sub-detectors, relevant for the presented photon measurement, and their working principles are explained. A brief overview over the tracking procedure and the primary vertex finding in ALICE is given. The analysis-software framework ROOT and its superstructure dedicated to the ALICE detector AliRoot are described.

5.1 The Large Hadron Collider

The Large Hadron Collider (LHC) is the world's largest particle accelerator and collider. It is located at the European Organization for Nuclear Research (CERN) in Geneva, Switzerland. It is designed to collide hadrons with hadrons. In an additional program, it is also suitable for colliding heavy ions like lead. In pp collisions, higher rates can be achieved since the production of anti-particles is challenging in the needed amount. Furthermore, it makes the collision of equally charged ions feasible.

First proton-proton collisions were provided to the experiments during 2009. These collisions had a center-of-mass energy of $\sqrt{s} = 900\,\text{GeV}$. The energy was increased in steps, from $\sqrt{s} = 2.76\,\text{TeV}$ to $\sqrt{s} = 7\,\text{TeV}$ and finally up to $\sqrt{s} = 8\,\text{TeV}$ in 2011. In late fall of 2010, the LHC accelerated and collided Pb–Pb ions with an energy of $\sqrt{s_{\text{NN}}} = 2.76\,\text{TeV}$ (center-of-mass energy per nucleon pair). The LHC is designed as a two-ring hadron accelerator and installed in the LEP (Large Electron Positron Collider) tunnel. The tunnel was build between 1984 and 1989. It has a perimenter of 26.7 km and has eight straight segments connected with eight arc sectors. The construction of the LEP tunnel and the injection system was realized with a larger diameter than needed. This gave room for a larger follow-up collider like the LHC. In addition to the LEP tunnel, two caverns for experiments are reused for the LHC.

Since the available space is limited inside the tunnel, a compact magnet design has to be used. The LHC operates superconducting magnets cooled by superfluid helium. Since it collides particles with particles (not anti-particles), it needs two opposite field configurations. They are provided by a complex field structure of one set of single magnets. For the two beams, two separated beam pipes are used, encompassed by the 1232 dipole magnets. All magnets share the same cryostat. Beam focusing is archived by 392 quadrupole magnets. The maximum field provided by the magnets is 8.33 T.

After the final upgrade, the LHC will collide protons with an maximum energy of $\sqrt{s} = 14$ TeV. More important for the ALICE experiment is the capability of colliding ions. The design energy for the heavy-ion collisions will be $\sqrt{s_{\mathrm{NN}}} = 5.5$ TeV per nucleon pair. The proton collisions will have a design luminosity $\mathcal{L} = 10^{34}$ cm^{-2}s^{-1}, the Pb–Pb collisions a luminosity of $\mathcal{L} = 10^{27}$ cm^{-2}s^{-1}, respectively.

Before particles are accelerated to these high energies inside the LHC, they pass several pre-accelerators. Protons are first accelerated to 50 MeV in the Linear Particle Accelerator LINAC2. They are further accelerated with the Proton Synchrotron Booster (PBS) up to 1.4 GeV and afterward with the Proton Synchrotron (PS) (26 GeV). The Super Proton Synchrotron (SPS) boosts the protons to an energy of 450 GeV. The final energy is reached after the protons are injected in one of the two beam pipes of the LHC.

Lead ions are accelerated slightly differently. After the vaporization of the lead and the selection of the Pb^{+29} state, the ions are accelerated in the LINAC3 up to an energy of 4.2 MeV per nucleon. A carbon foil is used to strip the ions down to the Pb^{+54} state. They are further accelerated (up to 72 MeV per nucleon) and are accumulated and cooled in the Low Energy Ion Ring (LEIR). Similar to the protons, they are further boosted in the PS (5.9 GeV per nucleon) and the SPS (177 GeV per nucleon). Between the two acceleration levels the ions reach their final ionization level of Pb^{+82} via an additional striping foil. Afterwards, the ions are injected into the LHC. The structure of the numerous (pre-)accelerators used at CERN are shown in Fig. 5.1. Additionally, the location of the different experimets is sketched.

The main design goal of the LHC was and still is the confirmation of the standard model. This explicitly includes the search for the last missing particle, predicted by the standard model, the Higgs boson. This boson is the manifestation of the electroweak spontaneous symmetry breaking. It is responsible for a part of the mass generation of several particles such as quarks and electroweak gauge bosons. The two high luminosity proton-proton experiments at LHC, ATLAS and CMS, reported a discovery of a new particle in 2012. It has a mass of 125 GeV/c^2 and
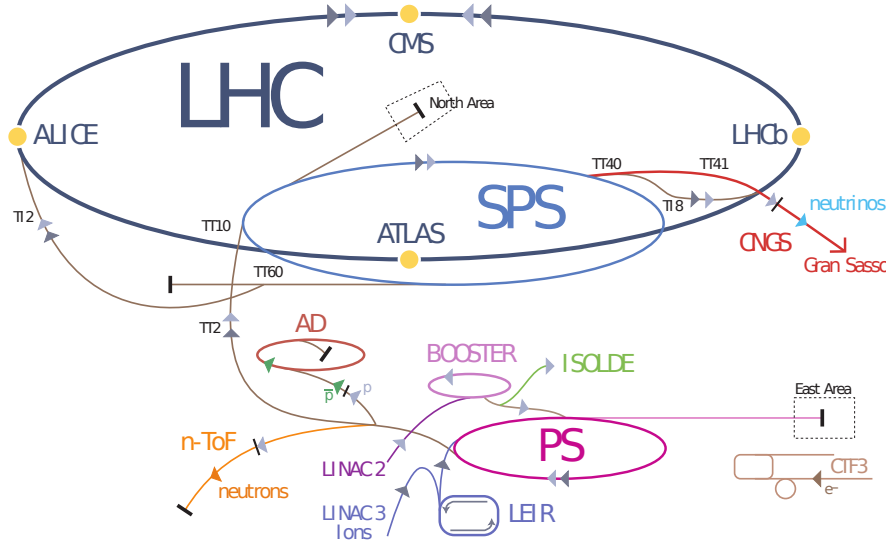
Figure 5.1: The design layout of the CERN accelerators complex. [136]

it is fully consistent with the Higgs proclaimed by the Standard Model [137–139]. Future precision measurements will show if this new found particle is the Standard Model Higgs bosons or only one of multiple Higgs bosons not included in the SM.

An additional goal of the LHC is the search of physics beyond the Standard Model. Since the Standard Model is not able to describe the unification of all four fundamental forces, more advanced theories such as supersymmetry (SUSY) were developed. The existence of supersymmetry should result in the existence of additional particles, properly produced and measurable by the LHC and its experiments. The question for the type and existence of dark matter is closely related to this search of supersymmetric particles. Hypothetical extra dimensions should be detectable by the measurement of missing total energy in collision, deposited in that unknown dimension. No evidence or even hints of SUSY physics or extra dimensions have yet been found.

The main physics question investigated by the ALICE experiment is the survey of the QGP. Its existence was already confirmed by former experiments like PHENIX and STAR at RHIC. First hints were already found by the SPS and the Alternating Gradient AGS in the 90s of the last century. Questions about the structure and initial conditions of the created QGP as well as its viscosity and evolution will be answered by the ALICE experiment. Insights into the strong interactions will be given by detailed measurements of the suppression of identified particles carrying strange, charm or bottom quarks.

5.2 ALICE - A Large Ion Collider Experiment

ALICE [140, 141] was designed as a general-purpose heavy-ion detector with the goal of enabling a deeper understanding of the strong QCD sector of the Standard Model. It will survey the extreme states of matter created in nucleus-nucleus collisions. The quark-gluon plasma, already discussed in Chap. 2, will be produced with much higher energy density, volume and temperatures compared to all predecessor colliders like RHIC.
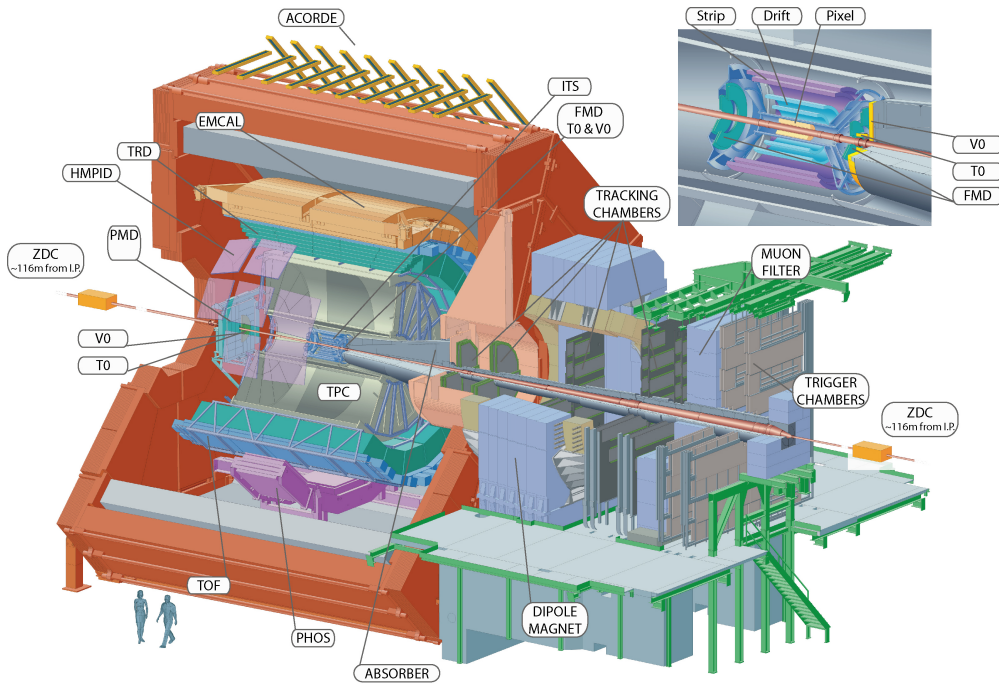
Figure 5.2: A sketch of the the ALICE detector at CERN. All sub-detectors are labeled. In the upper right a more detailed view of the ITS and some of the forward detectors are shown. [140]

An important task of heavy-ion experiments is the separation of the physics originating from the plasma phase from the follow-up phase of a hot hadronic gas. For that purpose, dedicated detectors with well developed particle identification (PID) capabilities and very precise low p_{T} tracking are needed. The heavy-ion environment is complicated due to the enormous number of produced particles. The ALICE detector is, therefore, designed to measure charged-particle densities up to $\mathrm{d}N/\mathrm{d}y \approx 8000$. The actual measured particle density at mid rapidity in central lead-lead collisions in ALICE is $\mathrm{d}N/\mathrm{d}y \approx 1600$ [20]. A more detailed description of particles densities produced in heavy-ion collisions is given in Sec. 2.4.

ALICE has measured proton-proton collisions to study QCD in the absence of a strongly interacting medium. These measurements provide a baseline for heavy-ion collisions. In this context, an even more important baseline is given by the study of the proton-lead collision system. This system should provide insights into cold nuclear matter effects, without a phase transition to the QGP. Hence, it will help to disentangle hot and cold medium effects in heavy-ion collisions. The first p–Pb collisions were recorded in late 2012.

To cover for all possible observables for the study of the QGP, ALICE is equipped with a broad range of different detector types. The ALICE setup can be divided into two independent groups of detectors. The first set is located inside the central barrel, the second component is the forward muon arm (Fig. 5.2). The muon arm will not be discussed further. The corresponding detectors are not used for the analysis presented in this thesis.

The central barrel consists of many sub-detectors with all commonly used particle identification methods. As depicted in Fig. 5.2, these detectors are the Inner Tracking System (ITS), the large Time Projection Chamber (TPC), the Transition Radiation Detector (TRD), the Time of Flight (TOF) and the High Momentum Particle Identification Detector (HMPID). In addition, ALICE is equipped with two different electromagnetic calorinmeters, the Electromagnetic Calorimeter (EMCal) and the Photon Spectromenter (PHOS). The centrality of nucleus-nucleus collisions and the timing information of the primary interaction is provided by the two V0 (V0A and V0C) and the T0 detectors installed in beam direction close to the beam pipe. All additional detectors are not discussed in the context of this thesis. The central barrel is embedded in a large solenoid magnet that was built for the L3 experiment at LEP. It is able to provide a magnetic field of 0.5 T.

The acceptance and the spatial coverage of the relevant detectors are listed in the Tab. 5.1.

All sub-detectors that are used for the photon analysis are described in more detail in the following section.

5.2.1 The Inner Tracking System

The Inner Tracking System (ITS) [141, 143, 144] is the detector closest to the beam pipe and to the collision point. It consists of six cylindrical layers of silicon detectors. Three different pad designs are used, whereas two neighboring layers (1+2, 3+4, 5+6) share an identical design. For the innermost layers, a silicon pixel (SPD) design is used. It has the largest granularity and the highest spatial resolution in z-direction. The high granularity is chosen for a good primary vertex

Detector	η	φ	Radius (m)	X/X_0 (%)
ITS				
Layer 1+2	$\pm 2.0, \pm 1.4$	360°	0.039 - 0.076	2.80
Layer 3+4	± 0.90	360°	0.150 - 0.239	2.64
Layer 5+6	± 0.97	360°	0.380 - 0.430	2.22
TPC		360°	0.606 - 2.780	3.50
at $r = 2.8\,\mathrm{m}$	± 0.9			
at $r = 1.4\,\mathrm{m}$	± 1.4			
TRD	± 0.84	360°	2.900 - 3.680	23.40
TOF	± 0.9	360°	3.700 - 3.990	29.50
EMCal	± 0.7	80° - 187°	4.500	20.10
PHOS	± 0.12	220° - 320°	4.600	20 +5(CPV)
HMPID	± 0.6	1.2° - 58.8°	5.000	18.00

Table 5.1: Acceptance and spatial coverage of the relevant detector systems. The material budget is given for a track perpendicular to the detector surface for $\eta = 0$. All values are taken from [141, 142].

resolution and a good secondary vertex separation since the track density is highest close to the interaction point. The second and the third layers are built as a silicon drift detector (SDD). The fifth and the sixth layers are designed as silicon double-sided micro strip detectors (SSD). The size of the ITS, as well as the fraction of the total radiation length can be found in Tab. 5.1. The detector is shown in a zoomed version in Fig. 5.3.

The main purpose of the ITS is the primary vertex finding and the separation of secondary vertices coming from the decays of long living B or D mesons and from photon conversions. The momentum resolution of the ITS is below $\sim 2\%$ for a pion between 100 MeV and 3 GeV. The primary vertex finding is limited by the distance of the detector from the interaction point. It can be measured with an accuracy of $100\,\mu$m in pp collisions. To keep the distance to the interaction point as short as possible, the SPD is installed directly around the beam pipe $(R_{\mathrm{BeamPipe}} = 2.94\,\mathrm{cm})$. The outer radius of the ITS is given by the inner radius of the TPC to guarantee a good track matching between those two detectors. Due to the short distance between the primary vertex and the SPD, the pseudorapidity
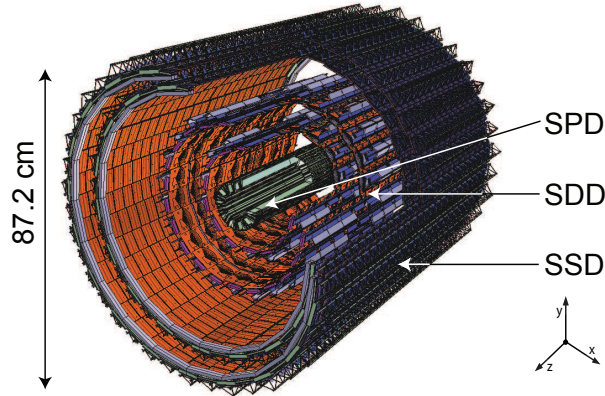
Figure 5.3: A detailed view on the layout of the Inner Tracking System and all three sub-detectors with two layers each. [144]

range is larger compared to the more outer detectors. For that reason it is also used as a charged particle multiplicity discriminator.

The ITS is able to do particle identification via the measurement of the specific energy loss $(\mathrm{d}E/\mathrm{d}x)$. A truncated-mean method that requires a minimum of four measurements (SDD + SSD) and a correlation with the deposited charge is used. The resolution of the ITS $\mathrm{d}E/\mathrm{d}x$ measurement varies with particle species and momentum. It has values of $\sim 9-11\,\%$ and is, therefore, much worse compared to the particle identification capabilities of the TPC.

5.2.2 Time Projection Chamber

The Time Projection Chamber (TPC) [141, 145, 146] is the largest tracking and PID detector in ALICE and provides the longest segment of the total track length. It is located inside the central barrel directly beyond the ITS.

The TPC consists of a cylindrical field cage with a central electrode ($\eta = 0$, $Z = 0\,\mathrm{cm}$) and read-out chambers at the end-plates of the barrel. The field cage is filled with a gas mixture of neon, nitrogen and carbon-dioxide. Until the end of 2010, the gas mixture was $85.7\,\%$ Ne, $9.5\,\%$ CO_2 and $4.8\,\%$ N_2. For later data taking, the nitrogen was removed from the mixture ($90\,\%$ Ne, $10\,\%$ CO_2). It is optimized for drift speed, low diffusion and radiation length. The volume of the TPC is approximately $90\,\mathrm{m}^3$ with a length of approximately $500\,\mathrm{cm}$. A sketch of the TPC is shown in Fig. 5.4

The TPC operates with a homogeneous electrostatic field in z-direction. The
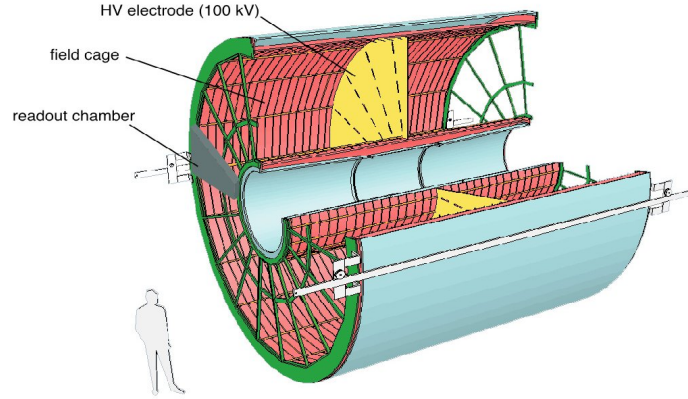
Figure 5.4: A sketch of the layout of the Time Projection Chamber. [147]

TPC covers a pseudo-rapidity range of $\eta = \pm 0.9$ with a full radial track length. For shorter track length it can provide tracking in a region of $|\eta| < 1.5$ with a minimal radial track length of 1/3 of the TPC. The charged particles traversing the TPC ionize the gas molecules, and the produced electrons are transported by the field to the read-out champers in a maximum distance of 250 cm from the central electrode. The voltage gradient is about 400 V/cm with a high voltage of 100 kV at the central electrode. This translates to a maximum drift time for electrons of 92 μs.

The drift time is the limiting factor for the maximum luminosity that can be processed by ALICE. At a proton-proton luminosity of $\mathcal{L} = 5 \cdot 10^{30}\,\mathrm{cm}^{-2}\mathrm{s}^{-1}$) with an interaction rate of 350 kHz, tracks from ~ 60 events are stored at the same time as the current event in the TPC drift volume. Such tracks can be partially eliminated by track matching with the ITS. The ITS has a much faster read-out and stores and thus no additional events. Tracks that do not have ITS information, such as electrons from conversion at the inner TPC shield, have to be eliminated by other techniques. The method for the presented analysis is explained in Sec. 7.4. In case of high multiplicity Pb–Pb collisions, the occupancy of the TPC will be even larger despite the smaller interaction rate. The TPC is designed to handle charged particle multiplicity densities of $\mathrm{d}N_{ch}/\mathrm{d}\eta = 8000$. This corresponds to 20000 charged tracks in the TPC acceptance.

The read-out chambers are located at the two end plates of the TPC. They are constructed as multi-wire proportional chambers with cathode read-out. The read-out area is separated in φ in 18 individual sectors and has a trapezoidal form. Since the track density changes with increasing radii, each of the 18 sectors is

further segmented in r into two segments. The inner segments have a smaller single read-out pad size of $4 \times 7.5\,\mathrm{mm}$ ($\varphi \times r$), while the outer part has pads of the size $6 \times 10\,\mathrm{mm}$ and $6 \times 15\,\mathrm{mm}$ ($\varphi \times r$). The overall active zone of the detector is $32.5\,\mathrm{m}^2$. The dead, inactive zones between the segments are aligned for the inner and outer region to optimize the high p_T momentum measurements. This setup has the disadvantage of cracks in the φ-acceptance of the TPC.

A three-dimensional track is reconstructed by combining the x,y-position information provided by the pads at the end plates with the timing information from the drift time (z-coordinate). The starting time is provided by the T0 detector. From the curvature of the reconstructed track, the momentum is calculated. The TPC is able to measure primary tracks (tracks originating from the primary vertex) from $100\,\mathrm{MeV}$ up to $100\,\mathrm{GeV}$. The lower bound is defined by the large curvature of low momentum tracks. Such tracks will be bend away by the magnetic field before traversing more than the minimum required $1/3$ of the radial length of the TPC. Particles which are produced displaced from the primary vertex can be tracked down to $50\,\mathrm{MeV}$ limited by the tracking algorithm.

In addition The TPC is the main charged particle identification unit in ALICE. The energy loss via ionization in the drift gas can be described with the Bethe-Bloch formula. It relates the mean energy loss of a particle with its $\beta\gamma$. Together with the momentum information from the particle, its identity (mass) can be derived. PID with the TPC as used for this analysis is explained in more detail in Sec. 7.2.2.

5.2.3 Time-Of-Flight

The Time-Of-Flight (TOF) [141, 148, 149] detector is designed for intermediate momentum ($0.5\,\mathrm{GeV}/c$ to $2.5\,\mathrm{GeV}/c$) particle identification. The electron identification, used for this analysis, is possible for the momentum range of 0.3 to $0.5\,\mathrm{GeV}/c$. TOF has full azimuth coverage and is installed beyond the TPC with a pseudo-rapidity coverage of $|\eta| = \pm 0.9$. It is segmented into 18 sectors separated in φ with up to 5 segments in z-direction. In the region of the PHOS spectrometer, no TOF segments are installed to reduce the amount of material in front of the calorimeter.

The PID capability for a TOF detector depends on the intrinsic time resolution. The working principle of the detector is the measurement of the time of flight of a particle from the primary vertex to the TOF array. The ALICE TOF has more than 10^5 independent channels to give a well defined response even for high multiplicity Pb–Pb collisions.

Due to the large area that is covered by TOF, a Multi-gap Resistive-Plate gas Chamber (MRPC) design is used. The used gas mixture is $C_2H_2F_4$ (90 %), i-C_4H_{10} (5 %), SF_6 (5 %). The main advantage of an MRPC based system is the symmetric signal peak around zero and the very good time resolution. The final test setup of TOF reaches a time resolution of around 70 ps.

5.2.4 V0 Detector

The V0 detector [141, 150] consists of two scintillator arrays called V0A and V0C. They are located on both sides of the ALICE interaction point and cover a pseudo-rapidity region of $2.8 > \eta < 5.1$ (V0A) and $-3.7 < \eta < -1.7$ (V0C), respectively. The distance from the collision point is dictated by the other central barrel detectors. The V0A array is displaced by 340 cm in z-direction with a diameter of 100 cm. The V0C detector is closer to the interaction point in respect to the absorber of the ALICE muon arm. Is has a z-distance of 90 cm in the opposite direction. The diameter of the V0C is 76 cm.

The arrays are used as a Minimum Bias (MB) trigger detector and as a very fast multiplicity counter for the centrality determinations of Pb–Pb or p-Pb events. It uses the monotonous dependence of the number of particles measured with the V0 arrays to the overall primary particle multiplicity. For flow measurements, like the measurement of direct-photon flow, V0A and V0C provide two independent event plane estimates.

5.2.5 Calorimeters - EMCal and PHOS

In ALICE two different calorimeters are installed, the smaller Photon Spectrometer (PHOS) with a high resolution and the larger Electromagnetic Calorimeter (EMCal) for high p_T particle and jet studies.

PHOS

The PHOton Spectrometer (PHOS) [141, 151] consists of a single-arm electromagnetic calorimeter with high granularity and an additional Charged-Particle Veto (CPV) detector. PHOS was originally designed to consist of five modules, containing a pair of a PHOS and a CPV each. Only three of the five modules have yet been installed. PHOS is located at the bottom of ALICE in the central rapidity region in 4.6 m distance from the interaction point. The detailed coverage of PHOS can be seen in Tab. 5.1.

Each of the three PHOS units is segmented into 3584 (56 rows of 64 cells) detecting cells (scintillator crystals) with a volume of one cell of $22 \times 22 \times 180 \, \text{mm}^3$. This fine granularity is on the order of the Moliere radius of PbWo. The crystals are built of $PbWO_4$ (PWO). At the outer side of each channel, a $5 \times 5 \, \text{mm}^2$ Avalanche Photo-Diode (APD) junked with a low-noise preamplifier is attached. The time resolution of this array is on the order of a few nano seconds. PHOS operates at a temperature of $-25 \, ^\circ\text{C}$ to increase the light yields of the PWO crystals with a stability of the temperature of $0.3 \, ^\circ\text{C}$. The pressure of the system is close to $1 \, \text{atm}$.

The CPV detector is installed in front (seen from the collision point) of the PHOS calorimeter modules with a distance of $5 \, \text{mm}$ from the calorimeter. It is designed as a Multi-Wire Proportional Chamber (MWPC) with cathode-pad read-out. To not disturb the measurement of PHOS and the photon shower development in the crystals it has less than $5 \, \%$ of radiation length with a thickness of $14 \, \text{mm}$. The used gas mixture is 80% Ar and $20 \, \%$ CO_2. The detector has a charged particle veto efficiency of about $99 \, \%$.

PHOS is designed to measure, with high position and energy resolution, low p_T direct photons such as thermal photons. It provides a congruent method of testing the thermal and dynamical evolution of heavy-ion collisions compared to the external conversion method discussed in this thesis. To separate direct photons from decay photons, invariant mass analyses (low p_T) or shower shape discrimination (high p_T) can be used. In addition, PHOS measures neutral meson yields like π^0 or η up to higher p_T as it is possible with conversions. It will also measure jets and jet quenching and correlations of jets with photons.

EMCal
In contrast to PHOS, the ElectroMagnetic CALorimeter (EMCal) [141, 152] has an inferior position and energy resolution but a much larger acceptance (see. Tab. 5.1). The EMCal increases the active calorimeter area by nearly one order of magnitude. It is designed to extend the jet measurement capability of ALICE to full jets over a large kinetic range in a larger acceptance. Still, the acceptance is very small for jet studies. With this, EMCal improves the full jet energy resolution of ALICE and completes the capability of measuring jet quenching. Single particle spectra, like π^0 or electron, are measurable up to high p_T. It is also used as an unbiased and fast trigger unit for jets, photons and electrons.

EMCal is a large Pb-scintillator sampling calorimeter with longitudinal wavelength-shifting fibre light collection and a cylindrical geometry. It is designed to fit in the available space between the ALICE spaceframe and the

ALICE magnet coils inside the L3 magnet. Like PHOS, it is 4.5 m away from the interaction point and located almost opposite in azimuth. It is subdivided into two types of super-modules. The ten full size modules have a coverage of $\Delta\eta = 0.7$ and $\Delta\varphi = 20°$, the two smaller super-modules have only half the acceptance in φ. Each super-module consists of 12 (6 for the smaller modules) stripes of 24 modules. A module contains 2×2 towers. In sum, the EMCal uses 12288 towers aligned to point to the interaction zone. They are alternatingly built up from 76 layers of 1.44 mm Pb and 77 layers of 1.76 mm polystyrene based, injection molded scintillators (Shashlik).

The gaps between the super-modules (in η or z-direction) with a width of 3 cm are aligned with the boundaries of the TPC sectors. The material amount of the TPC frame would be otherwise too large and would, therefore, degrade any electromagnetic measurements in the gap regions. The overall EMCal material budget of 20.10 X_0 is chosen to give an optimized linear dependence of the most probable energy response of EMCal.

5.3 Additional LHC Experiments

The five important experiments in addition to ALICE will be described briefly in this section.

A Toroidal LHC ApparatuS - ATLAS [153]
This apparatus is, with a length of 45 m and a diameter of 25 m, the largest detector operated at CERN. It is designed as a general-purpose detector and covers a broad spectrum of physical questions. One main task of the detector was the discovery of the Higgs boson. After the confirmed discovery, it measures the properties of the new found particle. It is designed to measure highly energetic probes like heavy particles containing bottom quarks. The CP violation for B-mesons will be investigated in detail. The top quark, first measured at Fermilab in 1995, will be measured to high precision. ATLAS is therefore designed to handle very high luminosities. The ATLAS collaboration has an additional small heavy-ion group.

Compact Muon Solenoid - CMS [154]
The CMS detector is much smaller compared to ATLAS (length: 25 m, diameter: 15 m) but targets very similar physics questions. It uses a complementary detector design to be able to confirm or disconfirm ATLAS (or vice versa). It has also

measured the new boson, most likely the Standard Model Higgs. Like ATLAS, it will search for extra dimensions and suppersymmetric partners of the known particles. It is mainly designed for high p_T probes in the TeV region. It has in addition, a dedicated heavy-ion program, and it is able to measure for example jet suppression in a wider solid angle and to higher p_T compared to ALICE. Since it has a spread of physics topics, similar to ATLAS, it can also handle the large luminoisties provided by the LHC.

LHC Beauty Experiment - LHCb [155]
The main goal of the LHCb experiment is the exact measurement of the decay of B and D mesons. This should lead to new insights and a deeper understanding of the CP-violation and the related matter and anti-matter imbalance fordable in the universe. The possible deviations of these decays from predictions are a precision test of the physics of the Standard Model. In contrast to the other large LHC experiments, LHCb is a one arm experiment and measures only in forward rapidity.

TOTEM, LHCf and MoEDAL
There are three additional smaller experiments at the LHC. The Total Elastic and Diffractive Cross Section Measurement (TOTEM) [156] measures the radius of the proton with high precision. The Large Hadron Collider forward (LHCf) experiment [157] measures cosmic rays and particles in forward direction nearly parallel to the LHC beam. The last experiment is the Monopole and Exotics Detector At the LHC (MoEDAL) [158]. It is dedicated to the search for magnetic monopoles and dyons.

5.4 The ROOT and AliROOT Framework

ROOT [159,160] is a replacement of the software package PAW (Physical Analysis Workstation) [161]. PAW had been developed since 1986 at CERN. It is written in the programming language FORTRAN. In contrast, ROOT is written in C++ and was initially developed by René Brun and Fons Rademakers since PAW was not expected to be able to handle the amount of LHC data. The data was expected to be orders of magnitudes larger compared to previous experimental outputs. ROOT is designed as a framework, a set of C++ classes and software tools. All tools are integrated in a coherent ensemble. ROOT provides all types of mathematics operations like fitting and unfolding. It has many types of data

containers like histograms or graphs and is able to handle all data stored during physical analyses.

For an experiment like ALICE, not only the equipment for physics analysis is needed. In addition, the software must provide tools for the simulations of events and of the detector. Furthermore, a reconstruction is required for simulated and measured events. For this purpose, AliRoot [162] is used. AliRoot is based on ROOT and contains all C++ classes required exclusively by the ALICE experiment. It has been continuously developed following the challenges of ALICE since 1998.

A physics event, the collision of protons or lead ions, is simulated [163] with an event generator. The generator simulates all particles which are produced during the primary interaction. Further details of the event generators used for this thesis will be given in Sec. 6.2. The simulated particles and the corresponding attributes like particle type, momentum, etc. are stored in a kinematic tree. In addition, the tree stores the mother-daughter relationship and the production vertex of the particles. They are transported through a simulated ALICE detector implemented in the software GEANT [164]. GEANT simulates the energy deposited in the detector and particles produced by material interactions such as electrons from photon conversions. All such created particles are stored with its additional characteristics in the tree. Afterwards, the response of the detector, including noise, is simulated.

From this point of data processing measured (in contrast to simulated) and simulated events are treated in an identical stream. The simulation provides the same information as obtained from a real ALICE measurement. Additionally, particle information, unbiased by the detector response, is available from the simulation.

The reconstructed events and all corresponding tracks can be stored and analyzed in two different data formats, the ESD format (Event Summary Data) with nearly all reconstruction and track parameters available and the compressed AOD format (Analysis Object Data). The latter should only contain the necessary information for the analysis. If additional information not stored in the AOD is required it can be provided by an additional deltaAOD file. It will be linked to the main AOD file during the analysis.

Also included in AliRoot is the AliEn system [165]. It gives access to the computing grid used by the ALICE collaboration. For this and other features, ROOT is extended with additional classes and libraries.

5.5 Charged Particle Tracking- and Vertex Reconstruction in ALICE

The first step of event reconstruction [142, 166] in the central barrel of ALICE is the determination of the primary interaction vertex. For this purpose, the two inner layers of the ITS, the SPD, are used. After the position of the primary vertex is determined, the reconstruction of tracks starts. For each track, the momentum and charge is stored in respect to its first track point, normally close to the point of creation.

Primary Vertex Reconstruction

The primary vertex reconstruction in ALICE is performed in two steps. A preliminary primary vertex is determined before the reconstruction of the tracks starts. The final vertex is optimized by the information available after the full tracking of global tracks pointing to the primary vertex.

The preliminary vertex position is determined by a linear extrapolation of the tracklets found in the first two ITS layers. A tracklet is defined as a pair of hits in two neighbouring ITS layers. The resulting z-distribution at $x = y = 0$ has a Gaussian shape and its centroid is taken as the first vertex guess in z. In case of a vertex position not centered at $z = 0$, the distribution is biased by the resulting geometrical unequal ITS track acceptance in the $+z$ or $-z$-direction. In a second step, the same algorithm is applied in the transverse plane (x, y). For both coordinates, the tracks are approximated by straight lines. The x,y measurement is less accurate due to the bending of the tracks in the magnetic field. Nevertheless, the straight line assumption is valid since the two first ITS layer have similar radii ($4 \, \text{cm}$, $7 \, \text{cm}$), and the curvature of the tracks is normally small. Only tracklets with a distance $< 4\sigma_z$ are considered for the preliminary primary vertex determination.

By chance it might happen that more than one primary interaction occurs in a single bunch crossing. This results in additional primary vertices, called same-bunch pileup. If such pileup is expected, the vertex algorithm runs several times. After each iteration, a most probable vertex and all corresponding tracklets are removed. The primary vertex is finally defined as the one with the highest number of contributing tracklets [166]. Normally such events are discarded for the analyses.

The resolution of the procedure depends on the multiplicity of the event with a better resolution for more contributing tracklets. In case of central Pb–Pb events ($\mathrm{d}N_{\text{ch}}/\mathrm{d}\eta \sim 1500$), a resolution in z of $5 \, \mu\text{m}$ can be reached. In case

of a non-central vertex position, a resolution up to $\pm 10\,\mu$m is possible. In the transverse (x,y) plane the resolution is worse due to the magnetic field ($35\,\mu$m for $B = 0.5\,$T) [142]. The resolution as a function of charged particle multiplicity can be described by the formula:

$$\sigma_z = \frac{A}{\sqrt{\mathrm{d}N_{\mathrm{ch}}/\mathrm{d}\eta}} + C. \tag{5.1}$$

In Pb–Pb collisions, the two free parameters A,C have the value of $A = 292\,\mu$m and $C = 1.8\,\mu$m, respectively. In pp collisions, the multiplicity is smaller, and thus, the resolution is worse. Still, the same function is able to describe the resolution. With a multiplicity of $\mathrm{d}N_{\mathrm{ch}}/\mathrm{d}\eta = 6$, the resolution in pp is on the order of $155\,\mu$m in z-direction [142].

The final step of the primary vertex reconstruction is performed after the completion of the tracking [142, 167]. Each reconstructed track in the TPC and in the ITS is fitted with a straight line constrained with the reconstructed preliminary primary vertex position found by the SPD. The tracks are paired (i,j) and the central point at the distance of closest approach between the track pair is determined. An intermediate vertex position in x,y,z is given by the mean coordinates of all pairs:

$$\mathbf{r}_v = \frac{1}{N_{\mathrm{pair}}} \sum_i \mathbf{r}_{ij}, \qquad \mathbf{r}_v = (x_v,y_v,z_v). \tag{5.2}$$

The final vertex position is determined by the minimization of the χ^2 distribution obtained from all vertex points for each track i and its covariance matrix $\mathbf{V}_i$ and the derived mean vertex positron $\mathbf{r}_v$:

$$\chi^2(\mathbf{r}_v) = \sum_i (\mathbf{r}_v - \mathbf{r}_i)^T \mathbf{V}_i^{-1} (\mathbf{r}_v - \mathbf{r}_i). \tag{5.3}$$

Some tracks, like electrons from photon conversion or strange particle decays, do not originate from the primary vertex. Such tracks would contribute with a very large value of χ^2 to the total value and are, therefore, not considered in the calculation. They are removed from the sample one-by-one.

If more than one primary vertex due to pileup is possible, an alternative more robust algorithm inspired by [168] can be used instead. It is designed to exclude outliers originating from the additional vertices. The algorithm is based on an iterative re-weighted least squares method and was first introduced by the CERES/NA45 experiment. For vertex fitting it uses Tukey bisquare weights.

Track Reconstruction in the Central Barrel

As discussed above, the full track finding is applied after the prelimniary primary vertex reconstruction. The procedure starts with track segments inside the TPC. Here, sets of close TPC cluster are combined. A TPC cluster is defined as a set of several digitized detector signals (digits) in pad-row and time direction. To localize the geometrical position of the traversing particle candidate, the center of gravity is calculated for five pads and five time bins. A typical cluster size is on the order of $\sigma_{\text{cluster}} \sim 0.75$ bins. In high multiplicity events, where pads may contain several clusters, a more sophisticated method for cluster finding, including cluster unfolding, is used. The identified clusters are used for the seed finding of a Kalman filter. The Kalman filter was first introduced in [169] and is nowadays widely used in high energy physics [141, 170].

The general idea of Kalman filtering is the statistical estimation of a state vector successively optimized by a comparison of the measurements with a prediction. It can be used for problems which are determined by a deterministic process, like the track propagation through the detector. The process might be additionally disturbed by noise, e.g. multiple scattering of that particle, changing its state vector (momentum, position, etc.). A first guess, called seed, of the state vector and the corresponding covariance matrix has to be estimated.

For the Kallman filter used in ALICE, two different types of seeds are used. One set of seeds is obtained from two clusters combined with the constraint that the track helix can be projected to the primary vertex. The number of possible combinations is reduced by a certain set of p_{T} and z requirements for the track candidate. For the primary vertex position the preliminary ITS vertex is used, already available at this stage of the event reconstruction. If a proper cluster pair is identified, intermediate clusters are searched. If such clusters exist, the first guess of the helix parameters and the covariance matrix are estimated. These kind of track patterns are used as seeds for track candidates originating from the primary vertex.

The second approach uses a very similar algorithm and starts with the same initial clusters as used for the first method. Here no vertex constraint is assumed. A central intermediate cluster between the two initial ones is combined with its two nearest clusters in the neighboring pad rows. For the finding of those clusters, a straight line fit is used. More and more pad rows are added until the initial two clusters are added to the track candidate. If seven pad rows are combined, the straight line approximation is replaced by a polynomial track hypothesis. The helix parameters and the covariance matrix are calculated from all added clusters.

Starting from the collected seeds, the Kallman filter performs three different steps. First it "predicts" the values of the state vector and the covariance matrix at the

next pad row. For this prediction, the state vector is propagated to the next inner pad row. Here the guessed covariance matrix is updated ("measured") under consideration of noise. As the final step, the "filtering" is applied. A cluster that matches reasonably with the prediction is searched. If such a cluster is found, it is added to the track candidate and the state vector, and the covariance matrix is updated accordingly. This procedure is repeated until the innermost pad row of the TPC is reached.

The quality of the reconstructed TPC tracks can be expressed as an χ^2 value calculated during the Kalman filtering. Via this quantity, bad track candidates can be removed. In addition, if tracks share more than 25 %-50 % clusters, the worse track (χ^2) is removed.

After the track reconstruction in the TPC is finished, the track parameters are propagated to the outer side of the ITS. Here they are used as seeds for the Kalman filter based track finding for the six ITS layers. The tracks obtained by the first type of seeding (vertex constrained) are transported twice. Once under the assumption of being primary tracks originating from the primary vertex and once without that constraint. Both sets of track parameters are stored independently. The second set of non-constrained tracks is just processed once without vertex constraint.

If more than one path trough the ITS is possible for a track candidate, all are processed subsequently. A single TPC track might thus create a larger set of possible ITS tracks. From the sample, the most probable track parameters are selected based on the χ^2 value calculated during the prolonging. If the selected track shares too many clusters with an other independent track, an alternative set of track parameters is chosen that minimizes the sharing. Alternatively, all tracks can be stored. In this case, the χ^2 of the different possible tracks is used as a penalty factor.

After the TPC-ITS tracking has finished, the Kalman filter is reversed, starting now from the innermost ITS layer. It uses the already reconstructed tracks as seeds and recalculates and optimizes the track parameters by removing fake ITS hits and TPC clusters. When the outer wall of the TPC is reached, the tracks are prolonged further to the TRD. If possible, tracklets from the six TRD layers are added to the track. The same is done with the TOF clusters and the calorimeter cells of PHOS and EMCal.

As a last step, all tracks are refitted inwards again, starting from the outer layer of the TRD, and the final track parameters are stored. In this backward fitting, both sets of tracks, with and without vertex constraint, are again included.

Additionally, an ITS standalone tracking can be performed. Depending on the

momentum and particle mass, not all tracks reach the TPC (e.g. pions below $\sim 200\,\mathrm{MeV}$, protons below $400\,\mathrm{MeV}$). Also, high energy tracks traversing the dead zones of the TPC are not reconstructable by global tracking. For the ITS standalone tracking, only ITS hits which are not yet taken into account by the global TPC-ITS tracks are considered. As seeds, two hits from the three innermost layers are required. This method allows the tracking of particles down to $\sim 80\,\mathrm{MeV}$. In pp event reconstruction the ITS standalone tracking is additionally applied with all available clusters to create an independent set of ITS-only tracks.

The full tracking procedure including the primary vertex finding is visually summarized in Fig. 5.5. Additionally, the secondary vertex finding, discussed in Sec. 7.1, and the cascade finding is shown.
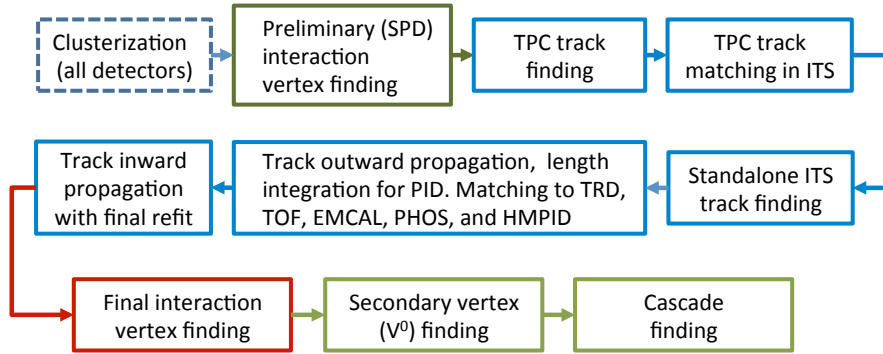
Figure 5.5: Tracking and vertex finding during the event reconstruction in ALICE. [166]

Part II

Direct-Photon Analysis

6 Analyzed Data Samples and Monte Carlo Simulations

The general principle of the direct-photon analysis is based on the reconstruction of the inclusive-photon spectrum. To identify direct photons, the expected decay-photon background is subtracted from the inclusive measurement. The photons are measured via external conversions. An external conversion is the transformation of a photon into a lepton pair (normally into e^+e^-) by the interaction with matter. The electron and positron are produced displaced from the primary vertex. The conversion point is, therefore, called a secondary vertex. The conversions are identified by a secondary vertex finder introduced in Sec. 7.1.

In this chapter, the used data event samples and the corresponding Monte Carlo (MC) simulations are introduced. To distinguish between real events measured by the ALICE detector and simulated Monte Carlo events, the terms "data" and "Monte Carlo simulation" will be used respectively. The analyzed center-of-mass energies are for pp collisions $\sqrt{s} = 2.76\,\mathrm{TeV}$ and $7\,\mathrm{TeV}$ and for Pb–Pb $\sqrt{s_{\mathrm{NN}}} = 2.76\,\mathrm{TeV}$. The $7\,\mathrm{TeV}$ data set has the largest amount of recorded events. Therefore, it can be used as a precise base-line measurement and as a proof of concept with small statistical uncertainties. Furthermore, this data set is less complicated to analyze compared to the pp collisions at $2.76\,\mathrm{TeV}$ or to the Pb–Pb collisions. While the Pb–Pb is complicated due to the much larger track multiplicities, the pp data at $2.76\,\mathrm{TeV}$ is strongly affected by different-bunch pileup. This kind of pileup will be discussed in Sec. 7.4.

The chapter is organized as follows: First, the data events and event selection criteria are described. For Pb–Pb the collisions, the centrality determination and selection is discussed. Afterwards, the event generators used by ALICE are briefly introduced. The quality and comparability of the data to the simulations in respect to track and photon multiplicity is tested.

6.1 Data Samples in pp and Pb–Pb

The proton-proton events at $\sqrt{s} = 7\,\text{TeV}$ used for this analysis were collected by the ALICE experiment between March and June 2010. During that time, $\sim 3.8 \times 10^8$ minimum bias pp events were recorded with a total luminosity of $0.5\,\text{pb}^{-1}$ [166]. It is the largest data sample available for the presented analysis. The $7\,\text{TeV}$ data is separated into four different sub-samples, called periods. These periods are LH10b, LHC10c, LHC10d and LHC10e. They were realized successively. The periods are further subdivided into runs. A run corresponds to a continuous time of ALICE data taking. All periods and runs have slightly different reconstruction conditions. This results in deviating track reconstruction and thus photon finding efficiencies. The purities of the reconstructed photon candidates might change under the different conditions. This makes dedicated Monte Carlo productions for each period (and run) necessary. The simulations have to reproduce all specifications of the data taking as precisely as possible. The Monte Carlo productions will be discussed in section 6.2.

The $2.76\,\text{TeV}$ pp data sample is much smaller compared to the $7\,\text{TeV}$ sample. It consists of 4.53×10^7 events and was recorded in 2011. For the analysis, only one period, LHC11a, is available. This makes the analysis slightly easier since only one set of similar Monte Carlo events is required. Nevertheless, the significantly smaller statistics limits the precision of the analysis.

In general, a pp event is accepted if it fulfills the minimum bias trigger MB_{OR} of ALICE. This requires a hit in one of the two V0 detectors (V0A or V0C) or a hit in the first two layers of the ITS. The pp analysis is performed for the sum of all data listed in Table 6.1.

$\sqrt{s}$	Period	Reco. Pass	Rec. Events	Acc. Events
$7\,\text{TeV}$	LHC10b	pass2	3.29×10^7	2.35×10^7
	LHC10c		7.34×10^7	6.18×10^7
	LHC10d		1.68×10^8	1.26×10^8
	LHC10e		1.68×10^8	1.03×10^8
summed $7\,\text{TeV}$ data			4.42×10^8	3.15×10^8
$2.76\,\text{TeV}$	LHC11a	pass4	8.12×10^7	5.34×10^7

Table 6.1: Number of events used for this analysis for pp data at $\sqrt{s} = 7\,\text{TeV}$ and $2.76\,\text{TeV}$.

Period	Centrality	Rec. Pass	Rec. Events	Acc. Events
LHC10h	0-80%	pass2	4.6×10^7	13.6×10^6
	0-20%			3.4×10^6
	0-40%			6.8×10^6
	20-40%			3.4×10^6
	40-80%			6.8×10^6

Table 6.2: Number of events for Pb–Pb data in all analyses centrality bins at $\sqrt{s_{\mathrm{NN}}} = 2.76\,\mathrm{TeV}$.

After the $7\,\mathrm{TeV}$ pp data collection, the LHC started to operate with lead ions at the end of 2010. ALICE recorded $\sim 46 \times 10^6$ Pb–Pb minimum bias events during 2010 from which $\sim 13.6 \times 10^6$ were finally used for the analysis. The heavy-ion period is called LHC10h. The number of events is much smaller compared to the pp data. However, the number of reconstructed photons and neutral pions is nearly compensated by the much larger track multiplicities of Pb–Pb collisions. Here the difference in track multiplicity is a factor of ~ 250 for central Pb–Pb, compared to pp at $7\,\mathrm{TeV}$.

The recorded data in pp and Pb–Pb is normally reconstructed several times. In each reprocessing step, called a pass, the reconstruction conditions and the detector calibration are optimized. Normally the second pass (pass2) is used as the final reconstruction result. For the pp data at $2.76\,\mathrm{TeV}$, the fourth pass is taken. This reflects the complicated data taking conditions of this period.

6.1.1 Event Selection in pp Collisions

Not every recorded event is considered for the analysis. In general, events that fulfill the following criteria are used for the presented analysis:

1. Must pass the AliPhysicsSelection. This AliRoot class selects the correct assignment of event triggers. For this analysis, the minimum required trigger is the $\mathrm{MB_{OR}}$ trigger. It tags beam-beam interactions and discards calibration events, beam-gas interactions, noise and cosmic ray events.

2. A reconstructed primary vertex is required. A vertex is accepted if at least one global track or SPD tracklet is assigned. Events with tracks with only TPC clusters assigned are discarded.

3. The reconstructed z-position of the primary vertex has to be within $|z_{\mathrm{vtx}}| <$

10 cm from the origin of the coordinate system of ALICE. This selection is demanded to guarantee comparable reconstruction conditions for all events.

4. Same-bunch pileup events are rejected. If more than one primary vertex is reconstructed by the SPD, the event is not used for the analysis. The average number of pp collisions per bunch crossing is on the order of $\mu = 0.05$ [166]. This leads to the average number of pp collisions N_{pileup} in bunches with at least one collision of:

$$N_{\text{pileup}}(\mu = 0.05) = \frac{\mu}{1 - \exp(-\mu)} \approx 1.025. \tag{6.1}$$

The number of proton-proton events used for the analysis and for the normalization of the reconstructed spectra are defined as:

$$N_{\text{event}} = N_{\text{MB}_{\text{OR}},|z_{\text{vtx}}| < 10\,\text{cm}} + \frac{N_{\text{MB}_{\text{OR}},\ |z_{\text{vtx}}| < 10\,\text{cm}}}{N_{\text{MB}_{\text{OR}},\ |z_{\text{vtx}}| < 10\,\text{cm}} + N_{\text{MB}_{\text{OR}},\ |z_{\text{vtx}}| > 10\,\text{cm}}} N_{\text{MB}_{\text{OR}},\ \text{noVtx}}. \tag{6.2}$$

This number corresponds to events with reconstructed primary vertex ($N_{\text{MB}_{\text{OR}},|z_{\text{vtx}}|<10\,\text{cm}}$) plus the number of events without a reconstructed vertex in the same z-range. The number of events without reconstructed primary vertex is on the order of 10%. A similar number of events has a reconstructed primary vertex outside the accepted z-region.

6.1.2 Event Selection in Pb–Pb Collisions and Centrality Determination

The Pb–Pb events considered for the analysis have to fulfill identical criteria as listed in the previous section. An exception is the same-bunch pileup rejection applied during the primary vertex reconstruction by the SPD. It is not necessary for Pb–Pb collisions. The number of lead ions per bunch is much smaller compared to the number of protons in a proton bunch. This results in much smaller probabilities of a beam-beam interaction per bunch crossing. Same-bunch pileup is suppressed accordingly. The interaction rate per Pb–Pb bunch crossing is only on the order of $\mu = 10^{-5}$-10^{-4} and the luminosity of the 2010 Pb–Pb run was about $10^{25}\,\text{s}^{-1}\text{cm}^{-2}$ [166].

For the normalization of the spectra the number of events that pass the selection criteria are taken. In contrast to pp collisions, events without reconstructed primary vertex are negligible ($\ll 1\%$) and not considered for normalization.

Heavy-ion collisions can be separated into centrality classes. The centrality is a measure of the impact parameter b of the collision as already discussed in Sec. 2.4. While the more-central events (small b) are expected to show strong medium effect, the more-peripheral events (larger b) are expected to be more similar to pp. The centrality percentile is defined as the corresponding fraction of the total cross section σ for a given impact parameter range:

$$c(b) = \int_0^b \frac{\mathrm{d}\sigma}{\mathrm{d}b'} \mathrm{d}b' \bigg/ \int_0^\infty \frac{\mathrm{d}\sigma}{\mathrm{d}b'} \mathrm{d}b'. \tag{6.3}$$

The denominator of the formula is the total hadronic cross section of nucleus-nucleus collisions. For experiments it is easier to use the total number of events N_{event} instead, since the impact parameter is not directly accessible. In addition, the impact parameter is related to the number of charged tracks N_{ch} produced by the collision. The centrality can be alternatively written as the percentage of events with a lower interval of charged tracks over the total number of events.

$$c \approx \frac{1}{N_{\mathrm{event}}} \int_{N_{\mathrm{ch}}}^\infty \frac{\mathrm{d}n}{\mathrm{d}N'_{\mathrm{ch}}} \mathrm{d}N'_{\mathrm{ch}}. \tag{6.4}$$

For the presented analysis the charged tracks, used in Eq. (6.4), are substituted by the amplitude measured with the two V0 detectors (sum of A and C). This distribution is separated in different centrality bins defined by fixed amplitude intervals. ALICE is alternatively able to measure the centrality with the SPD or the TPC. In these cases, the underlying distributions are the charged track multiplicities. As a third option, the ZDC can be used. Here the surviving fragments of the interacted nuclei are measured at the zero degree calorimeters [171, 172].

In Fig. 6.1, the V0 amplitude is shown. The slices representing the centrality bins are marked. The distribution is fitted with a Negative Binomial Distribution (NBD) times the number of ancestors $N_{\mathrm{ancestors}} = f N_{\mathrm{part}} + (1 - f) N_{\mathrm{coll}}$. The ancestors can be understood as the number of particle-producing sources and f as the fraction of soft production-sources. The latter is expected to scale with N_{part} [172]. The N_{part} and N_{coll} values are estimated from the Glauber Model (Sec. 3.3).

From the Glauber Model, geometrical properties of the Pb–Pb collisions can be extracted. The most interesting quantities are the number of binary collisions (N_{coll}), the number of participants and spectators (N_{part}, N_{spec}) and the nuclear overlap function T_{AA}. For that purpose, a Monte Carlo ansatz is normally used. The values are required, for example, for the geometrical scaling as discussed in
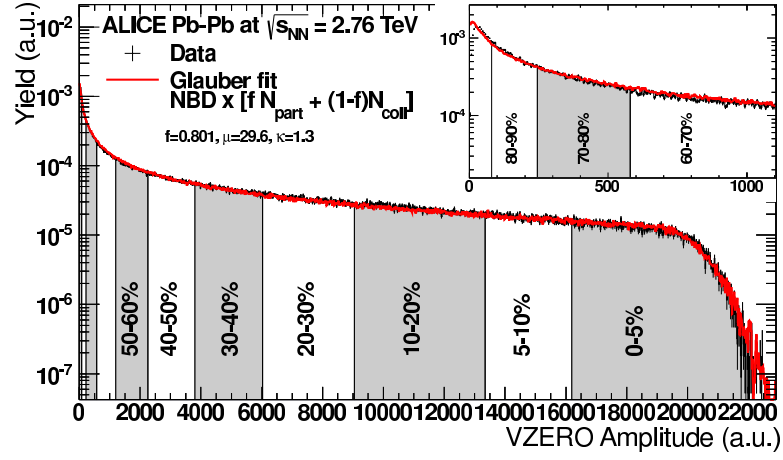
Figure 6.1: Total V0 amplitude plotted against the number of events as used for the ALICE centrality determination. The red line is obtained by a NBD-Glauber fit to the measured distribution. [172]

Sec. 3.3. The quantities are determined as mean values from the corresponding Monte Carlo simulations.

6.2 Event Generators and Monte Carlo Productions

From the reconstructed events in pp or Pb–Pb collisions, only raw p_T particle spectra can be extracted. Raw spectra consist of all particle candidates which are found in a specified spatial area (Θ, φ, Radius, etc.). To compare a measurement to theoretical predictions or to the results of other experiments, the raw spectra must be corrected to obtain the spectrum of produced particles. These corrections normally include detector effects, reconstruction efficiencies, geometrical acceptance or impurity (background) of the found particle candidate sample. Normally, specific selection criteria are applied to improve the signal to background ratio. Many corrections can only be deduced from Monte Carlo simulations. Therefore, events are simulated and reconstructed with a simulated detector applying identical algorithms as used for the data event reconstruction. Since the generated particle spectra are known from the simulation, the detector effects can be studied. If the simulated detector response, including e.g. the particle transport through the detector, is comparable to the real detector response and the generated events are similar to the data events, all correction quantities can be deduced. Via these corrections, spectra of produced particles can be deduced from the raw measured spectrum.

6.2.1 Event Generators Used by ALICE

The simulated detector implementation and the particle transport through the detectors is handled by GEANT3 [164]. The event generators used for pp collisions are PHOJET [173] and PYTHIA 6.4 [174] or PYTHIA 8.1 [175, 176]. For Pb–Pb event generation, the HIJING [177] event generator is used in ALICE. All programs are briefly explained in the following:

PHOJET is a Monte Carlo implementation of the Dual Parton Model [178] combined with the Quark-Gluon String Model [179, 180] for soft physics. The latter component is based on the exchange of the phenomenonical pomeron quasi particles. For the hard region of the cross sections, leading order pQCD processes are used. The two components of the total cross section are separated via a momentum cut-off around $3\,\mathrm{GeV/c}$. It does not include various sources of prompt photons (NLO). Parton showering is handled via the DGLAP equations [181–183], the hadronization via the Lund string model [184, 185].

PYTHIA is a pQCD inspired general purpose event generator. In ALICE two different versions of the program are in use. The older version 6.4 [174] is taken

for the simulations of the 7 TeV pp data. In contrast, the simulated events for the 2.76 TeV data set is generated with the newer version 8.1 [175, 176]. While PYTHIA 6.4 is written in Fortran, PYTHIA 8.1 is a reimplementation in C++.

PYTHIA includes and calculates nearly all leading order $2 \rightarrow 1$ and $2 \rightarrow 2$ interactions following in principle Eq. (4.1). Additionally, is has selective $2 \rightarrow 3$ processes included. PYTHIA 6.4 and 8.1 use the CTEQ 5L [186] as the default PDF, but alternative functions are also available. Parton showering is based on the leading log approximation to perturbative QCD [187, 188]. The process is transverse-momentum ordered and handles the initial- and final-state radiation. It contains the splitting of $q \rightarrow qg$, $g \rightarrow gg$, $g \rightarrow q\bar{q}$, $f \rightarrow f\gamma$ and $\gamma \rightarrow f\bar{f}$ (f is a lepton or a quark). Therefore, it includes direct-photon production from Bremsstrahlung. The hadronization is based, like in PHOJET, on the Lund fragmentation picture.

The underlying event is generated via multiple $2 \rightarrow 2$ parton interactions based on the standard QCD matrix elements but are damped for $p_T \rightarrow 0$. For this kind of "soft" interactions the parton distributions are rescaled after the initial hard collisions. In version 8.1, additional processes for prompt photons and virtual photons are included.

In contrast to PHOJET, PYTHIA has a lot of tunable parameters with a large influence on the generated cross sections. This is especially true for the more phenomenological describtion of soft parton-interactions. The cut-off parameter between soft and hard physics is per default set to $p_T = 2\,\mathrm{GeV}/c$. PYTHIA 8.1 is not yet fully adjusted to the LHC energies.

HIJING (**H**evy-**I**on **J**et **IN**teraction **G**enerator) [177] is a Monte Carlo event generator designed for pA and AA collisions but is also able to generate pp collisions. It combines pQCD models for multiple jet production with a phenomenological description of the low momentum part of the cross section via multistrings. It includes multiple minijet production (jet-like low p_T objects), nuclear shadowing of the PDF (see. Sec. 3.3, 4.1.2) as well as a schematic description of jet-medium interactions. For the calculation of the number of colliding nucleons, the Glauber Model is used.

HIJING is based on a combination of the Lund FRITIOF model [189, 190], the dual-parton model [178] for the soft interactions and on the pQCD PYTHIA model for hard physics. No medium effects from a collective behavior of an equilibrated plasma like flow is included. For jet physics, a formal quenching algorithm is optional. Minijets are expected to be an important aspect of the overall transverse energy production. An eikonal approximation [191] is used to calculate the multiplicity of minijets. Their properties, like initial- and final-state radiation, are based on PYTHIA.

The dominant amount of particles are produced in the soft regime. This is handled via soft-gluon exchange between the constituent quarks leading to longitudinal string-like excitations. The exchange might introduce small momentum kicks and the radiation of soft gluons, resulting in quark-antiquark production. The hadronization of those quarks is again realized with Lund model.

The HIJING version 2.0, used by the ALICE experiment, is tuned for LHC energies [192]. It has updated nPDF and minijet calculations. The gluon shadowing is adjusted [193]. The most important update is the tuning on the total charged-particle multiplicity.

GEANT (**GE**ometry **AN**d **T**racking) [194] is a transport Monte Carlo that simulates the traversing of particles through matter with all known material interactions. The particles which are generated by the generators are transported to an implementation of the ALICE detector. It simulates the detector response and thus, the generated events can be reconstructed like a data event. Two versions exist and are used by ALICE. The Fortran based GEANT3 is the standard version in ALICE. An updated C++ version, GEANT4, is also available but rarely used.

6.2.2 Monte Carlo Simulations for pp Collisions

For each pp data period, two dedicated Monte Carlo simulations exist. One is generated with PYTHIA 6.4 or 8.1, the other one with PHOJET. They are listed in Tab. 6.3. The table summarizes the corresponding data and MC period names together with the number of simulated events. As discussed for data events, not every generated event fulfills the required selection criteria. Thus both numbers, generated and accepted events, are given.

Each data taking run of ALICE has unique properties due to detector settings, drift-gas composition or gain, disabled detector modules etc. To have Monte Carlo productions as precise as possible, many parameters are stored during the ALICE measurements and re-applied by the reconstruction of the Monte Carlo events. The Monte Carlo runs are "anchored" to their corresponding data runs. The size of the Monte Carlo runs is matched to the number of events of the data runs.

For $\sqrt{s} = 7\,\text{TeV}$, both generators (PYTHIA 6.4 and PHOJET) are able to describe the measured raw photon p_T spectra with a fair accuracy. At high p_T, the difference is given only by a constant offset of 20%. While PHOJET under-predicts the spectrum, PYTHIA over-predicts it on the same level. Below $3\,\text{GeV}/c$, both generated spectra are similar and under-predict the data. The difference is largest at $p_\text{T} \sim 1\,\text{GeV}/c$, with a deviation of again 20%. For 2.76 TeV, both generators under-predict the measured photon spectrum by 25%. Here the agreement

$\sqrt{s}$	Period	Anchored To	Generator	Rec. Events	Acc. Events
2.76 TeV	LHC12f1a	LHC11a.pass4	PHOJET	2.7×10^7	2.1×10^7
	LHC12f1b		PYTHIA 8.1	2.6×10^7	1.8×10^7
	LHC12i3		PYTHIA 8.1	9.6×10^6	8.9×10^6
7 TeV	LHC10d1	LHC10b.pass2	PYTHIA 6.4	2.1×10^7	1.7×10^7
	LHC10d2		PHOJET	1.5×10^7	1.4×10^7
	LHC10d4	LHC10c.pass2	PYTHIA 6.4	5.8×10^7	4.8×10^7
	LHC10d4a		PHOJET	6.7×10^7	6.0×10^7
	LHC10f6	LHC10d.pass2	PHOJET	1.5×10^8	1.3×10^8
	LHC10f6a		PYTHIA 6.4	1.5×10^8	1.1×10^8
	LHC10e20	LHC10e.pass2	PYTHIA 6.4	1.4×10^7	1.1×10^7
	LHC10e21		PHOJET	1.5×10^7	1.2×10^7

Table 6.3: Monte Carlo simulations and corresponding number of events for pp collisions at $\sqrt{s} = 7$ TeV and 2.76 TeV.

in shape is better. The difference is in contrast to the 7 TeV data just given by a constant offset. The comparison of the measured raw-photon spectra to the generated spectra is shown in Fig. 6.2.
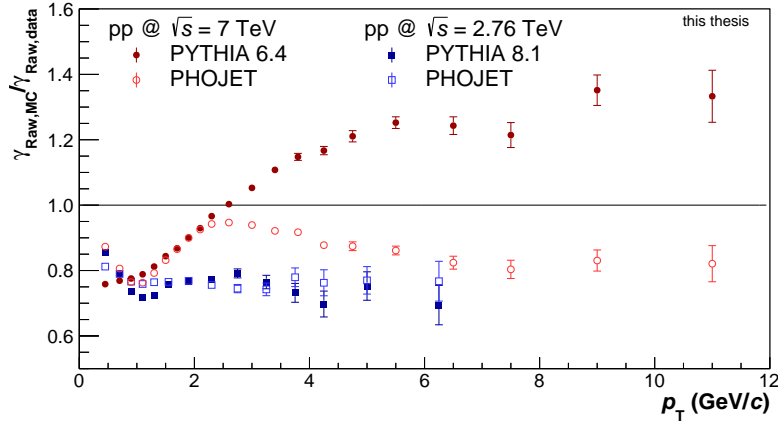

Figure 6.2: Ratio of generated raw-photon spectra over measured raw-photon spectra for pp collisions at $\sqrt{s} = 7$ TeV and 2.76 TeV.

To have a larger event sample, both event sets are combined. This reduces the statistical and systematic uncertainties of the results. The systematic difference between the two corrected photon spectra (PHOJET and PYTHIA) for 7 TeV and

2.76TeV are on the order of 1% over the whole considered p_T range. The difference in the π^0 spectra is slightly larger and on the order of 2-4%. Due to the larger statistical uncertainties of the π^0 spectra, the systematic difference is hardly (if at all) distinguishable from statistical fluctuations.

For the 2.76 TeV data set, a third production LHC1012i3 exists. This PYTHIA 8.1 production has exactly the same settings as the PYTHIA production LHC12f1b. For a reduction of the statistical uncertainties, ten additional neutral pions are added to each event inside the TPC and ITS ($|\eta| < 1.2$) acceptance. The momentum range of the added particles is $0 \, \text{GeV}/c < p_T < 30 \, \text{GeV}/c$ following a flat p_T distribution. Ten additional η mesons are added for future studies of the transverse momentum spectrum of that meson. The unphysical flat shape of the Monte Carlo generated spectra is taken into account by reweighting the generated spectra (Sec. 8.2).

Statistics is the limiting factor for the direct-photon analysis. Here the limiting part is the measurement of the π^0 spectrum. Without the extra signals, the available minimum bias statistics for 2.76 TeV would be insufficient for the analysis.

6.2.3 Monte Carlo Simulations for Pb–Pb Collisions

In contrast to pp, only the event generator HIJING is available. For the Monte Carlo correction of the Pb–Pb measurement, two large simulations were produced. They are adapted to the special requirements of the π^0 and direct-photon analysis. Like the proton-proton production LHC1012i3 extra neutral mesons (π^0 and η) are added to each event. In pp, the overall track multiplicity is magnitudes smaller compared to heavy-ion collisions. Consequently, the number of added particles is larger. A too large number of added particles in a detector environment with large occupancy might disturb the single particle and the secondary vertex tracking. Thus, the number of extra mesons depends on the impact parameter of the simulated event. The amount of extra π^0 and η is given by the exponential:

$$n_{\pi^0}(b) = 30 + 30 \exp\left(-\frac{0.5b^2}{5.12^2}\right). \tag{6.5}$$

In central events $\sim$ 40-50 in most peripheral 30 particles per species are added. As for pp, they follow a flat momentum distribution. The pseudorapidity window is set to $|\eta| < 1.2$. Similar to pp, the extra high p_T neutral mesons makes an extension of the analysis up to higher momenta possible. To have a realistic reconstruction efficiency, the Monte Carlo π^0 spectrum shape is again weighted to reproduce the measured spectra from data events (Sec. 8.2).

Two different Monte Carlo productions exist. The first set of events, LHC13d, is the larger production with a nearly flat centrality distribution between 0-90%. The number of events slightly rises towards peripheral events. Furthermore, to have sufficient statistics for the lower multiplicity peripheral events, the second production LHC13db, is dedicated to peripheral events with an impact factor of $6\,\mathrm{fm} < b < 20\,\mathrm{fm}$. This corresponds to a centrality range of 20-90%.

A standard procedure in ALICE (see. Sec. 6.1.2) is the selection via percentiles of the measured V0 amplitude. This is handled within AliRoot by the standard class Ali Centrality. Selecting the same percentile of centrality in the V0 amplitude in the Monte Carlo was found to result in a slightly larger number of tracks in the TPC volume. In general, the tracking efficiency can depend on the multiplicity of an event. To test if this is the case for the photon finding efficiency, a second centrality selection criterion is applied.

To get a better charged track multiplicity matching, the centrality of the Monte Carlo was redefined. The track multiplicity in the TPC in Monte Carlo is directly used as the centrality discriminator. It is applied via constant cuts in the track multiplicity in the Monte Carlo. By still using the V0 amplitude as the discriminator in data, the resulting track distributions are Gaussian-like. To define the cut value used in Monte Carlo, the intersection point of two data track distribution of two neighboring centrality bins is taken.

The number of events of the centrality classes used for this analysis are summarized in Tab. 6.4. The number of events corresponds to the TPC track centrality criterion discussed above.

Period Name	Centrality	Anchored To	Generator	Rec. Events	Acc. Events
LHC13d2	0-80%	LHC10h.pass2	HIJING	9.1×10^6	6.5×10^6
	0-20%				1.2×10^6
	0-40%				2.7×10^6
	20-40%				1.5×10^6
	40-80%				3.8×10^6
LHC13d2b	0-80%	LHC10h.pass2	HIJING	4.1×10^6	3.1×10^6
	0-20%				2.3×10^5
	0-40%				1.2×10^6
	20-40%				7.7×10^5
	40-80%				2.0×10^6

Table 6.4: Monte Carlo simulations and corresponding number of events for Pb–Pb collisions at $\sqrt{s_{\mathrm{NN}}} = 2.76\,\mathrm{TeV}$.

6.3 Quality Assurance for pp and Pb–Pb Simulations

Quality Assurance for pp Collisions

The QA tests are performed run-wise by comparing data and simulation. During a single run, the detector should operate under stable conditions. Between two runs, the conditions may change.

In the figures 6.3, 6.4, 6.5, 6.6 and 6.7, the available runs of all data periods are compared to its anchored Monte Carlo productions. The comparison includes the number of primary tracks in $|\eta| < 0.8$ and the number of photon candidates. Both are normalized to the number of events stored in the run. Since the conditions are sightly different for each run, the event multiplicity should be comparable between data and Monte Carlo.

Both generators (PYTHIA and PHOJET) are not able to reproduce the number of charged tracks for 7 TeV and 2.76 TeV, respectively. The number is underpredicted by roughly one track per event with an average multiplicity of six tracks in the data events. Correspondingly, the number of photons per event is also underpredicted. This observation coincide with the ratio of raw photon-spectra described in Sec. 6.2. The photon multiplicity is on the order of 0.12 photon per event.

In general, PHOJET describes the multiplicities slightly better than PYTHIA 6.4 used for 7 TeV. The simulations for the 2.76 TeV data (PHOJET, PYTHIA 8.1) have exactly the same multiplicities. As discussed, the low detector occupancy in pp collision in a detector designed for heavy-ion collisions is not crucial for the analysis. The slightly different number of tracks will not change the single photon or neutral pion finding efficiency.

For the periods LHC10b, LHC10c and LHC10d all data runs have corresponding Monte Carlo runs with nearly the same number of events from both generators. For the LHC10e data set, only a fraction of all runs have a corresponding simulated event set. Furthermore, the simulated runs are only produced with 10% of the recorded statistics of the data run.

The reconstruction properties in LHC10e were similar to LHC10d, the largest of all productions. The two periods LHC10b and LHC10c had also similar reconstruction properties. Nevertheless, the missing statistic for LHC10e results in a disbalance in the number of events available in data and Monte Carlo. To avoid an overemphasis of the simulated events from LHC10b and LHC10c, all events are weighted accordingly to the number of data events of the different periods.

Additionally, it was checked if the different Monte Carlo runs have consistent reconstruction efficiencies and photon purities. For data and Monte Carlo, the raw photon-spectra normalized to the number of events of the runs are compared. This test was applied to exclude runs with unphysical high p_T outliers not visible in the integrated numbers.

Quality Assurance for Pb–Pb Collisions

The same procedure used for the pp data is applied in Pb–Pb. In contrast to pp only one data period and one event generator is available. To have a sufficient statistic in all centralities, the intervals 0-20%, 0-40%, 20-40% and 40-80% are taken.

Like for the pp data, the number of charged tracks and the number of photons per event are compared. Since both simulations, LHC13d2 and LHC13d2b, have identical simulation parameters, the data is only compared to the larger production with the flat impact parameter distribution. In addition, the event number in data and Monte Carlo is compared. Here roughly the same number of events is available from the LHC13d2 production. The comparison in shown in Fig. 6.8, 6.9 and 6.10.

The centrality discriminator used for Monte Carlo is the number of charged tracks. Thus, the difference in data and simulation should be small. This is true for the 0-20% and the 20-40% bin. For the 40-80%, the number in Monte Carlo is slightly smaller. This can be understood by the steeply falling distribution towards larger

centralities of the V0 amplitude (see Fig. 6.1) and the corresponding number of tracks.

As for pp, the number of photon candidates in HIJING is clearly below the measured values. The reconstruction efficiency of photons should not depend on the number of photons per event. The difference is not considered as an issue for the analysis.

It was found that the photon reconstruction via displaced vertices is limited to $|\eta| \leq 0.65$ in the Monte Carlo simulation LHC1013d and LHC13d2b. In contrast to photon multiplicity, the reconstruction efficiency depends on the pseudorapidity windows due to different track length in the ITS and TPC. To avoid deviating efficiencies in data and simulation, the analyzed η region is restricted to to $|\eta| \leq 0.6$ in the Pb–Pb analysis.

Like for pp, the efficiencies and purities were checked run-wise. The raw spectra of photons in data and Monte Carlo and the spectra of secondary photons are checked. It was found that some events of the run 138275 of the LHC13d2 production have an unphysical number of secondary photon candidates at large transverse momenta. This changes the secondary photon correction factor as introduced in Sec. 7.3.1. All such unphysical events are removed from the final event sample.
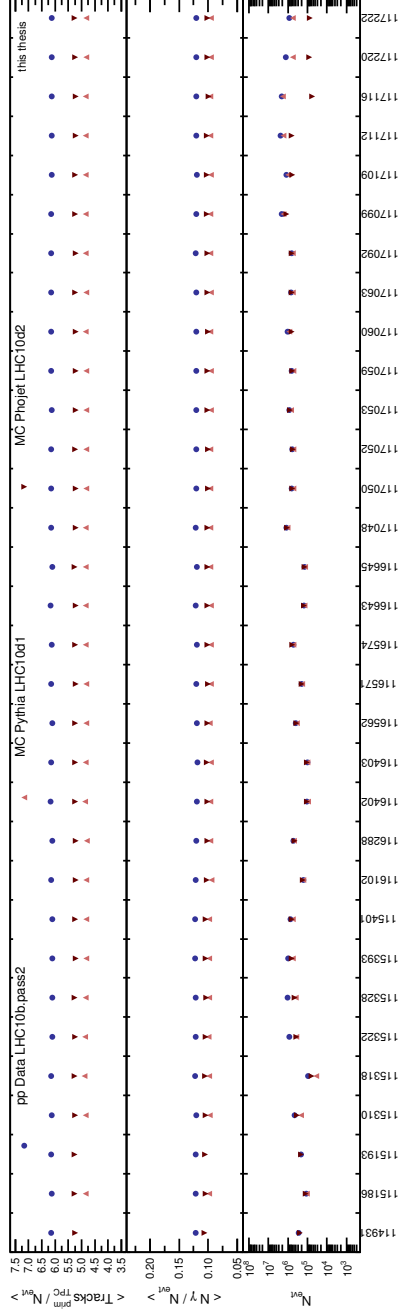
Figure 6.3: Number of primary TPC tracks and γ candidates per event and N_{event} for LHC10b, LHC10d1 and LHC10d2 ($\sqrt{s} = 7\,\text{TeV}$) for all analyzed runs.
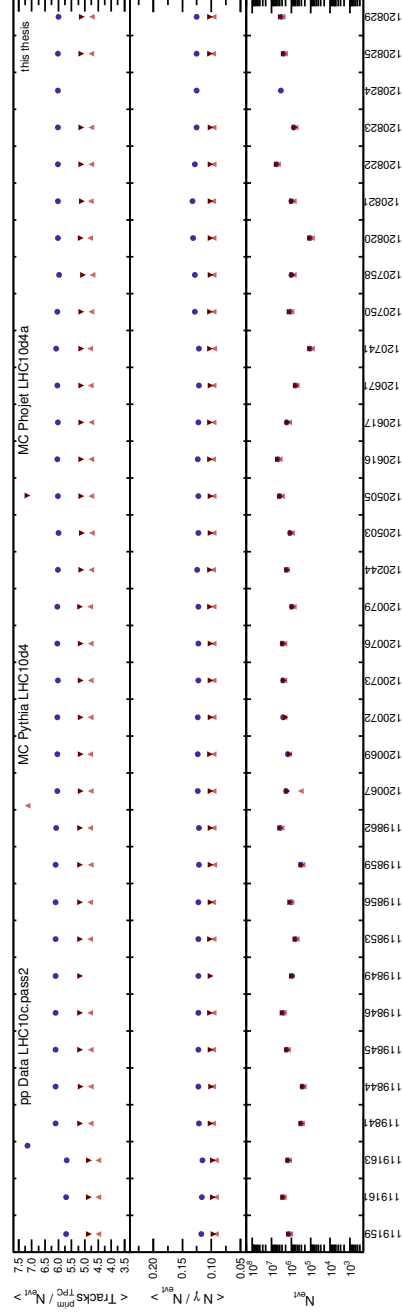
Figure 6.4: Number of primary TPC tracks and γ candidates per event and N_{event} for LHC10c, LHC10d4 and LHC10d4a ($\sqrt{s} = 7\,\text{TeV}$) for all analyzed runs.
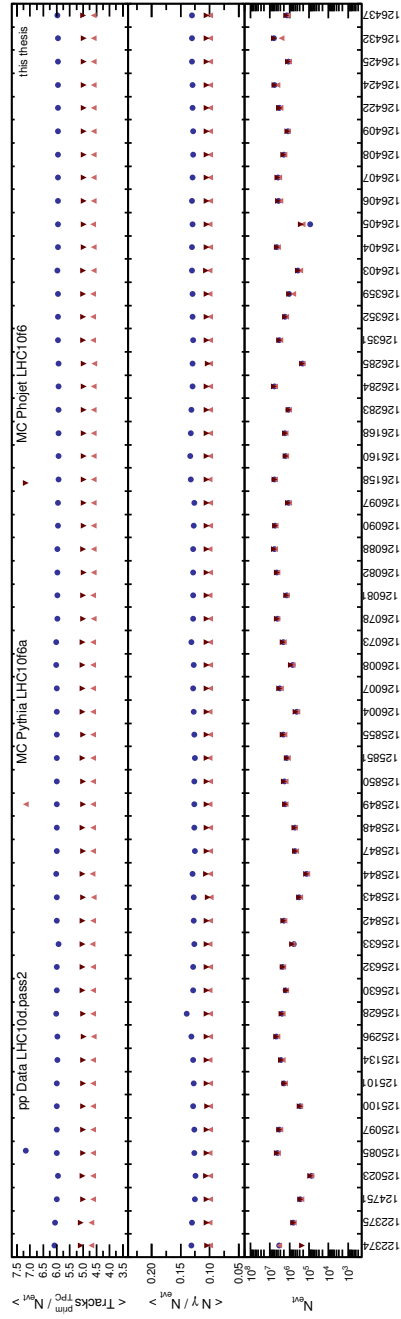
Figure 6.5: Number of primary TPC tracks and γ candidates per event and N_{event} for LHC10d, LHC10f6a and LHC10f6 ($\sqrt{s} = 7$ TeV) for all analyzed runs.
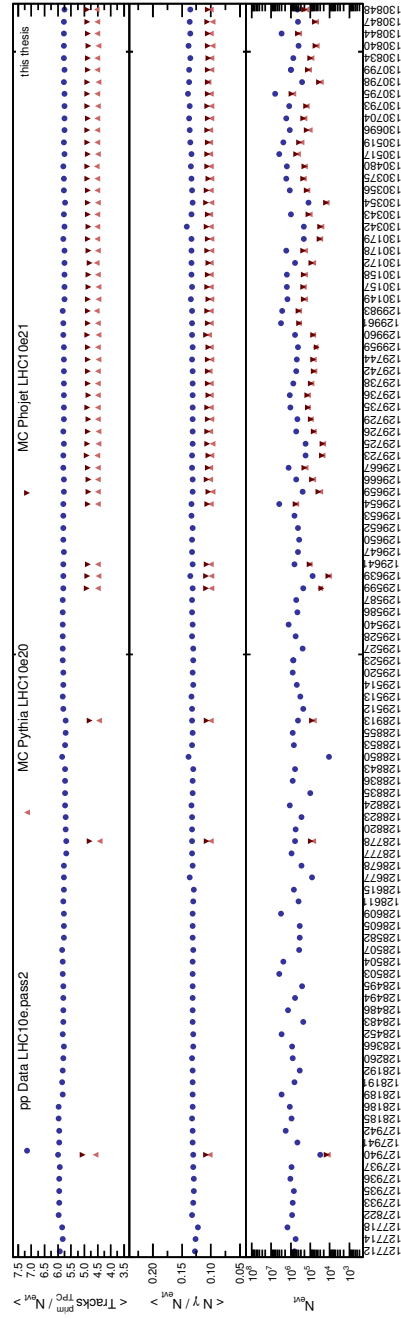
Figure 6.6: Number of primary TPC tracks and γ candidates per event and N_{event} for LHC10e, LHC10e20 and LHC10e21 ($\sqrt{s} = 7$ TeV) for all analyzed runs.
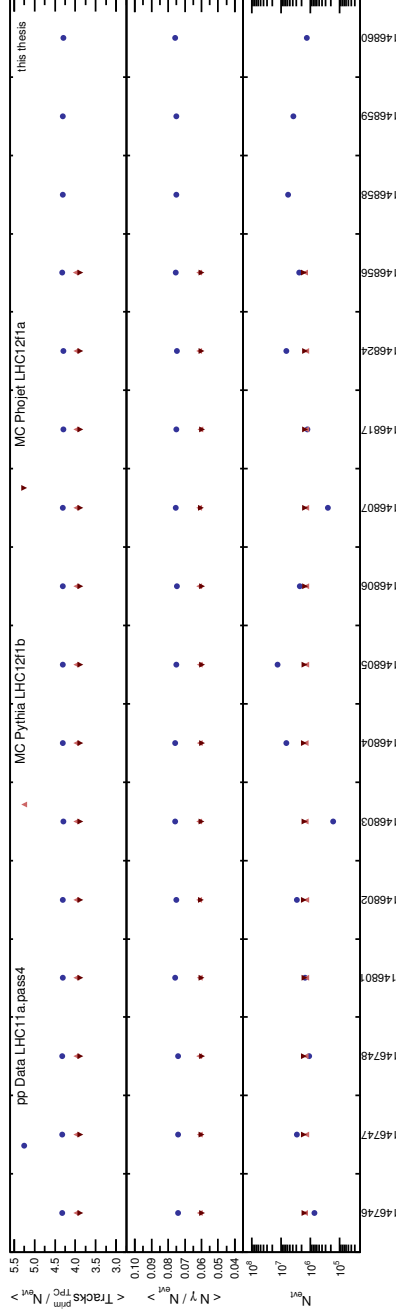
Figure 6.7: Number of primary TPC tracks and γ candidates per event and N_{event} for LHC11a, LHC12f1b and LHC12f1a ($\sqrt{s} = 2.76\,\text{TeV}$) for all analyzed runs.
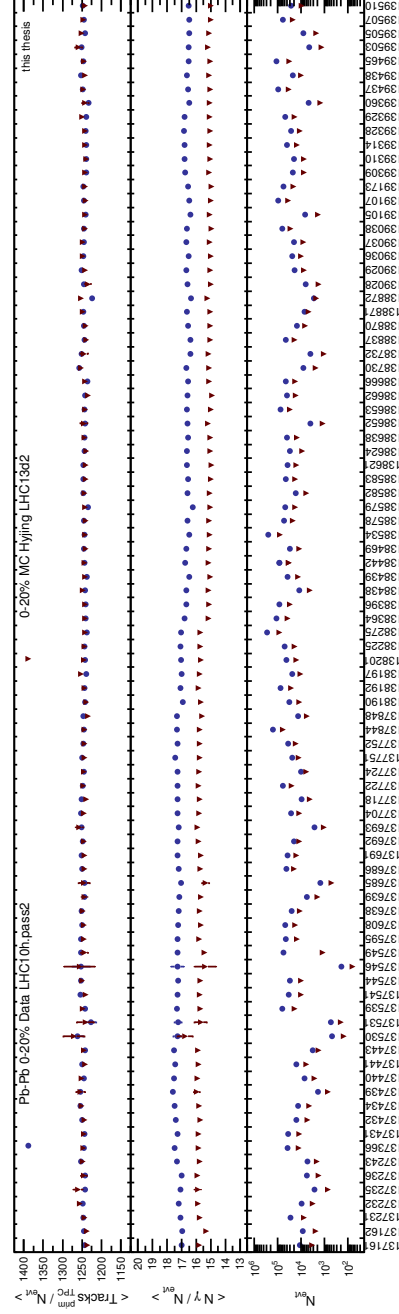
Figure 6.8: Number of primary TPC tracks and γ candidates per event and N_{event} for LHC10h and LHC13d2 in 0-20% centrality ($\sqrt{s_{\text{NN}}} = 2.76\,\text{TeV}$) for all analyzed runs.
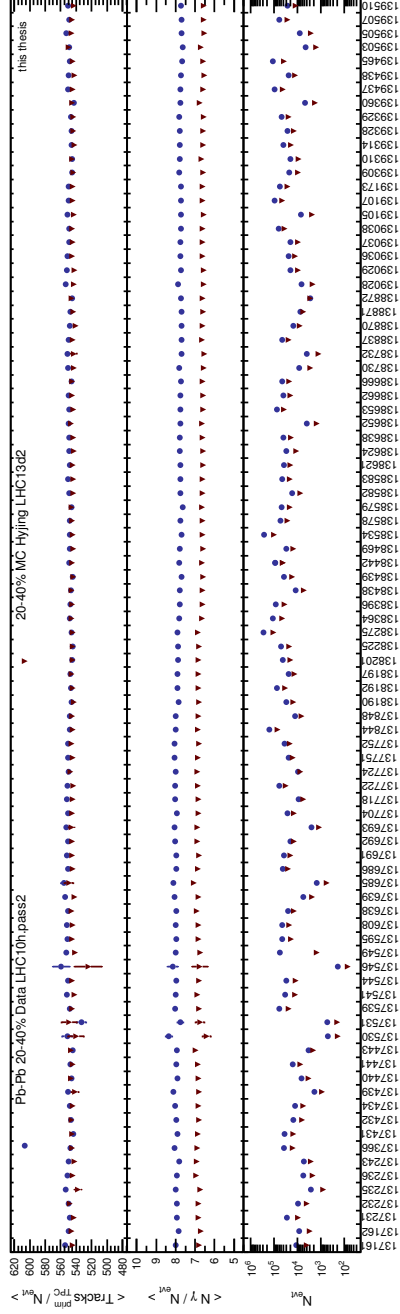
Figure 6.9: Number of primary TPC tracks and γ candidates per event and N_{event} for LHC10h and LHC13d2 in 20-40% centrality ($\sqrt{s_{\text{NN}}} = 2.76\,\text{TeV}$) for all analyzed runs.
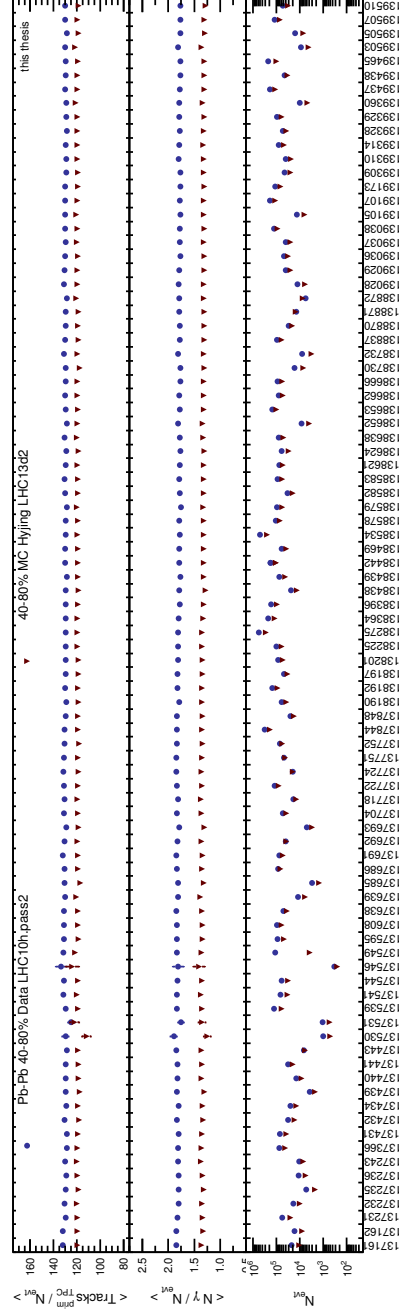
Figure 6.10: Number of primary TPC tracks and γ candidates per event and N_{event} for LHC10h and LHC13d2 in 40-80% centrality ($\sqrt{s_{\text{NN}}} = 2.76\,\text{TeV}$) for all analyzed runs.

7 Photon Reconstruction Using the Conversion Method

The most common approach to measure photons in high-energy experiments like ALICE is the detection with electromagnetic calorimeters. This technique is also applied in ALICE with the two calorimeters EMCal and PHOS (Sec. 5.2.5). ALICE has an excellent charged particle tracking. Therefore, it is possible to detect converted photons via their conversion products, electron-positron pairs. The topology of a photon conversion is identical to a secondary vertex produced by a decaying particle with long life-time. Those particles are typically Λ or K_s^0. Even though a photon conversion is not a decay, it can be handled by the same tracking algorithm.

7.1 Secondary Vertex Finder

The algorithms which are used for the secondary vertex finding are called V0 finder. The name originates from the decay topology of a decaying neutral particle. The two charged tracks form a V in the detector, the 0 refers to the charge of the decaying particle. A sketched V0 decay is shown in Fig. 7.1. In ALICE, two slightly different V0 reconstruction algorithms exist.

In general, both secondary vertex finder algorithms are based on the same principle. The main difference of the two finders is the stage of the track finding process during the reconstruction of the event. While the *on-the-fly finder* already runs during the initial reconstruction of the tracks, the *offline finder* runs after all tracks are already processed and stored as ESD objects. Due to this, the on-the fly finder has more track related information available and thus a better spatial and momentum resolution. In pp collisions, both finders are tuned to result in similar finding efficiencies and particle yields. In Pb–Pb collisions, the selection criteria for secondary tracks for the offline finder are strongly tightened to reduce the amount of combinatorial background and computing time. This reduces the raw photon-signal in central Pb–Pb events by a factor of 2. In peripheral events,
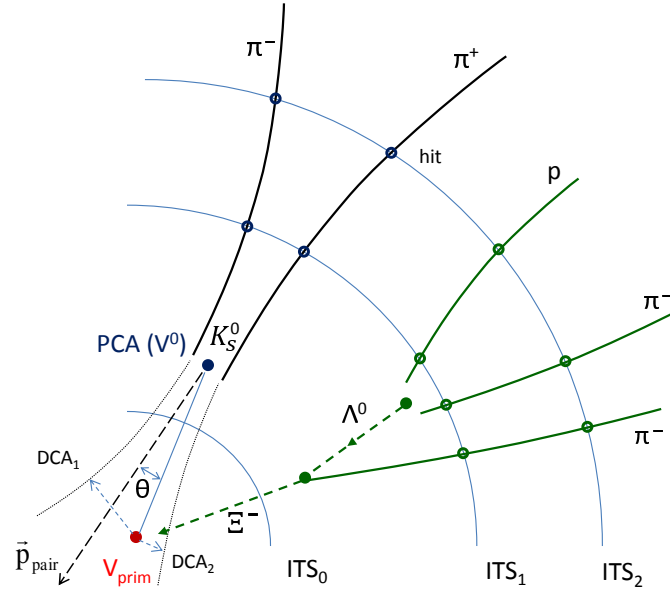
Figure 7.1: Schematic view on a secondary vertex decay of a K_s^0 and a cascade of a Ξ^- in the ALICE detector. A γ conversion looks identical to the neutral kaon decay. The charged tracks are drawn as solid lines, the neutral particles as dashed lines. [166]

the reduction is slightly smaller and on the level of 30%. The corresponding Monte Carlo simulations are very sensitive to this tight selection criteria and not fully able to reproduce the finding efficiencies. In contrast, the on-the-fly finder has more relaxed finding criteria, and the finding efficiency is reproduced much better. As a default, the on-the-fly finder is used.

On-the-Fly V0 Finder

The on-the-fly V0 finder runs during the reconstruction of the ITS tracks. In this stage of tracking, all cluster and hit information of the ITS and the TPC, as well as the covariance matrices, are still available. It is able to refit the track parameters with the assumption of originating from the identified secondary vertex. During the successive adding of clusters to the tracks of the V0 candidate, the likelihood of having a V0 is continuously tested. The algorithm is able to consider multiple scattering and energy loss of the decay or conversion products. This leads to a good position and momentum resolution of the identified secondary vertices.

The steps of the algorithm are:

1. The track quality is tested. This includes the maximal and minimal radial distance to the primary vertex. Here a distance of 0.5 mm (1 mm for Pb–

Pb) is required. The minimum distance of the closest approach (DCA) of the two tracks has to be below 1.5 cm. The pointing angle between the momentum vector of the V0 and the vector pointing to the primary vertex (Θ in Fig. 7.1) is estimated. The pair is accepted if the cosine of this angle is above 0.9.

2. If a track pair is accepted as originating from a common secondary vertex, an AliRoot V0 object containing all required information is stored. The corresponding track information is updated under the assumption of a common displaced origin. For the recalculated track parameters the radius, the distance of closest approach and the pointing angle, is updated. If one of the required criteria are missed after the recalculation, the candidate is rejected.

3. If all requirements are fulfilled, the candidate is accepted as an on-the-fly V0.

4. If additional TPC cluster information can be associated to the V0 tracks, the V0 is recalculated with the additional track information.

The V0 finding efficiencies of K_s^0, Λ ($\bar{\Lambda}$) and photons of the on-the-fly finder in pp collisions at $\sqrt{s} = 7$ TeV is shown in Fig. 7.2. The efficiency for photonic V0s
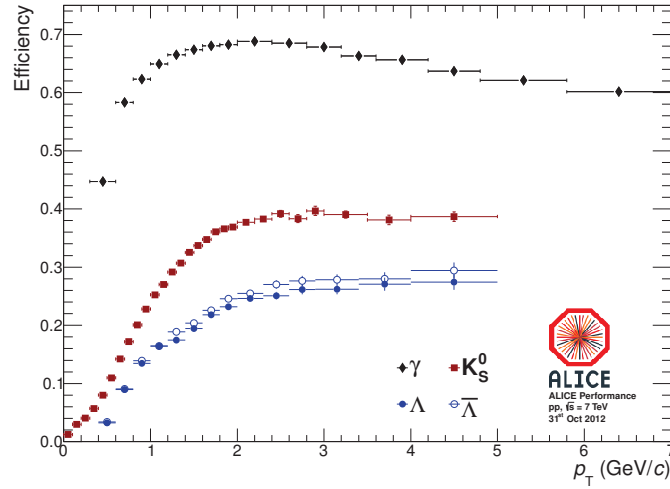
Figure 7.2: Reconstruction efficiencies of photon, K_s^0 and Λ ($\bar{\Lambda}$) with the on-the-fly V0 finder. [195]

are obtained with additional PID cuts on the tracks.

Offline V0 Finder

The algorithm is very similar to the on-the-fly method. The most important difference is the time of the finding process. The offline finder runs after the tracks are reconstructed on the level of ESD tracks. At this late stage, no recalculation of tracks under a secondary vertex assumption is possible. This includes the V0 likelihood determination available for the on-the-fly finder.

The performed steps are:

1. All tracks with opposite charge are paired. The tracks require a TPC refit (see Sec. 5.5).

2. Each pair has to fulfill, like the on-the-fly pairs, a minimum impact parameter ($0.5\,\mathrm{mm}$) to the primary vertex and distance of closest approach ($1.5\,\mathrm{cm}$) between the pair. Furthermore, the vertex is required to lie between a maximum and minimum radius of 0.2-200 cm.

3. If these requirements are fulfilled, the cosine of the pointing angle is calculated and pairs with a value > 0.9 are rejected.

Recalculation of the Photon Conversion Point

The standard decay hypothesis for a V0 candidate is the decay of the K_s^0. Due to the expected opening angle of the K_s^0 decay, a conversion point might be displaced from the secondary vertex position estimated by the finder. With the additional constraint of a vanishing opening angle between the lepton pair, the momenta of the e^+e^- pair have to be parallel at its production point, the conversion point can be recalculated. The recalculation is performed during the photon analysis in the AliV0ReaderV1 class [196].

For this calculation, the helix centers of the two tracks are obtained from the ESD track parameters. The x,y-position of the conversion point is assumed to be located on the connecting line of the two helix centers (parallel momenta). For this purpose the x,y-projection of the helices are used. The final conversion x,y-position, located on the line, is shifted to the center of gravity in respected to the radii (momenta) of the two helices (tracks). From the corresponding x,y-coordinates on the helices (also on this connection line), the corresponding z-coordinate can be estimated from the three-dimensional track information. The z-coordinate of the conversion point is again located on the connection line of the two z-coordinates on the helices. Its exact position is again at the center of gravity obtained from the momenta of the two tracks. A more detailed description is given in [197].

7.2 Selection of Photon Candidates from Secondary Vertices

From the large sample of secondary vertices found by the V0 finder, photon candidates have to be identified. The largest fraction of the V0 sample is combinatorial background, false combinations of charged tracks. Without an improved signal to background ratio, the corresponding photon purity correction would be enormous. The corrected spectra would depend very sensitively on the correct description of the background in the Monte Carlo.

The applied photon selection criteria can be separated in three different groups. The first set is given by the spatial orientation and the reconstruction quality of the charged tracks forming the V0 candidates. The second group contains particle identification (PID) methods of the ALICE detectors. The last set of criteria is dedicated to the topology of photon conversions. Due to the zero mass of photons, the opening angle should be close to zero. From this characteristic, several sophisticated criteria can be formulated.

7.2.1 Track Selection Criteria

In the first step of the photon selection, the global track quality of all tracks building the V0s are validated. This includes the requirement of a TPC refit (Sec. 5.5) and the rejection of tracks with kink topology. A kink in a track is normally caused by a decay of a particle into an equally charged and a neutral particle. Since electrons or positions do not decay, V0s with tracks with kinks are removed from the sample. The ratio of the theoretically findable TPC cluster, given by the track path through the TPC, over the actually found clusters is tested. If the ratio is too small, the corresponding track might only be a wrong combination of non-related clusters. In this calculation, the crossing of rows between TPC sections is included. The crossing might reduce the number of findable clusters. Furthermore, tracks require a minimum p_T. The minimum p_T is added as a criterion since it reduces the amount of combinatorial background. Such tracks are strongly curled and might produce a large number of combinatorial background V0s.

The analysis is limited to a fiducial region in pseudo-rapidity. This η cut is applied for tracks and V0s, respectively. Due to their non-zero decay length, most of the secondary vertices are not located at $Z = 0$. They might lie outside the accepted fiducial η region defined in respect to the origin, despite an accepted pseudo-rapidity value. To remove such V0s, an additional condition is formulated. V0s

have to satisfy an η related condition depending on the reconstructed conversion point $(R_{\mathrm{conv}}, Z_{\mathrm{conv}})$. This selection is referred to as Line Cut and is given by:

$$R_{\mathrm{conv}} > |Z_{\mathrm{conv}}| \cdot \tan\left(2 \arctan\left(\exp\left(-\eta_{\mathrm{fiducial}}\right)\right)\right) - Z_0. \qquad (7.1)$$

The constant value Z_0 is set to $7\,\mathrm{cm}$ for the pp and the Pb–Pb analysis.

Additional geometrical constraints are a minimum and maximum allowed radius R_{conv} and a maximum Z_{conv} value of the conversion point. The minimum value of R_{conv} is normally set to $5\,\mathrm{cm}$ to remove π^0 Dalitz decays ($\pi^0 \rightarrow e^+e^-\gamma$) from the π^0 analysis. In that case, the lepton pair coming from the virtual photon is misidentified as an external conversion and identified as a secondary vertex located close to the primary vertex. All parameters used for the track-quality selection are summarized in Tab. 7.3. All values are identical for all analyzed center-of-mass

Selection Criterion	2.76 TeV (pp)	7 TeV (pp)	2.76 TeV (Pb–Pb)
fiducial $|\eta_{\mathrm{track,V0}}|$	0.9	0.9	0.65
min – max R_{conv}	$5\,\mathrm{cm} - 180\,\mathrm{cm}$	$5\,\mathrm{cm} - 180\,\mathrm{cm}$	$5\,\mathrm{cm} - 180\,\mathrm{cm}$
max Z_{conv}	$240\,\mathrm{cm}$	$240\,\mathrm{cm}$	$240\,\mathrm{cm}$
min track p_{T}	$50\,\mathrm{MeV}/c$	$50\,\mathrm{MeV}/c$	$50\,\mathrm{MeV}/c$
findable cluster ratio	$> 60\%$	$> 60\%$	$> 60\%$

Figure 7.3: Values for the electron track selection for the direct-photon analysis for all analyzed collision energies.

energies.

7.2.2 Electron Identification with the ALICE PID

The most powerful method of rejecting non-electronic particles is given by the particle identification (PID) capability of ALICE. The size of the rejection power is unique among the LHC experiments [198,199]. ALICE is equipped with almost all available types of particle identification detectors. The most important system of PID for the direct-photon analysis is provided by the TPC with its measurement of the specific energy loss $\mathrm{d}E$ per unit length $\mathrm{d}x$. With the large number of readout channels (Sec. 5.2.2), it provides up to 159 individual ionization samples with a resolution obtained from a truncated mean of $\sigma_{\mathrm{d}E/\mathrm{d}x} \approx 5\%$. The truncated mean is required since the distribution is non-Gaussian but Landau-shaped. The energy loss can be described by the famous Bethe-Bloch formula. It relates the mean

energy loss $\mathrm{d}E$ per path length $\mathrm{d}x$ with the charge number z, the velocity of the traversing charged particle v ($\beta = v/c$) and the atomic (mass) number Z and A of the stopping medium.

$$-\left\langle \frac{\mathrm{d}E}{\mathrm{d}x} \right\rangle = K z^2 \frac{Z}{A} \frac{1}{\beta^2} \left[\frac{1}{2} \ln \left(\frac{2 m_e c^2 \beta^2 T_{\max}}{I^2} \right) - \beta^2 - \frac{\delta(\beta\gamma)}{2} \right] \tag{7.2}$$

$K = 4\pi N_A r_e^2 m_e c^2$ is a constant factor including the classical electron radius r_e, the electron mass m_e and Avogardo's number N_A. The maximum possible energy transferred by an interaction with an atomic electron is given by $T_{\max}$. I is the mean excitation energy of the medium. The density effects are considered with the term $\delta(\beta\gamma)/2$. It depends on the energy of the traversing particle and its extension of its electric field. The extension is limited by the polarization of the traversed medium. The Bethe-Bloch formula is able to describe the energy loss of heavy particles over several magnitudes of particle velocities ($0.1 \lesssim \beta\gamma \lesssim 1000$) within a few percent.

The formula depends, in addition to the traversed medium, only on the charge and the velocity of the traversing particle. The particle species can be estimated by comparing the energy loss of different particles at the same value of momentum. Different particles will have, for a given momentum value, different velocities caused by deviating particle masses. The deviating velocities result in different energy loss values.

The most probable values of the energy loss of each species is estimated by parameterizations of the measured energy loss distributions. The used parameterizations were originally introduced by the ALEPH collaboration [200]:

$$f(\beta\gamma) = \frac{P_1}{\beta^{P_4}} \left(P_2 - \beta^{P_4} - \ln \left(P_3 + \frac{1}{(\beta\gamma)^{P_5}} \right) \right). \tag{7.3}$$

The function has five free parameters (P_{1-5}). β is the particle velocity and γ the Lorentz factor. The probability of the identification of a particle can be expressed via the distance in terms of the number of σ of a Gaussian distribution away from the most probable values given by Eq. (7.3). The width of the distribution is given by the energy loss resolution $\sigma_{\mathrm{d}E/\mathrm{d}x}$. The probability of a track of being a particle of type i is calculated as:

$$P(i) = \frac{1}{\sqrt{2\pi}\sigma_{\mathrm{d}E/\mathrm{d}x}} \exp \left(-\frac{\left((\mathrm{d}E/\mathrm{d}x)_{\mathrm{meas}} - (\mathrm{d}E/\mathrm{d}x)_{\mathrm{param},i} \right)^2}{2\sigma_{\mathrm{d}E/\mathrm{d}x}^2} \right). \tag{7.4}$$

In the analysis, two different selections via the energy loss dE/dx are applied. In a first step, all tracks are accepted which are within a certain σ-band around the momentum dependent parameterization of the energy loss curve for electrons. In a second step, all tracks within a second band around the expected charged pion energy loss are rejected. The Bethe-Bloch curves of electrons and pions cross at $p \sim 0.2\,\mathrm{GeV}/c$. The pion rejection is only applied down to a minimum momentum value slightly larger than this crossing point. The specific p value is tuned to the width of the electron loss band at this momentum value for the corresponding collision system. For a cut through the maximum of the electron distribution, the matching between data and Monte Carlo has to be very precise. To avoid large uncertainties, the rejection of electrons in the crossing region is skipped.

In Fig. 7.4, the specific energy loss of all tracks associated with V0 candidates versus its momentum are shown for pp collisions at $7\,\mathrm{TeV}$. In Fig. 7.5, the same quantities are shown for central Pb–Pb (0-20%) events. In the upper rows, the TPC dE/dx signal is plotted while in the lower rows, the distance in terms of σ of each track to the electron parameterization is presented. In the left column, the TPC signal is shown for all V0 tracks before any track or V0 selection is applied. The right column shows only electron candidates after all cuts are applied.

It is clearly visible that before the electron and photon selection the sample contains many non-electronic particles. The dominating particle species are pions frequently produced in particle collisions. Kaons and protons also contribute to the track sample. Even muons and deuterons can be identified via their characteristic energy loss bands. After all cuts are applied, the pp sample is nearly free of visible non-electron background. For Pb–Pb collisions, contributions from other particles are still clearly contained in the sample. The corresponding contamination of the photon sample is discussed in Sec. 7.3.2.

A second PID method used for the analysis is the time-of-flight measurement with the TOF (Sec. 5.2.3) detector. This criterion is only used for the Pb–Pb analysis. The cut is applied on the difference of the measured time-of-flight from the expected time-of-flight. It is again expressed in terms of the number of σ given by the width of the TOF resolution σ_{TOF}. The resolution is $120\,\mathrm{ps}$ in Pb–Pb collisions. Only 3-5% of V0 tracks in the analyzed sample have usable TOF information. The cut is only applied if the track has the required information. This PID cut has nearly no influence on the purity of the sample. In the pp case, the sample was already found to be very clean and the cut as not required.

In Tab. 7.6, all PID cuts used for the direct-photon analysis in all center-of-mass energies are summarized. Due to the larger number of tracks produced in heavy-ion collisions, the pion rejection was chosen to be tighter. As a consequence, the
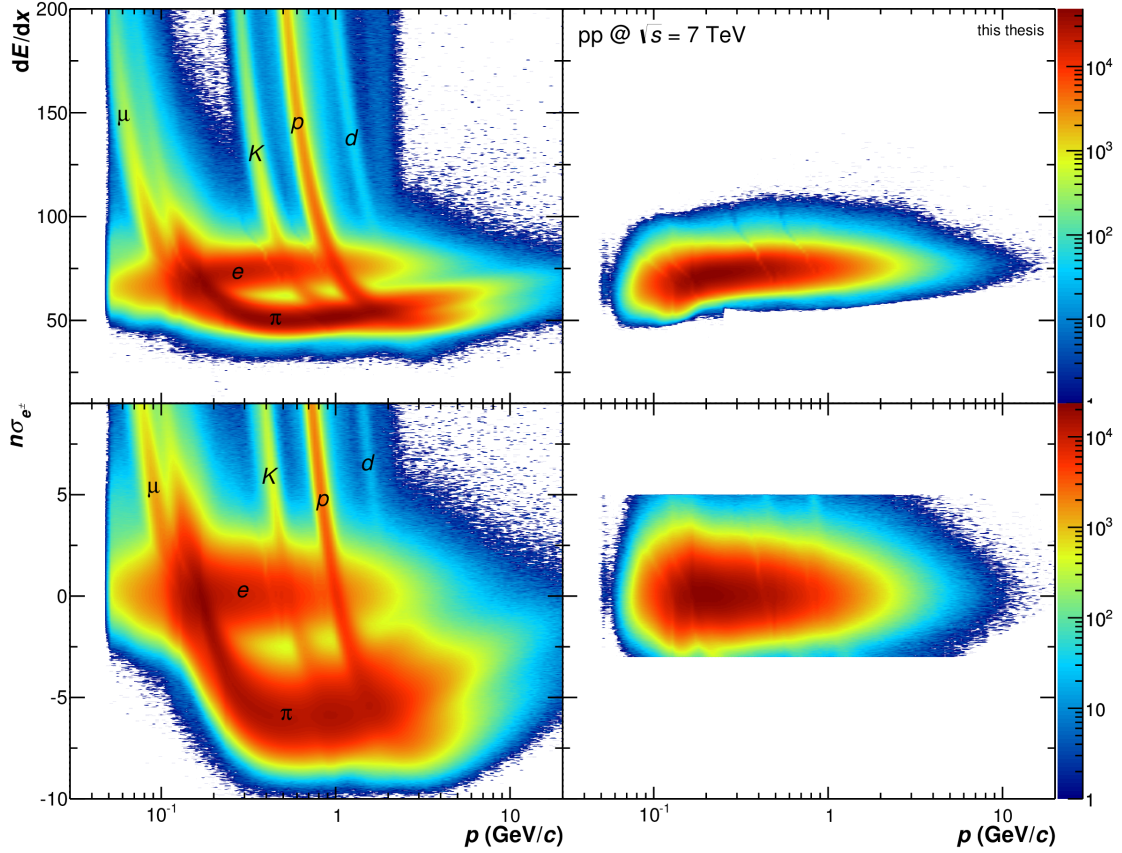
Figure 7.4: TPC $\mathrm{d}E/\mathrm{d}x$ and $n\sigma_e$ before and after photon and track selection criteria for pp at 7 TeV

minimum cut value of p has to be larger to avoid the rejection of electron candidates close to the crossing point of the two Bethe-Bloch curves. The maximum electron/positron momentum cut at $100\,\mathrm{GeV}/c$ is equivalent to a momentum cut at infinity.

In principle, ALICE has further PID capabilities provided for example by the TRD, the ITS or via calorimeter measurements. These techniques are not used for the analysis. All of those would not significantly improve the signal to background ratio. On the other hand, it will even lower the efficiency and add additional contributions to the systematic uncertainties.

7.2.3 Photon Selection Criteria

All selection criteria introduced in the previous section remove V0s with non-electronic tracks. With these methods, secondary vertices from decaying parti-
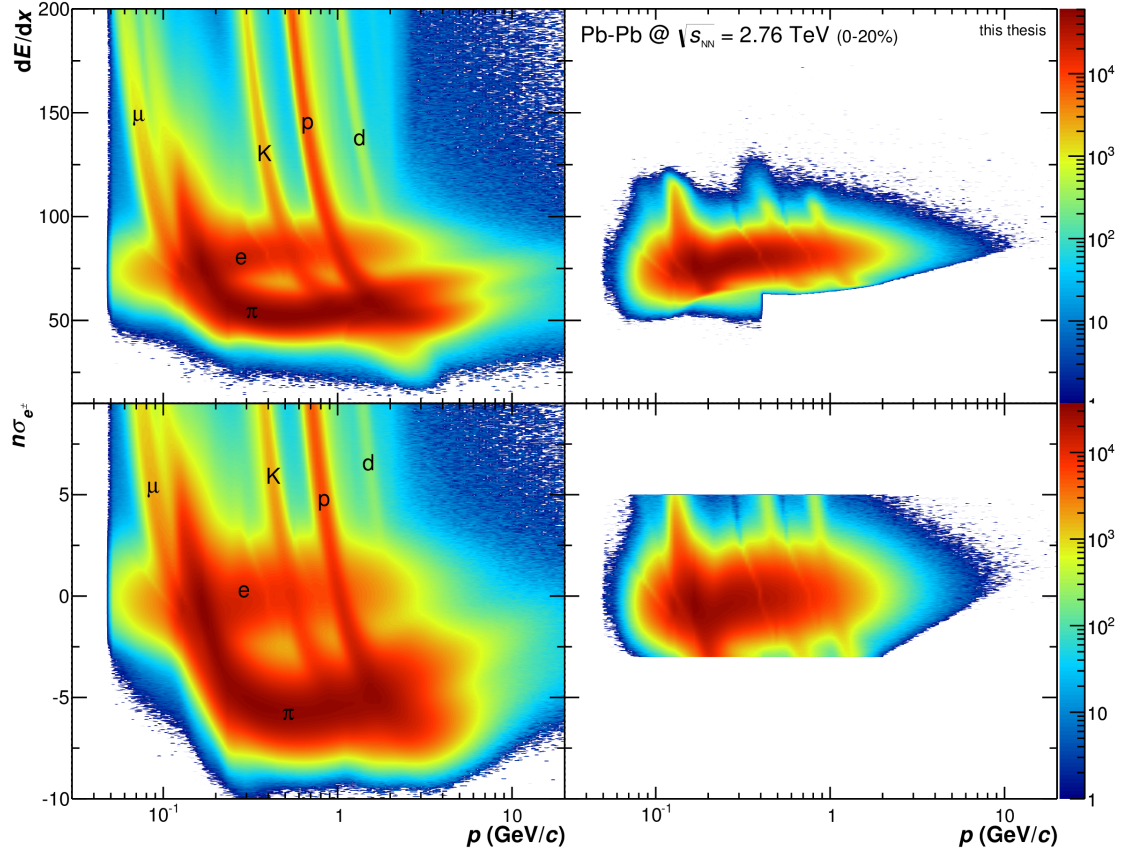
Figure 7.5: TPC dE/dx and $n\sigma_e$ before and after photon and track selection criteria for Pb–Pb at 2.76 TeV in the 0-20% centrality bin.

Selection Criterion	900 GeV (pp)	2.76 TeV (pp)	7 TeV (pp)	2.76 TeV (Pb–Pb)
accepted TPC n$\sigma_{e\pm}$		-3,5	-3,5	-3, 5
rejected TPC n$\sigma_{\pi\pm}$	-10, 1	-10, 1	-10, 1	-10, 3
min track p for n$\sigma_{\pi\pm}$	0.25 GeV/c	0.25 GeV/c	0.25 GeV/c	0.4 GeV/c
max track p for n$\sigma_{\pi\pm}$	100 GeV/c	100 GeV/c	100 GeV/c	100 GeV/c
accepted TOF n$\sigma_{e\pm}$	-	-	-	-5, 5

Figure 7.6: Values for the electron particle identification for the direct-photon analysis for all analyzed collision energies.

cles, like the K_s^0 or the Λ, can be rejected efficiently from the photon candidate sample. The contamination with such V0s is generally only a minor source of the

total background. The main impurity is related to random combinations of two tracks not originating from secondary vertices. In case of non-electronic tracks, mostly pions, they can be removed by the introduced PID cuts. If two electron tracks build such a misidentified vertex, it can only be removed by rejecting V0 candidates via photon specific properties. These are generally the pointing direction of the combined pair momentum to the primary vertex, the opening angle of the pair and the related invariant mass.

The first cut applied is based on the AliKF (AliRoot-Kalman-Filter) package included in AliRoot. It is explained in detail in [201] and is based on a Kalman filter method [202]. A brief description is given below.

During the filter process, the two tracks building the V0 are successively added to the state vector **r** given by:

$$\mathbf{r} = (x, y, z, p_x, p_y, p_z, E, s) \,, \tag{7.5}$$

It contains the spatial coordinates, the four-momentum and the decay length s of the candidate. The algorithm performs a mass constraint fit to the decay topology of the secondary vertex candidate, returns a χ^2 value and the corresponding number of degrees of freedom. For photon candidates, the mass hypothesis for the fitting process is set to zero. The four-momentum of the V0s has to point to the primary event vertex. The selection is finally based on the χ^2/ndf value providing a measure for the correct mass, pointing and photon conversion topology. The number of the degrees of freedom depends on the V0 construction and has always a value of four. The photon candidates have to have smaller values as given in Tab. 7.9.

The second cut performed during the analysis is in respect to the angle between the plane defined by the opening angle of the two V0 tracks and the plane perpendicular to the magnetic field of the ALICE experiment. In ALICE, the latter plane is identical to the x,y-plane. The angle is referred to as ψ_{Pair} angle [203]. The selection is based on the small opening angle of a conversion due to the vanishing invariant mass of a photon in the absent of a magnetic field. Thus, every non-zero opening angle is caused by the bending of the tracks in the magnetic field (z-direction) combined with measured spatial track coordinates displaced from the real conversion point. Due to the geometry of the magnetic field, it will only bend the tracks in azimuth (φ) direction. The opening angle of the pair in the plane defined by the momenta of the tracks, ξ_{Pair}, is given by:

$$\xi_{\text{Pair}} = \arccos\left(\frac{\vec{p}_{e^+} \cdot \vec{p}_{e^-}}{|\vec{p}_{e^+}| \cdot |\vec{p}_{e^-}|}\right). \tag{7.6}$$

The opening in respect to the polar angle (ϑ) is simply given by the difference of the individual polar track angles:

$$\Delta\vartheta_{e^+,e^-} = \vartheta_{e^-} - \vartheta_{e^+}. \tag{7.7}$$

The angle ψ_{pair} between the two planes can be finally defined by these two angles. It is given as:

$$\psi_{\text{Pair}} = \arcsin\left(\frac{\Delta\vartheta_{e^+,e^-}}{\xi_{\text{Pair}}}\right). \tag{7.8}$$

The orientation of the angles and planes is shown in Fig. 7.7. The ψ_{pair} angle
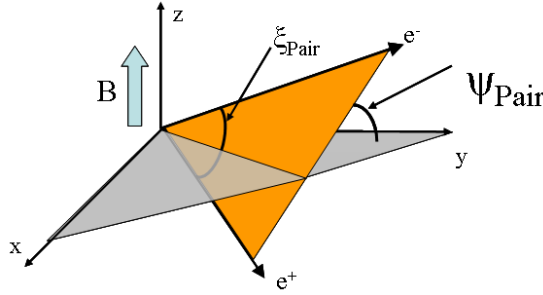
Figure 7.7: Orientation of the opening angles and the corresponding planes used for the calculation of the ψ_{Pair} angle. The ALICE magnetic field is pointing in z-direction. [203]

is a measure for the contribution of the azimuth component to the total opening angle of the pair. For photons with vanishing opening angles, ψ_{Pair} is close to and peaked at zero radiant. For heavier particles or Dalitz decays it usually has larger values. Combinatorial background has nearly random values of invariant mass and opening angles. The corresponding ψ_{Pair} distribution is flat.

The last cut is also related to the photon conversion topology. The selection is done in respect to the q_{T} variable:

$$q_{\text{T}} = \frac{|\vec{p}_{e^+} \times \vec{p}_{V0}|}{|\vec{p}_{V0}|}. \tag{7.9}$$

$\vec{p}_{V0}$ is the three-momentum of the V0 candidate and $\vec{p}_{e^+}$ is the momentum of the positive track (in case of a photon conversion, the momentum of the positron). In general, it can alternatively be defined with the momentum of the electron. The area defined by $|\vec{p}_{e^+} \times \vec{p}_{V0}|$ is related to the opening angle of the V0 pair via $q_{\text{T}} = |\vec{p}_{e^+}| \cdot \sin(\theta_{V0,e^+})$. Here, θ_{V0,e^+} is the angle between the V0 (photon) momentum and the momentum of the positive track. The motivation of cutting

in this rather complex variable is becoming clear in case of plotting q_T as a function of the asymmetry of the track pair in the longitudinal direction α:

$$\alpha = \frac{q_L^{e^+} - q_L^{e^-}}{q_L^{e^+} + q_L^{e^-}} \quad \text{with} \quad q_L^{e^\pm} = \frac{|\vec{p}_{e^\pm} \cdot \vec{p}_{V0}|}{|\vec{p}_{V0}|}. \tag{7.10}$$

The resulting two-dimensional plot is called Armenteros-Podolanski plot [204]. It is shown in Fig. 7.8 for pp collisions at $\sqrt{s} = 7$ TeV (left) and for minimum bias Pb–Pb at $\sqrt{s_{NN}} = 2.76$ TeV (right). The plot shows half-ellipses corresponding to
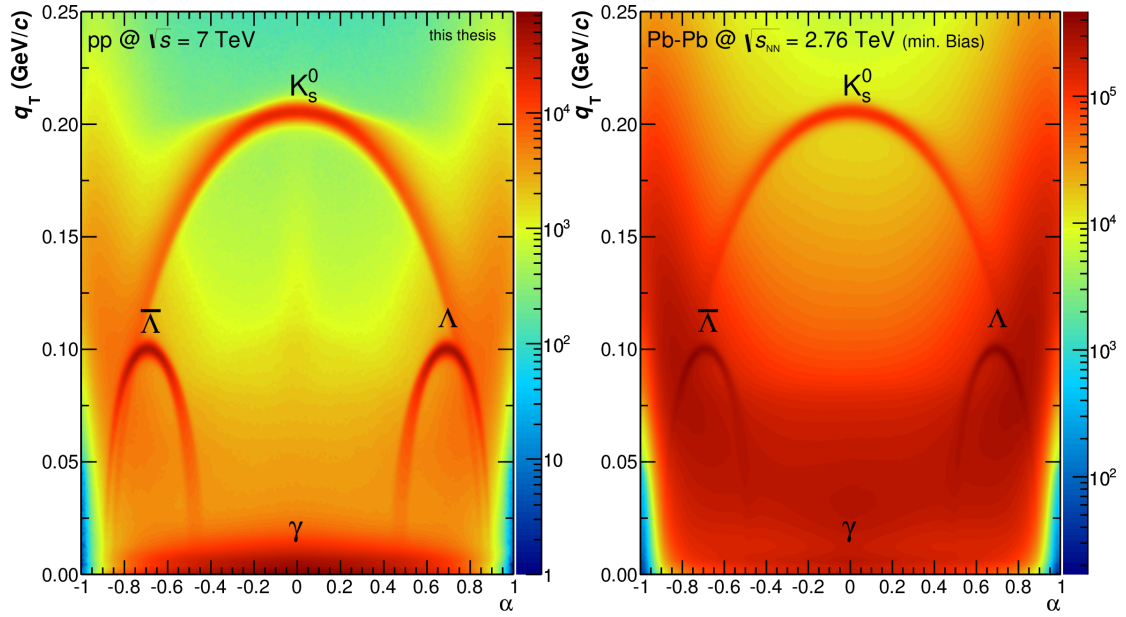
Figure 7.8: Armenteros-Podolanski plots for all tracks associated with V0s for pp collisions at 7 TeV (left) and minimum bias (0-80%) Pb–Pb collisions (right). Due to smaller combinatorial background, the particle ellipses are more pronounced for pp collisions.

the q_T and α values of the V0s from K_s^0, Λ, $\bar{\Lambda}$ decays and photon conversions. For a decay with equally heavy daughter particles like the decay of the $K_s^0 \to \pi^+\pi^-$ or $\gamma \to e^+e^-$ the ellipses are centered around $q_T = 0$ and $\alpha = 0$. In case of non-equal masses, the center is shifted away from $\alpha = 0$ due to the minimum energy required for the creation of the particle mass. The width of the bands building the ellipses originating from the momentum and spatial resolution of the tracks. Since no physical relation between the opening angle (invariant mass) and the track momentum exists for combinatorial background, such V0s are located randomly in the q_T, α-plane. The randomly distributed values are much more

pronounced for Pb–Pb, related to the larger amount of combinatorial background in this system. For pp collisions, all ellipses are clearly visible.

All photon selection values for all analyzed energies and collisions systems are summarized in Tab. 7.9. To have comparable results and systematic uncertainties

Selection Criterion	900 GeV (pp)	2.76 TeV (pp)	7 TeV (pp)	2.76 TeV (Pb–Pb)
Kalman filter (χ^2/ndf)	30	30	30	30
Armenteros q_T (GeV/c)	0.05	0.05	0.05	0.05
pair cut ψ_Pair (rad)	0.05	0.05	0.05	0.05

Figure 7.9: Values for photon selection criteria for the direct-photon analysis for all analyzed collision energies.

for all beam energies, the photon selection criteria are identical. Despite all criteria acting on similar properties of the conversion pair, their separated implementation improves the signal over background ratio significantly.

7.3 Monte Carlo Corrections of the Raw Photon-Spectrum

With the selection criteria for photons and electrons described in the previous section only a small sub-sample of the initially identified V0s is left. These candidates should be correctly selected photons or background with very similar characteristics. The invariant mass of those secondary vertices should be peaked at zero. In Fig. 7.10, the invariant mass spectrum of all V0s identified by the on-the-fly V0 finder are shown in red. To demonstrate the selection power of the applied criteria, the remaining invariant mass spectrum is plotted in black. The structures visible in the unfiltered mass spectrum originate from particle decays like $K_s^0 \to \pi^+\pi^-$. Since the electrons mass is assumed for the, calculation the resulting invariant mass of the V0s is shifted to smaller values.

The remaining V0 sample after all selections are applied is far from being the required inclusive primary-photon spectrum. Some additional steps, mainly including corrections deduced from Monte Carlo productions, are required. These corrections are explained in the following.
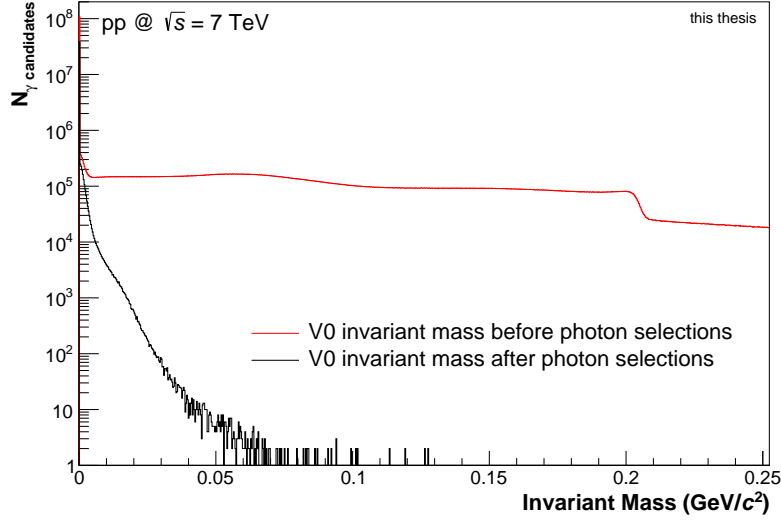
Figure 7.10: Invariant Mass of all V0s of the pp data sample at $\sqrt{s} = 7\,\text{TeV}$. Compared
are the distribution for all V0s found by the on-the-fly finder (red) and the
same distribution after all selection criteria described in Sec. 7.2.

7.3.1 Secondary-Photon Subtraction

The final photon (and π^0) p_T spectra should only contain primary particles. A
primary photon is defined as a photon produced directly during the initial collision
or as a photon produced by the decay of a primary particle. Secondary particles are
all decay products (including photons) produced by a weak or a subsequent decay.
A primary particle is a promptly produced particle and all its decay products,
except products from weak decays of strange Photons originating from weak decays
or from subsequent decays in a decay chain including weak decays, are defined as
secondary particles. The main source of secondary neutral pions and photons is
the decay of the neutral kaon via $K_s^0 \rightarrow 2\pi^0 \rightarrow 4\gamma$. Such photons and π^0 are not
produced at the primary collision vertex due to the long $(8.953 \pm 0.005 \times 10^{-11}\,\text{s})$
life time of the K_s^0. The second largest but subordinated contribution is the decay
chain of the Λ particle $(\Lambda \rightarrow n\pi^0 \rightarrow 2\gamma p e^- \bar{\nu}_e)$.

Despite the rejection of V0s with too large pointing angles during the finding pro-
cess and the selection via the χ^2/ndf of the Kalman filter, which includes a vertex
pointing, the sample contains secondary photon candidates. These secondary
photons have to be subtracted from the raw photon-spectra.

The sub-samples of validated secondary photons divided by all reconstructed pho-
ton candidates found in the Monte Carlo productions are shown in Fig. 7.11. They
are plotted against the photon transverse momentum. All three fractions are sim-
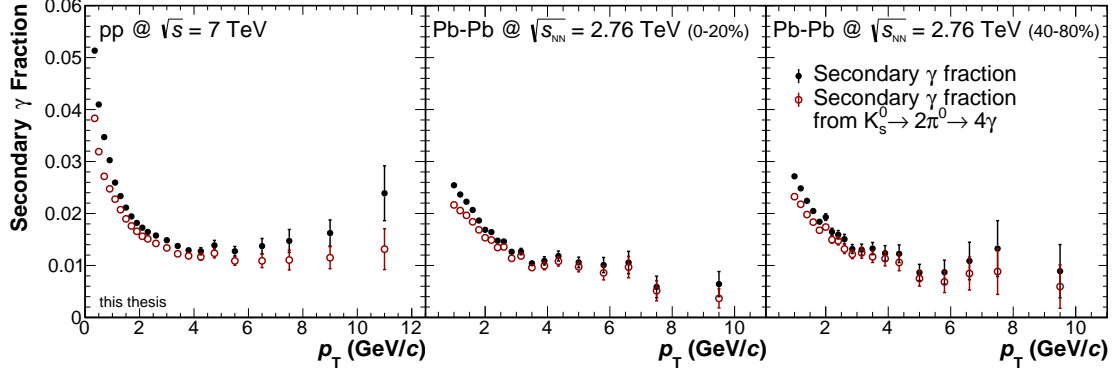
Figure 7.11: Fraction of Monte Carlo validated secondary photons over all photon candidates for pp 7 TeV and central (0-20%) and peripheral (40-80%) Pb–Pb collisions.

ilar within statistical uncertainties. They rise towards low p_T up to $\sim 5\%$ and saturate at $p_T = 4\,\mathrm{GeV}/c$ at $\sim 1.2\%$. Due to the larger minimum momentum value measured, this rise is less pronounced in Pb–Pb. A corresponding result for pp collisions at 2.76 TeV is not shown. It is nearly identical to the 7 TeV data with less statistics available.

As mentioned, the dominating contribution is added by the decay chain of the K_s^0. It was found that all MC productions for pp and Pb–Pb are not able to reproduce the measured spectra of (neutral) kaons. Thus, the estimated fraction of secondary photons extracted from the Monte Carlo is not correct. In pp collisions at 7 TeV, the K_s^0 are underestimated in the range $1.0 - 2.5\,\mathrm{GeV}/c$ by 25%. For pp collisions at 2.76 TeV, no measured K_s^0 spectrum is available. Nevertheless, the difference to the Monte Carlo has to be estimated. Therefore, the spectra at pp 900 GeV [205] and 7 TeV [206,207] are interpolated. With this ansatz, an underestimation of 31% was found. For Pb–Pb collisions, the mismatch between data and simulated K_s^0 additionally depends slightly on centrality. The missing amount of neutral kaons is on the order of 70% [207] in the p_T range used for the direct-photon analysis.

The secondary photon spectra are subtracted from the measured raw photon-spectra containing primary and secondary photons. To obtain the spectral shape of the secondary photon spectra in data, the raw spectra measured in data events are multiplied with the secondary fraction (Fig. 7.11) deduced from the Monte Carlo productions. To cure the mismatch, the fractions of secondary photons produced by neutral kaons are scaled with the differences found for the K_s^0 spectra.

The formula used for the secondary photon correction is given by:

$$\gamma_{\text{rec}}^{\text{data}}(p_{\text{T}})_{\text{sec.corr}} = \gamma_{\text{rec}}^{\text{data}}(p_{\text{T}}) - \gamma_{\text{rec}}^{\text{data}}(p_{\text{T}}) \cdot \frac{\gamma_{\text{rec}}^{\text{MC}}(p_{\text{T}})^{\text{secondary,true}}}{\gamma_{\text{rec}}^{\text{MC}}} \tag{7.11}$$
$$- \gamma_{\text{rec}}^{\text{data}}(p_{\text{T}}) \cdot \mathcal{K} \cdot \frac{\gamma_{\text{rec}}^{\text{MC}}(p_{\text{T}})^{\text{secondary from } K_s^0,\text{true}}}{\gamma_{\text{rec}}^{\text{MC}}(p_{\text{T}})}.$$

Since in the formula the secondary photons produced by neutral kaons are subtracted twice, the actual scaling factors $\mathcal{K}$ are modified accordingly to avoid double counting. These factors are consecutive calculated as $\mathcal{K} = K_s^{0\,\text{data}}/K_s^{0\,\text{MC}} - 1$.

The superpositions "data" and "MC" refer to real events and Monte Carlo generated events. The index "rec" refers to a reconstructed spectrum. The superposition "true" labels MC validated spectra - via Monte Carlo information a reconstructed V0 is identified as a photon conversion.

The values of $\mathcal{K}$ used for the correction are given in Tab. 7.12. Additionally, the

Collision System	Mismatch	Correction Factor $\mathcal{K}$
pp Collisions		
7 TeV	25.0%	0.33
2.76 TeV	31.5%	0.46
Pb–Pb Collisions at 2.76 TeV		
0-20%	69.8%	2.31
0-40%	69.8%	2.31
20-40%	69.2%	2.25
40-80%	64.0%	1.78

Figure 7.12: Mismatch of K_s^0 from data and Monte Carlo in terms of missing yield in Monte Carlo. In addition, the secondary photon correction factor $\mathcal{K}$ as used in Eq. (7.11) is given.

corresponding mismatch between data and Monte Carlo is given.

7.3.2 Purity of the Photon Sample and Background Composition

Although the selection criteria are rather strict, the remaining sample is not free of background. The main contribution to the background are random combinations

of tracks without a common secondary production vertex. Since such candidates have passed all selection criteria, their topology is very similar to a photon conversion. Different sets of selection criteria are tested to reduce the number of such wrong combinations. The set introduced in the previous section is found to result in a good signal to background ratio.

Not only combinatorial V0s contribute to the impurity of the sample. In addition, particle decays, misidentified as photon conversions, enter. The main contribution is the decay of the K_s^0 into two oppositely charged pions. The second contribution, but already highly subordinated, is the decay of the Λ and $\bar{\Lambda}$. These contributions are removed efficiently by the q_{T} (Sec.7.2.3) cut.

To obtain an inclusive primary-photon spectrum, the raw spectrum is multiplied with the purity of the photon candidate sample. This quantity is deduced from the Monte Carlo production as the ratio of all validated true primary photons over all photon candidates found in the simulated events. Here, identical selection criteria as used for the data events are applied. The resulting purity is considered to reproduce, within systematic uncertainties, the contamination inherent in the data events.

As discussed in the previous section, secondary photons are removed from the raw photon-spectra. Thus, a downstream correction that includes the raw spectra must use the secondary subtracted spectra. Otherwise, the corresponding correction would be based on a deviating main unit. The purity is calculated via:

$$\mathcal{P}_\gamma\left(p_{\mathrm{T}}\right) = \frac{\gamma_{\mathrm{rec}}^{\mathrm{MC}}\left(p_{\mathrm{T}}\right)^{\mathrm{primary,true}}}{\gamma_{\mathrm{rec}}^{\mathrm{MC}}\left(p_{\mathrm{T}}\right)^{\mathrm{all}} - \gamma_{\mathrm{rec}}^{\mathrm{MC}}\left(p_{\mathrm{T}}\right)^{\mathrm{secondary,true}}} \qquad (7.12)$$

For the indices and superpositions, the same nomenclature as for Eq. (7.11) is used. The only new label is "all". This refers to all reconstructed photons containing background as well as primary and secondary photons.

The purities for pp collisions at $7\,\mathrm{TeV}$ and $2.76\,\mathrm{TeV}$ and for central and peripheral Pb–Pb collisions are shown in Fig. 7.13.

In general, the purity is larger in the low multiplicity pp environment. Here the number of possible track pairs is much smaller compared to Pb–Pb just by combinatorial arguments. The resulting purity is above 99% at low p_{T}. As a general trend, the purity decreases towards larger transverse momenta. This is mainly caused by the poor discrimination power between the electron and pion band of the TPC $\mathrm{d}E/\mathrm{d}x$ at larger momenta.

For $7\,\mathrm{TeV}$, the purity starts to drop above $p_{\mathrm{T}} = 4\,\mathrm{GeV}/c$ with a final value of $\sim 94\%$ at $p_{\mathrm{T}} = 11\,\mathrm{GeV}/c$. In contrast, for $2.76\,\mathrm{GeV}$, the purity is nearly constant
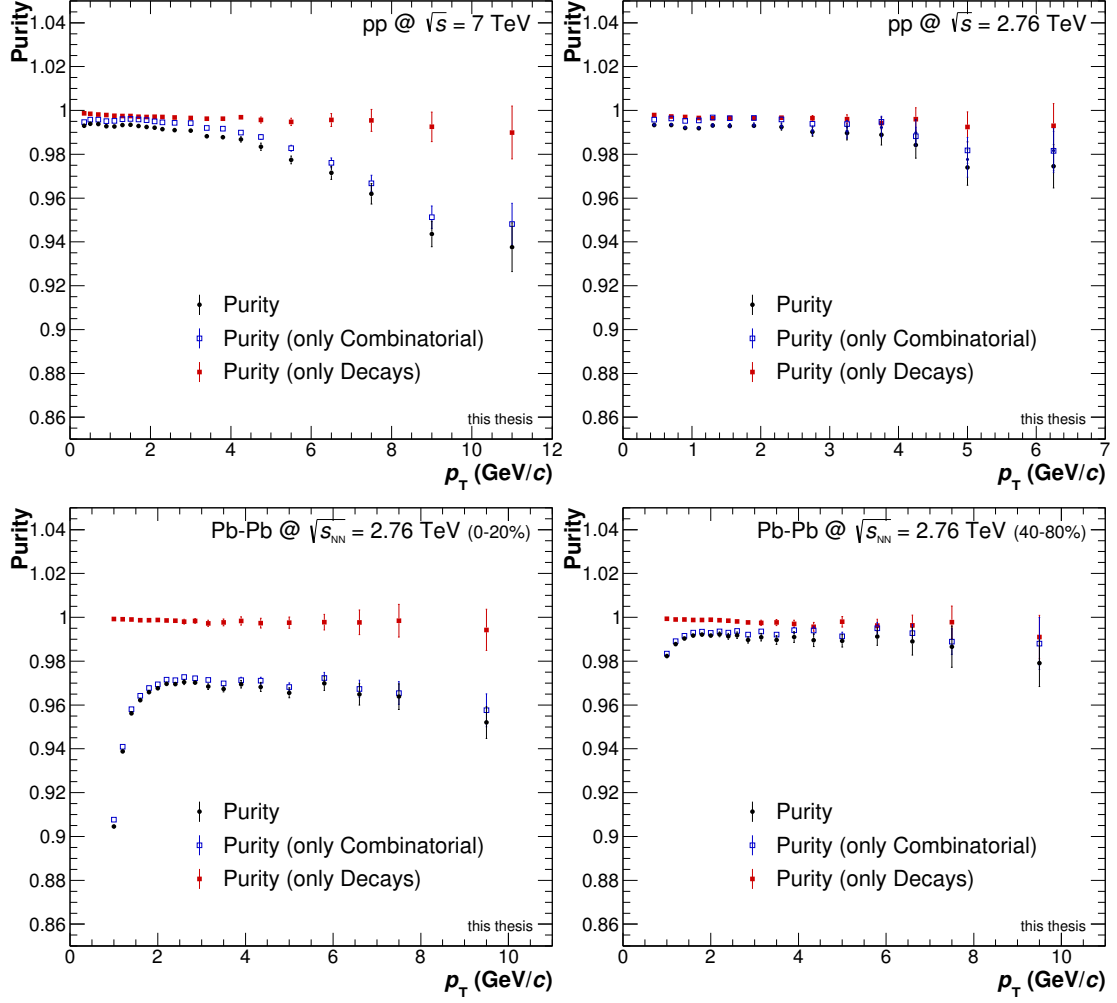
Figure 7.13: Purities of the reconstructed photons from the Monte Carlo simulations generated for the ALICE detector for pp and Pb–Pb collisions. The black points correspond to the purity of the photon sample. The blue points represent the purity with a subtracted contributions from particle decays. The red data points correspond to the contamination of the sample with particle decay.

within the statistical uncertainties. The measured p_T range is not wide enough to show a significant decreasing behavior.

In Pb–Pb collisions, the situation is different. The contamination from combinatorial background is substantially larger. In contrast to pp collisions, the purity rises strongly with p_T until it saturates at $p_T \sim 2\,\mathrm{GeV}/c$. This is clearly an effect of the much larger track multiplicities found in heavy-ion collisions. Consequently,

the rise is much less pronounced for peripheral events. In general, the estimated purity for all centralities is well above 90%.

In addition, the contamination of the photon sample with particle decays is shown. This component has a similar size in all systems and is highly subordinated. Therefore, the possibility of having a misidentified particle decay in the sample do neither depends on the multiplicity nor on the center-of-mass energy of the collision. It is important to mention that the purities extracted for pp and Pb–Pb collisions are not directly comparable. As discussed in Sec. 7.2.2, a slightly different electron PID is applied for both cases.

The composition of the combinatorial background in Pb–Pb collisions is shown in Fig. 7.14 as a signal over background ratio. The dominating source of background for both centrality bins are combinations of electrons with positrons. This source cannot be removed by PID cuts. It can only be eliminated by geometrical cuts like the q_{T}, ψ_{pair} or χ^2 (see 7.2.3). To reject it further, a substantial part of the signal would be removed, too. The second largest contribution with nearly the same size is combinations of charged pion with electrons/positrons. It rises slightly towards higher transverse momenta where the energy loss curves of electrons and pions become similar. The contribution from all other combinations are not relevant. Even $\pi^{\pm} + \pi^{\mp}$ combinations are subordinated by more than a factor 10 compared to combinations of electrons with pions.
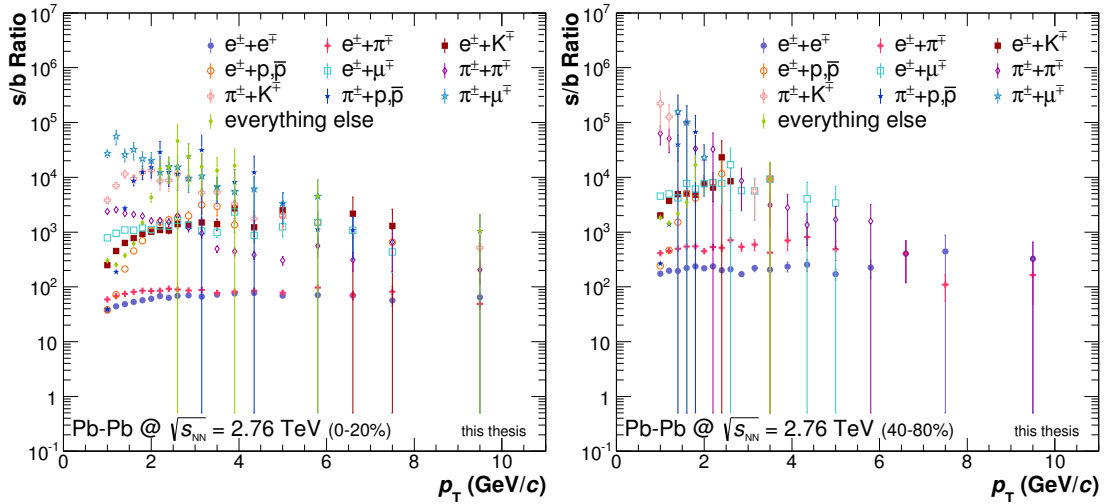
Figure 7.14: Composition of the remaining combinatorial background for central (0-20%) and peripheral (40-80%) Pb–Pb collisions at $\sqrt{s_{\mathrm{NN}}} = 2.76\,\mathrm{TeV}$.

Corresponding figures for pp collisions are not shown. The background is much too small to be split into components with reasonable statistical uncertainties.

7.3.3 Efficiency of the Conversion Method - Unfolding

The calculation of the efficiency of the V0 method has been restricted to re-constructable photon conversions. The corresponding tracks require a minimum length of the TPC track of $50\,\mathrm{cm}$ and a maximum value of $200\,\mathrm{cm}$. Only converted photons and tracks in the fiducial spatial region defined by the (pseudo-)rapidity and R are considered for the estimation. The converted photon finding efficiency is defined as the ratio of all Monte Carlo validated primary-photon candidates over all Monte Carlo converted photons in the fiducial region. Additionally, the photons have to pass the minimum p_T criterion given in Sec. 7.2.1. The efficiency is defined as:

$$\mathcal{E}_\gamma\left(p_\mathrm{T}\right) = \frac{\gamma_\mathrm{rec}^\mathrm{MC}\left(p_\mathrm{T}\right)^\mathrm{primary,true}}{\gamma_\mathrm{MC}\left(p_\mathrm{T}\right)^\mathrm{primary,converted}}. \tag{7.13}$$

The notation is similar to the one introduced for Eq. (7.12). The additional superscript "converted" refers to all converted Monte Carlo generated photons that fulfill the mentioned criteria.

In contrast to the purity estimation, an efficiency as given above is a ratio of two spectra with two different ways to determine the transverse momentum. While the photon candidates are reconstructed at a given p_T value, the Monte Carlo reference photons are only available at their generated p_T values. The measured value of p_T is different due to a non-perfect reconstruction and biased by resolution effects and energy loss via Bremsstrahlung. In principle, such an efficiency will partially cure those smearing effects automatically since the same difference between generated (by nature) and measured p_T is inherent in the data. This correction is called bin-to-bin unfolding. Nevertheless, the size of the smearing effects of the measured spectrum depends on the shape of the input spectra. As discussed in Sec. 6.2, the spectra differ up to 20% in magnitude and more important they differ in shape. Thus the bin-to-bin unfolding will only partially remove smearing effects from the final results.

For a more correct treatment of the smearing effects, Bayesian unfolding is applied. The unfolding routines used for this purpose are not part of the AliRoot framework. Instead, the package RooUnfold [208] is used. It is an extension of ROOT and can be easily included in the framework.

The general idea of unfolding (here: removing Bremsstrahlung and the detector effects from the p_T spectrum) is given by the solution of the following equation:

$$p_\mathrm{T}^\mathrm{rec} = \mathbf{A} \cdot p_\mathrm{T}^\mathrm{true}. \tag{7.14}$$

In this equation, $p_\mathrm{T}^\mathrm{rec}$ refers to the measured and thus smeared p_T distribution.

$p_{\mathrm{T}}^{\mathrm{true}}$ is the true distribution with generated transverse momentum values. The mapping between those two spectra is given by the detector response matrix **A**. The response matrices for pp at 7 TeV and 0-20% central Pb–Pb are shown in Fig. 7.15.
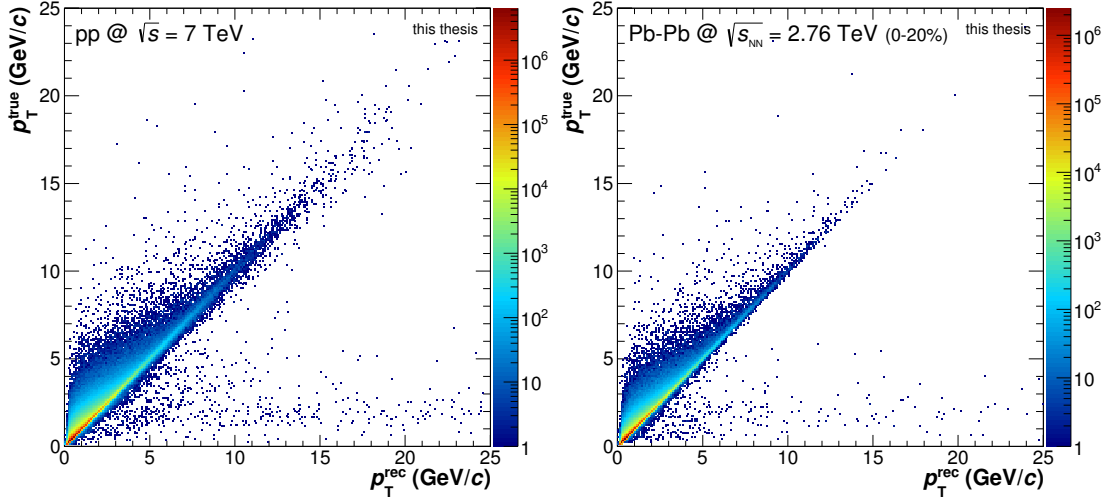
Figure 7.15: Unnormalized response matrices for pp collisions at $\sqrt{s} = 7$ TeV (left) and central (0-20%) Pb–Pb collisions at $\sqrt{s_{\mathrm{NN}}} = 2.76$ TeV (right) as used by RooUnfold.

In Fig. 7.16, two slices of the response matrices for two different generated photon momentum values are shown. Via these slices, the resolution of the two different collision systems can be compared. Therefore, a Gaussian shape is assumed and the peaks are fitted. On the left side of the peaks, an exponential tail is visible. This tail is caused by electron and positron Bremsstrahlung. While for small momenta the momentum resolution is very similar for pp and Pb–Pb, it starts to divert at larger p_{T} values. The main reason for the better momentum resolution is the better spatial resolution of the primary vertex in the high multiplicity Pb–Pb events. While the difference between pp and Pb–Pb is sizable, the difference between the centrality bins used for this thesis is small. It can be inferred that the number of tracks in peripheral events is already large enough for a precise primary vertex measurement.

If the response matrix is known, the $p_{\mathrm{T}}^{\mathrm{true}}$ spectrum can be estimated. For that purpose, different methods exist. The most straight forward way of solving Eq. (7.14) is given by the inversion of the matrix **A**. However, an inversion may be largely biased by statistical fluctuation or even impossible.

In the Bayesian theorem [209, 210], the conditional probability distribution of a
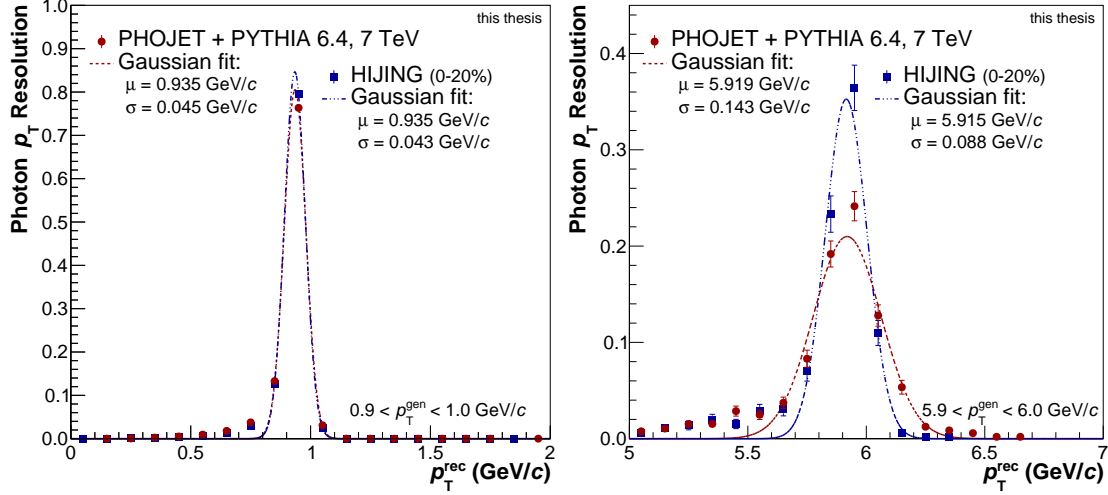
Figure 7.16: Slices of the pp and Pb–Pb response matrices (Fig. 7.15) for the transverse momentum bins $0.9\,\mathrm{GeV}/c < p_\mathrm{T}^\mathrm{true} < 1.0\,\mathrm{GeV}/c$ (left) and $5.9\,\mathrm{GeV}/c < p_\mathrm{T}^\mathrm{true} < 6.0\,\mathrm{GeV}/c$ (right), respectively. The slices are normalized to its integral. In addition, Gaussian fits are shown. From these fits, the mean μ and the σ parameter is given.

cause (here: generated $p_\mathrm{T}^\mathrm{true}$ value) in case of measuring an effect (here: measured $p_\mathrm{T}^\mathrm{rec}$ value) is given by:

$$P\left(p_\mathrm{T}^\mathrm{true}|p_\mathrm{T}^\mathrm{rec},\mathbf{A},I\right) \propto P\left(p_\mathrm{T}^\mathrm{rec}|p_\mathrm{T}^\mathrm{true},\mathbf{A},I\right) P\left(p_\mathrm{T}^\mathrm{true}|I\right). \qquad (7.15)$$

In this formula, the conditional probability is proportional to the likelihood of the observed data for a given response matrix and true distribution times a prior. The prior represents the knowledge of the true distribution. The variable I summarizes the underlying assumptions of the analysis used for the prior.

An unfolded result will depend on the choice of the prior. To avoid this, an iterative approach is used by RooUnfold. In a first step, the Monte Carlo true distribution is used as the prior. In the following iterations, the unfolded result of the previous iteration is taken as an updated prior. If the number of iterations is too large, the result will start to follow the statistical fluctuations of the measured data. Since the Monte Carlo spectra are similar to the data spectra, the number of iteration is small and found to be optimal with a number of 4 iterations. During the process, the covariance matrix is derived from the error propagation matrix. The uncertainties are calculated from the square root of this matrix. To quantify and control the effect of statistical uncertainties in the unfolding error propagation, the used response matrix is smeared with a Gaussian in a toy Monte Carlo.

The results are cross checked with the Singular Value Decomposition (SVD) unfolding method [211]. This algorithm is also available within the RooUnfold framework. The differences between the SVD and the Bayesian unfolding method were found to be on the order of 0.2%. Thus, the unfolding process is considered to be stable and well controlled. No additional systematic uncertainty is added beside the uncertainties originating from the RooUnfold error calculation including the toy Monte Carlo.

As a further check, the unfolding process was tested with the two different Monte Carlo generators (PHOJET, PYTHIA) available for pp. For this purpose, the reconstructed photon candidate spectrum of the first generator was taken as the measured distribution. With the response matrix extracted from the second generator, the unfolding was applied. Since the truth is known in both cases, the unfolded distribution can be compared to the corresponding true distribution. After unfolding, the measured distribution is clearly more similar to the generated distribution. Nevertheless, the difference to the efficiency corrected (bin-to-bin unfolding) spectrum is only small ($\lesssim 3\%$). It has to be mentioned that the difference of the data spectrum to both generators is even smaller compared to the difference between the two generators.

With unfolding applied, the spectrum $\gamma_{\mathrm{rec}}^{\mathrm{MC}}(p_{\mathrm{T}})^{\mathrm{primary,true}}$ has to be substituted by a similar spectrum with generated transverse momentum values. In addition, the raw photon-spectrum measured in data is replaced by the spectrum obtained as the result for $p_{\mathrm{T}}^{\mathrm{true}}$ of Eq. (7.14), solved with Bayesian unfolding.

In Fig. 7.17, the efficiencies estimated for the inclusive-photon analysis are shown. Efficiencies following Eq. (7.13) are plotted in red. In this case, the two different p_{T} scales are used, where the numerator spectrum has reconstructed values. In contrast, the efficiencies obtained with a reconstructed photon spectrum with generated momentum values are shown in black. As a general trend, the latter efficiencies are larger by a factor of ~ 1.2 for higher transverse momenta. This trend is reversed for lower p_{T} ($< 0.7\,\mathrm{GeV}/c$). The effect is clearly caused by the shifting of the momenta towards lower values by radiative energy loss. This feature is also visible on the level of the response matrices in Fig. 7.15.

The steeply falling shape of the efficiency towards zero p_{T} is caused by very low p_{T} electrons not reconstructable by ALICE. This effect is enhanced due to the low momentum cut-off for electrons introduced in Sec. 7.2.1.
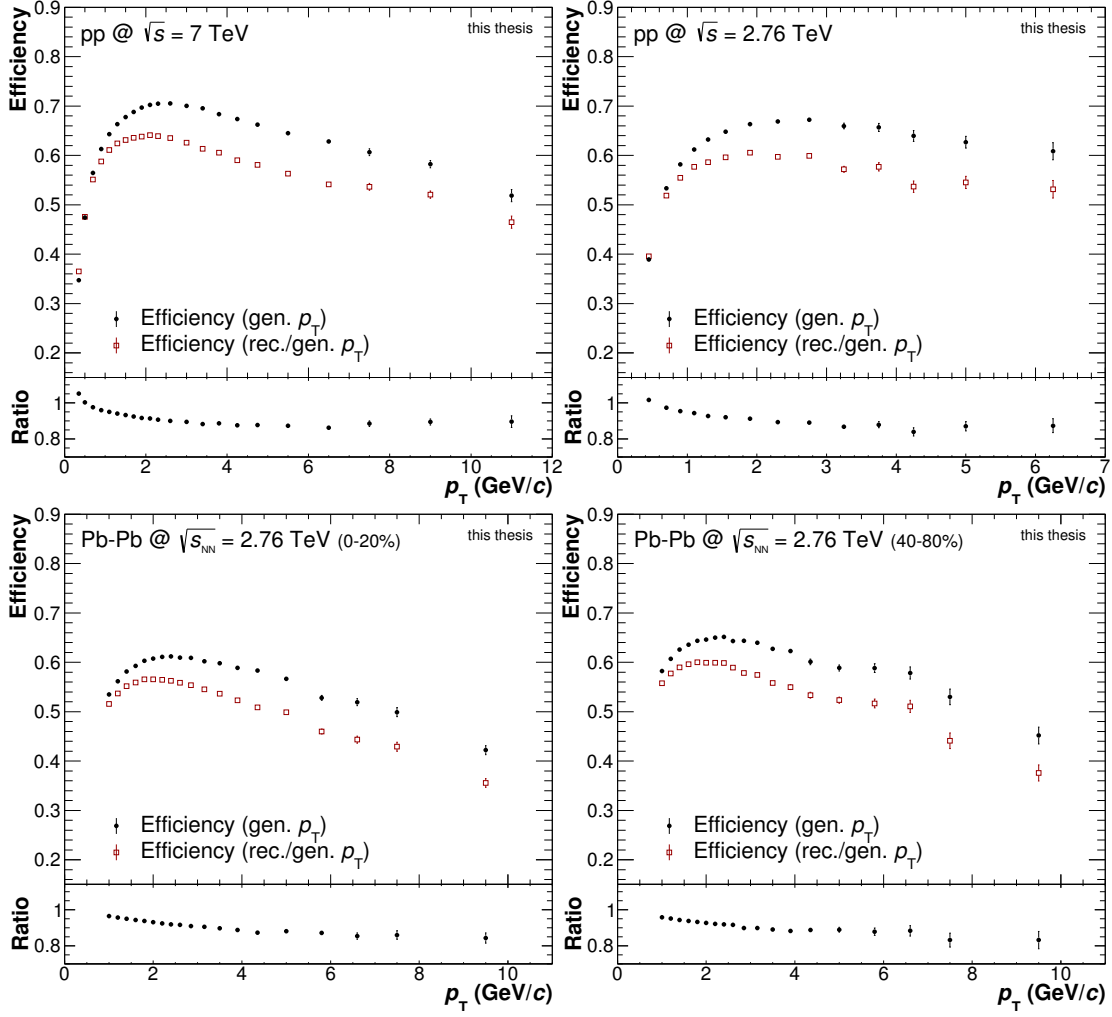
Figure 7.17: Efficiencies of the reconstructed photons from the Monte Carlo simulations generated for the ALICE detector for pp and Pb–Pb collisions. The red points correspond to an efficiency obtained from two different p_T scales, generated and reconstructed p_T. The black points correspond to a similar efficiency obtained from two spectra with generated p_T values.

7.3.4 Conversion Probability of Photons – ALICE Material Budget

A photon conversion is the transformation of a photon into a pair of leptons, normally into an electron-positron pair. Only a small fraction of all photons produced in collisions converts inside the inner part of the ALICE detector. By means of an iterative comparison of photon conversions in ALICE measurements

and simulations, the determination of the material budget of the ALICE detector is feasible [212]. Vice versa, when the material budget is understood with high precision, the conversion probability within the detector material is known. The radiation length x/X_0 is related to the conversion probability $\mathcal{C}$ via the expression:

$$\mathcal{C} = 1 - \exp\left(-\frac{7}{9}\frac{x}{X_0}\right). \tag{7.16}$$

Since the matching between data and Monte Carlo is never perfect, a systematic uncertainty of the material budget d_{Material} is calculated in [212]. It is deduced by comparing the number of reconstructed photon candidates integrated in $0\,\text{cm} < R < 180\,\text{cm}$ from data and Monte Carlo via the formula:

$$d_{\text{Material}} = \left(\frac{\gamma_{\text{rec}}}{N_{\text{event}}N_{\text{ch}}}\right)_{\text{data}} - \left(\frac{\gamma_{\text{rec}}}{N_{\text{event}}N_{\text{ch}}}\right)_{\text{MC}}. \tag{7.17}$$

In principle, such a quantity has to be normalized to the number of photons. This number is not accessible since it depends on the conversion probability itself. Instead, the number of charged particles is used. To have a precise uncertainty estimation the V0 finder (on-the-fly, offline), the Monte Carlo Generator (PYTHIA, PHOJET) and the p_{T} range of photons used for the analysis are varied. In Fig. 7.18, the conversion point distribution inside the ALICE central barrel is shown.
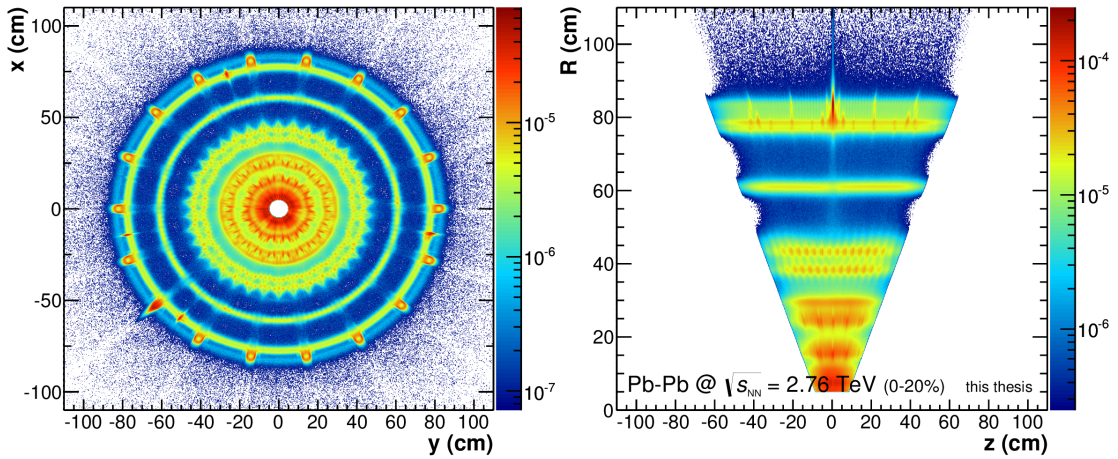
Figure 7.18: Reconstructed photon conversion points in the x,y-plane (left) and z,R-plane (right) for 0-20% Pb–Pb collisions inside the ALICE detector.

In Fig. 7.19, the conversion probability for the three analyzed collision types is

presented. It is calculated via:

$$\mathcal{C}_\gamma \left(p_{\mathrm{T}} \right) = \frac{\gamma_{\mathrm{MC}} \left(p_{\mathrm{T}} \right)^{\mathrm{primary,converted}}}{\gamma_{\mathrm{MC}} \left(p_{\mathrm{T}} \right)^{\mathrm{primary,all}}}. \tag{7.18}$$

The conversion probability is only obtained from generated Monte Carlo particles. It does not depend on any kind of detector response. It only depends on the fiducial spatial region chosen for the analysis, defining the amount of material which is traversed. For the spectrum given by $\gamma_{\mathrm{MC}} \left(p_{\mathrm{T}} \right)^{\mathrm{primary,all}}$, all photons in the fiducial η region are taken. In the spectrum of converted photons ($\gamma_{\mathrm{MC}} \left(p_{\mathrm{T}} \right)^{\mathrm{primary,converted}}$) only converted photons are accepted if their conversion products have larger transverse momenta as $p_{\mathrm{T}}^{e^{\pm}} = 50 \, \mathrm{MeV}/c$. Furthermore, the conversion points have to have a conversion radius $R_\gamma < 180 \, \mathrm{cm}$ and a conversion $Z_\gamma < 240 \, \mathrm{cm}$. The difference of the conversion probability between pp and Pb–Pb can be understood by the different η reconstruction ranges and material composition used for the analysis.
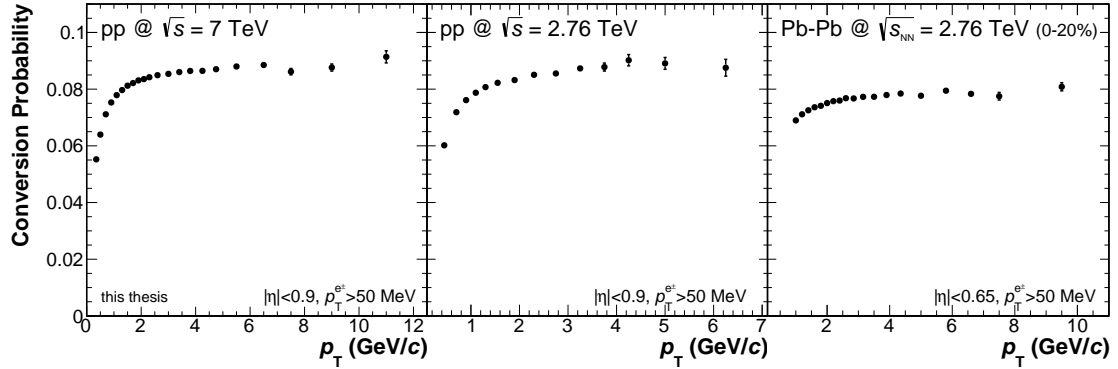
Figure 7.19: Conversion probability of photons inside the ALICE detector for the different collision systems and energies. The different min $p_{\mathrm{T}}^{e^{\pm}}$ and η ranges are specified in the plots.

7.4 Correction for Photons from Different-Bunch Pileup Events

ALICE is not suited to handle events with multiple primary vertices. As discussed in Sec. 5.5 and 6.1.1, the SPD is able to selected events with multiple vertices referred to as same-bunch pileup. These vertices and the corresponding tracks can be removed from the event sample. For Pb–Pb collisions, this source of pileup

is not removed. The particle density of the bunches and the interaction probability μ (Sec. 6.1.1) is much smaller and pileup very unlikely.

The TPC has a drift velocity of $2.7 \, \mathrm{cm}/\mu \mathrm{s}$ [145, 146]. The read-out time ($92 \, \mu \mathrm{s}$) is large compared to the read-out time of the SPD ($< 200 \, \mathrm{ns}$ [143]). The TPC time corresponds to approximately one full turn of the bunches in the LHC ($90 \, \mu \mathrm{s}$). The TPC might therefore contain the drifting electrons and ions of all tracks of all bunch crossings happened during this full turn. This sort of pileup is called different-bunch pileup. If the analysis is restricted to primary particles, pointing to the primary vertex, the pre- and post-event tracks can be efficiently removed by TPC-ITS matching.

The situation becomes more complicated if the analysis requires secondary tracks like electrons and positrons from conversions. In general, V0 tracks with an origin of $R_\gamma > 50 \, \mathrm{cm}$ cannot have ITS tracklets since at least two consecutively ITS clusters are required. This pertains for approximately 35% of all photon conversions in the selected sample. The number does not depend on the collision energy, it is only related to the transversed material.

The filling scheme of the LHC was successively changed from 2010 ($7 \, \mathrm{TeV}$ data) to 2011 ($2.76 \, \mathrm{TeV}$ data). The filling scheme used predominantly for the $2.76 \, \mathrm{TeV}$ data is shown in Fig. 7.20. While single bunches where used in the beginning of 2010, in 2011 trains, containing multiple bunches, where filled in the LHC. Thus pileup should be enhanced in the $2.76 \, \mathrm{TeV}$ data. The pileup tracks will manifest as TPC tracks without a matching to the ITS. Because of the wrong timing information of the production event, their z-coordinate will be shifted while the x,y-coordinate should remain undistorted.

In case of photon conversion, the pileup conversion point is shifted in z-direction. These photons will also have shifted momentum vectors no longer pointing to the primary vertex. Consequently, the distance of closest approach of the vectors to the primary vertex in z-direction (DCA_z) will be larger for pileup photons. Since the Monte Carlo production does not include pileup, the corresponding DCA_z distribution should be narrower in the simulation. If a pileup track crosses the central membrane of the TPC, its reconstruction will be unlikely. Due to the opposite drift directions, the track will be cut in two unconnected parts, drifting to $+z$ and $-z$, respectively.

In Fig. 7.21, the p_T integrated DCA_z distribution for the $7 \, \mathrm{TeV}$ data and for the corresponding Monte Carlo simulations are shown. For the data (left) a clearly larger DCA_z background not visible in the simulation (right) is found. The Monte Carlo distribution is separated into primary and secondary photons, as well as into the remaining non-photonic background. The width of all distributions are

LHC circumference: 26.659 km
LHC circumference: 88.92485 µs
35570 RF buckets

Δbucket: 2.5 ns ~ 75 cm
Δbunch: 525 ns ~ 1580 cm

8-wagon train: 3.675 µs
1-wagon train gap: 925 ns

8-wagon train bunch: 100B protons
1-wagon train bunch: 10B protons
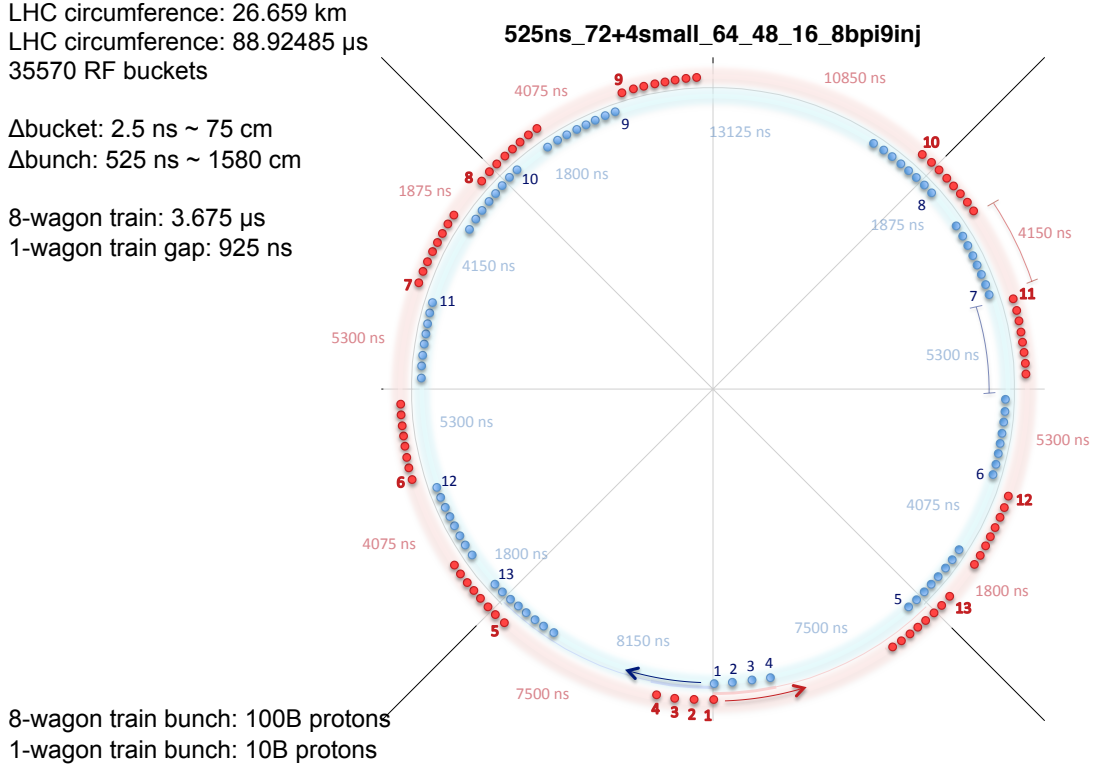
Figure 7.20: LHC filling scheme $525ns\_72 + 4small\_64\_48\_16\_8bpi9inj$ used for nearly all runs of the pp at 2.76 TeV data. [213]

comparable with a slightly narrower distribution for primary photons. The pileup background is removed from the reconstructed photon candidate sample. For that purpose, the reconstructed DCA_z distribution (black, left) it is fitted with the ROOT function ShowBackground (blue line, left). The function calculates the background and returns it as an additional histogram. This histogram is then subtracted from the distribution. The remaining sample is shown additionally (red, left). For the correction of the p_T spectrum, this procedure is performed in the transverse momentum bins used for the spectrum.

The corresponding p_T integrated DCA_z distributions for pp at 2.76 TeV and for Pb–Pb collisions are shown in Fig. 7.22. The background is largest for the 2.76 TeV pp data. This is expected from the large interaction probability due to the large number of protons per bunch and the used LHC filling scheme. The Pb–Pb data is not strongly influenced by pileup, despite the similar filling scheme. This can be understood by the much smaller interaction probability due to less ions per
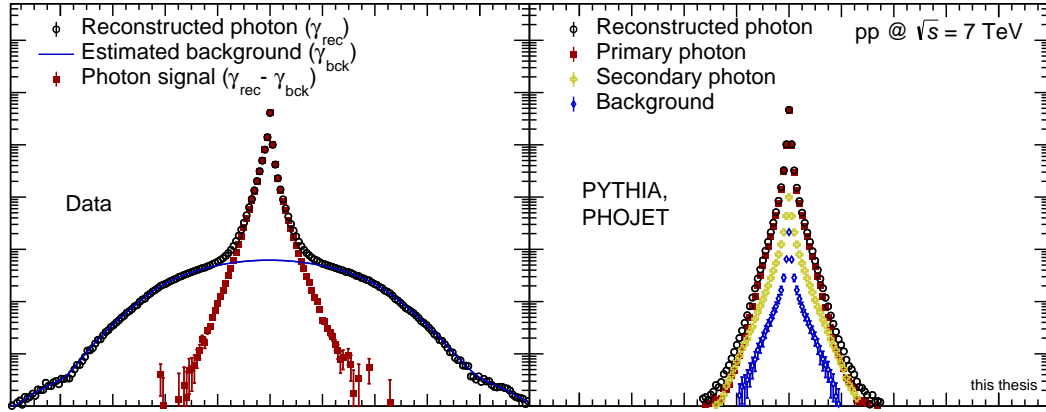
Figure 7.21: left: DCA_z distribution for all photon candidates reconstructed in the 7 TeV data normalized to the number of events. In addition, the estimated background from pileup events and the background subtracted distribution are shown. right: DCA_z distribution for all photon candidates reconstructed in the Monte Carlo simulations tuned to the 7 TeV data. In addition, Monte Carlo validated primary and secondary photons as well as background are plotted.
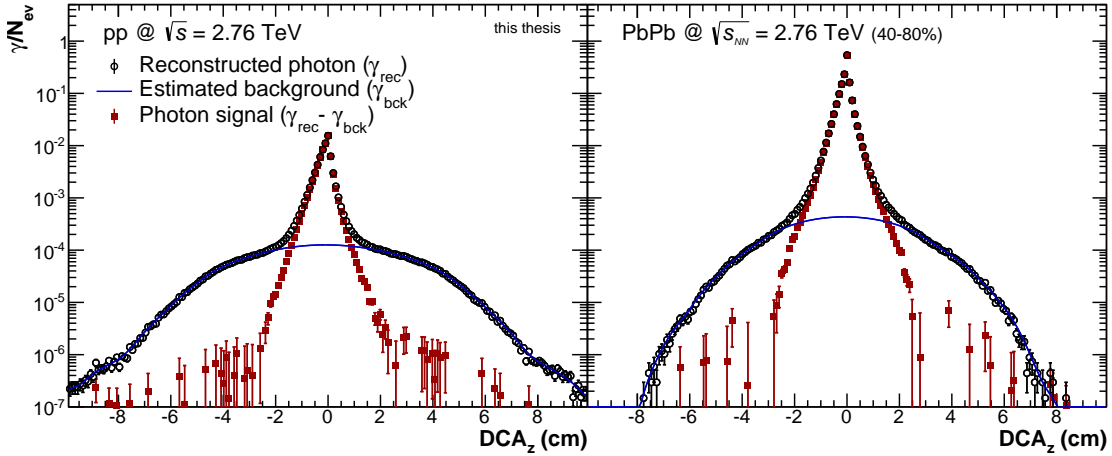
Figure 7.22: p_T integrated DCA_z distribution for pp at 2.76 TeV (left) and for peripheral (40-80%) Pb–Pb collisions (right). The distribution for pp is broader and has a worse signal to background ratio, caused by a larger amount of pileup.

bunch. Moreover, only peripheral events should be significantly influenced by pileup. Central events would only be affected if the number of tracks from the additional events is sufficiently large.

In Fig. 7.23, the ratio between the p_T differential pileup subtracted and the ini-

tially found spectra are shown. As seen from the integrated DCA_z distributions
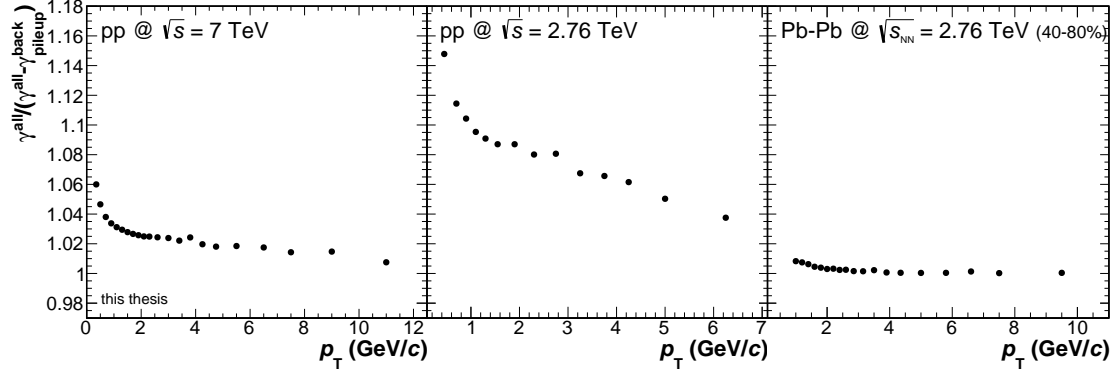
Figure 7.23: Ratio of the raw photon candidate p_T spectra with pileup contribution divided by the pileup subtracted spectra. The ratio is shown for pp at 7 TeV and 2.76 TeV as well as for peripheral (40-80%) Pb–Pb collisions.

(Fig. 7.22), the pileup contribution for pp at 2.76 TeV is largest. In general, the contribution of pileup photons decreases towards high p_T. At low p_T, the multiplicity of pileup and the curvature of tracks are larger. This will result in more pileup V0s. In peripheral Pb–Pb events, different-bunch pileup is not a large effect. Due to the higher minimum transverse momentum value of the spectrum, the rise towards low p_T is cut. As discussed, no pileup correction is applied for more central events. The contribution was found to be well below 1%.

7.4.1 Inclusive-Photon Spectra for pp and Pb–Pb

All the corrections discussed above are applied to the raw spectrum of the selected V0 candidates. The correction formula reads:

$$
\gamma_\mathrm{rec}^\mathrm{data}\left(p_\mathrm{T}\right)_\mathrm{full\ corr}^\mathrm{primary} = \gamma_\mathrm{rec}^\mathrm{data}(p_\mathrm{T})_\mathrm{sec.corr}^\mathrm{pileup\ corr} \times \mathcal{P}_\gamma\left(p_\mathrm{T}\right) \times \frac{1}{\mathcal{E}_\gamma\left(p_\mathrm{T}\right)} \times \frac{1}{\mathcal{C}_\gamma\left(p_\mathrm{T}\right)}. \qquad (7.19)
$$

The spectrum $\gamma_\mathrm{rec}^\mathrm{data}(p_\mathrm{T})_\mathrm{sec.corr}^\mathrm{pileup\ corr}$ includes the secondary photon correction applied via Eq. (7.11) and the pileup subtraction, discussed in Sec. 7.4 (if applied). The spectrum $\gamma_\mathrm{rec}^\mathrm{data}\left(p_\mathrm{T}\right)_\mathrm{full\ corr}^\mathrm{primary}$ consists of all primary photons produced in the fiducial η region given in Tab. 7.3.

The invariant primary inclusive-photon yield is obtained by the formula:

$$
E\frac{\mathrm{d}^3N^\gamma}{\mathrm{d}^3p} = \frac{\mathrm{d}^3N^\gamma}{p_\mathrm{T}\mathrm{d}p_\mathrm{T}\mathrm{d}y\mathrm{d}\varphi} = \frac{1}{2\pi N_\mathrm{event}p_\mathrm{T}}\frac{\gamma_\mathrm{rec}^\mathrm{data}\left(p_\mathrm{T}\right)_\mathrm{full\ corr}^\mathrm{primary}}{\Delta y\Delta p_\mathrm{T}}. \qquad (7.20)
$$

For the massless photon, pseudo-rapidity and rapidity are identical ($\eta_\gamma = y_\gamma$). The yield is normalized to the number of events N_{event}. It is obtained with the event selections described in Sec. 6.1.1 and 6.1.2, respectively. In the latter case, the number of selected events in a given centrality range is used.

In pp collisions, the invariant yields can be rescaled to invariant cross sections. The invariant differential cross section for pp at $\sqrt{s} = 7\,\text{TeV}$ and $2.76\,\text{TeV}$ of the inclusive-photon spectra is calculated from the invariant yields via:

$$E\frac{\mathrm{d}^3\sigma^\gamma}{\mathrm{d}p^3} = \frac{1}{2\pi}\frac{\sigma_{\text{MB}_{\text{OR}}}}{N_{\text{event}}}\frac{1}{p_{\text{T}}}\frac{\gamma_{\text{rec}}^{\text{data}}\,(p_{\text{T}})_{\text{full corr}}^{\text{primary}}}{\Delta y \Delta p_{\text{T}}}. \tag{7.21}$$

$\sigma_{\text{MB}_{\text{OR}}}$ is the interaction cross section for the MB_{OR} trigger which is used as the minimum bias trigger in pp collisions.

The determination of the cross sections in ALICE is explained in [214]. They are listed in Tab. 7.24.

$\sqrt{s}$ (TeV)	$\sigma_{\text{MB}_{\text{OR}}}$	$\sigma_{\text{MB}_{\text{INEL}}}$
2.76	55.42	$62.8^{+2.4}_{-4.0}$(model)±1.2(lumi)
7	62.37	$73.2^{+2.0}_{-4.6}$(model)±2.6(lumi)

Figure 7.24: Invariant cross sections for the trigger condition MB_{OR} and the total inelastic cross section for pp collisions at $7\,\text{TeV}$ and $2.76\,\text{TeV}$. [215, 216]

Finite Bin-Width Correction

Particle spectra decrease steeply with increasing p_{T}. The measured photon spectra are given in finite p_{T} bins with increasing width towards larger momenta. Due to the shape of the spectra, the value of the underlying distributions at the center of a bin is not identical to the bin value – the measured number of particles summarized in that bin. The effects becomes larger with growing bin width. This feature can be removed by bin-shift corrections. Such a correction can be applied by shifting the data points either in yield or in p_{T}. For this thesis and the presented results, the shifts are applied in p_{T} direction (and also slightly in yield due to the used method). For the correction for finite bin-width, the method introduced in [217] is used.

The "correct" value x_{lw} (large width) of the bin with a lower bound of x_1 and an upper bound of x_2 is given by

$$g(x_{\text{ls}}) = \frac{1}{\Delta x}\int_{x_1}^{x_2} g(x)\mathrm{d}x, \tag{7.22}$$

with $g(x)$ the underlying density function. Normally $g(x)$ is not known, since it is the underlying truth of the measured quantity. Instead, a function $f(x) = \alpha g(x) + \beta$, which describes the measured data reasonably well (e.g. a model or a fit function), can be used. It can be shown that:

$$f(x_{\text{ls}}) = \frac{1}{\Delta x} \int_{x_1}^{x_2} f(x)\mathrm{d}x. \tag{7.23}$$

From this, the value of x_{lw} can be extracted. For the prediction, $f(x)$, the spectrum is fitted with different functions (Sec. 9.1). The overall size of the correction is small except for the very broad high p_{T} bins. The shift for the last bin ($8.0 < p_{\text{T}} < 11.0\,\text{GeV}/c$) of the inclusive primary-photon spectrum in 0-20% most central Pb–Pb collisions is $0.22\,\text{GeV}/c$.

Inclusive Primary-Photon Spectra in pp and Pb–Pb

The resulting spectra for the pp and Pb–Pb analysis are shown in Fig. 7.25. The boxes correspond to the systematic uncertainties. The statistical uncertainties are not visible. They are smaller than the plotted markers. These spectra are the first ingredient required for the direct-photon measurement. The second contribution is the neutral pion spectrum. Its measurement via the photon conversion method is discussed in the next section.

A detailed description of the systematic uncertainties of the inclusive-photon spectra is presented in Section 10.3.
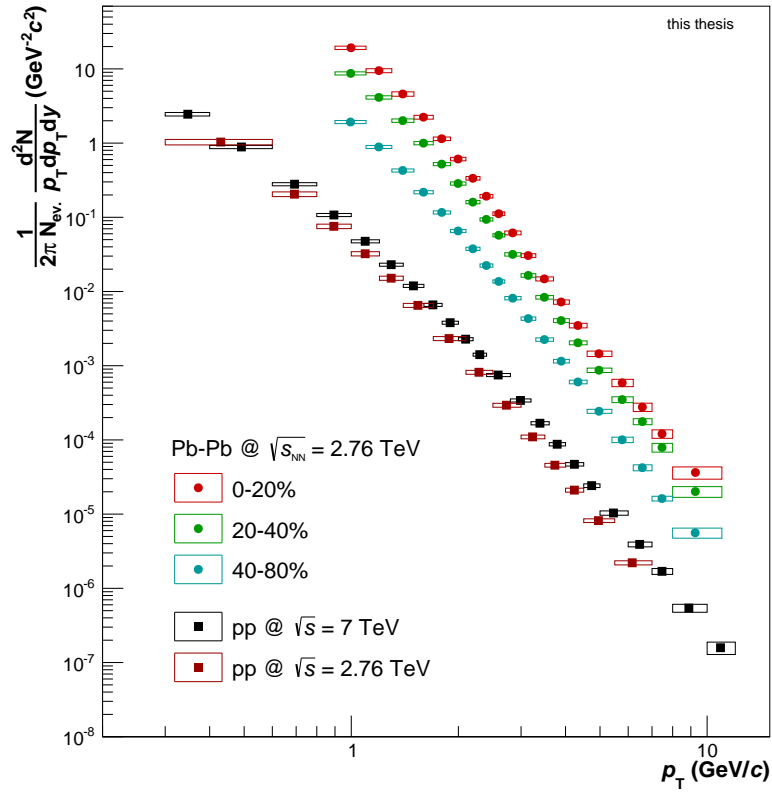
Figure 7.25: Inclusive primary-photon invariant yields for pp and Pb–Pb collisions. For the heavy-ion case, three different centrality bin are plotted.

8 Neutral Pion Reconstruction with Converted Photons

The second particle spectrum crucial for the direct-photon analysis is the neutral pion spectrum. The neutral pion decays, with a branching ratio of 98.789% [6], into two photons. The properties of the pion can be calculated from these decay products. For the presented analysis, the photons are identified by their conversion products, electron-positron pairs. The neutral pion reconstruction chain is hence given by $\pi^0 \to \gamma + \gamma \to e^+e^- + e^+e^-$. The V0 sample used for the π^0 reconstruction is identical to the sample used for the inclusive-photon measurement.

The neutral pion extraction is an important part of the direct-photon analysis. Nevertheless, the description is kept short. The π^0 results are published for 7 TeV pp data in [215] and for pp and Pb–Pb at 2.76 TeV in [216]. A comprehensive description of the analysis is given in [195]. Basic work about the π^0 extraction with the conversion method in ALICE can be found in [197, 218].

8.1 Neutral Pion Reconstruction and Signal Extraction

In the analysis a neutral pion is identified and selected by its invariant mass calculated from V0 pairs. The invariant mass $m_{\gamma\gamma}$ is defined as:

$$m_{\gamma\gamma} = \sqrt{2E_{\gamma_1}E_{\gamma_2}(1 - \cos(\Theta_{12}))}. \tag{8.1}$$

The mass is deduced from the energy and the opening angle Θ_{12} of the V0 pair. A π^0 has an invariant mass of $0.135\,\text{GeV}/c$. Photons, originating from the same π^0 decay, should result in a mass close to the theoretical value. To find the correct combinations, all photon candidates of an event are paired.

Example invariant mass spectra for pp at 7 TeV and central Pb–Pb collisions are shown in Fig. 8.1. The presented spectra consist of all possible pairs with a summed pair momentum of $1.0\,\text{GeV}/c < p_\text{T} < 1.2\,\text{GeV}/c$ for pp and $1.1\,\text{GeV}/c <$
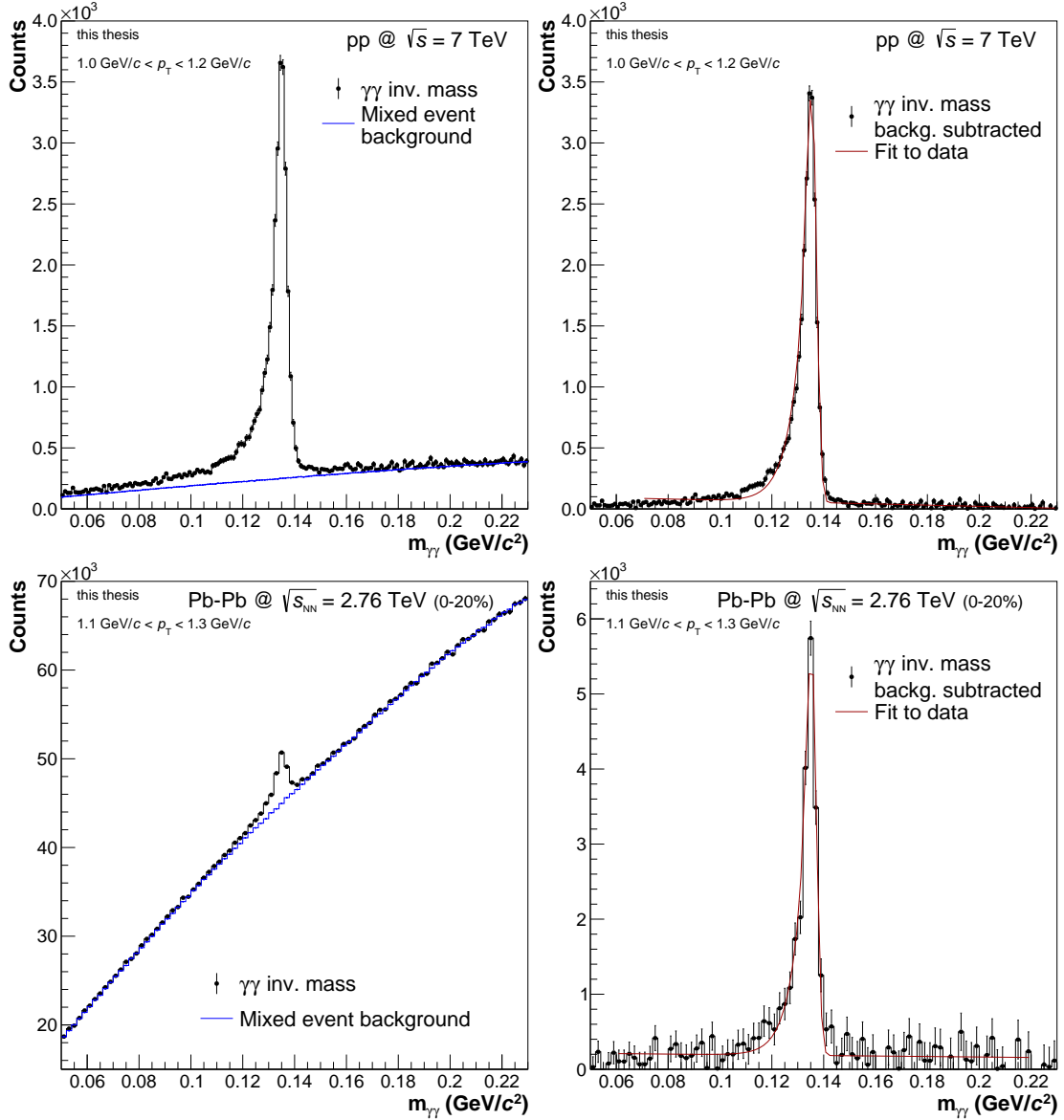
Figure 8.1: π^0 peaks without and with combinatorial background for pp at 7 TeV and central (0-20%) Pb–Pb collisions. For both examples a p_T bin slightly above $1.0\,\mathrm{GeV}/c$ is shown. In addition, a fit (Eq. (8.2)) to the peak is plotted. Due to the much higher photon multiplicity, the combinatorial background is magnitudes larger in Pb–Pb.

$p_T < 1.3\,\mathrm{GeV}/c$ for Pb–Pb. In case of a neutral pion decay, this momentum is equal to the original pion p_T.

The left plots show clear peaks at the expected pion mass. In addition, a back-

ground rising towards higher masses is visible. It originates from V0 pairs not produced by the decay of the (same) neutral pion. This sort of background is referred to as combinatorial background. The overall multiplicity of photons is much smaller in pp collisions. The mean number of identified photon candidates per event in pp collisions is ~ 0.12 (Fig. 6.3), in a central Pb–Pb events ~ 17 (Fig. 6.8). Consequently, the possible number of pairs is much larger in Pb–Pb collisions, leading to a much larger combinatorial background. The larger background is clearly visible in the lower left plot.

It is not possible to distinguish signal and background on the level of individual photon pairs. The π^0 decays directly at the primary vertex. Moreover, a background pair might result in an invariant mass identical to the π^0 mass. To distinguish signal and background, a statistical subtraction method is used. For that purpose, a mixed-event technique is applied.

In this method, photon candidates of the current event are combined with candidates from other events. Photons originating from different events are clearly uncorrelated. To have a better description of the background, the events are grouped by two characteristics. The first is the primary vertex position in z-direction (seven bins). As a second event property, the photon multiplicity (five bins) is taken. For each combination of bins, the photon candidates of 80 (pp) or 50 (Pb–Pb) events are stored in a first-in-first-out buffer. The number of Pb–Pb events is smaller because of the larger multiplicity in these events. The final background is calculated as a weighted sum of all background bin combinations. The advantage of this method is the very high statistics of photon pairs available for the background description. The background is normalized to the measured same-event background at a mass range slightly above the π^0 mass. This normalized mixed-event combinatorial background is shown in blue in the left plots of Fig. 8.1.

On the right hand side of the figure, this background is subtracted. The remaining part of the spectra is the invariant mass peak of the neutral pion. The tail on the left side of the peaks is caused by Bremsstrahlung of the electrons and positrons used for the photon reconstruction. Additionally, a fit to the peak is shown in red. It has the functional form:

$$c(m_{\gamma\gamma}) = A\left(G(m_{\gamma\gamma}) + \exp\left(\frac{m_{\gamma\gamma} - m_{\pi^0}}{\lambda}\right)(1 - G(m_{\gamma\gamma}))\Theta(m_{\gamma\gamma} - m_{\pi^0})\right) + B + Cm_{\gamma\gamma}$$

$$\text{with} \quad G(m_{\gamma\gamma}) = \exp\left(-0.5\left(\frac{m_{\gamma\gamma} - m_{\pi^0}}{\sigma_{m_{\gamma\gamma}}}\right)^2\right). \tag{8.2}$$

The fit is a modified Gaussian, expressed by the function $G(m_{\gamma\gamma})$, peaked at the

pion mass m_{π^0}. Bremsstrahlung is implemented as an exponential with an inverse slope parameter λ. It contributes only for $m_{\gamma\gamma} < m_{\pi^0}$ controlled by a Heavyside function $\Theta(m_{\gamma\gamma} - m_{\pi^0})$. Since a residual background might still be left after the background subtraction, a linear part $(B + Cm_{\gamma\gamma})$ is added to the fit.

The raw π^0 yield is obtained by integrating the invariant mass peak after subtraction in transverse momentum bins. The peak integration range is dynamically calculated around the peak position obtained by the fit. The range is set to $[m_{\pi^0} - 0.035\,\mathrm{GeV}/c^2, m_{\pi^0} + 0.010\,\mathrm{GeV}/c^2]$, with m_{π^0} the estimated π^0 mass in the momentum bin. If a residual background is identified, the linear part of the fit is subtracted additionally.

The π^0 reconstruction is restricted to a sightly narrower rapidity region as used for the photon analysis. This guarantees a minimized π^0 loss due to the opening angle of the photon pairs. As already mentioned in Sec. 7.2.1, the conversion points have to have larger radii than $R_{\mathrm{conv}} > 5\,\mathrm{cm}$. This selection removes efficiently π^0 Dalitz decays. To have a better signal to background ratio in the high multiplicity environment of Pb–Pb collisions a cut on the asymmetry of the photon momenta is applied. The asymmetry is given by $\alpha_{\pi^0} = |E_{\gamma_1} - E_{\gamma_2}|/(E_{\gamma_1} + E_{\gamma_2})$. Due to the strongly rising multiplicity of photons at low momenta, the cut removes a lot of possible combinations with low p_{T} photons. The possibility of removing the correct partner is, in contrast, nearly equally distributed over all momenta.

All selection criteria exclusively applied to the π^0 candidates are listed in Tab. 8.2.

Selection Criterion	2.76 TeV (pp)	7 TeV (pp)	2.76 TeV (Pb–Pb)
fiducial $|y_{\pi^0}|$	0.8	0.8	0.6
max. asymmetry α_{π^0}	1.0	1.0	0.6 (0-40%) 0.8 (40-80%)
N_{event} background	80	80	50

Figure 8.2: Selection criteria values used for the neutral pion analysis for all analyzed collision energies.

8.2 Corrections to the Raw Neutral Pion Spectrum

Like the photon spectrum, the raw neutral pion spectrum has to be corrected for efficiency. Furthermore, a geometrical acceptance correction for neutral pions in

the fiducial rapidity region with photons outside their accepted region has to be applied. As for photons, the secondary particle contribution has to be removed. The secondary π^0 are again predominantly produced by the decay of the K_s^0. Finally, neutral pions originating from different-bunch pileup has to be subtracted. All corrections are briefly discussed in this section.

8.2.1 Pileup and Secondary π^0 Correction

The main contribution of secondary photons originates from neutral pions produced by K_s^0 decays. Consequently, the same decay dominates the secondary π^0 production. The subtraction is identical to the inclusive-photon procedure as given by Eq. (7.11). The scaling factors used for the π^0 subtraction are identical to the values given in Tab. 7.12. Due to limited statistics for the neutral pion reconstruction (and even more limited for secondary π^0), the largest event sample (pp at 7 TeV) is used exclusively for the extraction of the secondary π^0 fraction. Instead of using this fraction directly, a fit of the form $f(p_T) = a/p_T^b$ is taken. As for the photon analysis, the subtraction is separated into a K_s^0 and a total secondary particle component. Both ratios are shown in Fig. 8.3. The shown
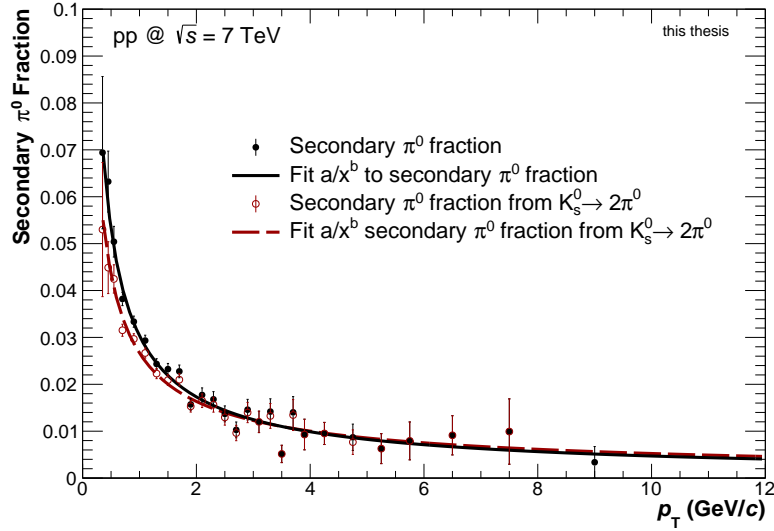
Figure 8.3: Fraction of Monte Carlo validated secondary π^0 over all π^0 candidates for pp 7 TeV. Due to the limited statistics, the fractions are fitted with $f(p_T) = a/p_T^b$.

secondary π^0 fractions are very similar to the corresponding secondary photon fractions.

The second correction applied to the raw spectrum is the subtraction of neutral pions originating from different-bunch pileup events. The method is again identical to the subtraction performed for the inclusive-photon measurement, introduced in Sec. 7.4. Exemplary, the DCA_z distributions are shown for the 7 TeV data in Fig. 8.4. The measured DCA_z distributions of the reconstructed π^0 have again
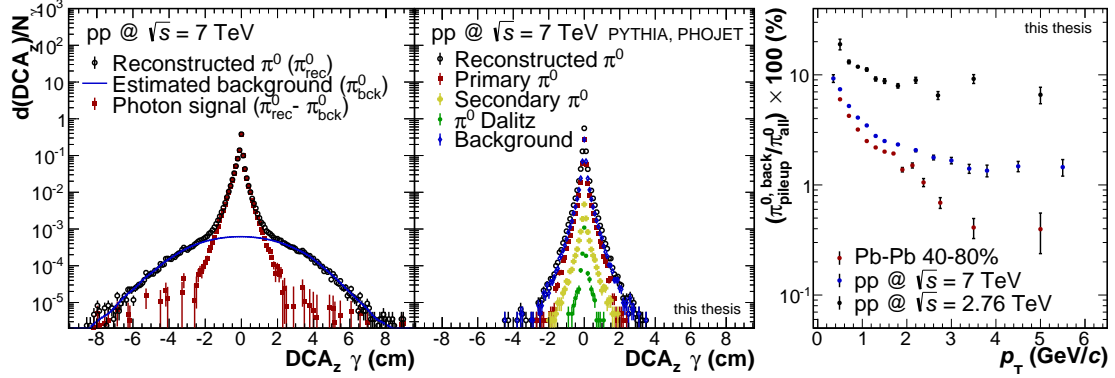
Figure 8.4: p_T integrated DCA_z distribution for reconstructed π^0 candidates for pp at 7 TeV before and after background subtraction (left). Corresponding distribution for validated π^0s and background (center). p_T differential correction factors for pp at 7 TeV and 2.76 TeV and Pb–Pb collisions (right).

a broader background compared to the corresponding Monte Carlo distributions. On the right hand side, all estimated pile-up contributions are shown. Like for photons, the contribution is largest for the pp at 2.76 TeV data.

8.2.2 Efficiency and Acceptance Correction

The efficiency correction for π^0 includes the conversion probability of photons. This results in a much larger correction as found for the photon finding efficiency. The acceptance of photon candidates is inherent in the conversion probability of photons. For the neutral pions, it is shifted to an extra correction factor. No purity correction has to be applied in the π^0 analysis. As discussed in section 8.1, the background is subtracted from the signal and the signal is deduced by peak integration.

The efficiency is calculated as:

$$\mathcal{E}_{\pi^0}\left(p_\mathrm{T}\right) = \frac{\pi^{0\;\mathrm{MC}}_{\mathrm{rec}}\left(p_\mathrm{T}\right)^{\mathrm{primary,true}}}{\pi^0_{\mathrm{MC}}\left(p_\mathrm{T}\right)^{\mathrm{primary,in\;acceptance}}}. \tag{8.3}$$

$\pi_{\text{rec}}^{0\,\text{MC}}\,(p_{\text{T}})^{\text{primary,true}}$ is the number of validated true primary π^0, reconstructed in the Monte Carlo events. $\pi_{\text{MC}}^{0}\,(p_{\text{T}})^{\text{primary,in acceptance}}$ refers to generated π^0 which are in the acceptance defined by the rapidity of the meson and its decay products (γ and e^+e^-). As found for the photons, the spectra used for the efficiency calculation differ from the measured data spectra. This difference is even more pronounced if the added π^0, following a flat p_{T} distribution, are considered (Sec. 6.2). For a correct efficiency, the Monte Carlo spectra (additional flat added signal and minimum bias distribution) are weighted to match with the data spectra.

The geometrical acceptance for neutral pions is:

$$\mathcal{A}_{\pi^0}\,(p_{\text{T}}) = \frac{\pi_{\text{MC}}^{0}\,(p_{\text{T}})^{\text{primary,in acceptance}}}{\pi_{\text{MC}}^{0}\,(p_{\text{T}})^{\text{primary,all}}}. \tag{8.4}$$

Like the conversion property of photons, the correction is only based on generated Monte Carlo p_{T} spectra. Thus, no unfolding or weighting is required. The spectrum $\pi_{\text{MC}}^{0}\,(p_{\text{T}})^{\text{primary,in acceptance}}$ is identical to the denominator spectrum of Eq. (8.3). $\pi_{\text{MC}}^{0}\,(p_{\text{T}})^{\text{primary,all}}$ refers to all π^0 produced in the fiducial rapidity region.

In Fig. 8.5 (left), the efficiency for the π^0 reconstruction is shown for all collision systems and centralities. On the right hand side, the corresponding geometrical acceptances are plotted. The efficiency depends clearly on the centrality and thus
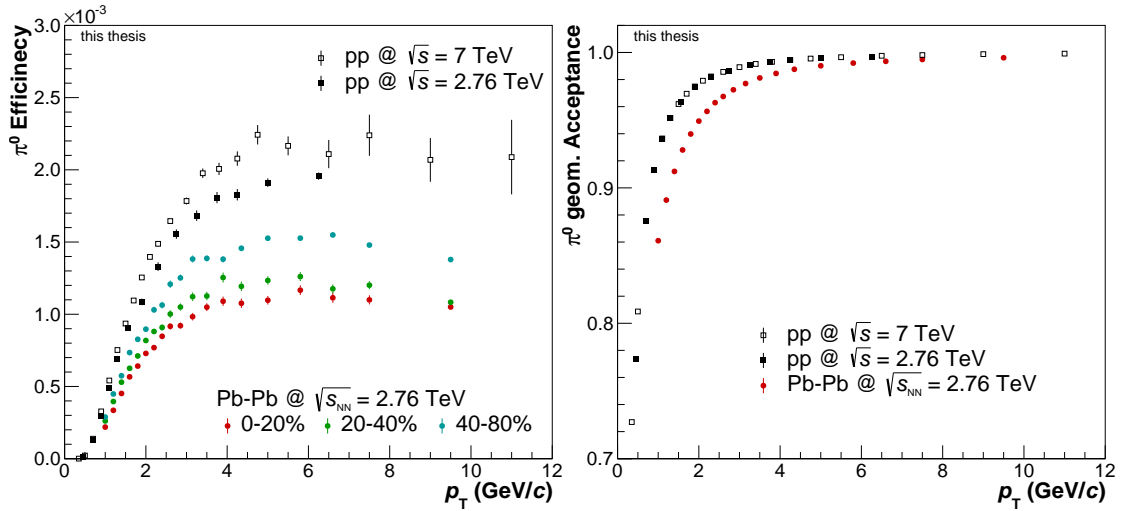
Figure 8.5: π^0 reconstruction efficiency (left) for all collisions systems and centralities and the corresponding geometrical acceptances (right). The smaller acceptance in Pb–Pb is caused by the smaller rapidity region used in the analysis.

on the multiplicity of the events. In contrast, the geometrical acceptance depends

only on the rapidity region used for the photon and π^0 reconstruction. As found for photons, the efficiency for the 2.76 TeV pp data is smaller compared to 7 TeV due to the missing SDD read-out.

8.2.3 Neutral Pion Spectra in pp and Pb–Pb

With all corrections applied, the final correction formula for the neutral pions is given by:

$$\pi_{\text{rec}}^{0 \text{ data}} (p_{\text{T}})_{\text{full corr}}^{\text{primary}} = \pi_{\text{rec}}^{0 \text{ data}} (p_{\text{T}})_{\text{sec.corr}}^{\text{pileup corr}} \times \frac{1}{\mathcal{E}_{\pi^0} (p_{\text{T}})} \times \frac{1}{\mathcal{A}_{\pi^0} (p_{\text{T}})} \times \frac{1}{\text{BR}}. \qquad (8.5)$$

The invariant primary neutral pion yield is defined as:

$$E \frac{\text{d}^3 N^{\pi^0}}{\text{d}^3 p} = \frac{\text{d}^3 N^{\pi^0}}{p_{\text{T}} \text{d}p_{\text{T}} \text{d}y \text{d}\varphi} = \frac{1}{2\pi N_{\text{event}} p_{\text{T}}} \frac{\pi_{\text{rec}}^{0 \text{ data}} (p_{\text{T}})_{\text{full corr}}^{\text{primary}}}{\Delta y \Delta p_{\text{T}}}. \qquad (8.6)$$

In contrast to the correction of the inclusive-photon spectrum, the neutral pion spectrum has to be scaled additionally with the branching ratio (BR) of the decay $\pi^0 \to \gamma\gamma$. The raw π^0 spectrum does not contain π^0 decaying into other channels. The branching ratio of the two photon decay is 98.798% [6]. The second largest contribution is the π^0 Dalitz decay with a branching ratio of 1.174%.

Finally, the invariant cross section in pp is given by:

$$E \frac{\text{d}^3 \sigma^{\pi^0}}{\text{d}p^3} = \frac{1}{2\pi} \frac{\sigma_{\text{MB}_{\text{OR}}}}{N_{\text{event}}} \frac{1}{p_{\text{T}}} \frac{\pi_{\text{rec}}^{0 \text{ data}} (p_{\text{T}})_{\text{full corr}}^{\text{primary}}}{\Delta y \Delta p_{\text{T}}}. \qquad (8.7)$$

The cross section $\sigma_{\text{MB}_{\text{OR}}}$ is the same as in Eq. (7.21), the values are listed in Tab. 7.24.

The final invariant π^0 yields are shown in Fig. 8.6. These spectra are for Pb–Pb and pp at 2.76 TeV identical to the published spectra [216]. The spectra for the 7 TeV data are slightly different compared to the published results. At time of publication, no different-bunch pileup correction was considered, leading to a difference on the order of $5 - 8\%$ at low p_{T} and $1 - 2\%$ at high p_{T} (compare Fig. 8.4). Moreover, the selection criteria used for the presented analysis were harmonized with the more recent Pb–Pb and pp at 2.76 TeV analyses. The new criteria lead to no significant change of the result.

With the knowledge about the spectral shape of the neutral pion spectrum, the expected decay photons from pion decays can be calculated. It is by far the largest contribution to the inclusive-photon spectrum. Nevertheless, to extract
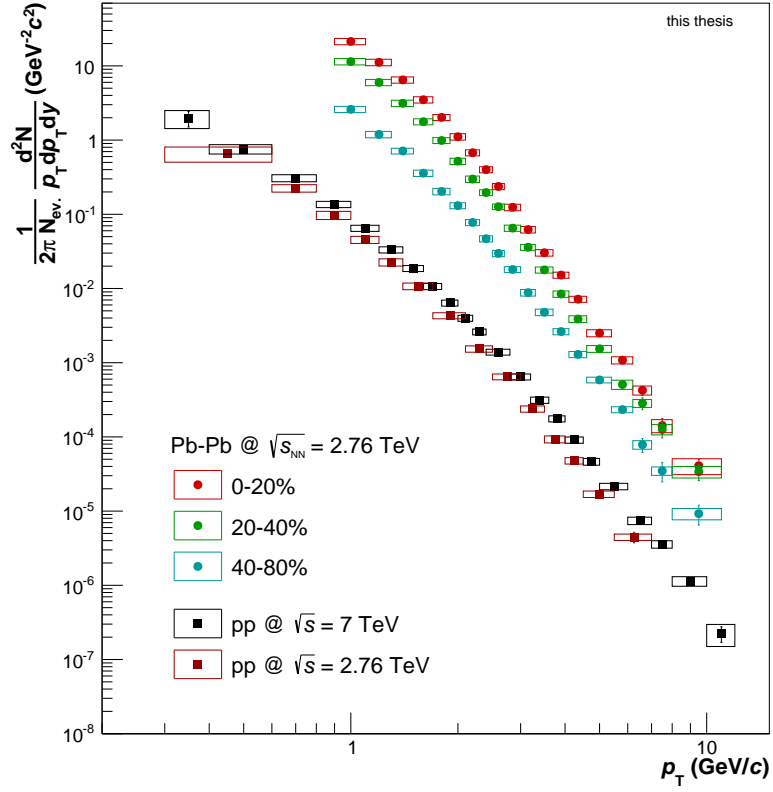
Figure 8.6: Primary neutral pion spectra for pp and Pb–Pb collisions. For the heavy-ion case, three different centrality bins are plotted.

direct photons all decay photons from all decays have to be considered. For that purpose, the corresponding meson spectra have to be estimated. The calculation of the total amount of decay photons is discussed in the next chapter.

9 Decay-Photon Cocktail Calculation

For the direct-photon analysis, the photons originating from particle decays have to be estimated. This is done via the decay algorithms of PYTHIA 6.4 included in the AliRoot framework. From measured particles spectra, e.g. the neutral pion spectrum discussed in Chap. 8, the expected decay-photon spectrum is calculated. This calculation includes all possible decays with the corresponding branching ratios contained in PYTHIA 6.4. The branching ratios and the corresponding decays are summarized in Tab. 4.7. Since the final decay-photon spectrum is the sum of many individual contributions, it is referred to as cocktail spectrum, the corresponding calculation routine as cocktail generator. For the decay photon calculation, no detector implementation is required. The determination of the decay-photon spectra is performed exclusively on the level of fully corrected spectra which are independent of the detector response.

9.1 Cocktail Calculation Method and Fit Functions

From an input spectrum of a particle with photon decay branches a decay-photon spectrum is estimated by a so called cocktail generator. As input it uses parameterizations of the corresponding spectra. To have good results, the chosen parameterization has to be as precise as possible. On the other hand, the neutral pion reconstruction is afflicted with large statistical uncertainties. The fluctuations are non-physical and should thus not be considered by the fit. Furthermore, decay photons will originate not only from the measured p_{T} region but also from larger momentum values. To constrain the fits above the measured region, charged pion measurements are used.

No functional form was found in literature which was able to describe the measured π^0 spectra on the requested level for all collision systems. The most prominent

existing parameterizations are the Tsallis function originally developed in [219] but normally used in the different representation [220]:

$$\frac{\mathrm{d}^2 N}{\mathrm{d}y \mathrm{d}p_\mathrm{T}} = p_\mathrm{T} \frac{\mathrm{d}N}{\mathrm{d}y} \frac{(n-1)(n-2)}{nT(nT + m_0(n-2))} \left(1 + \frac{m_\mathrm{T} - m_0}{nT}\right)^{-n}. \tag{9.1}$$

It is deduced from the generalized Boltzmann-Gibbs distribution. A second QCD inspired parameterization, proposed by Hagedorn [221], is given by:

$$E\frac{\mathrm{d}^3 N}{\mathrm{d}p^3} = A \left(\frac{p_0}{p_0 + p_\mathrm{T}}\right)^n \rightarrow \begin{cases} \exp\left(-\frac{np_\mathrm{T}}{p_0}\right) & \text{for } p_\mathrm{T} \rightarrow 0 \\ \left(\frac{p_0}{p_\mathrm{T}}\right)^n & \text{for } p_\mathrm{T} \rightarrow \infty \end{cases} \tag{9.2}$$

Both functions are able to describe the π^0 spectra in pp collisions rather precisely.

The situation becomes different for Pb–Pb collisions. Here the spectra are modified by e.g. radial flow and it is not expected that the parameterizations Eq. (9.1) and (9.2) are able to describe the spectra. PHENIX proposed a modified Hagedorn parameterization [222], given by:

$$E\frac{\mathrm{d}^3 N}{\mathrm{d}p^3} = A \left(\exp\left(ap_\mathrm{T} + bp_\mathrm{T}^2\right) + \frac{p_\mathrm{T}}{p_0}\right)^{-n}. \tag{9.3}$$

This function was found to result in good fits for the Au–Au spectra at RHIC. For the Pb–Pb data, it is much better suited compared to the parameterizations developed for pp but still does not give precise results at high p_T.

Thus, to have a reliable decay-photon cocktail, new parameterizations have been developed. The first parameterization is given by:

$$E\frac{\mathrm{d}^3 N}{\mathrm{d}p^3} = A p_\mathrm{T}^{-(n + c/(p_\mathrm{T}^d + e))} \rightarrow A p_\mathrm{T}^{-n} \quad \text{for} \quad p_\mathrm{T} \rightarrow \infty \tag{9.4}$$

This parameterization is a modified power-law (p_T^{-n}) and converges against a constant power n for increasing values of p_T. It is, therefore, able to give a correct high momentum behavior. At lower momenta, it describes phenomenologically the different effects caused by the medium.

A second function which was tested is a modified Tsallis function [223]. It has more parameters compared to the other functions presented. It has the form:

$$E\frac{\mathrm{d}^3 N}{\mathrm{d}p^3} = A \frac{b + cp_\mathrm{T} + p_\mathrm{T}^2}{d + ep_\mathrm{T} + p_\mathrm{T}^2} \left(1 + \frac{m_\mathrm{T} - m_0}{nT}\right)^{-n} \tag{9.5}$$

Since it is not important that the parameterization used for the cocktail has a physical meaning, the π^0 spectra are fitted with all available functions. The comparison of the fits to the spectra are shown in Fig. 9.1 for pp collisions and in Fig. 9.2 for Pb–Pb collisions, also for different centrality bins. To have a correct
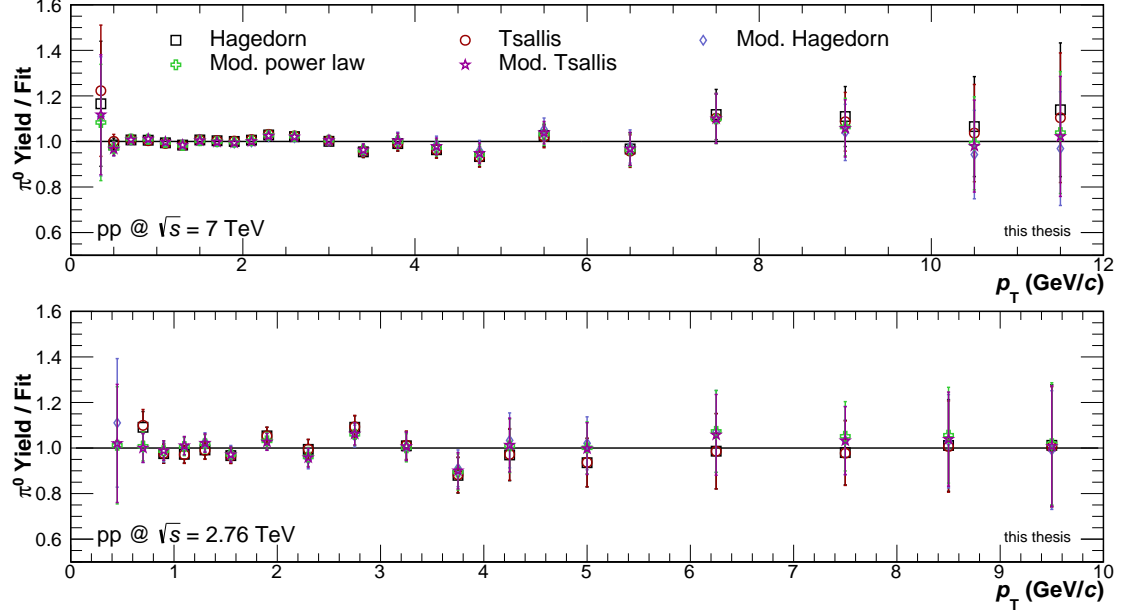
Figure 9.1: π^0 yield over fit for various parameterizations for pp collisions at 7 TeV and 2.76 TeV. For $p_T > 10\,\mathrm{GeV}/c$ respectively $p_T > 7\,\mathrm{GeV}/c$ charged pions data points are used

high p_T behavior of the fits in the region where the neutral pions are not measured, the charged pion spectra are used as a constraint. If a systematic offset to the charged pions is found [215, 216], the charged pion spectra are scaled to match with the neutral pion spectra. This is necessary due to the correlation between photon and π^0 measurement and, therefore, between $\gamma_{\mathrm{inc}}/\gamma_{\mathrm{decay}}$. In an alternative ansatz, the charged pion spectra are used not only to constrain the neutral pion spectra above the measured p_T region but already at an intermediate momentum $(3 - 4\,\mathrm{GeV}/c)$. This eliminates the large statistical fluctuations of the π^0 spectra used as cocktail input. These fluctuations might not be smoothed by the fit in case of unluckily large upwards or downward fluctuations. The difference between both methods is considered in the systematic uncertainties.

For pp collisions, all parameterizations do a reasonable job and describe the neutral meson spectra. In Pb–Pb collisions, the pp parameterizations fail to describe the spectra. The modified Hagedorn function, used by PHENIX, is much better in reproducing the shape of the ALICE neutral pion spectra. Still, at high p_T it
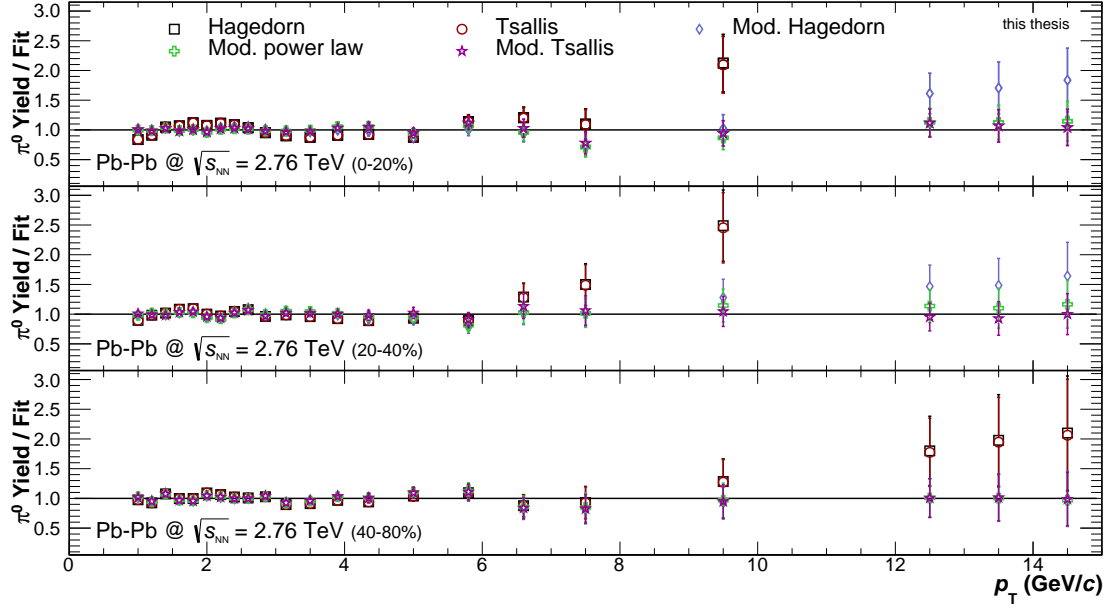
Figure 9.2: π^0 yield over fit for various parameterizations for Pb–Pb collisions in the centrality bins 0-20%, 20-40% and 40-80%. For $p_{\rm T} > 11\,{\rm GeV}/c$ charged pion data points are used.

starts to deviate from the data points. The two newly developed functions are both able to describe the spectra over the full $p_{\rm T}$ range on a similar precision level. For the final cocktail input, the modified Tsallis function Eq. (9.5) is chosen for Pb–Pb. For pp collisions, the modified power law function Eq. (9.4) is used.

The neutral meson fit parameters together with the corresponding $\chi^2/{\rm ndf}$ for all analyzed systems are given in the appendix (Tab. B.1).

9.2 Decay-Photon Cocktail Input

Not only the neutral meson spectrum is needed for the cocktail calculation. The second largest contribution to the decay-photon cocktail is the decay of the η meson. Depending slightly on the $p_{\rm T}$ region, this contribution is on the level of 10-15%. For pp collisions at 7 TeV, a measurement of the η invariant yield is available. The measurements still lacks the subtraction of the pileup background. Due to this, not a direct fit to the spectrum is used as input to the cocktail. Instead, the η to π^0 ratio is fitted with the ratio of two fit functions. For the fit function, the fit parameters from Tab. B.1 are used for the pion part. For the η

contribution, a function following Eq. (9.4) is used. With this method, a similar pileup contribution to the η as found for the π^0 spectrum is assumed automatically.

For pp at 2.76 TeV, a η measurement exists, too. This measurement is too limited in p_T and by statistics to be used as an input to the cocktail calculation. Instead, the 7 TeV ratio is assumed and the η is estimated with the ratio fit method introduced above. Here, a fit to the measured pp at 2.76 TeV π^0 spectrum is used for the numerator function.

In Pb–Pb, no η meson measurement is yet available. The signal to background ratio as well as the statistics are not large enough to make such a measurement feasible. Different approaches are considered to predict the η contribution. The first ansatz previously used for direct-photon analyses is the η spectrum prediction via m_T scaling. In the transverse mass scaling (m_T), the η spectrum is determined from the measured π^0 spectrum. The transverse mass is defined as:

$$m_T = \sqrt{p_T^2 + m_0^2}. \tag{9.6}$$

The m_T scaling phenomenology was first reported by the WA80 collaboration [224]. They report a similarity of the η and π^0 spectrum if expressed as a function of the transverse mass. As a consequence, at low momenta, where the rest mass m_0 is still sizable (compare Eq. (9.6)), the ratio depends strongly on the mass of the particles. At higher values of p_T with $p_T \gg m_0$, the ratios show a constant behavior and do not depend on the center of mass energy of the collisions. In [225, 226], this method is extended to a broader set of different mesons. An excellent agreement was found in most cases. The η meson p_T spectrum is for example obtained via the formula:

$$E\frac{\mathrm{d}N^\eta}{\mathrm{d}p^3} = C_m \cdot P_{\pi^0} \left(\sqrt{p_T^2 + m_\eta^2} \right). \tag{9.7}$$

The factor C_m represents the relative normalization of the η meson m_T spectrum to the neutral π^0 m_T spectrum and must be obtained from experimental results. P_{π^0} represents a parameterization of the π^0 spectrum, and m_η is the mass of the η meson. Using that method, not only the η spectrum can be predicted. With an identical assumption, all meson spectra with photon decay branches can be estimated. In every case, if no better prediction is available, transverse mass scaling is used to obtain the required spectra. The m_T scaling factors used for the analysis are listed in Tab. 9.1. Additionally, the reference of the scaling factors is given. If m_T scaling is used in the analysis, it is marked in the last column of the table.

The second approach to obtain a prediction for the η spectrum in Pb–Pb is given

Meson (C_m)	Coll. System	C_m	Reference	m_T scaling used
η	Pb–Pb	0.46	measured [227]	partially
	pp	0.48	measured [228]	no
ω	Pb–Pb	0.81	measured [229]	yes
	pp	0.81	measured [229]	no
ρ^0	Pb–Pb	1.0	prediction [174]	yes
	pp	1.0	prediction [174]	yes
η'	Pb–Pb	0.4	prediction [174]	yes
	pp	0.4	prediction [174]	yes
ϕ	Pb–Pb	0.35	measured [230]	yes
	pp	0.13	measured [231]	no
Σ^0	Pb–Pb	0.49	estimate	yes
	pp	0.49	estimate	yes

Table 9.1: m_T scaling parameters for pp and Pb–Pb collisions. Since some particle spectra are measured, m_T scaling is not used for every decay-photon contribution. In case of the η meson in Pb–Pb, m_T scaling is used as one alternative approach.

by using the pp η to π^0 ratio. This ansatz is justified by the R_{AA} of neutral pions and η mesons measured by RHIC. In Fig. 9.3, taken from [232], the nuclear
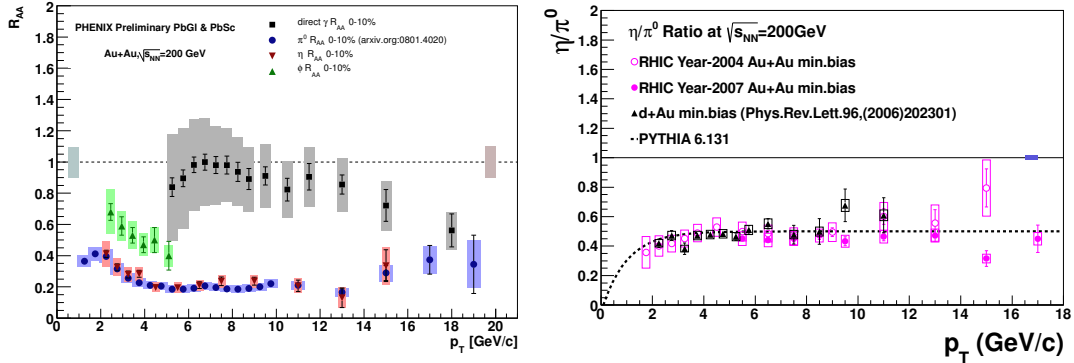
Figure 9.3: Left: Neutral pion and η nuclear suppression factor for 0-10% most central Au–Au data at $\sqrt{s_{NN}} = 200\,\text{GeV}$ measured by PHENIX. In addition, the R_{AA} of direct photons and of the ϕ meson are shown. [232] Right: η to π^0 ratio for minimum bias Au–Au data at $\sqrt{s_{NN}} = 200\,\text{GeV}$ measured by PHENIX. [227]

modification factor of π^0 and η mesons are shown. Both mesons show a very

similar suppression. With the simple mathematical conversion

$$R_{AA} \propto \frac{\pi^0_{\text{pp}}}{\pi^0_{\text{Pb–Pb}}} \approx \frac{\eta_{\text{pp}}}{\eta_{\text{Pb–Pb}}} \quad \rightarrow \quad \frac{\eta_{\text{pp}}}{\pi^0_{\text{pp}}} \approx \frac{\eta_{\text{Pb–Pb}}}{\pi^0_{\text{Pb–Pb}}}, \tag{9.8}$$

follows directly the similarity of the η to π^0 ratio in pp and Pb–Pb. The same conclusion can be drawn from the minimum bias Au–Au η over π^0 ratio measured by PHENIX. It is within uncertainties compatible with the corresponding ratio of the pp generator PYTHIA (Fig. 9.3 (right)). A conceptual problem of that method is the unknown strength of the particle suppression at LHC energies and the influence of the larger radial flow. In addition, the η spectrum is only measured by PHENIX down to $p_{\text{T}} = 2\,\text{GeV}/c$, the most important region for thermal-photon production might be still below.

To include the effect of radial flow into the prediction of the η meson, the spectrum of the K^0_s measured with ALICE are used [207]. Both particles should be similarly influenced by radial flow due to their similar masses ($m_\eta = 547.862\,\text{MeV}/c^2$, $m_{K^0_s} = 497.614\,\text{MeV}/c^2$). On the other hand, the kaon over pion ratio is not necessarily expected to be similar to the η over pion ratio. Thus, the K^0_s over pion ratio is scaled such that it matches at high p_{T} ($p_{\text{T}} > 5\,\text{GeV}/c$) with the world data of the η/π^0 ratio. In contrast to the prediction by m_{T} scaling or by a pp like η to π^0 ratio, this ratio shows a horn structure most likely originating from radial flow effects. The η to π^0 ratios as produced by the cocktail calculation are shown in Fig. 9.4 (left). The plot contains all three introduced methods (m_{T}, K^0_s, pp ratio). In addition, the measured η to π^0 ratio in pp [215] is presented. For the final result, the average η spectrum of all three methods is used for Pb–Pb. The difference between the three methods is added to the systematic uncertainty.

The third largest decay-photon contribution originates from the decay of the ω meson. In pp, the spectrum and thus the ω to π^0 ratio is measured for $p_{\text{T}} > 2.5\,\text{GeV}/c$ by ALICE. Only preliminary results exist. Smaller values of transverse momentum are taken from a similar ratio measured by PHENIX at 200 GeV [229]. For the cocktail input in pp, the ratio is again fitted with a constrained π^0 fit as already used for the η contribution. For the contribution in Pb–Pb, only m_{T} scaling is used. The ratio is shown on the right hand side of Fig. 9.4.

All further contributions to the decay-photon spectrum are highly subordinated. For them, only m_{T} scaling is used. At 7 TeV, the spectrum of the ϕ meson is measured by ALICE. Here the measured spectrum is used as input to the cocktail generator.
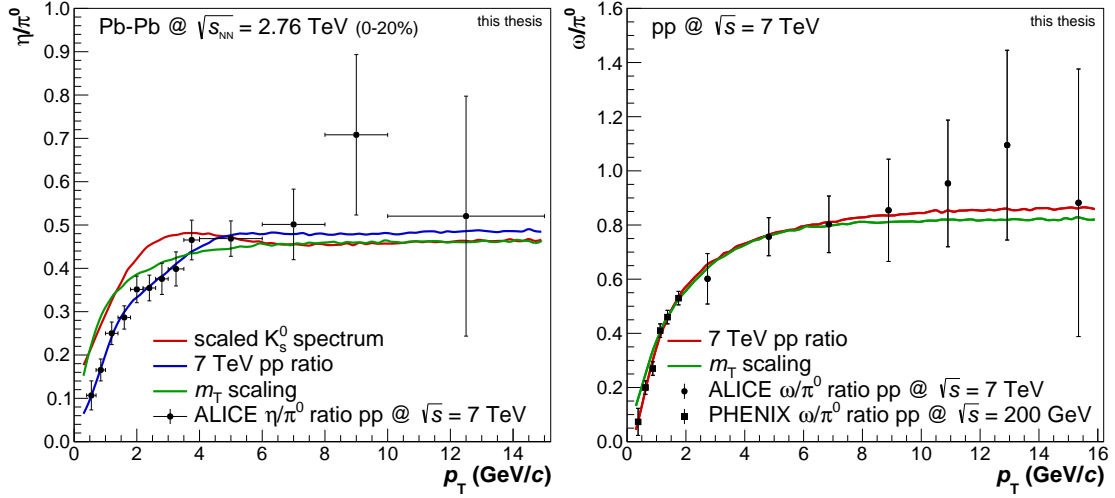
Figure 9.4: (left) η to π^0 ratio for central Pb–Pb events. Shown are all three methods used for the η prediction. red: η estimated from a scaled K_s^0 spectrum; green: m_T prediction for the η spectrum; blue: η deduced from the measured π^0 spectrum and the measured ratio in pp at 7 TeV. The measured 7 TeV ratio is additionally plotted [215]. (right) ω to π^0 ratio. Plotted are the preliminary ALICE results, and the low p_T data points are taken from PHENIX [229]. The red curve is the result of the cocktail calculation obtained with the measured π^0 spectrum and the ratio. For comparison, the result from m_T scaling is plotted in green.

9.3 Decay-Photon Cocktail Results

The output of the decay-photon cocktail is shown in Fig. 9.5. Here only the contribution for the central (0-20%) Pb–Pb collisions are presented. On the left hand side, the individual contributions from the various particle decays to the total decay-photon spectrum are shown. For all other collision systems, the corresponding ratios are very similar. The by far largest contribution are photons from the decay of the neutral pion. The π^0 spectrum is measured in each analyzed collision system. Therefore, this decay-photon contribution should be well defined. The fraction to the total amount of decay photons is 85-90%.

The second largest contribution originates from the decay of the η meson. It is measured for pp at 7 TeV and thus, the contribution for this system is well controlled. For the other systems, only estimates are available. Since the total contribution is only on the order of 10-15% the systematic uncertainties related to this are rather small.
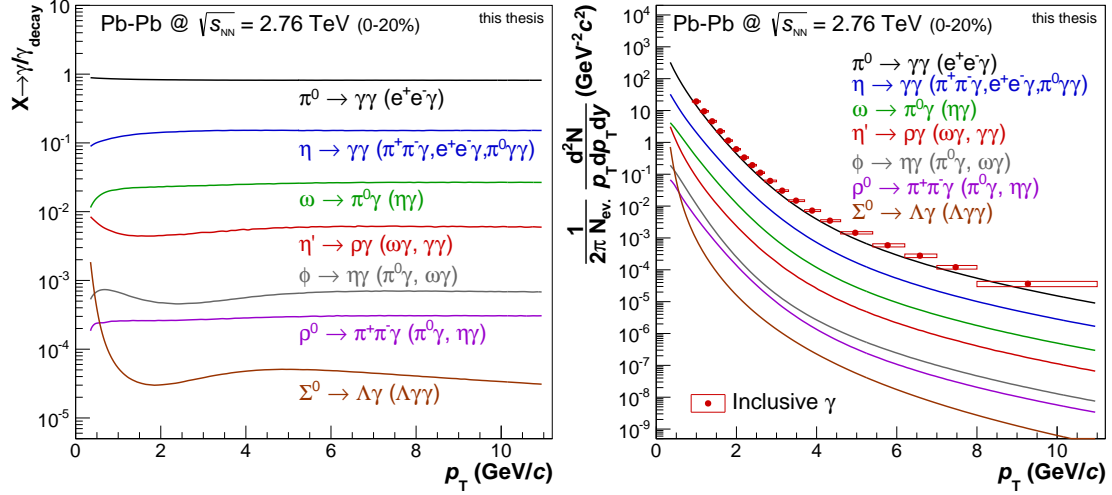
Figure 9.5: Left: Relative contribution of the individual contributions to the total decay-photon spectrum for central Pb–Pb collisions. Right: Individual decay-photon spectra for central Pb–Pb collisions. For comparison, the measured inclusive spectrum is shown.

All other photon sources are nearly negligible. Only the ω with a relative contribution of 1-3% might have a sizable influence on the final result.

On the right hand side, the corresponding decay-photon spectra are shown for the same data sample. For comparison, the inclusive primary-photon spectra (Fig. 7.25) is plotted. The size of this spectrum is clearly larger compared to the largest individual photon decay background contribution.
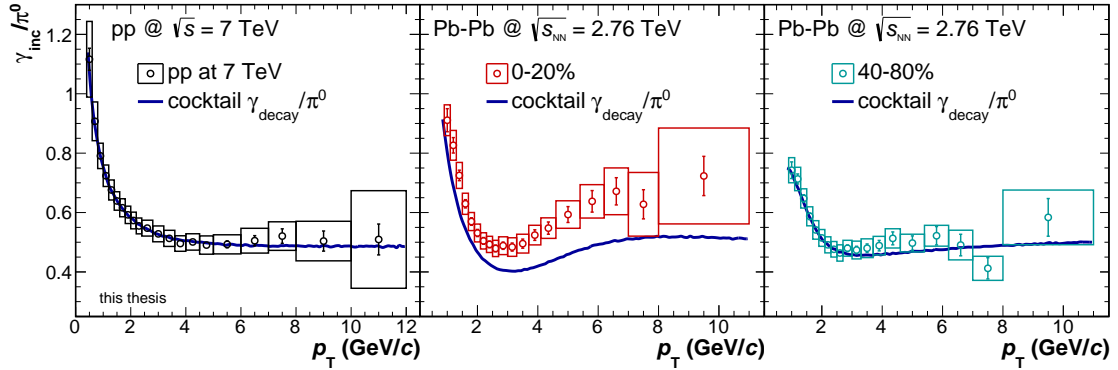
Figure 9.6: Inclusive photon over neutral pion ratio for pp at 7 TeV, central and peripheral Pb–Pb collisions. Additionally, the decay photon over cocktail π^0 ratio is shown.

For a first comparison between the estimated decay-photon background and the

measured photon spectrum, Fig. 9.6 can be used. The plot shows the measured inclusive photon over neutral pion ratio. Instead of the pion spectra, parameterizations (Sec. 9.1) are used in the ratios. This reduces the statistical fluctuations introduced by the neutral pion measurement dramatically. Moreover, the cancellation in a ratio of the inclusive-photon ratio with the cocktail ratio, as introduced in the next chapter, will be better. The cocktail generated ratio, photons from decays over the cocktail π^0 spectrum, is plotted as a blue line. While the two ratios (measured, cocktail) are very similar for pp and peripheral Pb–Pb collisions, a clear difference for central Pb–Pb collisions is found. This deviation can be interpreted as an excess originating from direct photons. A better illustration of the excess will be introduced in the next section.

10 Direct-Photon Extraction

For the direct-photon extraction, three components are required. These are the inclusive-photon spectrum, the neutral pion spectrum and the calculated decay-photon background. After all those contributions are available, the final steps towards the direct-photon spectra can be taken. In an intermediate step, double ratios, representing the direct-photon excess over the calculated decay-photon background, are build. If these ratios show a significant excess, direct-photon spectra can be extracted. Otherwise, only upper limits for the direct-photon production can be given.

10.1 Direct-Photon Excess Ratio

The excess ratios indicating the size of the direct-photon signal are obtained by the two ratios shown in each panel of Fig. 9.6. Thus, they consist of the measured γ_{inc} over π^0 ratio and the calculated $\gamma_{\text{cocktail}}^{\text{decay}}$ over π^0_{cocktail} ratio:

$$R_\gamma = \frac{\gamma_{\text{inc}}}{\pi^0_{\text{param}}} \bigg/ \frac{\gamma_{\text{cocktail}}^{\text{decay}}}{\pi^0_{\text{cocktail}}} \approx \frac{\gamma_{\text{inc}}}{\gamma_{\text{cocktail}}^{\text{decay}}} = 1 + \frac{\gamma_{\text{direct}}}{\gamma_{\text{cocktail}}^{\text{decay}}} \geq 1. \qquad (10.1)$$

They describe, after the approximate cancellation of the π^0 contributions, the ratio of measured inclusive primary photons over the calculated decay-photon background. All possible deviating normalization factors between the cocktail and the measurement are canceled. Additionally, some uncertainties related to the Monte Carlo corrections are reduced. As a further and very important uncertainty reduction, the material budget is canceled partially. The uncertainties and their cancellation will be discussed in detail in Sec. 10.3.

In case of the absence of an extra contribution of direct photons ($\gamma_{\text{direct}} = 0$), the ratio is by construction unity. Nevertheless, statistical or systematic uncertainties might shift the points even below one. If this ratio is significantly above unity, more inclusive photons are measured as expected from particle decays. This indicates a contribution of $\gamma_{\text{direct}} > 0$.

The excess ratios measured in pp collisions for 7 TeV and 2.76 TeV are shown in Fig. 10.1. They are again obtained with parameterizations of the neutral pion
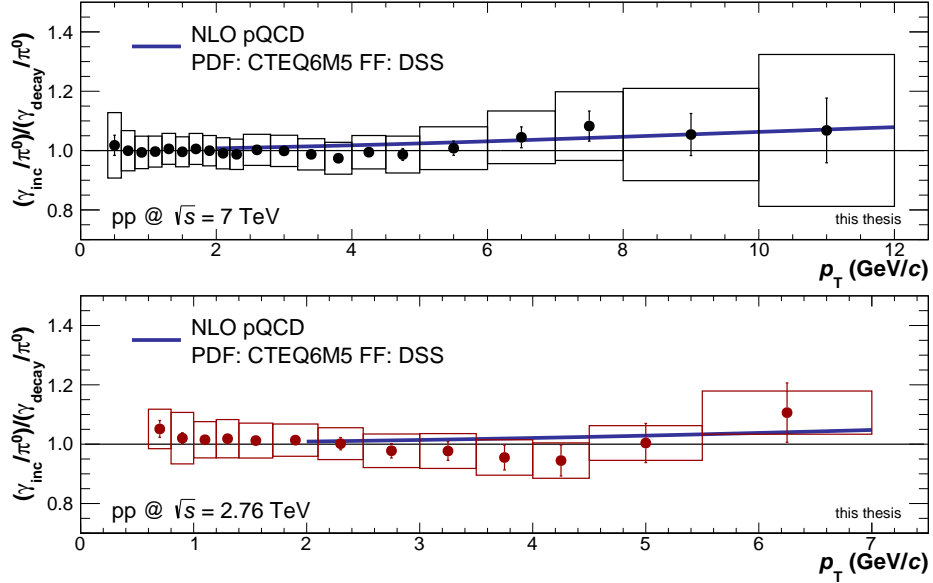
Figure 10.1: Direct-photon excess ratios R_γ for pp at 7 TeV and 2.76 TeV. In addition, a NLO pQCD prediction is shown, following [233]. It is recalculated to a ratio representation with Eq. (10.2).

spectra. Similar ratios with measured π^0 spectra can be found in appendix C. Both ratios in Fig. 10.1 are in agreement with unity and no significant direct-photons excess is found for pp collisions.

For comparison with NLO pQCD calculations, predictions following [233] are plotted. The width of the blue band represents the uncertainty of the prediction arising from the p_T scale used in the calculation. The scale is set to $\mu = 0.5\,p_T$, $\mu = 1.0\,p_T$ and $\mu = 2.0\,p_T$, respectively. The calculations are based on the concepts introduced in Sec. 4.1.1. Such calculations are normally provided as direct-photon spectra. For a comparison with the excess ratios, the theory spectra $\gamma_{\text{direct,NLO}}$ are reformulated:

$$R_{\gamma,\text{pQCD}} = 1 + \left(N_{\text{coll}} \cdot \frac{\gamma_{\text{direct,NLO}}}{\gamma_{\text{cocktail}}^{\text{decay}}}\right). \tag{10.2}$$

Within uncertainties, the measured ratios agree with the prediction.

The number of binary collisions becomes a crucial quantity in case of Pb–Pb collisions. Here the number depends on the centrality of the events and is normally extracted with Monte Carlo Glauber calculations. The provided NLO pQCD calculations are always available as cross sections for $N_{\text{coll}} = 1$. They have to

be scaled accordingly before comparing to the measured ratios. The numbers estimated by the ALICE collaboration can be found in [172]. For the presented centrality bins, the numbers are additionally quoted in Tab. 10.1.

Centrality Bin	N_{coll}	(syst %)
pp	1	-
0-20%	1210.9	(11.0)
0-40%	824.7	(10.0)
20-40%	438.4	(9.7)
40-80%	77.2	(8.0)

Table 10.1: Number of binary collisions N_{coll} taken for the normalization of the pQCD NLO predictions. [172]

The excess ratios for Pb–Pb in the centrality bins 0-20%, 0-40%, 20-40% and 40-80% are shown in Fig. 10.2. To focus on the low p_{T} part, where thermal photons are expected, the ratios are plotted with a logarithmic abscissa. The ratio for the peripheral events is comparable with the pp results. In the semi-central centrality class, a small enhancement compared to the peripheral result is measured. The growing enhancement towards central events becomes more obvious if the two central classes are considered. For them, a clear enhancement above unity is found at low p_{T}.

For Pb–Pb, three different NLO pQCD predictions are available. The first calculation is identical to the 2.76 TeV prediction for pp and again plotted as a blue band. The only difference is the scaling with the number of binary collisions. In addition, two predictions taken from [90] are shown. They are obtained by JETPHOX calculations and are plotted as filled blue areas. They differ by the used Parton Distribution Functions. One setup is obtained with the CT10 proton PDF (dark blue), the second with the EPS09, a nuclear PDF (light blue). For both results, the BFG2 Fragmentation Function is assumed. The proton PDF results are slightly larger than the nPDF results. Within the given uncertainties, originating for the JETPHOX calculations from the PDF, all predictions agree.

The high p_{T} part ($> 4\,\text{GeV}/c$) is well described by the QCD predictions for all centralities. For peripheral and semi-central events, the low p_{T} part is consistent with unity and, therefore, with an extrapolated NLO curve. For central events, the ratio is clearly not described by the pQCD predictions at low p_{T}, indicating an additional source of photons. These photons are most likely produced by the thermal production mechanisms discussed in Sec. 4.2.
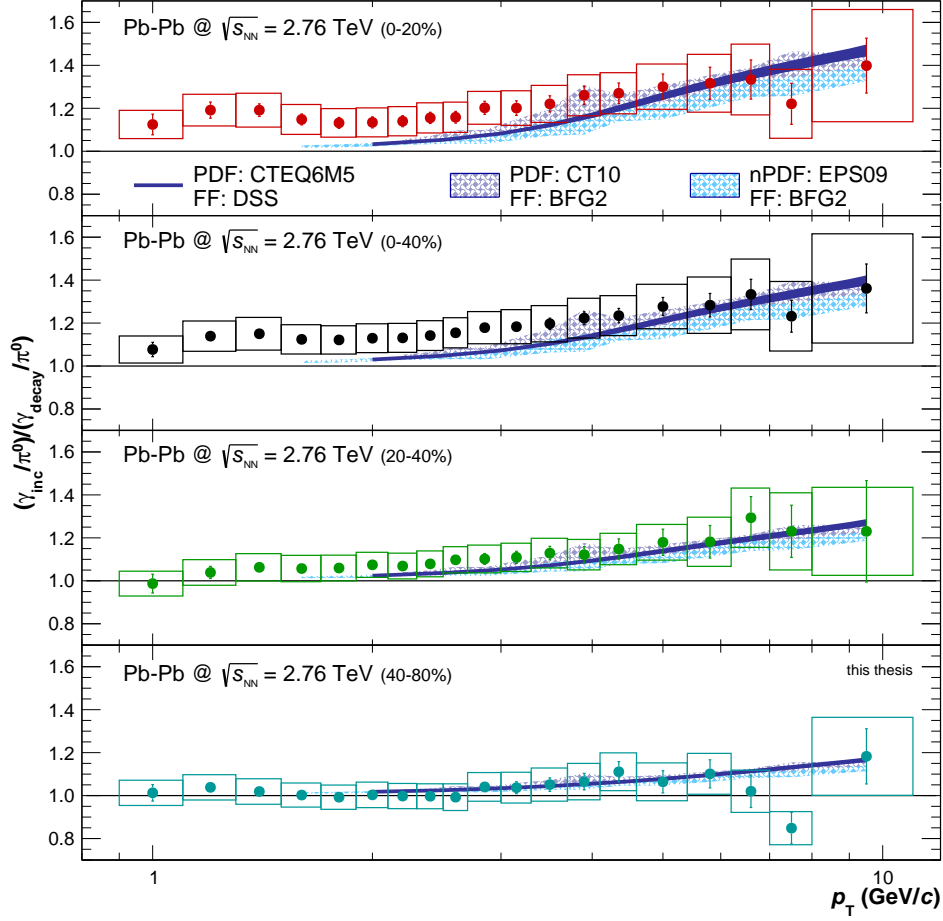
Figure 10.2: Direct-photon excess ratios R_γ for Pb–Pb at 2.76 TeV in the centrality bins 0-20%, 0-40%, 20-40% and 40-80%. Additionally, three scaled NLO pQCD calculations are shown [90,233]. All are recalculated to ratio representations with Eq. (10.2).

10.2 Direct-Photon Spectra

From the direct-photon excess ratios, the direct-photon spectra (γ_{direct}) can be extracted. For this purpose, the formula

$$\gamma_{\text{direct}} = \gamma_{\text{inc}} - \gamma_{\text{decay}} = \left(1 - \frac{1}{R_\gamma}\right) \cdot \gamma_{\text{inc}} \tag{10.3}$$

is applied.

In pp collisions, no significant data points are found for both analyzed energies. Combined with the large systematic uncertainties, the signal size is too small.

In general, the uncertainties of the direct-photon spectra are dominated by the excess ratios. By construction, the size of the direct-photon fraction is given by $\left(1 - \frac{1}{R_\gamma}\right)$. Therefore, the estimated systematic uncertainties in pp are magnitudes larger than the signal size. For both analyzed pp energies, only upper limits are extracted. They are defined as a 95% confidence level of the corresponding data point.

The resulting upper limits for pp collisions are shown in Fig. 10.3. As found for the
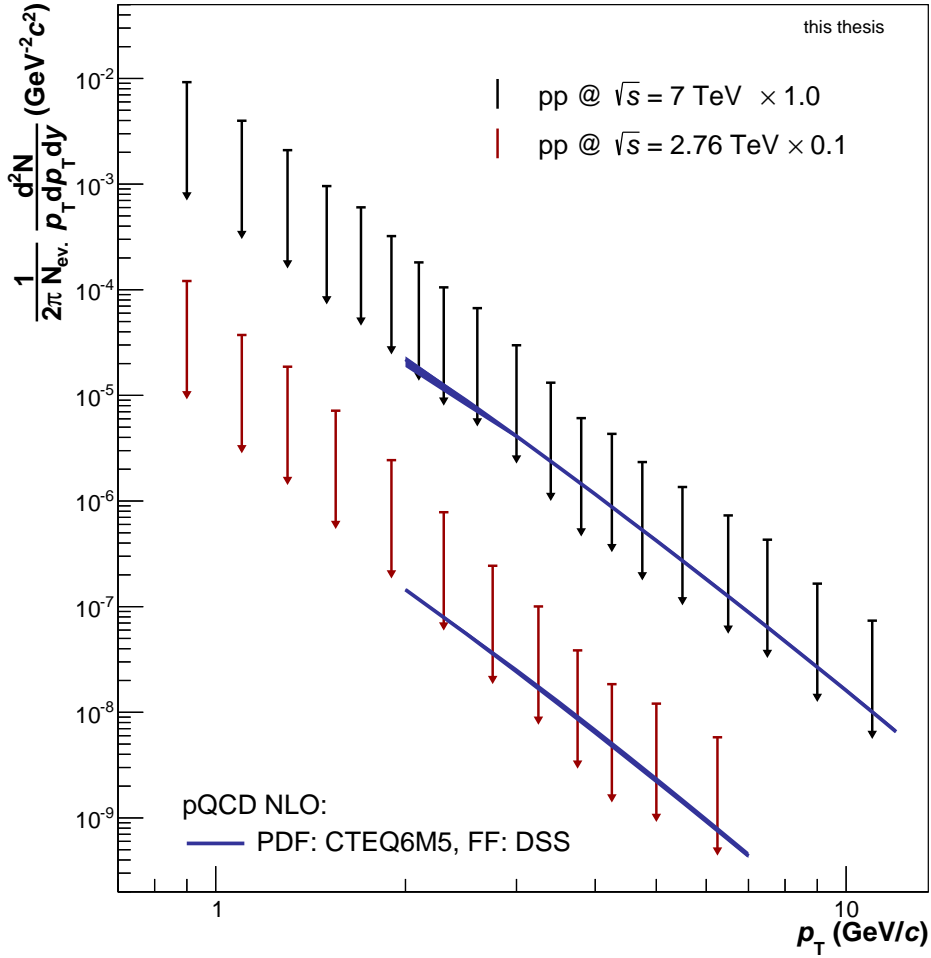
Figure 10.3: Direct-photon 95% confidence upper limits for pp at 7 TeV and 2.76 TeV. In addition, an NLO pQCD prediction is shown. [233]

excess ratios (Fig. 10.1), the spectra agree with the NLO pQCD predictions [233]. Apparently, the discrepancy to a prediction extrapolated to zero p_T seems to grow

towards lower momenta. This delusion can be explained by the upper-limit values that are in this momentum region magnitudes larger than the signal size.

In Fig. 10.4, the direct-photon spectra for Pb–Pb collisions are shown. As for pp
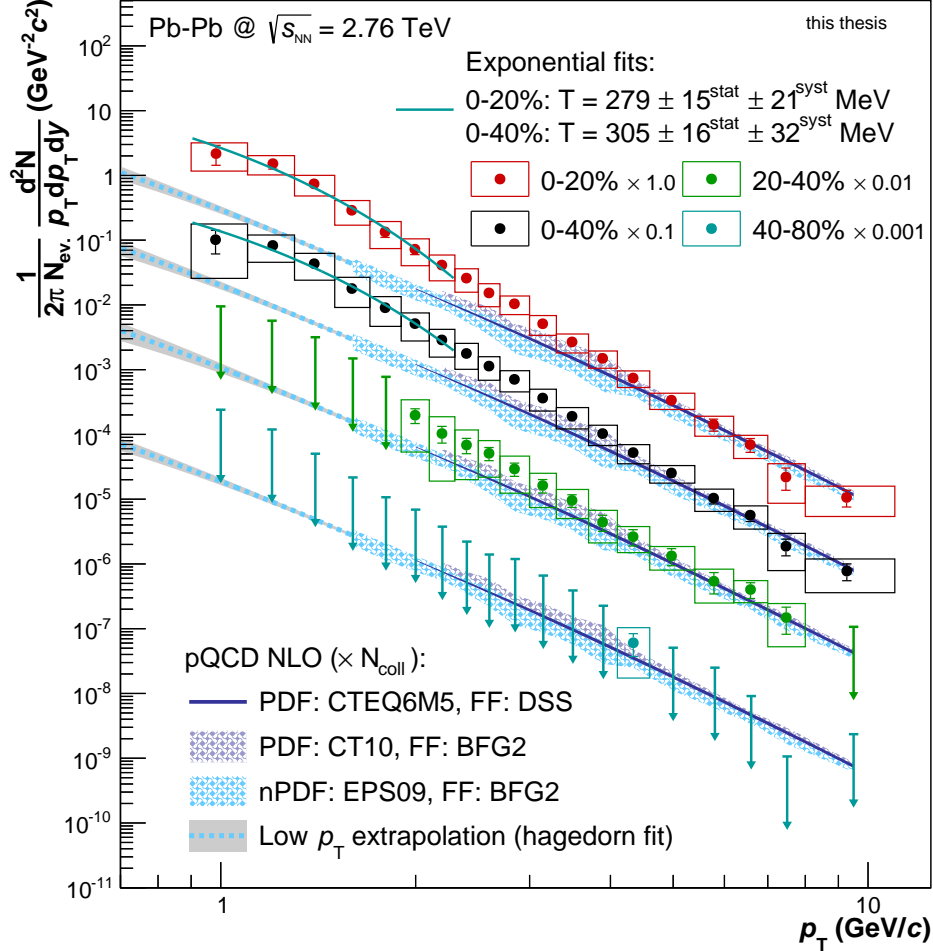
Figure 10.4: Direct-photon spectrum for Pb–Pb collisions at $\sqrt{s_{NN}} = 2.76\,\text{TeV}$. The two central event classes are fitted with an exponential function. In addition, three NLO pQCD predictions are shown [90, 233]. The EPS09 prediction is extrapolated with a Hagedorn fit towards zero momentum.

collisions, nearly exclusively upper limits can be extracted for peripheral events. In semi-central events, direct-photon data points are calculated for $p_T = 2\,\text{GeV}/c$. For comparison with preliminary results [234], the 0-40% bin is shown additionally. For the two central bins, data points are available in the full measured p_T range.

All spectra agree at high p_T with the N_{coll} scaled NLO predictions. They are

identical to the predictions shown for the excess ratios (Fig. 10.2) [90, 233]. To be able to compare the spectra at low momenta, the EPS09 prediction is extrapolated towards zero momentum. For that purpose, a Hagedorn parameterization (Eq. (9.2)) is used. As discussed in [221], the parameterization should result in a reasonable prediction for the spectral shape of particles at low p_T. The measured direct-photon spectra for central events clearly disagree with the extrapolation.

If the low momentum enhancement is caused by thermal radiation, theory predicts an exponential shape of the leading order contribution (Eq. (4.8)). Therefore, the two results for central events are fitted with an exponential function in the region $0.9\,\mathrm{GeV/c} < p_T < 2.3\,\mathrm{GeV/c}$ where thermal photons dominate. The resulting inverse slope parameters should be related to the average effective production temperature of the thermal photons producing medium. The fits result in $T_\mathrm{eff}^{0-20\%} = 279 \pm 15^\mathrm{stat} \pm 21^\mathrm{syst}\,\mathrm{MeV}$ for the 0-20% bin and $T_\mathrm{eff}^{0-40\%} = 305 \pm 16^\mathrm{stat} \pm 32^\mathrm{syst}\,\mathrm{MeV}$ for the 0-40% bin. Within their uncertainties, both slopes agree. The 0-40% value is nearly identical to the value quoted previously ($T_\mathrm{eff}^{0-40\%} = 304 \pm 51^\mathrm{stat+syst}\,\mathrm{MeV}$) in [234]. The values are dominated by the slopes of the inclusive-photon spectra. The excess ratios are rather flat and do not strongly influence the slope.

The assumed exponential shape of the total direct-photon spectrum is distorted for various reasons. The first reason, which can be removed, is the additional contribution of prompt photons. Prompt photons are the only expected contribution of direct-photons in pp collisions and should follow a point-like scaling. The corresponding contribution in Pb–Pb collisions can hence be removed by subtracting the N_coll scaled pp result. Since no significant measurement is available, a pQCD prediction for prompt-photons is subtracted instead. For that purpose, the extrapolated EPS09 calculation is chosen. The resulting spectra are shown in Fig. 10.5. The subtraction is only applied for the two central event classes. As systematic uncertainties below the predicted momentum values, the relative uncertainties of the lowest available p_T bin is taken. As uncertainty arising from the fit, a 95% confidence interval is added in quadrature. The interval is indicated by the grey band in Fig. 10.4.

After subtraction, the spectra are again fitted with an exponential. Without the prompt-photon contribution, the inverse slope parameter is reduced by $16\,\mathrm{MeV}$ in both centrality bins. The new slope values are $T_\mathrm{eff}^{0-20\%} = 263 \pm 17^\mathrm{stat} \pm 37^\mathrm{syst}\,\mathrm{MeV}$ and $T_\mathrm{eff}^{0-40\%} = 289 \pm 18^\mathrm{stat} \pm 47^\mathrm{syst}\,\mathrm{MeV}$, respectively.

Still, no exact exponential shape is expected. Only the leading order production mechanisms of thermal photons should follow an exponential. The magnitude and shape of the higher order photon production is unknown. Furthermore, the
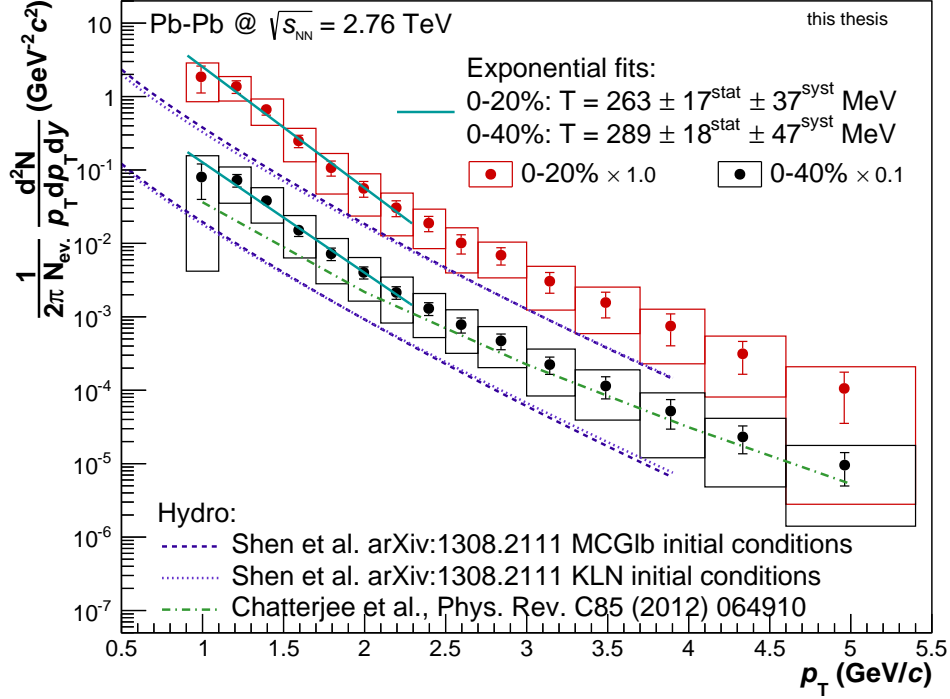
Figure 10.5: Direct-photon spectra with subtracted pQCD NLO contribution. The cal-
culations are obtained from [90] and extrapolated to zero momentum with
a Hagedorn parameterization Eq. (9.2). The thermal-photon predictions
are taken from [235, 236].

exponential might be distorted by photons from jet-medium interactions not con-
sidered in the calculations. These are expected at intermediate p_T and might have
a sizable effect on the direct-photon spectrum.

The extracted inverse slope values are only average effective temperatures. As
discussed in Sec.3.2, the photons are not emitted at a constant temperature. The
medium evolution might have a complicated non-linear temperature and flow evo-
lution. The photon momentum is blue-shifted by the flow according to Eq. (3.2),
depending on the transverse flow at production time.

For further theory comparisons, two (2+1)-hydrodynamic predictions are plot-
ted [235, 236]. Chatterjee et al. [235] (only available for 0-40%) are able to re-
produce the thermal-photon spectrum within uncertainties. Still, the prediction
is systematically below the data points. Shen et al. [236] are not able to describe
the magnitude of the measured spectra. The discrepancy between the two indicate
the difficulties of thermal-photon predictions. More predictions exist [237–239].
They all are in fair agreement with the data. For a hydrodynamic calculation,

the time evolution of the medium has to be parameterized, and an appropriate equation of state is required. The initial conditions at which the hydrodynamic evolution starts are unknown, including the existence and size of primordial flow and photons. In addition, the phase transition from the QGP to the HHG has to be modeled. A crucial point are the assumed production rates of photons in both phases. For the plasma, a common set of rates [240] is normally used. It again includes only leading order contributions extended by photon Bremsstrahlung. Many additional modifications are considered by the different groups. The most important are fluctuating initial conditions (hot spots) and viscous corrections to the medium evolution.

An alternative representation of classifying the differences in pp and Pb–Pb is given by the nuclear modification factor R_{AA}. The concept of R_{AA} is introduced in Sec. 3.3. It parameterizes the difference between pp and Pb–Pb spectra under the assumption of point-like scaling. The resulting direct-photon nuclear modification factors are shown in Fig. 10.6. As an additional uncertainty, the freedom arising from the chosen QCD scales is plotted. All three modifications factors are in
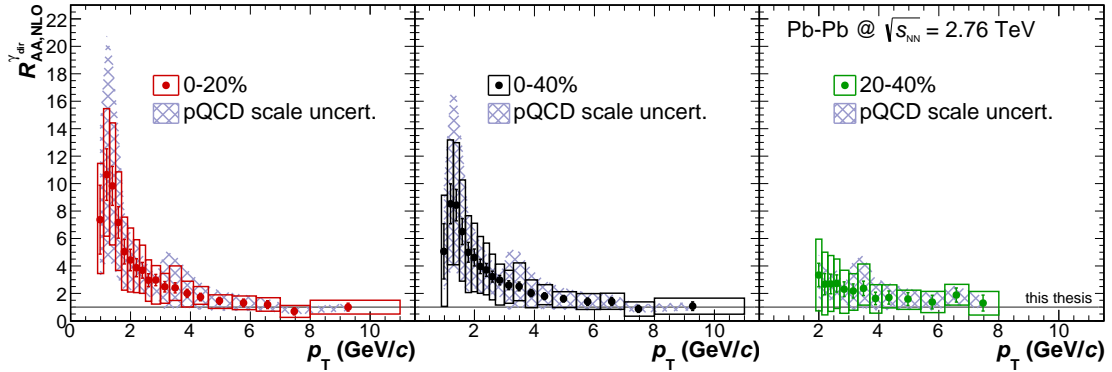
Figure 10.6: Direct-photon R_{AA}. Since no significant pp at 2.76 TeV measurement exists, the extrapolated nuclear PDF JETPHOX calculation [90] is used instead. In addition, the uncertainties arising from different scales are shown.

agreement with unity above $4\,\mathrm{GeV}/c$. This indicates the validity of binary scaling for the hard direct-photon component. The observation agrees with the high p_T isolated photon results obtained by CMS and ATLAS [76, 96] and extends the finding towards intermediate momenta for LHC energies. At low momenta, where thermal photons are expected, the R_{AA} for the most central event classes are enhanced up to a factor of 8-10. In the semi-central 20-40% bin, no significant measurement exists for the thermal region ($p_T < 2\,\mathrm{GeV}/c$).

10.3 Systematic Uncertainties

In this section, the systematic uncertainties of the direct-photon analysis are discussed. The focus is hereby on the direct-photon excess ratio and on the inclusive-photon spectrum. The ratio dominates the final systematic uncertainties of all direct-photon results.

Nearly all individual components of the uncertainties are estimated by comparing the standard result, obtained with the standard method, to a deviating result obtained under slightly alternative conditions. The idea of the method is to sample the underlying probability distributions of the tested modification. The only exception is the uncertainty of the material budget. It has a p_T independent and ALICE specific value.

The individual contributions to the systematic uncertainty of the direct-photon analysis are:

ALICE Material Budget
The budget of the ALICE detector material acting as a photon converter is not perfectly known. Nevertheless, this quantity is crucial for the estimation of the conversion probability based on Monte Carlo simulations. In [212], the uncertainty of the material is estimated. The resulting discrepancy between simulation and experiment is found to be 4.5%. In this uncertainty, the variation of the (pseudo-)rapidity range is included. It also contains the uncertainty arising from different event generators is contained.

This number is directly added to the uncertainty of the inclusive-photon spectra. Since two converted photons are required for the neutral pion analysis, the uncertainty is doubled in this case. In the inclusive-photon to π^0 ratio, the uncertainty is canceled out for one of the converted photons. Thus, the uncertainty on the ratio is again only 4.5%.

Monte Carlo Efficiency and Purity Correction
The uncertainty arising from the non-perfect description in the Monte Carlo of the tracking, V0 finding and of photon characteristics is considered by the variation of the selection criteria introduced in Sec. 7.2. By varying these selections, the estimated efficiencies and purities from simulation will change along with the measured raw photon spectrum. In case of an ideal description by the simulation, the final fully corrected spectra (inclusive photon and π^0) will remain unchanged. Vice verse, a deviating result indicates a source of systematic uncertainty.

To be able to handle the underlying uncertainty distribution, each single criterion is varied twice. Once it is varied towards a tighter and once towards a more relaxed value. If the standard value is already on a maximum or minimum, it is varied twice in one direction. The resulting final uncertainty is defined as the mean of the positive and negative deviations for each p_{T} bin.

The final systematic uncertainty is derived by quadratically adding up the individual contributions. Since the effects of nearly all variations will act on the neutral meson and on the inclusive-photon spectrum in the same direction, the uncertainties are expected to cancel partially in the photon over π^0 ratio. To benefit from this cancellation, the uncertainties are also directly calculated on the level of this ratio.

The final uncertainty is the sum of many individual contributions. The uncertainties are summarized in several groups:

- Track Selection: In this uncertainty, all cuts acting on the track properties are summarized. These are the minimum electron/positron momentum cut, the requested minimum number of findable TPC clusters and the minimum conversion radius required for the analysis.

- PID Selection: Here the TPC $\mathrm{d}E/\mathrm{d}x$ for charged pion rejection and electron/positron selection enter. In case of Pb–Pb collision, the TOF selection is also included in this uncertainty.

- Photon Selection: All selection criteria based on the properties of converted photons are summarized at this point. These are the minimum q_{T}, the χ^2/ndf and the Ψ_{pair} cut.

All variations used for the uncertainty estimation are given in Tab. 10.2. The standard values are listed additionally. For most cases, they are identical for all analyzed collision systems. Only the TPC based criteria differ between Pb–Pb and pp collisions. Also, the TOF cut was only applied for Pb–Pb.

Signal Extraction
The raw neutral pion yield is obtained via integration of the background-subtracted invariant mass peaks. Residual background might bias the yield. An opposite bias might occur from a too small integration window. To include these effects, the integration window is varied in size. The standard interval is set to [0.1,0.145] GeV but is shifted by the difference of the reconstructed π^0 peak position and the theoretical value. The two alternative ranges are [0.08,0.16] GeV and [0.12,0.14] GeV, respectively. An additional effect on the π^0 signal extraction is caused in Pb–Pb by the α_{π^0} cut. Its uncertainty is handled like the other selection criteria but added to the signal extraction uncertainty.

Selection Criterion	Std. Value	Variation A	Variation B
Track Selection			
min $-$ max R_{conv}	$5\,\mathrm{cm} - 180\,\mathrm{cm}$	$2.8\,\mathrm{cm} - 180\,\mathrm{cm}$	$7.5\,\mathrm{cm} - 180\,\mathrm{cm}$
min track p_{T}	$50\,\mathrm{MeV}/c$	$75\,\mathrm{MeV}/c$	$100\,\mathrm{MeV}/c$
findable cluster ratio	$> 60\%$	$> 35\%$	$> 70\%$
PID Selection			
accepted TPC $\mathrm{n}\sigma_{e\pm}$	-3, 5	-2.5, 4	-5, 5
rejected TPC $\mathrm{n}\sigma_{\pi\pm}$	pp: -10, 1	-10, 0.5	-10, 3
	Pb–Pb: -10, 3	-10, 2.5	-10, 3.5
accepted TOF $\mathrm{n}\sigma_{e\pm}$	Pb–Pb: -5, 5	-2, 3	-3, 5
Photon Selection			
Kalman filter χ^2/ndf	30	20	50
Armenteros q_{T} (GeV/c)	0.05	0.03	0.07
pair cut ψ_{Pair} (rad)	0.05	0.035	0.1

Table 10.2: Selection criteria variations used for the systematic uncertainties arising from a non-perfect event and reconstruction description by the simulation.

Also included is the uncertainty arising from the pileup rejection discussed in Sec. 7.4 for photons and in Sec. 8.2.1 for neutral pions. Like the Monte Carlo related uncertainties, the effect of the pileup is partially canceled by building a ratio of the two individual spectra. To have a conservative estimate of the uncertainties of the effect, half of the correction size is taken.

Decay-Photon Cocktail

The last set of uncertainties is related to the cocktail calculation. It is only relevant for the excess ratios and the direct-photon spectra. The first uncertainty is the unknown normalization size of the particle spectra used by the cocktail. Here the η and ω spectra are varied by 10% in its total size. This uncertainty is also used in case of measured η and ω spectra to cover the normalization uncertainties of the measurement.

In Pb–Pb, the shape of the η spectrum is not known. As discussed in Sec. 9.2, three different methods are used to estimate the shape of the η to π^0 ratio in Pb–Pb. With a measured π^0 spectrum, this method also constrains the shape of the η spectrum. The maximum difference in the total cocktail by using the three methods is taken as an uncertainty. As the default decay cocktail, the mean of all three methods is used.

In general, the cocktail is based on a fit to the π^0 spectrum. The same fit is used in

the γ to π^0 ratio as a replacement for the neutral meson spectrum. This fit might be biased by the statistical fluctuation of the spectra. To have a handle on the bias, the charged pion spectrum is used for $p_T > 3\,\mathrm{GeV}/c$ where the fluctuations in the π^0 spectrum become sizable. From this, an alternative cocktail is calculated and used with the corresponding fit. The difference of the two methods is added to the uncertainties.

The resulting relative uncertainties of the inclusive-photon spectra and of the direct-photon excess ratios are shown in Fig. 10.7 for pp collisions. Identical
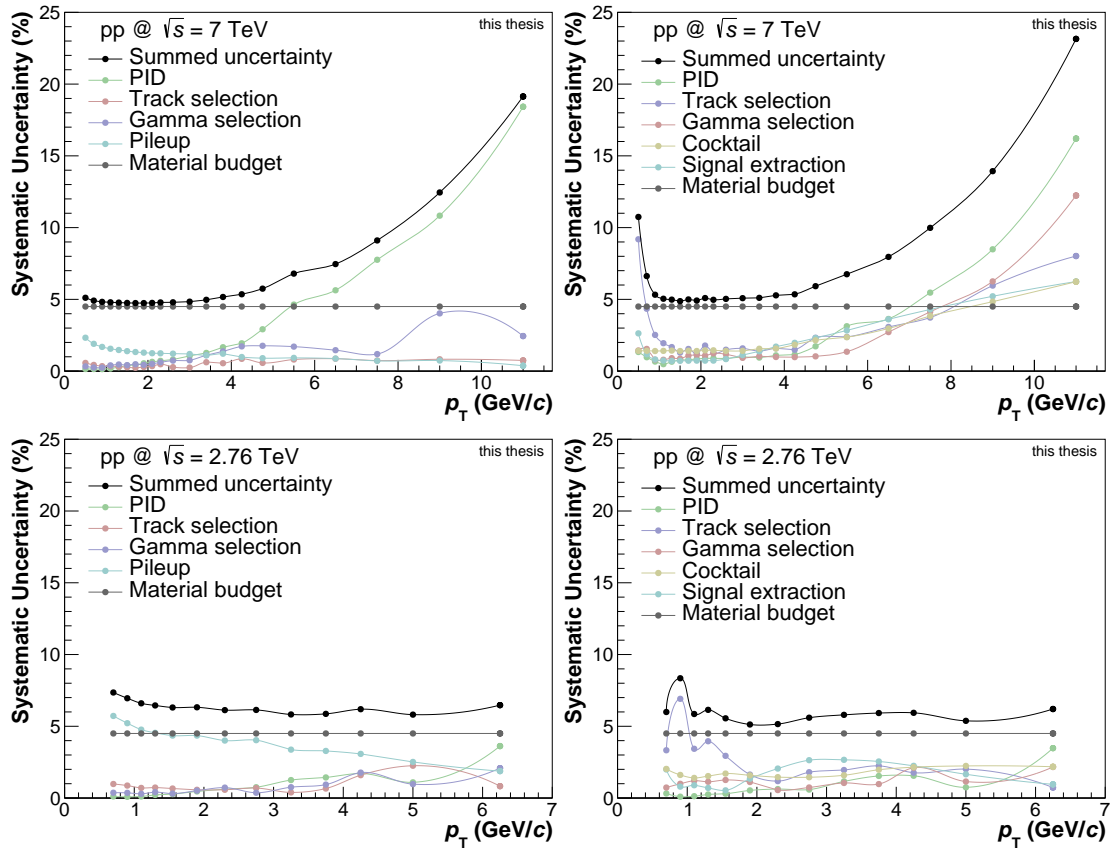
Figure 10.7: Inclusive photon (left) and direct-photon excess ratio systematic uncertainties (right) for pp collisions.

figures for the Pb–Pb analysis are shown in Fig. 10.8. The centrality bin 0-40% is not shown. For this bin, all uncertainties based on the PID, photon and track selection are identical to the 0-20% class. All further uncertainties of those two bins are similar.
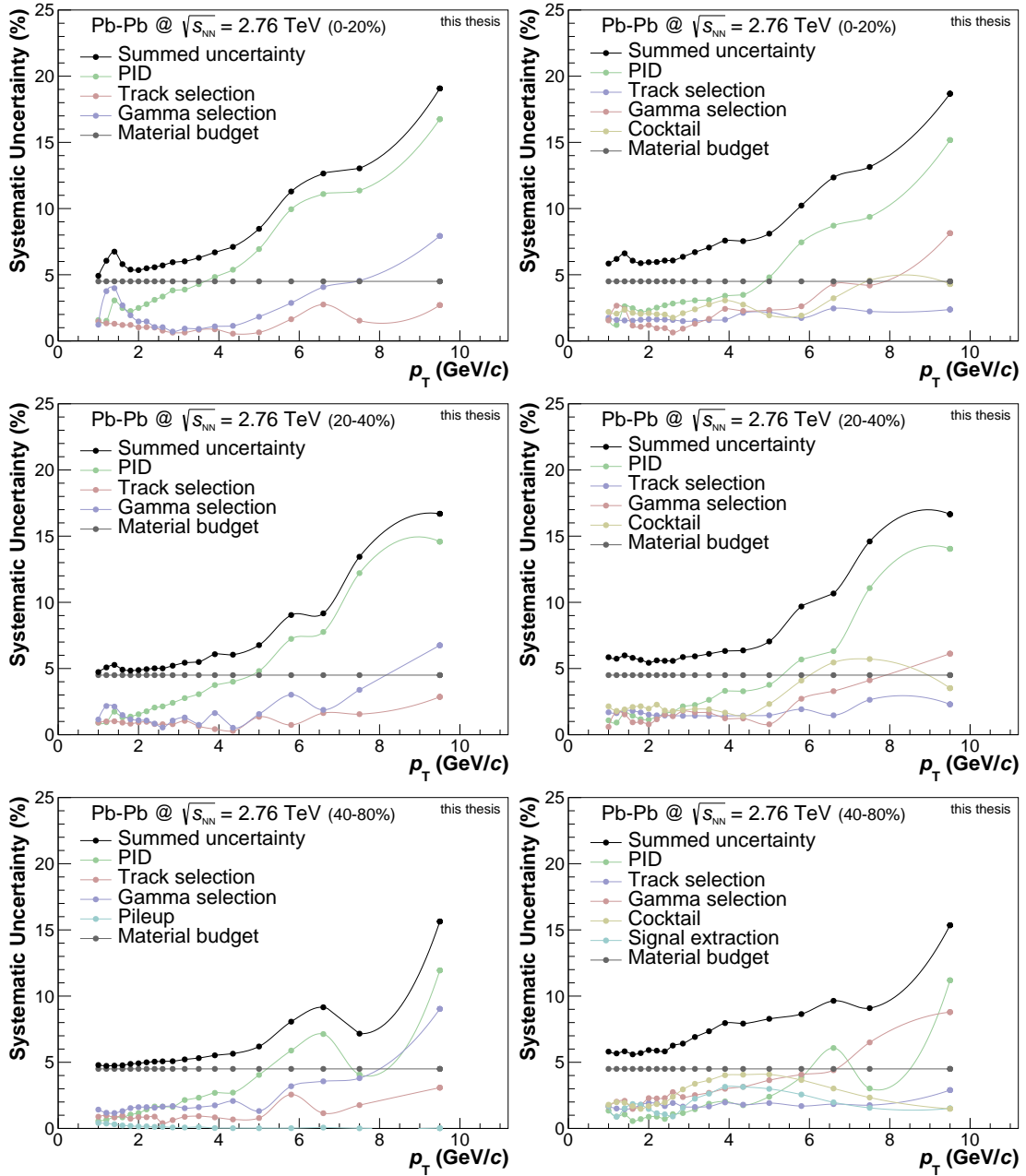
Figure 10.8: Inclusive photon (left) and direct-photon excess ratio systematic uncertainties (right) for Pb–Pb collisions.

At low p_T, the dominating systematic uncertainty of the spectra and of the ratios is the material budget. A better defined material would strongly reduce the total systematic uncertainty. For Pb–Pb and pp at 7 TeV, it is replaced for $p_T >$

4.5 GeV/c by the uncertainties originating from the PID. Here the dominating contribution is the charged pion rejection with the TPC. In this momentum region, the energy loss of electrons/positrons and charged pions becomes similar. In general, the systematic uncertainties grow with increasing momenta.

For pp collisions at 2.76 TeV, the inclusive-photon spectrum uncertainty is also dominated by the material budget and, at low p_{T}, by the pileup contribution. For all measurements which include pileup (pp, 40-80%), the corresponding uncertainty is nearly canceled out in the excess ratios. The inclusive photon and π^0 spectra have similar uncertainties and deviation caused by pileup. The 2.76 TeV results depend, in contrast to the other energies, only weakly on the PID selection. One reason is the smaller p_{T} range of the analysis. A second reason are updated reconstruction parameters used for data and simulation.

10.4 Direct-Photon Flow Puzzle

It is often stressed that the inverse slope parameter T_{eff}, as extracted in Sec. 10.2, is a measure for the average production temperature of thermal photons. Its value is clearly larger than the critical temperature T_c of the QGP phase transition. Consequently, the main contribution of thermal photons is expected to be produced in the plasma phase.

From hydrodynamic calculations, an initial QGP temperature T_i can be extracted. This temperature corresponds to the temperature of the system after the completion of thermalization. In order to deduce the initial temperature, hydrodynamic calculations and their initial conditions are tuned to describe the measured direct-photon yield. In [239], a value of $T_i = 546$ MeV is found. Here, a very rapid thermalization with $\tau_i = 0.1$ fm/c is assumed. A very similar value is extract in [238]. They quote a value of $T_i = 550$ MeV, but with a much larger thermalization time of $\tau_i = 0.6$ fm/c. Therefore, the initial average energy density at $\tau = 0$ might be substantially different in both cases.

The idea of a QGP dominated thermal-photon production is contradicted by elliptic flow measurements of direct photons. Such measurements for v_2 are available for ALICE [241] and PHENIX [242] data. Both experiments extract very similar results of direct-photon elliptic flow. The LHC results are shown in Fig. 10.9. The elliptic flow of direct photons is non-zero and only slightly smaller than the flow of light hadrons (Fig. 3.5). For comparison, two different hydrodynamic calculations are shown. They are strongly related to the prediction for the thermal-photon spectra shown in Fig. 10.5. There it was found that Chatterjee et al. are able to
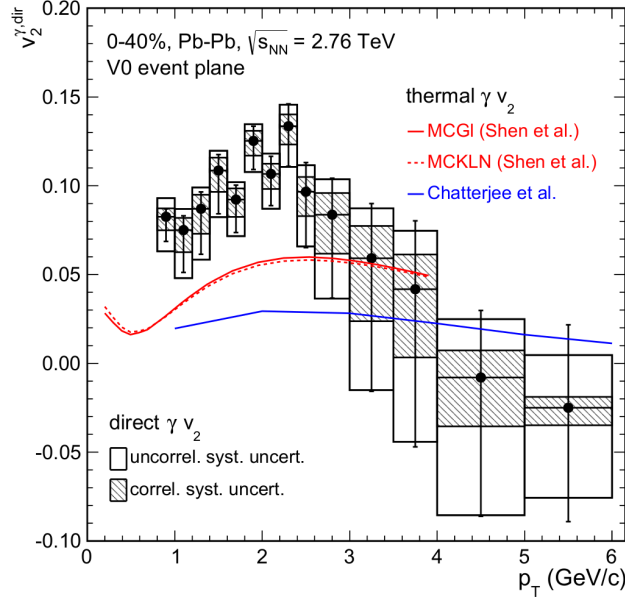
Figure 10.9: Elliptic flow of direct photons measured in 0-40% Pb–Pb collisions with ALICE. For comparison, two hydrodynamic calculations are shown [236, 243]. The plot is taken from [244].

describe the magnitude of the spectrum. In contrast, it is clearly under-predicted by Shen et al. For direct-photon flow, this finding is nearly reversed. Still, both are not able to reproduce the v_2.

Chatterjee et al. use a much smaller thermalization time of $\tau_i = 0.14\,\mathrm{fm}/c$ compared to Shen et al. $(0.6\,\mathrm{fm}/c)$. Thus, the flow has more time to develop and is built up more slowly. As discussed in Sec. 3.2, the flow of photons is fixed at production time. Therefore, the less flowing early QGP phase contributes stronger to the direct-photon v_2, resulting in a smaller total flow. On the other hand, this additional amount of direct photons results in a better description of the spectrum.

Shen et al. have larger relative contributions from the later stages where the flow is already stronger. Naturally, they are better suited to describe the large measured flow values but fail to describe the spectrum. This inconsistency, inherent in all hydrodynamic models, is often referred to as "direct-photon flow puzzle".

A very important part for solving the puzzle is the blue-shift of the photon momenta and the related increase of the effective temperature T_{eff}. The size of the shift depends on the radial flow and is given by Eq. (3.2). By assuming an average of $\beta_r = 0.3 - 0.4$ and homogeneous photon production rates a temperature of $T \approx 160 - 200\,\mathrm{MeV}$ is derived from ALICE result of $T_{\mathrm{eff}} \approx 300\,\mathrm{MeV}$. This simple

consideration already shows that the true medium temperature is clearly below the values indicated by the effective slope.

More advanced studies are performed in [245]. In Fig. 10.10, the photon production versus the temperature T of the medium is shown. The temperature
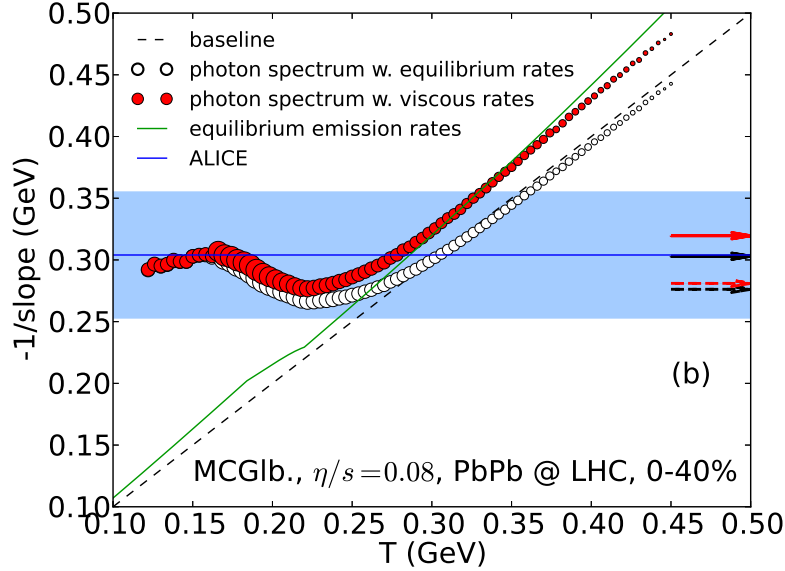
Figure 10.10: Inverse slope parameter as extracted by an exponential fit to measured thermal-photon spectra plotted against the temperature T of photon producing cells. [245]

corresponds to a cell, the small volume that produces the photon within the hydrodynamic model. The magnitude of the production rate is expressed as the size of the white (equilibrium rates) and red circles (viscous rates). The slope value measured by ALICE [234] is given as the blue band.

At very high temperatures, no radial flow is yet developed and the produced photons follow a slope similar to the cell temperature. The true cell temperature is given as the green line. At lower temperatures, flow starts to develop. The measured photon momenta are blue-shifted and the slope is larger than the cell temperature. At $T \sim 220\,\mathrm{MeV}$, the effect of the decreasing temperature is even overcompensated leading to increasing effective temperatures with decreasing cell temperature. In this region, the photon production is found strongest in the model. At freeze-out ($T \sim 160\,\mathrm{MeV}$) the blue-shift is saturated and the slope drops with decreasing medium temperature. The colored arrows on the right side of the plot shows resulting inverse slope parameters. They are all within the uncertainties of the measurement.

It can be concluded that blue-shift has to be clearly considered for the solution of the puzzle. As shown by Shen et al. in [245] the dynamic evolution of the thermalized medium has to be taken carefully into account before drawing conclusions from direct-photon slope measurements. Nevertheless, also in this publication they are, like all hydrodynamic calculations, not able to describe the direct-photon spectrum and the elliptic flow within one consistent model. Both discrepancies would be naturally cured if the photon rates of the strongly flowing hadronic phase would be enhanced. No justification for this has yet been found.

Summary

In this thesis, the measurement of direct photons in ultra-relativistic proton-proton and lead-lead collisions was presented. Photons, as penetrating probes, make a substantial contribution to the investigation of the quark-gluon plasma and the subsequent hot gas phase. The pp measurement, important on its own for a deeper understanding of hard scatterings, provides an important base-line for the Pb–Pb results. The analyzed data in pp and Pb–Pb was collected by the ALICE experiment at the Large Hadron Collider at CERN. The center-of-mass energies of the proton-proton collisions were $\sqrt{s} = 2.76\,\mathrm{TeV}$ and $7\,\mathrm{TeV}$, respectively. For the lead-lead data the energy $\sqrt{s_{\mathrm{NN}}} = 2.76\,\mathrm{TeV}$ per nucleon pair was available.

The presented analysis is based on a statistical subtraction method. In this method, the decay-photon background is subtracted from the inclusive-photon measurement, containing decay and direct photons. The background is estimated from spectra of hadrons that decay into photons. Since the most dominant background contribution originates from neutral pions, their measurement is explicitly part of this thesis. The most important advantage of the chosen method is the aptitude of measuring direct photons down to low momenta.

The only expected source of direct-photons in pp collisions are the initial interactions of the colliding nucleons. These photons are called prompt photons. The corresponding prompt photon over decay-photon ratio for the transverse momentum range presented in this thesis is small. Therefore, only upper limits for direct-photon production could be extracted for both analyzed pp center-of-mass energies. The signal size is within its systematic uncertainties also in agreement with no produced direct photons. Nevertheless, in a comparison of the results with theoretical predictions of next-to-leading order pQCD, a good agreement is found. This strengthens the current picture of the absence of additional relevant sources of direct photons in pp collisions besides those calculated with pQCD.

A maybe even more important reason for the study of direct photons is the exploration of ultra-relativistic heavy-ion collisions. As in pp collisions, prompt photons are produced during the initial collisions of the participating nucleons. Moreover, additional photons are produced during all stages of the subsequent evolution of the hot medium produced in the collision. Many measurements, like particle flow

or particle-number ratios, are in agreement with a thermal description and furthermore suggest a rapid thermalization of the quarks and gluons remaining in the overlap region of the nuclei. Consequently, photons that are expected to be produced by the medium are called thermal photons. Such photons should be the dominant source of direct photons at small transverse momenta.

In the analyzed heavy-ion data at larger values of photon transverse momentum ($p_{\mathrm{T}} \gtrsim 4\,\mathrm{GeV}/c$), a similar situation as for pp collisions was found. The results are again in good agreement with pQCD predictions, here scaled with the expected number of binary nucleon-nucleon collisions. These non-further modified photon spectra support a jet quenching caused predominately by strong medium interactions.

At smaller values of transverse momentum ($p_{\mathrm{T}} \lesssim 3\,\mathrm{GeV}/c$), a centrality dependent excess of direct photons was measured. Its total yield and relative size compared to the background show a decreasing trend from central to peripheral collisions. The excess is not explainable with prompt photons alone. To test if it is in agreement with a model predicted thermal-photon production, the prompt-photon component has to be subtracted. For that purpose, scaled pp data is commonly used, no hints of additional photon sources are found in this collision system. Since no significant measurement exists for LHC energies in pp at low momenta, an extrapolated pQCD prediction was subtracted instead.

The remaining photon p_{T} spectra have an exponential-like shape. Normally, the inverse slope parameter of an exponential fit is quoted for a classification of the thermal-photon production. The inverse slope is expected to be related to the effective average photon production temperature. The values extracted in this thesis are $T_{\mathrm{eff}}^{0-20\%} = 263 \pm 17^{\mathrm{stat}} \pm 37^{\mathrm{syst}}\,\mathrm{MeV}$ for the 0-20% most central events and $T_{\mathrm{eff}}^{0-40\%} = 289 \pm 18^{\mathrm{stat}} \pm 47^{\mathrm{syst}}\,\mathrm{MeV}$ for the larger centrality range of 0-40%. Due to radial flow, all measured direct-photon momenta are blue-shifted. Thus, the true production temperature should be smaller and should depend on the time profile of the size of the radial flow.

The measured spectra were furthermore compared to hydrodynamic model predictions for thermal-photon spectra. These models are able to reproduce the remaining spectra after the prompt-photon subtraction is applied. However, the theoretical predictions are at the lower bound of the systematic uncertainties of the results. For previous direct-photon measurements at smaller center-of-mass energies, a very similar situation was found. Therefore, signs are increasingly showing that a reweighing of photon production rates or even additional sources have to be considered for the description of low momentum direct photons in heavy-ion collisions. Moreover, with the current models is it impossible to describe the spec-

tra and the elliptic flow of direct photons at LHC and at RHIC within one closed approach. This situation is often summarized as the "direct-photon flow puzzle".

In conclusion, within the context of this thesis, a direct-photon signal in heavy-ion collisions at low and intermediate p_T has been measured for the first time at LHC. While the intermediate momentum range is in good agreement with pQCD, the low momentum part shows an excess over these predictions for central collisions. This excess is in qualitative agreement with the expectation from thermal production, but its overall magnitude poses a challenge to current theories.

Zusammenfassung

Diese Arbeit thematisiert die Messung von direkten Photonen in ultrarelativistischen Proton-Proton und Blei-Blei-Kollisionen. Als durchdringende Sonden liefern Photonen einen wichtigen Beitrag zur Erforschung des Quark-Gluon-Plasmas und der sich daran anschließenden heißen Gasphase. Die pp-Messung, welche für sich genommen wichtig für ein tieferes Verständnis von harten Streuungen ist, stellt eine existenzielle Vergleichsmessung dar. Die zugrunde liegenden Daten wurden mit dem ALICE Experiment am Large Hadron Collider des Forschungszentrums CERN genommen. Die Schwerpunktsenergien betrugen für Proton-Proton-Kollisionen $\sqrt{s} = 2.76\,\text{TeV}$ bzw. $7\,\text{TeV}$. Für die Schwerionenkollisionen stand eine Energie von $\sqrt{s_{\text{NN}}} = 2.76\,\text{TeV}$ pro Nukleonenpaar zur Verfügung.

Die Analyse basiert auf einem statistischen Subtraktionsverfahren. Bei dieser Methode wird der Zerfallsphotonenuntergrund von einer inklusiven Messung, bestehend aus direkten Photonen und Zerfallsphotonen, abgezogen. Der Untergrund wird dabei aus Spektren der in Photonen zerfallenden Hadronen berechnet. Da der dominierende Teil des Untergrundes aus Zerfällen von neutralen Pionen stammt, wurde die Messung diser explizit in die Arbeit aufgenommen. Der größte Vorteil der gewählten Methode ist, dass sie auch für kleine Impulse der direkten Photonen geeignet ist.

Die einzige erwartete Quelle von direkten Photonen in pp-Kollisionen ist die initiale Wechselwirkung der kollidierenden Nukleonen. Diese Photonen werden prompte Photonen genannt. Das zugehörige prompte Photonen-zu-Zerfallsphotonen-Verhältnis ist in dem in dieser Arbeit analysierten Transversalimpulsbereich klein. Als Folge dessen konnten nur obere Grenzen für die Produktion von direkten Photonen in beiden analysierte Schwerpunktsenergien bestimmt werden. Die Größe des Signals lässt sich somit ebenfalls ohne die Produktion von direkten Photonen erklären. Dennoch stimmen die gewonnenen Ergebnisse gut mit Vorhersagen der next-to-leading order pQCD überein. Dies stärkt das gegenwärtige Verständnis, dass keine weiteren relevanten Quellen für direkte Photonen in pp-Kollisionen, neben denen, die mit der pQCD berechnet werden können, existieren.

Ein vielleicht noch gewichtigerer Grund für die Untersuchung von direkten Pho-

tonen ist die Erforschung von ultrarelativistischen Schwerionenkollisionen. Wie in pp-Kollisionen werden auch hier prompte Photonen während der initialen Wechselwirkung der Nukleonen erzeugt. Jedoch werden zudem weitere Photonen während der gesamten zeitlichen Entwicklung des bei der Kollision erzeugten heißen Mediums produziert. Viele Messungen, z.B. der Teilchenfluss oder die Verhältnisse der Anzahl der erzeugten Teilchen, stimmen mit einer thermodynamischen Beschreibung überein und lassen darüber hinaus auf eine schnelle Thermalisierung der Quarks und Gluonen im Überlappbereich der Kerne schließen. Daher werden Photonen, die durch das Medium produziert werden, thermische Photonen genannt. Sie sollten den überwiegenden Anteil der Photonen bei kleineren Transversalimpulsen stellen.

In den analysierten Schwerionendaten wurde für größere Werte des Photonentransversalimpulses ($p_T \gtrsim 4\,\mathrm{GeV}/c$) eine ähnliche Situation wie in pp-Kollisionen vorgefunden. Die Resultate stimmen erneut gut mit den Vorhersagen der pQCD, nun skaliert mit der Anzahl der binären Nukleonenkollisionen, überein. Da darüber hinaus keine weitere Abweichung zu den pp-Resultaten gefunden wurde, unterstützt dies das Bild eines durch hauptsächlich starke Wechselwirkungen hervorgerufenen Energieverlustes von Jets im QGP-Medium.

Bei kleineren Werten des Transversalimpulses ($p_T \lesssim 3\,\mathrm{GeV}/c$) wurde ein zentralitätsabhängiger Überschuss von direkten Photonen gemessen. Sowohl der absolute Yield, als auch das relative Verhältnis zum Untergrund, zeigen einen abnehmenden Trend hin zu peripheren Kollisionen. Dieser Überschuss kann nicht allein durch prompte Photonen erklärt werden. Um zu testen, ob dieser mit von Modellen vorhergesagten thermischen Photonen erklärt werden kann, muss der Anteil der prompten Photonen subtrahiert werden. Dafür werden üblicherweise pp-Resultate verwendet, da hier keine Hinweise auf weitere Photonen neben prompten Photonen gefunden werden. Da keine signifikanten Resultate für LHC-Energien in dem relevanten Impulsbereich zur Verfügung stehen, wurde stattdessen eine zu niedrigen Impulsen extrapolierte pQCD-Rechnung verwendet.

Das verbleibende p_T-Spektrum hat eine exponentielle Form. Normalerweise wird zur Klassifizierung der thermischen Photonenproduktion die inverse Steigung eines exponentiellen Fits angegeben. Die inverse Steigung sollte mit der effektiven, durchschnittlichen Photonenproduktionstemperatur verknüpft sein. Die im Rahmen dieser Arbeit extrahierten Werte sind $T_{\mathrm{eff}}^{0-20\%} = 263 \pm 17^{\mathrm{stat}} \pm 37^{\mathrm{syst}}\,\mathrm{MeV}$ für die 0-20% zentralsten Kollisionen und $T_{\mathrm{eff}}^{0-40\%} = 289 \pm 18^{\mathrm{stat}} \pm 47^{\mathrm{syst}}\,\mathrm{MeV}$ in dem größerem Zentralitätsbereich von 0-40%. Durch den radialen Fluss sind alle gemessenen direkten Photonenimpulse blauverschoben. Die wahre Produktionstemperatur der Photonen sollte daher kleiner sein und darüber hinaus von dem zeitlichen Profil des radialen Flusses abhängen.

Des Weiteren wurden die gemessenen Spektren mit Modellvorhersagen für thermische Photonenspektren verglichen. Die Modelle sind in der Lage die Spektren nach der Subtraktion des prompten Photonenanteils zu beschreiben. Jedoch liegen die Vorhersagen am unteren Rand der systematischen Unsicherheiten der Resultate. Eine ähnliche Situation wurde bereits bei vorherigen Messungen, die bei niedrigeren Schwerpunktenergien durchgeführt wurden, vorgefunden. Die Anzeichen mehren sich demnach, dass eine Neugewichtung der Photonenproduktionsraten oder sogar zusätzliche Quellen von Photonen für die Beschreibung der direkten Photonen bei kleinen Impulsen benötigt werden. Des Weiteren ist es mit den derzeitigen Modellen innerhalb eines geschlossenen Ansatzes nicht möglich die Spektren und den elliptischen Fluss von direkten Photonen am LHC oder am RHIC zu beschreiben. Diese Situation wird häufig unter dem Begriff "direct-photon flow puzzle" zusammengefasst.

Zusammenfassend ist in der dieser Arbeit zugrunde liegenden Analyse zum ersten Mal am LHC die Messung von direkten Photonen in Schwerionenkollisionen bei niedrigen bis mittleren Impulsen durchgeführt worden. Während der mittlere Impulsbereich gut mit Rechnungen der pQCD übereinstimmt, findet sich bei niedrigeren Impulsen ein zentralitätsabhängiger Überschuss. Dieser stimmt qualitativ mit den Erwartungen für eine thermische Photonenproduktion überein, jedoch ist der genaue quantitative Vergleich eine Herausforderung für die gängigen theoretischen Beschreibungen.

A Inclusive and Direct-Photon Invariant Cross Sections

Data tables for the inclusive and direct-photon invariant cross sections. All p_T data points are bin shift corrected. For upper limits no such correction is applied.

p_T	Yield	Stat. Uncert.	%	Syst. Uncert.	%
0.430	1.033e+00	1.122e-03	0.1	8.722e-02	8.4
0.692	2.050e-01	4.079e-04	0.2	1.491e-02	7.3
0.893	7.562e-02	2.042e-04	0.3	5.219e-03	6.9
1.094	3.228e-02	1.221e-04	0.4	2.119e-03	6.6
1.295	1.512e-02	7.404e-05	0.5	9.714e-04	6.4
1.539	6.507e-03	3.451e-05	0.5	4.076e-04	6.3
1.883	2.323e-03	1.548e-05	0.7	1.456e-04	6.3
2.285	8.160e-04	9.247e-06	1.1	4.966e-05	6.1
2.729	2.936e-04	4.028e-06	1.4	1.789e-05	6.1
3.231	1.099e-04	2.171e-06	2.0	6.364e-06	5.8
3.734	4.565e-05	1.364e-06	3.0	2.666e-06	5.8
4.235	2.106e-05	8.238e-07	3.9	1.299e-06	6.2
4.949	8.170e-06	3.410e-07	4.2	4.700e-07	5.8
6.157	2.209e-06	1.298e-07	5.9	1.408e-07	6.4

Figure A.1: Inclusive-photon invariant cross section for pp collisions at $\sqrt{s} = 2.76\,\mathrm{TeV}$. The cross section is shown in Fig. 7.25.

p_T	Yield	Stat. Uncert.	%	Syst. Uncert.	%
0.347	2.451e+00	1.449e-03	0.1	1.333e-01	5.4
0.491	8.866e-01	4.030e-04	0.0	4.453e-02	5.0
0.693	2.793e-01	1.730e-04	0.1	1.358e-02	4.9
0.894	1.074e-01	9.852e-05	0.1	5.149e-03	4.8
1.094	4.751e-02	5.688e-05	0.1	2.267e-03	4.8
1.295	2.299e-02	3.300e-05	0.1	1.093e-03	4.8
1.495	1.191e-02	2.461e-05	0.2	5.644e-04	4.7
1.696	6.604e-03	1.448e-05	0.2	3.124e-04	4.7
1.896	3.799e-03	1.071e-05	0.3	1.798e-04	4.7
2.096	2.279e-03	7.271e-06	0.3	1.082e-04	4.7
2.296	1.410e-03	6.035e-06	0.4	6.738e-05	4.8
2.587	7.494e-04	2.644e-06	0.4	3.576e-05	4.8
2.988	3.406e-04	1.648e-06	0.5	1.642e-05	4.8
3.389	1.678e-04	1.077e-06	0.6	8.314e-06	5.0
3.790	8.742e-05	6.556e-07	0.7	4.506e-06	5.2
4.236	4.694e-05	4.163e-07	0.9	2.505e-06	5.3
4.737	2.420e-05	2.776e-07	1.1	1.387e-06	5.7
5.455	1.036e-05	1.147e-07	1.1	6.978e-07	6.7
6.461	3.910e-06	6.273e-08	1.6	2.899e-07	7.4
7.466	1.694e-06	3.843e-08	2.3	1.536e-07	9.1
8.885	5.424e-07	1.284e-08	2.4	6.666e-08	12.3
10.905	1.583e-07	6.943e-09	4.4	3.004e-08	19.0

Figure A.2: Inclusive-photon invariant cross section for pp collisions at $\sqrt{s} = 7\,\mathrm{TeV}$. The cross section is shown in Fig. 7.25.

p_T	Yield	Stat. Uncert.	%	Syst. Uncert.	%
0.998	1.926e+01	2.423e-02	0.1	9.876e-01	5.1
1.196	9.470e+00	1.469e-02	0.2	5.854e-01	6.2
1.395	4.593e+00	9.427e-03	0.2	3.144e-01	6.8
1.595	2.234e+00	6.039e-03	0.3	1.319e-01	5.9
1.795	1.145e+00	3.627e-03	0.3	6.310e-02	5.5
1.995	6.102e-01	2.375e-03	0.4	3.316e-02	5.4
2.196	3.355e-01	1.537e-03	0.5	1.871e-02	5.6
2.396	1.924e-01	1.153e-03	0.6	1.087e-02	5.6
2.596	1.119e-01	7.950e-04	0.7	6.432e-03	5.7
2.841	6.171e-02	4.259e-04	0.7	3.678e-03	6.0
3.142	3.051e-02	2.696e-04	0.9	1.840e-03	6.0
3.487	1.480e-02	1.369e-04	0.9	9.345e-04	6.3
3.888	7.220e-03	8.977e-05	1.2	4.858e-04	6.7
4.333	3.483e-03	5.125e-05	1.5	2.473e-04	7.1
4.964	1.452e-03	2.417e-05	1.7	1.224e-04	8.4
5.772	5.888e-04	1.379e-05	2.3	6.683e-05	11.4
6.576	2.772e-04	8.762e-06	3.2	3.575e-05	12.9
7.469	1.209e-04	4.803e-06	4.0	1.580e-05	13.1
9.271	3.642e-05	1.506e-06	4.1	6.846e-06	18.8

Figure A.3: Inclusive-photon invariant cross section for the 0-20% most central events for Pb–Pb collisions at $\sqrt{s_\mathrm{NN}} = 2.76\,\mathrm{TeV}$. The cross section is shown in Fig. 7.25.

p_T	Yield	Stat. Uncert.	%	Syst. Uncert.	%
0.998	1.396e+01	1.401e-02	0.1	7.156e-01	5.1
1.196	6.795e+00	8.449e-03	0.1	4.199e-01	6.2
1.395	3.300e+00	5.473e-03	0.2	2.259e-01	6.8
1.595	1.613e+00	3.468e-03	0.2	9.527e-02	5.9
1.795	8.315e-01	2.244e-03	0.3	4.584e-02	5.5
1.995	4.474e-01	1.379e-03	0.3	2.432e-02	5.4
2.196	2.477e-01	9.815e-04	0.4	1.381e-02	5.6
2.396	1.430e-01	6.726e-04	0.5	8.076e-03	5.6
2.596	8.458e-02	4.607e-04	0.5	4.863e-03	5.8
2.841	4.663e-02	2.526e-04	0.5	2.779e-03	6.0
3.142	2.347e-02	1.632e-04	0.7	1.416e-03	6.0
3.487	1.155e-02	8.731e-05	0.8	7.292e-04	6.3
3.888	5.637e-03	6.056e-05	1.1	3.794e-04	6.7
4.334	2.748e-03	3.361e-05	1.2	1.951e-04	7.1
4.965	1.162e-03	1.577e-05	1.4	9.799e-05	8.4
5.772	4.683e-04	8.742e-06	1.9	5.315e-05	11.4
6.576	2.257e-04	5.941e-06	2.6	2.911e-05	12.9
7.469	9.931e-05	2.855e-06	2.9	1.298e-05	13.1
9.270	2.856e-05	9.227e-07	3.2	5.368e-06	18.8

Figure A.4: Inclusive-photon invariant cross section for the 0-40% most central events for Pb–Pb collisions at $\sqrt{s_\mathrm{NN}} = 2.76\,\mathrm{TeV}$. The cross section is shown in Fig. 7.25.

p_{T}	Yield	Stat. Uncert.	%	Syst. Uncert.	%
0.997	8.701e+00	1.413e-02	0.2	4.179e-01	4.8
1.195	4.129e+00	7.976e-03	0.2	2.131e-01	5.2
1.395	2.010e+00	5.102e-03	0.3	1.075e-01	5.3
1.595	9.985e-01	3.077e-03	0.3	4.976e-02	5.0
1.795	5.210e-01	2.189e-03	0.4	2.554e-02	4.9
1.995	2.854e-01	1.377e-03	0.5	1.415e-02	5.0
2.196	1.602e-01	9.632e-04	0.6	8.066e-03	5.0
2.396	9.368e-02	6.514e-04	0.7	4.751e-03	5.1
2.596	5.728e-02	4.829e-04	0.8	2.902e-03	5.1
2.842	3.166e-02	2.640e-04	0.8	1.664e-03	5.3
3.142	1.647e-02	1.827e-04	1.1	9.098e-04	5.5
3.487	8.353e-03	1.042e-04	1.2	4.602e-04	5.5
3.889	4.059e-03	6.533e-05	1.6	2.467e-04	6.1
4.334	2.037e-03	3.970e-05	1.9	1.228e-04	6.0
4.966	8.692e-04	1.811e-05	2.1	5.957e-05	6.9
5.772	3.498e-04	1.065e-05	3.0	3.157e-05	9.0
6.577	1.768e-04	6.845e-06	3.9	1.640e-05	9.3
7.468	7.913e-05	3.546e-06	4.5	1.066e-05	13.5
9.266	2.015e-05	1.012e-06	5.0	3.328e-06	16.5

Figure A.5: Inclusive-photon invariant cross section for the 20-40% most central events for Pb–Pb collisions at $\sqrt{s_{\mathrm{NN}}} = 2.76\,\mathrm{TeV}$. The cross section is shown in Fig. 7.25.

p_{T}	Yield	Stat. Uncert.	%	Syst. Uncert.	%
0.995	1.923e+00	4.271e-03	0.2	9.288e-02	4.8
1.195	8.873e-01	2.368e-03	0.3	4.254e-02	4.8
1.395	4.278e-01	1.467e-03	0.3	2.050e-02	4.8
1.595	2.179e-01	1.006e-03	0.5	1.057e-02	4.9
1.795	1.164e-01	6.216e-04	0.5	5.723e-03	4.9
1.996	6.546e-02	4.447e-04	0.7	3.262e-03	5.0
2.196	3.765e-02	3.212e-04	0.9	1.904e-03	5.1
2.396	2.240e-02	2.412e-04	1.1	1.147e-03	5.1
2.596	1.366e-02	1.637e-04	1.2	6.940e-04	5.1
2.842	8.128e-03	1.044e-04	1.3	4.149e-04	5.1
3.143	4.315e-03	7.298e-05	1.7	2.278e-04	5.3
3.488	2.252e-03	4.068e-05	1.8	1.211e-04	5.4
3.889	1.152e-03	2.616e-05	2.3	6.421e-05	5.6
4.335	6.045e-04	1.614e-05	2.7	3.427e-05	5.7
4.966	2.433e-04	6.829e-06	2.8	1.509e-05	6.2
5.771	1.004e-04	3.767e-06	3.8	8.458e-06	8.4
6.574	4.227e-05	2.267e-06	5.4	3.886e-06	9.2
7.465	1.621e-05	1.074e-06	6.6	1.190e-06	7.3
9.256	5.608e-06	4.596e-07	8.2	8.708e-07	15.5

Figure A.6: Inclusive-photon invariant cross section for the 40-80% most central events for Pb–Pb collisions at $\sqrt{s_{\mathrm{NN}}} = 2.76\,\mathrm{TeV}$. The cross section is shown in Fig. 7.25.

p_T	Yield	Stat. Uncert.	%	Syst. Uncert.	%
0.450	3.988e-01	-	-	-	-
0.700	3.214e-02	-	-	-	-
0.900	1.210e-02	-	-	-	-
1.100	3.730e-03	-	-	-	-
1.300	1.868e-03	-	-	-	-
1.550	7.161e-04	-	-	-	-
1.900	2.437e-04	-	-	-	-
2.300	7.832e-05	-	-	-	-
2.750	2.438e-05	-	-	-	-
3.250	1.005e-05	-	-	-	-
3.750	3.856e-06	-	-	-	-
4.250	1.846e-06	-	-	-	-
5.000	1.208e-06	-	-	-	-
6.250	5.800e-07	-	-	-	-

Figure A.7: Direct-photon invariant cross section 95% confidence upper limits for pp at $\sqrt{s} = 2.76\,\mathrm{TeV}$. The the upper limits are shown in Fig. 10.3.

p_{T}	Yield	Stat. Uncert.	%	Syst. Uncert.	%
0.350	2.772e+00	-	-	-	-
0.500	1.780e-01	-	-	-	-
0.700	3.140e-02	-	-	-	-
0.900	9.229e-03	-	-	-	-
1.100	3.980e-03	-	-	-	-
1.300	2.096e-03	-	-	-	-
1.500	9.579e-04	-	-	-	-
1.700	6.026e-04	-	-	-	-
1.900	3.220e-04	-	-	-	-
2.100	1.815e-04	-	-	-	-
2.300	1.053e-04	-	-	-	-
2.600	6.697e-05	-	-	-	-
3.000	2.982e-05	-	-	-	-
3.400	1.319e-05	-	-	-	-
3.800	6.090e-06	-	-	-	-
4.250	4.322e-06	-	-	-	-
4.750	2.338e-06	-	-	-	-
5.500	1.357e-06	-	-	-	-
6.500	7.306e-07	-	-	-	-
7.500	4.304e-07	-	-	-	-
9.000	1.652e-07	-	-	-	-
11.000	7.370e-08	-	-	-	-

Figure A.8: Direct-photon invariant cross section 95% confidence upper limits for pp at $\sqrt{s} = 7\,\mathrm{TeV}$. The the upper limits are shown in Fig. 10.3.

p_T	Yield	Stat. Uncert.	%	Syst. Uncert.	%
0.983	2.172e+00	7.393e-01	34.0	1.007e+00	46.4
1.204	1.517e+00	2.675e-01	17.6	5.010e-01	33.0
1.394	7.411e-01	1.071e-01	14.4	2.601e-01	35.1
1.593	2.894e-01	4.638e-02	16.0	1.192e-01	41.2
1.794	1.339e-01	2.378e-02	17.8	5.985e-02	44.7
1.995	7.250e-02	1.279e-02	17.6	3.222e-02	44.4
2.195	4.123e-02	6.985e-03	16.9	1.770e-02	42.9
2.396	2.592e-02	4.031e-03	15.6	1.022e-02	39.4
2.596	1.531e-02	2.429e-03	15.9	5.933e-03	38.8
2.842	1.041e-02	1.435e-03	13.8	3.321e-03	31.9
3.143	5.118e-03	7.805e-04	15.3	1.731e-03	33.8
3.489	2.683e-03	4.116e-04	15.3	8.722e-04	32.5
3.890	1.496e-03	2.192e-04	14.6	4.456e-04	29.8
4.336	7.429e-04	1.159e-04	15.6	2.133e-04	28.7
4.968	3.378e-04	5.771e-05	17.1	9.477e-05	28.1
5.773	1.422e-04	3.008e-05	21.1	4.848e-05	34.1
6.576	6.964e-05	1.677e-05	24.1	2.717e-05	39.0
7.467	2.197e-05	8.256e-06	37.6	1.332e-05	60.6
9.265	1.064e-05	3.077e-06	28.9	5.240e-06	49.2

Figure A.9: Direct-photon invariant cross section for the 0-20% most central events for Pb–Pb collisions at $\sqrt{s_\mathrm{NN}} = 2.76\,\mathrm{TeV}$. The cross section is shown in Fig. 10.4.

p_T	Yield	Stat. Uncert.	%	Syst. Uncert.	%
0.982	1.016e+00	4.040e-01	39.8	7.596e-01	74.7
1.203	8.278e-01	1.410e-01	17.0	3.728e-01	45.0
1.394	4.328e-01	5.867e-02	13.6	1.921e-01	44.4
1.594	1.789e-01	2.603e-02	14.5	8.766e-02	49.0
1.795	9.044e-02	1.306e-02	14.4	4.383e-02	48.5
1.995	5.144e-02	6.867e-03	13.3	2.371e-02	46.1
2.196	2.877e-02	3.785e-03	13.2	1.315e-02	45.7
2.396	1.779e-02	2.241e-03	12.6	7.670e-03	43.1
2.596	1.135e-02	1.396e-03	12.3	4.497e-03	39.6
2.842	7.086e-03	8.305e-04	11.7	2.550e-03	36.0
3.143	3.643e-03	4.529e-04	12.4	1.348e-03	37.0
3.489	1.906e-03	2.411e-04	12.7	6.913e-04	36.3
3.890	1.030e-03	1.316e-04	12.8	3.562e-04	34.6
4.336	5.239e-04	7.088e-05	13.5	1.719e-04	32.8
4.969	2.537e-04	3.677e-05	14.5	7.673e-05	30.2
5.773	1.038e-04	1.946e-05	18.7	3.912e-05	37.7
6.576	5.665e-05	1.152e-05	20.3	2.213e-05	39.1
7.468	1.877e-05	5.432e-06	28.9	1.087e-05	57.9
9.274	7.765e-06	2.259e-06	29.1	4.169e-06	53.7

Figure A.10: Direct-photon invariant cross section for the 0-40% most central events for Pb–Pb collisions at $\sqrt{s_{NN}} = 2.76$ TeV. The cross section is shown in Fig. 10.4.

p_T	Yield	Stat. Uncert.	%	Syst. Uncert.	%
1.000	9.496e-01	-	-	-	-
1.200	5.703e-01	-	-	-	-
1.400	3.169e-01	-	-	-	-
1.600	1.491e-01	-	-	-	-
1.800	7.749e-02	-	-	-	-
1.996	1.980e-02	5.084e-03	25.7	1.446e-02	73.0
2.197	1.033e-02	2.985e-03	28.9	8.425e-03	81.6
2.397	6.863e-03	1.826e-03	26.6	4.857e-03	70.8
2.597	5.105e-03	1.174e-03	23.0	2.921e-03	57.2
2.843	2.930e-03	6.775e-04	23.1	1.693e-03	57.8
3.143	1.627e-03	3.843e-04	23.6	8.839e-04	54.3
3.489	9.579e-04	2.123e-04	22.2	4.548e-04	47.5
3.889	4.416e-04	1.230e-04	27.9	2.304e-04	52.2
4.335	2.637e-04	7.445e-05	28.2	1.141e-04	43.3
4.971	1.330e-04	3.918e-05	29.5	5.270e-05	39.6
5.780	5.398e-05	1.959e-05	36.3	2.907e-05	53.9
6.583	4.025e-05	1.100e-05	27.3	1.504e-05	37.4
7.475	1.486e-05	6.654e-06	44.8	9.600e-06	64.6
9.500	1.069e-05	-	-	-	-

Figure A.11: Direct-photon invariant cross section for the 20-40% most central events for Pb–Pb collisions at $\sqrt{s_\mathrm{NN}} = 2.76\,\mathrm{TeV}$. Data points without uncertainties correspond to 95% confidence upper limits. The cross section is shown in Fig. 10.4.

p_T	Yield	Stat. Uncert.	%	Syst. Uncert.	%
1.000	2.407e-01	-	-	-	-
1.200	1.193e-01	-	-	-	-
1.400	5.035e-02	-	-	-	-
1.600	2.167e-02	-	-	-	-
1.800	1.071e-02	-	-	-	-
2.000	6.898e-03	-	-	-	-
2.200	3.765e-03	-	-	-	-
2.400	2.213e-03	-	-	-	-
2.600	1.398e-03	-	-	-	-
2.850	1.191e-03	-	-	-	-
3.150	6.613e-04	-	-	-	-
3.500	3.896e-04	-	-	-	-
3.900	2.262e-04	-	-	-	-
4.339	6.053e-05	2.331e-05	38.5	4.325e-05	71.4
5.000	5.083e-05	-	-	-	-
5.800	2.502e-05	-	-	-	-
6.600	9.117e-06	-	-	-	-
7.500	1.065e-06	-	-	-	-
9.500	2.350e-06	-	-	-	-

Figure A.12: Direct-photon invariant cross section for the 40-80% most central events for Pb–Pb collisions at $\sqrt{s_\mathrm{NN}} = 2.76\,\mathrm{TeV}$. Data points without uncertainties correspond to 95% confidence upper limits. The cross section is shown in Fig. 10.4.

p_{T}	Yield	Stat. Uncert.	%	Syst. Uncert.	%
0.991	1.858e+00	7.404e-01	39.8	1.008e+00	54.3
1.209	1.370e+00	2.680e-01	19.6	5.013e-01	36.6
1.393	6.654e-01	1.077e-01	16.2	2.604e-01	39.1
1.593	2.490e-01	4.778e-02	19.2	1.198e-01	48.1
1.794	1.073e-01	2.489e-02	23.2	6.030e-02	56.2
1.994	5.612e-02	1.359e-02	24.2	3.254e-02	58.0
2.195	3.057e-02	7.462e-03	24.4	1.789e-02	58.5
2.396	1.887e-02	4.445e-03	23.5	1.039e-02	55.0
2.596	1.013e-02	2.971e-03	29.3	6.175e-03	60.9
2.842	6.899e-03	1.829e-03	26.5	3.509e-03	50.9
3.143	3.054e-03	9.597e-04	31.4	1.819e-03	59.6
3.488	1.565e-03	5.987e-04	38.3	9.746e-04	62.3
3.889	7.493e-04	3.465e-04	46.2	5.202e-04	69.4
4.333	3.136e-04	1.486e-04	47.4	2.327e-04	74.2
4.960	1.058e-04	7.047e-05	66.6	1.030e-04	97.4

Figure A.13: Prompt photon subtracted direct-photon invariant cross section for the 0-20% most central events for Pb–Pb collisions at $\sqrt{s_{\mathrm{NN}}} = 2.76\,\mathrm{TeV}$. The cross section is shown in Fig. 10.5.

p_T	Yield	Stat. Uncert.	%	Syst. Uncert.	%
0.994	8.020e-01	4.050e-01	50.5	7.601e-01	94.8
1.213	7.253e-01	1.415e-01	19.5	3.730e-01	51.4
1.394	3.813e-01	5.922e-02	15.5	1.923e-01	50.4
1.593	1.514e-01	2.718e-02	18.0	8.801e-02	58.1
1.794	7.230e-02	1.399e-02	19.4	4.412e-02	61.0
1.995	4.028e-02	7.548e-03	18.7	2.392e-02	59.4
2.195	2.151e-02	4.187e-03	19.5	1.327e-02	61.7
2.396	1.299e-02	2.578e-03	19.8	7.775e-03	59.9
2.596	7.827e-03	1.819e-03	23.2	4.646e-03	59.4
2.842	4.696e-03	1.134e-03	24.2	2.664e-03	56.7
3.143	2.237e-03	5.914e-04	26.4	1.401e-03	62.6
3.488	1.144e-03	3.819e-04	33.4	7.521e-04	65.7
3.889	5.207e-04	2.253e-04	43.3	4.004e-04	76.9
4.334	2.314e-04	9.506e-05	41.1	1.832e-04	79.2
4.963	9.560e-05	4.595e-05	48.1	8.152e-05	85.3

Figure A.14: Prompt photon subtracted direct-photon invariant cross section for the 0-40% most central events for Pb–Pb collisions at $\sqrt{s_\mathrm{NN}} = 2.76\,\mathrm{TeV}$. The cross section is shown in Fig. 10.5.

B π^0 Fit Parameter for pp and Pb–Pb

	mod. power law Eq. (9.4) Parameters					
$\sqrt{s}$	A	$-n$	b	c	d	χ^2/ndf
7 TeV	0.09	5.75	-4.91	0.91	1.27	0.60
	0.09	5.82	-5.10	0.89	1.29	0.54
2.76 TeV	0.0647	6.147	-4.128	0.7574	0.703	0.322

Figure B.1: Fit parameter of fits to the integrated bin values of the π^0 spectra for pp collisions $\sqrt{s} = 2.76\,\mathrm{TeV}$ and 2.76 TeV. The corresponding fits are used for the decay-photon cocktail calculation. The second set of parameters corresponds to the charged pion constrained pion spectra.

	mod. Tsallis Eq. (9.5)							
Cent.	A	$-n$	b	c	d	e	nT	χ^2/ndf
0-20%	85.34	0.44	4.78	82.54	-9.03	3.43	-2.76	0.41
	78.24	6.61	27.60	-7.72	4.20	-2.46	1.32	0.25
0-40%	33.73	1.16	6.08	38.23	-7.96	3.18	-2.03	0.44
	44.94	1.61	6.96	28.55	-7.90	3.65	-1.70	0.21
20-40%	7.86	2.38	7.41	32.30	-8.00	1.43	-0.68	0.40
	6.33	2.55	7.53	32.47	-8.09	1.29	-0.73	0.32
40-80%	217.82	0.13	4.93	124.55	387.63	3.76	-2.59	0.78
	907.42	0.078	4.53	334.17	149.52	4.04	-2.96	0.44

Figure B.2: Fit parameter of fits to the integrated bin values of the π^0 spectra for Pb–Pb collisions $\sqrt{s_{\mathrm{NN}}} = 2.76\,\mathrm{TeV}$. The corresponding fits are used for the decay-photon cocktail calculation. The second set of parameters corresponds to fits to the charged pion constrained pion spectra.
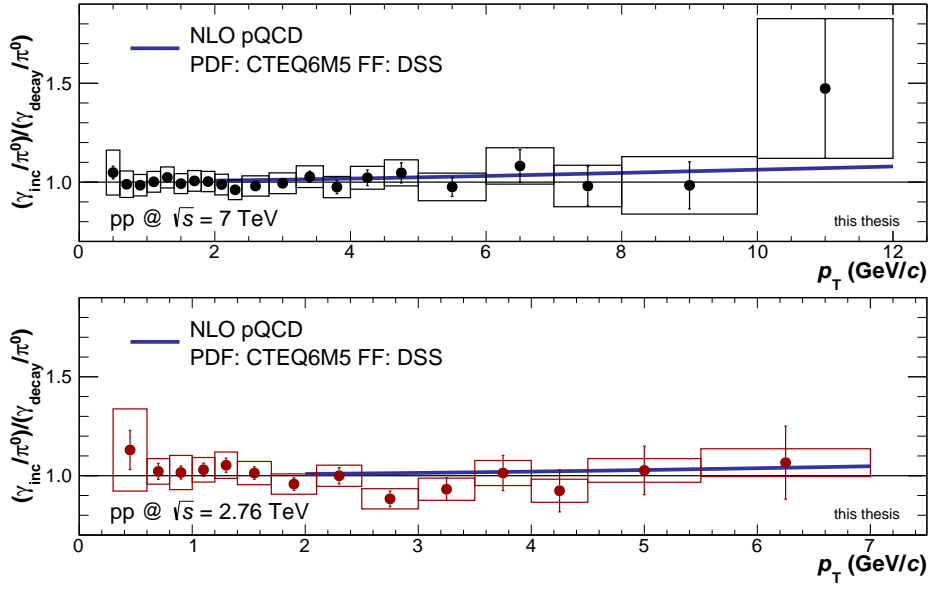
C Additional Figures

Figure C.1: Direct-photon excess ratios R_γ for pp at 7 TeV and 2.76 TeV. Additionally, a NLO pQCD prediction is shown, following [233]. Instead of fits to the π^0 spectra the spectra are used directly. The figure corresponds to Fig. 10.1.
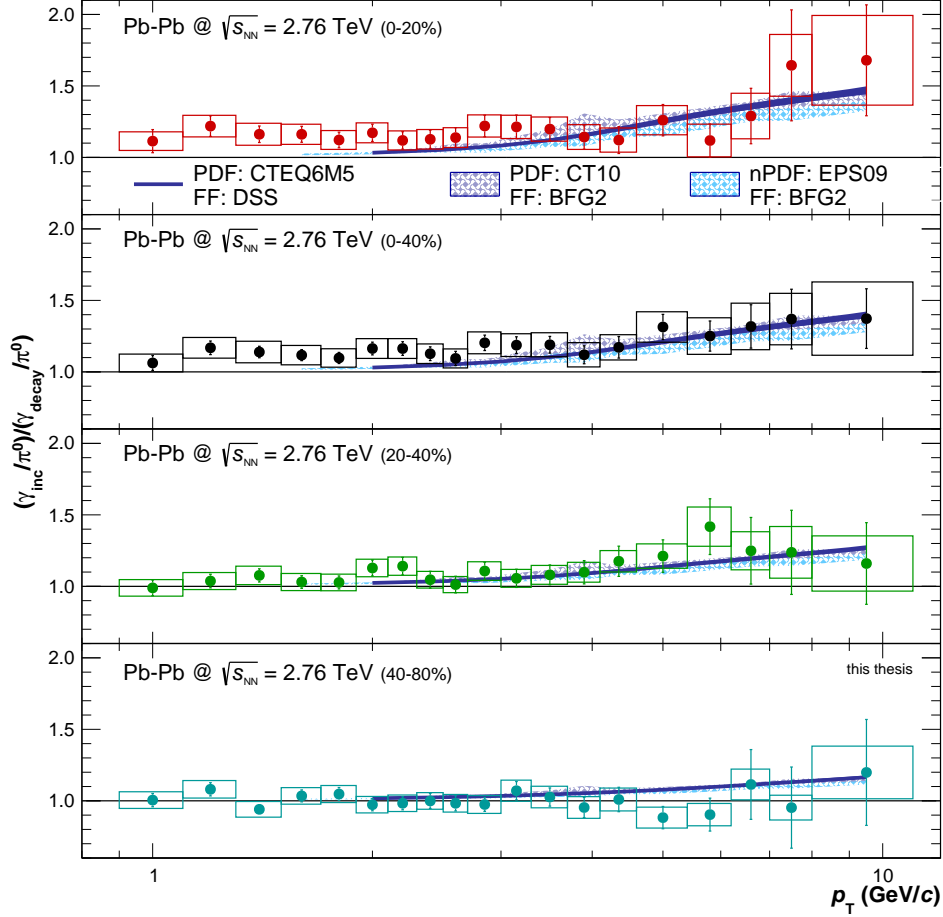
Figure C.2: Direct-photon excess ratios R_γ for Pb–Pb at 2.76 TeV in the centrality bins 0-20%, 0-40%, 20-40% and 40-80%. Additionally, three scaled NLO pQCD calculations are shown. They are identical to the calculations shown in Fig. 10.2. Instead of fits to the π^0 spectra the spectra are used directly. The figure corresponds to Fig. 10.2.

Bibliography

[1] R. Hagedorn, "Statistical thermodynamics of strong interactions at high-energies", *Nuovo Cim. Suppl.* **3** (1965) 147–186.

[2] N. Cabibbo and G. Parisi, "Exponential hadronic spectrum and quark liberation", *Phys. Lett. B* **59** (1975) 67–69.

[3] P. Blanchard, S. Fortunato, and H. Satz, "The Hagedorn temperature and partition thermodynamics", *Eur. Phys. J. C* **34** (2004) 361–366, `arXiv:hep-ph/0401103`.

[4] A. Chodos, R. L. Jaffe, K. Johnson, C. B. Thorn, and V. F. Weisskopf, "New extended model of hadrons", *Phys. Rev. D* **9** Jun (1974) 3471–3495.

[5] S. Sarkar, H. Satz, and B. Sinha, "The physics of the quark-gluon plasma", *Lect. Notes Phys.* **785** (2010) 1–369.

[6] **Particle Data Group**, J. Beringer *et al.*, "Review of Particle Physics (RPP)", *Phys. Rev. D* **86** (2012) 010001.

[7] K. G. Wilson, "Confinement of Quarks", *Phys. Rev. D* **10** (1974) 2445–2459.

[8] G. Münster and M. Walzl, "Lattice gauge theory: A Short primer", `arXiv:hep-lat/0012005`.

[9] I. Montvay and G. Münster, "Quantum fields on a lattice", Cambridge Univ. Press, Cambridge, 1994.

[10] J. Kuti, J. Polonyi, and K. Szlachanyi, "Monte Carlo Study of SU(2) Gauge Theory at Finite Temperature", *Phys. Lett. B* **98** (1981) 199.

[11] F. Karsch, "Lattice QCD at high temperature and density", *Lect. Notes Phys.* **583** (2002) 209–249, `arXiv:hep-lat/0106019`.

[12] B.-J. Schaefer and M. Wagner, "On the QCD phase structure from effective models ", *Prog. Part. Nucl. Phys.* **62** (2009), no. 2, 381 – 385.

[13] P. Bicudo, N. Cardoso, and M. Cardoso, "The Chiral crossover, static-light and light-light meson spectra, and the deconfinement crossover", *PoS* **BORMIO2011** (2011) 062, `arXiv:1105.0063`.

[14] K. Yagi, T. Hatsuda, and Y. Miake, "Quark-Gluon Plasma: From Big Bang to Little Bang", Cambridge Univ. Press, Cambridge, 2005.

[15] R. Snellings, "Elliptic Flow: A Brief Review", *New J. Phys.* **13:055008** (2011) `arXiv:arXiv:1102.3010`.

[16] R. Stock, "The Parton hadron phase transition in central nuclear collisions at the CERN SPS", *Prog. Part. Nucl. Phys.* **42** (1999) 295–309, `arXiv:hep-ph/9901415`.

[17] C. Klein-Bösing, "Study of the Quark-Gluon Plasma with Hard and Electromagnetic Probes", habilitation dissertation, Westfälischen Wilhelms-Universität Münster, 2013.

[18] J. Bjorken, "Highly Relativistic Nucleus-Nucleus Collisions: The Central Rapidity Region", *Phys. Rev. D* **27** (1983) 140–151.

[19] B. Muller, J. Schukraft, and B. Wyslouch, "First Results from Pb+Pb collisions at the LHC", *Ann. Rev. Nucl. Part. Sci.* **62** (2012) 361–386, `arXiv:1202.3233`.

[20] **ALICE Collaboration**, B. Abelev *et al.*, "Charged-particle multiplicity density at mid-rapidity in central Pb–Pb collisions at $\sqrt{s_{\mathrm{NN}}} = 2.76$ TeV", *Phys. Rev. Lett.* **105** (2010) 252301, `arXiv:1011.3916`.

[21] **ATLAS Collaboration**, G. Aad *et al.*, "Measurement of the centrality dependence of the charged particle pseudorapidity distribution in lead-lead collisions at $\sqrt{s_{\mathrm{NN}}} = 2.76$ TeV with the ATLAS detector", *Phys. Lett. B* **710** (2012) 363–382, `arXiv:1108.6027`.

[22] **CMS Collaboration**, S. Chatrchyan *et al.*, "Dependence on pseudorapidity and centrality of charged hadron production in PbPb collisions at a nucleon-nucleon centre-of-mass energy of 2.76 TeV", *JHEP* **1108** (2011) 141, `arXiv:1107.4800`.

[23] **CMS Collaboration**, K. Krajczar, "Charged hadron multiplicity and transverse energy densities in Pb Pb collisions from CMS", *J. Phys. G* **38** (2011) 124041.

[24] **PHENIX Collaboration**, S. Adler *et al.*, "Systematic studies of the centrality and $\sqrt{s_{\mathrm{NN}}}$ dependence of the $\mathrm{d}E_T/\mathrm{d}\eta$ and $\mathrm{d}N_{ch}/\mathrm{d}\eta$ in heavy ion collisions at mid-rapidity", *Phys. Rev. C* **71** (2005) 034908, `arXiv:nucl-ex/0409015`.

[25] J. E. Elias, W. Busza, C. Halliwell, D. Luckey, P. Swartz, L. Votta, and C. Young, "Experimental study of multiparticle production in

hadron-nucleus interactions at high energy", *Phys. Rev. D* **22** Jul (1980) 13–35.

[26] F. Cooper and G. Frye, "Single-particle distribution in the hydrodynamic and statistical thermodynamic models of multiparticle production", *Phys. Rev. D* **10** Jul (1974) 186–189.

[27] E. Schnedermann, J. Sollfrank, and U. W. Heinz, "Thermal phenomenology of hadrons from 200-A/GeV S+S collisions", *Phys. Rev. C* **48** (1993) 2462–2475, `arXiv:nucl-th/9307020`.

[28] **ALICE Collaboration**, B. Abelev *et al.*, "Centrality dependence of π, K, p production in Pb–Pb collisions at $\sqrt{s_{\mathrm{NN}}} = 2.76$ TeV", *Phys. Rev. C* **88** (2013) 044910, `arXiv:1303.0737`.

[29] E. V. Shuryak, "What RHIC experiments and theory tell us about properties of quark-gluon plasma?", *Nucl. Phys. A* **750** (2005) 64–83, `arXiv:hep-ph/0405066`.

[30] U. W. Heinz, "Concepts of heavy ion physics", `arXiv:hep-ph/0407360`.

[31] **STAR Collaboration**, B. Abelev *et al.*, "Systematic Measurements of Identified Particle Spectra in pp, d+Au and Au+Au Collisions from STAR", *Phys. Rev. C* **79** (2009) 034909, `arXiv:0808.2041`.

[32] J.-Y. Ollitrault, "Anisotropy as a signature of transverse collective flow", *Phys. Rev. D* **46** Jul (1992) 229–245.

[33] S. Voloshin and Y. Zhang, "Flow study in relativistic nuclear collisions by Fourier expansion of Azimuthal particle distributions", *Z. Phys. C* **70** (1996) 665–672, `arXiv:hep-ph/9407282`.

[34] **ALICE Collaboration**, K. Aamodt *et al.*, "Elliptic flow of charged particles in Pb–Pb collisions at 2.76 TeV", *Phys. Rev. Lett.* **105** (2010) 252302, `arXiv:1011.3914`.

[35] **ALICE Collaboration**, K. Aamodt *et al.*, "Harmonic decomposition of two-particle angular correlations in Pb–Pb collisions at $\sqrt{s_{\mathrm{NN}}} = 2.76$ TeV", *Phys. Lett. B* **708** (2012) 249–264, `arXiv:1109.2501`.

[36] **ALICE Collaboration**, B. Abelev *et al.*, "Directed flow of charged particles at midrapidity relative to the spectator plane in Pb–Pb collisions at $\sqrt{s_{\mathrm{NN}}} = 2.76$ TeV", *Phys. Rev. Lett.* **111** (2013) 232302, `arXiv:1306.4145`.

[37] **PHENIX Collaboration**, A. Adare *et al.*, "Measurements of Higher-Order Flow Harmonics in Au+Au Collisions at $\sqrt{s_{\mathrm{NN}}} = 200$ GeV", *Phys. Rev. Lett.* **107** (2011) 252301, `arXiv:1105.3928`.

[38] **ALICE Collaboration**, K. Aamodt *et al.*, "Higher harmonic anisotropic flow measurements of charged particles in Pb–Pb collisions at $\sqrt{s_{\mathrm{NN}}} = 2.76$ TeV", *Phys. Rev. Lett.* **107** (2011) 032301, `arXiv:1105.3865`.

[39] **ALICE Collaboration**, Y. Zhou, "Anisotropic flow of identified particles in Pb–Pb collisions at $\sqrt{s_{\mathrm{NN}}} = 2.76$ TeV with the ALICE detector", `arXiv:1309.3237`.

[40] U. Heinz, C. Shen, and H.-C. Song, "The viscosity of quark-gluon plasma at RHIC and the LHC", *AIP Conf. Proc.* **1441** (2012) 766–770, `arXiv:1108.5323`.

[41] S. A. Voloshin, A. M. Poskanzer, and R. Snellings, "Collective phenomena in non-central nuclear collisions", `arXiv:0809.2949`.

[42] J. Nagle, P. Steinberg, and W. Zajc, "Quantitative and Conceptual Considerations for Extracting the Knudsen Number in Heavy Ion Collisions", *Phys. Rev. C* **81** (2010) 024901, `arXiv:0908.3684`.

[43] H. Song, "QGP viscosity at RHIC and the LHC - a 2012 status report", *Nucl. Phys. A* **904-905** (2013) 114c–121c, `arXiv:1210.5778`.

[44] H. Niemi, G. S. Denicol, P. Huovinen, E. Molnar, and D. H. Rischke, "Influence of the shear viscosity of the quark-gluon plasma on elliptic flow in ultrarelativistic heavy-ion collisions", *Phys. Rev. Lett.* **106** (2011) 212302, `arXiv:1101.2442`.

[45] H. Song, S. A. Bass, U. Heinz, T. Hirano, and C. Shen, "200 A GeV Au+Au collisions serve a nearly perfect quark-gluon liquid", *Phys. Rev. Lett.* **106** (2011) 192301, `arXiv:1011.2783`.

[46] P. Kovtun, D. T. Son, and A. O. Starinets, "Viscosity in strongly interacting quantum field theories from black hole physics", *Phys. Rev. Lett.* **94** (2005) 111601, `arXiv:hep-th/0405231`.

[47] R. Glauber and G. Matthiae, "High-energy scattering of protons by nuclei", *Nucl. Phys. B* **21** (1970) 135–157.

[48] M. L. Miller, K. Reygers, S. J. Sanders, and P. Steinberg, "Glauber modeling in high energy nuclear collisions", *Ann. Rev. Nucl. Part. Sci.* **57** (2007) 205–243, `arXiv:nucl-ex/0701025`.

[49] N. Armesto, "Nuclear shadowing", *J. Phys. G* **32** (2006) R367–R394, `arXiv:hep-ph/0604108`.

[50] Y. Mehtar-Tani and G. Wolschin, "Baryon stopping and saturation physics in relativistic collisions", *Phys. Rev. C* **80** (2009) 054905, `arXiv:0907.5444`.

[51] A. Accardi, "Cronin effect in proton nucleus collisions: A Survey of theoretical models", `arXiv:hep-ph/0212148`.

[52] J. Cronin, H. J. Frisch, M. Shochet, J. Boymond, R. Mermod, *et al.*, "Production of Hadrons with Large Transverse Momentum at 200 GeV, 300 GeV, and 400 GeV", *Phys. Rev. D* **11** (1975) 3105.

[53] **ALICE Collaboration**, B. Abelev *et al.*, "Transverse Momentum Distribution and Nuclear Modification Factor of Charged Particles in p–Pb Collisions at $\sqrt{s_{\mathrm{NN}}} = 5.02$ TeV", *Phys. Rev. Lett.* **110** (2013) 082302, `arXiv:1210.4520`.

[54] M. Gyulassy, I. Vitev, X.-N. Wang, and B.-W. Zhang, "Jet quenching and radiative energy loss in dense nuclear matter", `arXiv:nucl-th/0302077`.

[55] Y. L. Dokshitzer, V. A. Khoze, and S. Troian, "On specific QCD properties of heavy quark fragmentation ('dead cone')", *J. Phys. G* **17** (1991) 1602–1604.

[56] A. Majumder and M. Van Leeuwen, "The Theory and Phenomenology of Perturbative QCD Based Jet Quenching", *Prog. Part. Nucl. Phys. A* **66** (2011) 41–92, `arXiv:1002.2206`.

[57] **PHENIX Collaboration**, K. Adcox *et al.*, "Suppression of hadrons with large transverse momentum in central Au+Au collisions at $\sqrt{s_{\mathrm{NN}}} = 130$ GeV", *Phys. Rev. Lett.* **88** (2002) 022301, `arXiv:nucl-ex/0109003`.

[58] R. Sharma, "Light Cone wavefunction approach to open heavy flavor dynamics in the QGP", *Nucl. Phys. A* **830** (2009) 857C–860C, `arXiv:0907.3764`.

[59] T. Renk, H. Holopainen, R. Paatelainen, and K. J. Eskola, "Systematics of the charged-hadron p_{T} spectrum and the nuclear suppression factor in heavy-ion collisions from $\sqrt{s} = 200$ GeV to $\sqrt{s} = 2.76$ TeV", *Phys. Rev. C* **84** (2011) 014906, `arXiv:1103.5308`.

[60] X.-F. Chen, T. Hirano, E. Wang, X.-N. Wang, and H. Zhang, "Suppression of high p_{T} hadrons in Pb+Pb Collisions at LHC", *Phys. Rev. C* **84** (2011) 034902, `arXiv:1102.5614`.

[61] A. Majumder and C. Shen, "Suppression of the high p_{T} charged hadron R_{AA} at the LHC", *Phys. Rev. Lett.* **109** (2012) 202301, `arXiv:1103.0809`.

[62] K. C. Zapp, F. Krauss, and U. A. Wiedemann, "Explaining Jet Quenching with Perturbative QCD Alone", `arXiv:1111.6838`.

[63] H. Song and U. W. Heinz, "Causal viscous hydrodynamics in 2+1 dimensions for relativistic heavy-ion collisions", *Phys. Rev. C* **77** (2008) 064901, `arXiv:0712.3715`.

[64] **PHENIX Collaboration**, S. Adler *et al.*, "Production of phi mesons at mid-rapidity in $\sqrt{s_{\mathrm{NN}}} = 200$ GeV Au+Au collisions at RHIC", *Phys. Rev. C* **72** (2005) 014903, `arXiv:nucl-ex/0410012`.

[65] **ALICE Collaboration**, K. Aamodt *et al.*, "Suppression of Charged Particle Production at Large Transverse Momentum in Central Pb–Pb Collisions at $\sqrt{s_{\mathrm{NN}}} = 2.76$ TeV", *Phys. Lett. B* **696** (2011) 30–39, `arXiv:1012.1004`.

[66] **ALICE Collaboration**, B. Abelev *et al.*, "Centrality Dependence of Charged Particle Production at Large Transverse Momentum in Pb–Pb Collisions at $\sqrt{s_{\mathrm{NN}}} = 2.76$ TeV", *Phys. Lett. B* **720** (2013), no. 1–3, 52 – 62, `arXiv:1208.2711`.

[67] **CMS Collaboration**, S. Chatrchyan *et al.*, "Study of high-p_{T} charged particle suppression in PbPb compared to pp collisions at $\sqrt{s_{\mathrm{NN}}} = 2.76$ TeV", *Eur. Phys. J. C* **72** (2012) 1945, `arXiv:1202.2554`.

[68] A. Milov, "Centrality dependence of charged particle spectra and RCP in Pb+Pb collisions at $\sqrt{s_{\mathrm{NN}}} = 2.76$ TeV with the ATLAS detector at the LHC", *J. Phys. G* **38** (2011) 124113, `arXiv:1107.0460`.

[69] **BRAHMS Collaboration**, I. Arsene *et al.*, "Quark gluon plasma and color glass condensate at RHIC? The Perspective from the BRAHMS experiment", *Nucl. Phys. A* **757** (2005) 1–27, `arXiv:nucl-ex/0410020`.

[70] B. Back, M. Baker, M. Ballintijn, D. Barton, B. Becker, *et al.*, "The PHOBOS perspective on discoveries at RHIC", *Nucl. Phys. A* **757** (2005) 28–101, `arXiv:nucl-ex/0410022`.

[71] **STAR Collaboration**, J. Adams *et al.*, "Experimental and theoretical challenges in the search for the quark gluon plasma: The STAR Collaboration's critical assessment of the evidence from RHIC collisions", *Nucl. Phys. A* **757** (2005) 102–183, `arXiv:nucl-ex/0501009`.

[72] **PHENIX Collaboration**, K. Adcox *et al.*, "Formation of dense partonic matter in relativistic nucleus-nucleus collisions at RHIC: Experimental evaluation by the PHENIX collaboration", *Nucl. Phys. A* **757** (2005) 184–283, `arXiv:nucl-ex/0410003`.

[73] A. Dainese, "Heavy-flavour production in Pb–Pb collisions at the LHC, measured with the ALICE detector", *J. Phys. G* **38** (2011) 124032, `arXiv:1106.4042`.

[74] **CMS Collaboration**, S. Chatrchyan *et al.*, "Suppression of non-prompt J/psi, prompt J/psi, and Y(1S) in PbPb collisions at $\sqrt{s_{NN}} = 2.76$ TeV", *JHEP* **1205** (2012) 063, `arXiv:1201.5069`.

[75] H. Appelshauser, "Particle Production at Large Transverse Momentum with ALICE", *J. Phys. G* **38** (2011) 124014, `arXiv:1110.0638`.

[76] **CMS Collaboration**, S. Chatrchyan *et al.*, "Measurement of isolated photon production in pp and PbPb collisions at $\sqrt{s_{NN}} = 2.76$ TeV", *Phys. Lett. B* **710** (2012) 256–277, `arXiv:1201.3093`.

[77] **CMS Collaboration**, Y.-J. Lee, "Nuclear modification factors from the CMS experiment", *J. Phys. G* **38** (2011) 124015, `arXiv:1107.2131`.

[78] **CMS Collaboration**, S. Chatrchyan *et al.*, "Study of W boson production in PbPb and pp collisions at $\sqrt{s_{NN}} = 2.76$ TeV", *Phys. Lett. B* **715** (2012) 66–87, `arXiv:1205.6334`.

[79] G. F. Sterman and S. Weinberg, "Jets from Quantum Chromodynamics", *Phys. Rev. Lett.* **39** (1977) 1436.

[80] S. Catani, Y. L. Dokshitzer, M. Seymour, and B. Webber, "Longitudinally invariant K_t clustering algorithms for hadron hadron collisions", *Nucl. Phys. B* **406** (1993) 187–224.

[81] M. Cacciari, G. P. Salam, and G. Soyez, "The Anti-k(t) jet clustering algorithm", *JHEP* **0804** (2008) 063, `arXiv:0802.1189`.

[82] **CMS Collaboration**, S. Chatrchyan *et al.*, "Studies of jet quenching using isolated-photon+jet correlations in PbPb and pp collisions at $\sqrt{s_{NN}} = 2.76$ TeV", *Phys. Lett. B* **718** (2013) 773–794, `arXiv:1205.0206`.

[83] **ATLAS Collaboration**, P. Steinberg, "Photon and Z production, and γ/Z-jet correlations in lead-lead collisions at the LHC with ATLAS", *Nucl. Phys. A* **904-905** (2013) 233c–240c.

[84] V. A. Khoze, S. Lupia, and W. Ochs, "QCD coherence and the soft limit of the energy spectrum", *Phys. Lett. B* **394** (1997) 179–187, `arXiv:hep-ph/9610204`.

[85] W. Ochs, V. A. Khoze, and M. Ryskin, "Limiting soft particle emission in e^+e^-, hadronic and nuclear collisions", *Eur. Phys. J. C* **68** (2010) 141–152, `arXiv:1003.2127`.

[86] J. C. Collins, D. E. Soper, and G. F. Sterman, "Factorization for Short Distance Hadron - Hadron Scattering", *Nucl. Phys. B* **261** (1985) 104.

[87] **ZEUS Collaboration**, S. Chekanov *et al.*, "An NLO QCD analysis of inclusive cross-section and jet-production data from the zeus experiment", *Eur. Phys. J. C* **42** (2005) 1–16, `arXiv:hep-ph/0503274`.

[88] P. Aurenche, M. Fontannaz, J.-P. Guillet, E. Pilon, and M. Werlen, "A New critical study of photon production in hadronic collisions", *Phys. Rev. D* **73** (2006) 094007, `arXiv:hep-ph/0602133`.

[89] "JETPHOX".
`http://lapth.cnrs.fr/PHOX_FAMILY/jetphox.html`

[90] M. Klasen, C. Klein-Bösing, F. König, and J. Wessels, "How robust is a thermal photon interpretation of the ALICE low-p_T data?", *JHEP* **1310** (2013) 119, `1307.7034`.

[91] J. F. Owens, "Large-momentum-transfer production of direct photons, jets, and particles", *Rev. Mod. Phys.* **59** Apr (1987) 465–503.

[92] M. H. Thoma, "Applications of high temperature field theory to heavy ion collisions", `arXiv:hep-ph/9503400`.

[93] M. Thoma, "Damping rate of a hard photon in a relativistic plasma", *Phys. Rev. D* **51** (1995) 862–865, `arXiv:hep-ph/9405309`.

[94] K. Eskola, H. Paukkunen, and C. Salgado, "EPS09: A New Generation of NLO and LO Nuclear Parton Distribution Functions", *JHEP* **0904** (2009) 065, `arXiv:0902.4154`.

[95] F. Arleo, "Hard pion and prompt photon at RHIC, from single to double inclusive production", *JHEP* **0609** (2006) 015, `arXiv:hep-ph/0601075`.

[96] **ATLAS Collaboration**, "Measurement of high-p_T isolated prompt photons in lead-lead collisions at $\sqrt{s_{\mathrm{NN}}} = 2.76$ TeV with the ATLAS detector at the LHC", Tech. Rep. ATLAS-CONF-2012-051, CERN, Geneva, May 2012.

[97] **PHENIX Collaboration**, S. Afanasiev *et al.*, "Measurement of Direct Photons in Au+Au Collisions at $\sqrt{s_{\mathrm{NN}}} = 200$ GeV", *Phys. Rev. Lett.* **109** (2012) 152302, `arXiv:1205.5759`.

[98] T. Peitzmann and M. H. Thoma, "Direct photons from relativistic heavy ion collisions", *Phys. Rept.* **364** (2002) 175–246, `arXiv:hep-ph/0111114`.

[99] P. Stankus, "Direct photon production in relativisticc heavy-ion collisions", *Ann. Rev. Nucl. Part. Sci.* **55** (2005) 517–554.

[100] C. Gale, "Photon Production in Hot and Dense Strongly Interacting Matter", `arXiv:0904.2184`.

[101] E. V. Shuryak, "Quark-Gluon Plasma and Hadronic Production of Leptons, Photons and Psions", *Phys. Lett. B* **78** (1978) 150.

[102] J. I. Kapusta, P. Lichard, and D. Seibert, "High-energy photons from quark - gluon plasma versus hot hadronic gas", *Phys. Rev. D* **44** (1991) 2774–2788.

[103] E. Bratkovskaya, S. Kiselev, and G. Sharkov, "Direct photon production from hadronic sources in high-energy heavy-ion collisions", *Phys. Rev. C* **78** (2008) 034905, `arXiv:0806.3465`.

[104] W. Cassing and E. Bratkovskaya, "Parton transport and hadronization from the dynamical quasiparticle point of view", *Phys. Rev. C* **78** (2008) 034919, `arXiv:0808.0022`.

[105] S. Turbide, R. Rapp, and C. Gale, "Hadronic production of thermal photons", *Phys. Rev. C* **69** (2004) 014903, `arXiv:hep-ph/0308085`.

[106] H. van Hees, C. Gale, and R. Rapp, "Thermal Photons and Collective Flow at the Relativistic Heavy-Ion Collider", *Phys. Rev. C* **84** (2011) 054906, `arXiv:1108.2131`.

[107] R. Chatterjee, H. Holopainen, T. Renk, and K. J. Eskola, "Enhancement of thermal photon production in event-by-event hydrodynamics", *Phys. Rev. C* **83** (2011) 054908, `arXiv:1102.4706`.

[108] D. K. Srivastava and B. Sinha, "Radiation of single photons from Pb+Pb collisions at the CERN SPS and quark hadron phase transition", *Phys. Rev. C* **64** (2001) 034902, `arXiv:nucl-th/0006018`.

[109] M. Dion, J.-F. Paquet, B. Schenke, C. Young, S. Jeon, *et al.*, "Viscous photons in relativistic heavy ion collisions", *Phys. Rev. C* **84** (2011) 064901, `arXiv:1109.4405`.

[110] C. Shen, U. W. Heinz, J.-F. Paquet, and C. Gale, "Thermal photons as a quark-gluon plasma thermometer revisited", *Phys. Rev. C* **89** (2014) 044910, `arXiv:1308.2440`.

[111] H. A. Weldon, "Simple Rules for Discontinuities in Finite Temperature Field Theory", *Phys. Rev. D* **28** (1983) 2007.

[112] C. Gale and J. I. Kapusta, "Vector dominance model at finite temperature", *Nucl. Phys. B* **357** (1991), no. 1, 65 – 89.

[113] V. Baier and V. Katkov, "Variation of radiation length due to LPM effect", *Phys. Lett. A* **327** (2004) 202–209, `arXiv:hep-ph/0403132`.

[114] S. Turbide, C. Gale, S. Jeon, and G. D. Moore, "Energy loss of leading hadrons and direct photon production in evolving quark-gluon plasma", *Phys. Rev. C* **72** (2005) 014906, `arXiv:hep-ph/0502248`.

[115] R. J. Fries, B. Muller, and D. K. Srivastava, "High-energy photons from passage of jets through quark gluon plasma", *Phys. Rev. Lett.* **90** (2003) 132301, `arXiv:nucl-th/0208001`.

[116] L. Bhattacharya and P. Roy, "Jet-photons from an anisotropic *Quark-Gluon-Plasma*", *J. Phys. G* **37** (2010) 105010, `arXiv:1001.1054`.

[117] F.-M. Liu, T. Hirano, K. Werner, and Y. Zhu, "Jet quenching and direct photon production", *J. Phys. G* **36** (2009) 064072, `arXiv:0811.0666`.

[118] I. Vitev and B.-W. Zhang, "A Systematic study of direct photon production in heavy ion collisions", *Phys. Lett. B* **669** (2008) 337–344, `arXiv:0804.3805`.

[119] E. Shuryak and L. Xiong, "Dilepton and photon production in the "hot-glue" scenario", *Phys. Rev. Lett.* **70** Apr (1993) 2241–2244.

[120] F. Gelis, H. Niemi, P. Ruuskanen, and S. Rasanen, "Photon production from nonequilibrium QGP in heavy ion collisions", *J. Phys. G* **30** (2004) S1031–S1036, `arXiv:nucl-th/0403040`.

[121] J. Sakurai, "Vector-meson dominance - present status and future prospects", *Conf. Proc.* **C690914** (1969) 91–104.

[122] L. Xiong, E. V. Shuryak, and G. Brown, "Photon production through A1 resonance in high-energy heavy ion collisions", *Phys. Rev. D* **46** (1992) 3798–3801, `arXiv:hep-ph/9208206`.

[123] **PHENIX Collaboration**, K. Reygers, "Direct-photon production from SPS to RHIC energies", *Eur. Phys. J. C* **43** (2005) 393–398, `arXiv:nucl-ex/0502018`.

[124] **PHENIX Collaboration**, S. Adler *et al.*, "Centrality dependence of direct photon production in $\sqrt{s_{\mathrm{NN}}} = 200$ GeV Au+Au collisions", *Phys. Rev. Lett.* **94** (2005) 232301, `arXiv:nucl-ex/0503003`.

[125] S. Adler *et al.*, "Measurement of Direct Photon Production in p+p Collisions at $\sqrt{s} = 200$ GeV", *Phys. Rev. Lett.* **98** (2007), no. 1, 12002.

[126] **PHENIX Collaboration**, A. Adare *et al.*, "Direct-Photon Production in p+p Collisions at $\sqrt{s} = 200$ GeV at Midrapidity", *Phys. Rev. D* **86** (2012) 072008, `arXiv:1205.5533`.

[127] **PHENIX Collaboration**, A. Adare *et al.*, "Enhanced production of direct photons in Au+Au collisions at $\sqrt{s_{\mathrm{NN}}} = 200$ GeV and implications for the initial temperature", *Phys. Rev. Lett.* **104** (2010) 132301, `arXiv:0804.4168`.

[128] **PHENIX Collaboration**, A. Adare *et al.*, "Centrality dependence of low-momentum direct-photon production in Au+Au collisions at $\sqrt{s_{\mathrm{NN}}} = 200$ GeV", `arXiv:1405.3940`.

[129] F.-M. Liu, T. Hirano, K. Werner, and Y. Zhu, "Centrality-dependent direct photon p(t) spectra in Au+Au collisions at RHIC", *Phys. Rev. C* **79** (2009) 014905, `arXiv:0807.4771`.

[130] **PHENIX Collaboration**, A. Adare *et al.*, "Detailed measurement of the e^+e^- pair continuum in p+p and Au+Au collisions at $\sqrt{s_{\mathrm{NN}}} = 200$ GeV and implications for direct photon production", *Phys. Rev. C* **81** (2010) 034911, `arXiv:0912.0244`.

[131] D. G. d'Enterria and D. Peressounko, "Probing the QCD Equation of State with Thermal Photons in Nucleus-Nucleus Collisions at RHIC", *Eur. Phys. J. C* **46** (2006) 451–464, `arXiv:nucl-th/0503054`.

[132] P. Huovinen, P. Ruuskanen, and S. Rasanen, "Photon emission in heavy ion collisions at the CERN SPS", *Phys. Lett. B* **535** (2002) 109–116, `arXiv:nucl-th/0111052`.

[133] J.-e. Alam, S. Sarkar, T. Hatsuda, T. K. Nayak, and B. Sinha, "Photons from Pb–Pb collisions at ultrarelativistic energies", *Phys. Rev. C* **63** Jan (2001) 021901.

[134] N. M. Kroll and W. Wada, "Internal pair production associated with the emission of high-energy gamma rays", *Phys. Rev.* **98** (1955) 1355–1359.

[135] P. Lichard, "Formalism for dilepton production via virtual photon bremsstrahlung in hadronic reactions", *Phys. Rev. D* **51** (1995) 6017–6035, `arXiv:hep-ph/9812211`.

[136] C. Lefevre, "LHC: the guide (English version). Guide du LHC (version anglaise)", Feb 2009, unpublished.

[137] **ATLAS Collaboration**, G. Aad *et al.*, "Observation of a new particle in the search for the Standard Model Higgs boson with the ATLAS detector at the LHC", *Phys. Lett. B* **716** (2012) 1–29, `arXiv:1207.7214`.

[138] **D0 Collaboration**, V. M. Abazov *et al.*, "Combined search for the standard model Higgs boson decaying to $b\bar{b}$ using the D0 Run II data set", *Phys. Rev. Lett.* **109** (2012) 121802, `arXiv:1207.6631`.

[139] **CMS Collaboration**, S. Chatrchyan *et al.*, "Observation of a new boson at a mass of 125 GeV with the CMS experiment at the LHC", *Phys. Lett. B* **716** (2012) 30–61, `arXiv:1207.7235`.

[140] **ALICE Collaboration**, "ALICE webpage". `http://aliceinfo.cern.ch/`

[141] **ALICE Collaboration**, K. Aamodt *et al.*, "The ALICE experiment at the CERN LHC", *JINST* **3** (2008) S08002.

[142] B. Alessandro, F. Antinori, J. Belikov, C. Blume, A. Dainese, P. Foka, P. Giubellino, B. Hippolyte, C. Kuhn, G. Martínez, *et al.*, "ALICE: Physics performance report, volume II", *J. Phys. G* **32** (2006) 1295–2040.

[143] **ALICE Collaboration**, G. Dellacasa *et al.*, "ALICE technical design report of the inner tracking system (ITS)", 1999.

[144] **ALICE Collaboration**, K. Aamodt *et al.*, "Alignment of the ALICE Inner Tracking System with cosmic-ray tracks", *JINST* **5** (2010) P03003, `arXiv:1001.0502`.

[145] J. Alme, Y. Andres, H. Appelshauser, S. Bablok, N. Bialas, *et al.*, "The ALICE TPC, a large 3-dimensional tracking device with fast readout for ultra-high multiplicity events", *Nucl. Instrum. Meth. A* **622** (2010) 316–367, `arXiv:1001.1950`.

[146] **ALICE Collaboration**, G. Dellacasa *et al.*, "ALICE: Technical design report of the time projection chamber", 2000.

[147] J. Wiechula, "Commissioning and Calibration of the ALICE-TPC", phd thesis, Goethe-Universität Frankfurt am Main, 2008.

[148] **ALICE Collaboration**, G. Dellacasa *et al.*, "ALICE technical design report of the time-of-flight system (TOF)", 2000.

[149] **ALICE Collaboration**, P. Cortese *et al.*, "ALICE: Addendum to the technical design report of the time of flight system (TOF)", 2002.

[150] **ALICE Collaboration**, P. Cortese *et al.*, "ALICE technical design report on forward detectors: FMD, T0 and V0", 2004.

[151] **ALICE Collaboration**, G. Dellacasa *et al.*, "ALICE technical design report of the photon spectrometer (PHOS)", 1999.

[152] **ALICE Collaboration**, P. Cortese *et al.*, "ALICE electromagnetic calorimeter technical design report", 2008.

[153] **ATLAS Collaboration**, "ATLAS webpage". `http://atlas.ch/`

[154] **CMS Collaboration**, "CMS webpage".
`http://cms.web.cern.ch/`

[155] **LHCb Collaboration**, "LHCb webpage".
`http://lhcb.web.cern.ch/lhcb/`

[156] **TOTEM Collaboration**, "TOTEM webpage".
`http://totem.web.cern.ch/Totem/`

[157] **LHCf Collaboration**, "LHCf webpage".
`http://home.web.cern.ch/about/experiments/lhcf`

[158] **MoEDAL Collaboration**, "MoEDAL webpage".
`http://moedal.web.cern.ch/`

[159] R. Brun and F. Rademakers, "ROOT – An object oriented data analysis
framework ", *Nucl. Instrum. Meth. A* **389** (1997), no. 1–2, 81 – 86.

[160] I. Antcheva *et al.*, "ROOT – A C++ framework for petabyte data storage,
statistical analysis and visualization", *CPC* **180** (2009), no. 12, 2499 –
2512.

[161] "PAW webpage".
`http://paw.web.cern.ch/paw/`

[162] **ALICE Collaboration**, "AliRoot".
`http://svnweb.cern.ch/world/wsvn/AliRoot/`

[163] F. Carminati and A. Morsch, "Simulation in ALICE", *ArXiv Physics
e-prints*, June 2003 `physics/0306092`.

[164] R. Brun, F. Bruyant, M. Maire, A. McPherson, and P. Zanarini,
"GEANT3", 1987.

[165] **ALICE Collaboration**, "AliEn @ GRID webpage".
`http://alien2.cern.ch/`

[166] **ALICE Collaboration**, B. B. Abelev *et al.*, "Performance of the ALICE
Experiment at the CERN LHC", *Int. J. Mod. Phys. A* **29** (2014) 1430044,
`arXiv:1402.4476`.

[167] V. Karimäki, "Effective Vertex Fitting", 1997.

[168] G. Agakishiev, O. Y. Barannikova, F. Ceretto, U. Faschingbauer,
P. Glassel, *et al.*, "A New robust fitting algorithm for vertex reconstruction
in the CERES experiment", *Nucl. Instrum. Meth. A* **394** (1997) 225–231.

[169] P. Billoir, "Track Fitting with Multiple Scattering: A new Method", *Nucl.
Instrum. Meth. A* **225** (1984) 352–366.

[170] R. Frühwirth, "Application of Kalman filtering to track and vertex fitting", *Nucl. Instrum. Meth. A* **262** (1987), no. 2–3, 444 – 450.

[171] **ALICE Collaboration**, K. Aamodt *et al.*, "Centrality dependence of the charged-particle multiplicity density at mid-rapidity in Pb–Pb collisions at $\sqrt{s_{\mathrm{NN}}} = 2.76$ TeV", *Phys. Rev. Lett.* **106** (2011) 032301, `arXiv:1012.1657`.

[172] **ALICE Collaboration**, B. Abelev *et al.*, "Centrality determination of Pb–Pb collisions at $\sqrt{s_{\mathrm{NN}}} = 2.76$ TeV with ALICE", *Phys. Rev. C* **88** (2013), no. 4, 044909, `arXiv:1301.4361`.

[173] R. Engel, J. Ranft, and S. Roesler, "Hard diffraction in hadron hadron interactions and in photoproduction", *Phys. Rev. D* **52** (1995) 1459–1468, `arXiv:hep-ph/9502319`.

[174] T. Sjöstrand, S. Mrenna, and P. Z. Skands, "PYTHIA 6.4 Physics and Manual", *JHEP* **0605** (2006) 026, `arXiv:hep-ph/0603175`.

[175] T. Sjöstrand, "PYTHIA 8 Status Report", `arXiv:0809.0303`.

[176] T. Sjöstrand, S. Mrenna, and P. Z. Skands, "A Brief Introduction to PYTHIA 8.1", *Comput. Phys. Commun.* **178** (2008) 852–867, `arXiv:0710.3820`.

[177] X.-N. Wang and M. Gyulassy, "HIJING: A Monte Carlo model for multiple jet production in p p, p A and A A collisions", *Phys. Rev. D* **44** (1991) 3501–3516.

[178] A. Capella, U. Sukhatme, C.-I. Tan, and J. Tran Thanh Van, "Dual parton model", *Phys. Rept.* **236** (1994) 225–329.

[179] A. Kaidalov and K. Ter-Martirosian, "Pomeron as Quark-Gluon Strings and Multiple Hadron Production at SPS Collider Energies", *Phys. Lett. B* **117** (1982) 247–251.

[180] A. Kaidalov and M. Poghosyan, "Predictions of Quark-Gluon String Model for pp at LHC", *Eur. Phys. J. C* **67** (2010) 397–404, `arXiv:0910.2050`.

[181] Y. L. Dokshitzer, "Calculation of the Structure Functions for Deep Inelastic Scattering and e^+e^- Annihilation by Perturbation Theory in Quantum Chromodynamics.", *Sov. Phys. JETP* **46** (1977) 641–653.

[182] V. Gribov and L. Lipatov, "Deep inelastic ep scattering in perturbation theory", *Sov. J. Nucl. Phys.* **15** (1972) 438–450.

[183] G. Altarelli and G. Parisi, "Asymptotic Freedom in Parton Language", *Nucl. Phys. B* **126** (1977) 298.

[184] B. Andersson, G. Gustafson, G. Ingelman, and T. Sjostrand, "Parton Fragmentation and String Dynamics", *Phys. Rept.* **97** (1983) 31–145.

[185] B. Andersson, S. Mohanty, and F. Söderberg, "Recent developments in the Lund model", `arXiv:hep-ph/0212122`.

[186] "The Coordinated Theoretical-Experimental Project on QCD". `http://www.phys.psu.edu/~cteq/`

[187] M. Bengtsson and T. Sjöstrand, "A comparative study of coherent and non-coherent parton shower evolution ", *Nucl. Phys. B* **289** (1987), no. 0, 810 – 846.

[188] M. Bengtsson and T. Sjöstrand, "Coherent parton showers versus matrix elements - implications of PETRA/PEP data ", *Phys. Lett. B* **185** (1987), no. 3–4, 435 – 440.

[189] B. Andersson, G. Gustafson, and B. Nilsson-Almqvist, "A Model for Low p_T Hadronic Reactions, with Generalizations to Hadron - Nucleus and Nucleus-Nucleus Collisions", *Nucl. Phys. B* **281** (1987) 289.

[190] B. Nilsson-Almqvist and E. Stenlund, "Interactions Between Hadrons and Nuclei: The Lund Monte Carlo, Fritiof Version 1.6", *Comput. Phys. Commun.* **43** (1987) 387.

[191] M. Levy and J. Sucher, "Eikonal approximation in quantum field theory", *Phys. Rev.* **186** (1969) 1656–1670.

[192] W.-T. Deng, X.-N. Wang, and R. Xu, "Hadron production in p+p, p+Pb, and Pb+Pb collisions with the HIJING 2.0 model at energies available at the CERN Large Hadron Collider", *Phys. Rev. C* **83** (2011) 014915, `arXiv:1008.1841`.

[193] W.-T. Deng, X.-N. Wang, and R. Xu, "Gluon shadowing and hadron production in heavy-ion collisions at LHC", *Phys. Lett. B* **701** (2011) 133–136, `arXiv:1011.5907`.

[194] "GEANT". `http://wwwasdoc.web.cern.ch/wwwasdoc/geant_html3/geantall.html`

[195] F. Bock, "Neutral Pion and Eta Meson Production in pp and Pb–Pb Collisions at the LHC with the ALICE Detector", Master's thesis, University Heidelberg, December 2012. `http://www.physi.uni-heidelberg.de//Publications/Bock-Masterthesis.pdf`

[196] A. Marín, F. Bock, M. Wilde, D. Lohner, K. Aamodt, and K. Koch, "ALICE Conversion Software".

`http://svnweb.cern.ch/world/wsvn/AliRoot/trunk/PWGGA/GammaConv/`

[197] K. Koch, "Measurement of π^0 and η mesons with photon conversions in ALICE in proton-proton collisions at $\sqrt{s} = 0.9$, 2.76, 7 TeV", PhD thesis, University of Heidelberg, February 2012.
`http://www.ub.uni-heidelberg.de/archiv/13113`

[198] **ALICE Collaboration**, A. Kalweit, "Particle Identification in the ALICE Experiment", *J. Phys. G* **38** (2011) 124073, `arXiv:1107.1514`.

[199] C. Lippmann, "Particle identification", *Nucl. Instrum. Meth. A* **666** (2012) 148–172, `arXiv:1101.3276`.

[200] L. Rolandi, W. Riegler, and W. Blum, "Particle Detection with Drift Chambers", 2008.

[201] S. Gorbunov and I. Kisel, "AliKF Package".
`http://alisoft.cern.ch/viewvc/branches/v4-18-Release/STEER/AliKFParticle.h`

[202] S. Gorbunov and I. G. Kisel, "Reconstruction of Decayed Particles Based on the Kalman Filter", 05 2007.
`http://www.gsi.documents/DOC-2007-May-14-1.pdf`

[203] T. Dahms, "Measurement of photons via conversion pairs with the PHENIX experiment at RHIC", Master's thesis, Stony Brook University, 2005.

[204] J. Podolanski and R. Armenteros, "ANALYSIS OF V-EVENTS", *Phil. Mag.* **7** (1954).

[205] **ALICE Collaboration**, K. Aamodt *et al.*, "Strange particle production in proton-proton collisions at $\sqrt{s} = 0.9$ TeV with ALICE at the LHC", *Eur. Phys. J. C* **71** (2011) 1594, `arXiv:1012.3257`.

[206] **CMS Collaboration**, V. Khachatryan *et al.*, "Strange Particle Production in pp Collisions at $\sqrt{s} = 0.9$ and 7 TeV", *JHEP* **1105** (2011) 064, `arXiv:1102.4282`.

[207] **ALICE Collaboration**, D. Chinellato, "Strange and Multi-Strange Particle Production in ALICE", `arXiv:1211.7298`.

[208] T. Adye, "Unfolding algorithms and tests using RooUnfold", `arXiv:1105.1160`.

[209] G. D'Agostini, "A Multidimensional unfolding method based on Bayes' theorem", *Nucl. Instrum. Meth. A* **362** (1995) 487–498.

[210] B. C. Smith, "Measurement of the transverse momentum spectrum of W bosons produced at $\sqrt{s} = 7$ TeV using the ATLAS detector", phd thesis, Harvard University, 2011.

[211] A. Hocker and V. Kartvelishvili, "SVD approach to data unfolding", *Nucl. Instrum. Meth. A* **372** (1996) 469–481, `arXiv:hep-ph/9509307`.

[212] F. Bock, "ALICE Capabilities for Studying Photon Physics with the Conversion Method at LHC Energies", bachelor's thesis, University of Heidelberg, June 2010.
`http://www.physi.uni-heidelberg.de//Publications/`
`Bock-Bachelorthesis.pdf`

[213] J. Kamin and M. Campos, "Private Communication", 2011-2012.

[214] **ALICE Collaboration**, B. Abelev *et al.*, "Measurement of inelastic, single- and double-diffraction cross sections in proton–proton collisions at the LHC with ALICE", *Eur. Phys. J. C*, 2012 `arXiv:1208.4968`.

[215] **ALICE Collaboration**, B. Abelev *et al.*, "Neutral pion and η meson production in proton-proton collisions at $\sqrt{s} = 0.9$ TeV and $\sqrt{s} = 7$ TeV", *Phys. Lett. B* **717** (2012) 162–172, `arXiv:1205.5724`.

[216] **ALICE Collaboration**, B. B. Abelev *et al.*, "Neutral pion production at midrapidity in pp and Pb–Pb collisions at $\sqrt{s_{\mathrm{NN}}} = 2.76$ TeV", `arXiv:1405.3794`.

[217] G. D. Lafferty and T. R. Wyatt, "Where to stick your data points: The treatment of measurements within wide bins", *Nucl. Instrum. Meth. A* **355** (1995) 541–547.

[218] K. Aamodt, "Photon, π^0 and η measurements in proton-proton collisions at $\sqrt{s} = 7$ TeV with the ALICE TPC at the LHC", phd thesis, University of Oslo, 2011.

[219] C. Tsallis, "Possible Generalization of Boltzmann-Gibbs Statistics", *J. Statist. Phys.* **52** (1988) 479–487.

[220] J. Cleymans and D. Worku, "Relativistic Thermodynamics: Transverse Momentum Distributions in High-Energy Physics", *Eur. Phys. J. A* **48** (2012) 160, `arXiv:1203.4343`.

[221] R. Hagedorn, "Multiplicities, p_{T} distributions, and the expected hadron-quark-gluon phase transition", Ed. Compositori, 1983.

[222] **PHENIX Collaboration**, A. Adare *et al.*, "Detailed measurement of the e^+e^- pair continuum in p+p and Au+Au collisions at $\sqrt{s_{\mathrm{NN}}} = 200$ GeV

and implications for direct photon production", *Phys. Rev. C* **81** (2010) 034911, `arXiv:0912.0244`.

[223] D. Peressounko, "Private Communication", 2012-2013.

[224] **WA80 Collaboration.**, R. Albrecht *et al.*, "Production of eta mesons in 200-A/GeV S+S and S+Au reactions", *Phys. Lett. B* **361** (1995) 14–20, `arXiv:hep-ex/9507009`.

[225] P. Khandai, P. Shukla, and V. Singh, "Meson spectra and m_T scaling in p+p, d+Au and Au+Au collisions at $\sqrt{s_{NN}} = 200$ GeV", *Phys. Rev. C* **84** (2011) 054904, `arXiv:1110.3929`.

[226] P. Khandai, P. Sett, P. Shukla, and V. Singh, "Transverse Mass Spectra and Scaling of Hadrons at RHIC and LHC Energies", `arXiv:1205.0648`.

[227] **PHENIX Collaboration**, A. Adare *et al.*, "Neutral pion production with respect to centrality and reaction plane in Au+Au collisions at $\sqrt{s_{NN}} = 200$ GeV", *Phys. Rev. C* **87** (2013), no. 3, 034911, `arXiv:1208.2254`.

[228] **PHENIX Collaboration**, S. Adler *et al.*, "High transverse momentum η meson production in p+p, d+Au and Au+Au collisions at $\sqrt{s_{NN}} = 200$ GeV", *Phys. Rev. C* **75** (2007) 024909, `arXiv:nucl-ex/0611006`.

[229] A. Adare, S. Afanasiev, C. Aidala, N. Ajitanand, Y. Akiba, *et al.*, "Production of ω mesons in p+p, d+Au, Cu+Cu, and Au+Au collisions at $\sqrt{s_{NN}} = 200$ GeV", *Phys. Rev. C* **84** (2011) 044902, `arXiv:1105.3467`.

[230] **ALICE Collaboration**, B. B. Abelev *et al.*, "K*(892)^0 and Φ(1020) production in Pb–Pb collisions at $\sqrt{s_{NN}} = 2.76$ TeV", `arXiv:1404.0495`.

[231] **ALICE Collaboration**, B. Abelev *et al.*, "Production of $K^*(892)^0$ and $\phi(1020)$ in pp collisions at $\sqrt{s} = 7$ TeV", *Eur. Phys. J. C* **72** (2012) 2183, `arXiv:1208.5717`.

[232] **PHENIX Collaboration**, B. Sahlmueller, "Measurement of π^0 and η Mesons with PHENIX in $\sqrt{s_{NN}} = 200$ GeV Au+Au Collisions at RHIC", *Indian J. Phys.* **85** (2011) 981–985, `arXiv:0806.0261`.

[233] L. Gordon and W. Vogelsang, "Polarized and unpolarized isolated prompt photon production beyond the leading order", *Phys. Rev. D* **50** (1994) 1901–1916.

[234] **ALICE Collaboration**, M. Wilde, "Measurement of Direct Photons in pp and Pb–Pb Collisions with ALICE", *Nucl. Phys. A* **904-905** (2013) 573c–576c, `arXiv:1210.5958`.

[235] R. Chatterjee, H. Holopainen, T. Renk, and K. J. Eskola, "Collision centrality and τ_0 dependence of the emission of thermal photons from fluctuating initial state in ideal hydrodynamic calculation", *Phys. Rev. C* **85** (2012) 064910, `arXiv:1204.2249`.

[236] C. Shen, U. Heinz, J.-F. Paquet, and C. Gale, "Thermal photon anisotropic flow serves as a quark-gluon plasma viscometer", `arXiv:1403.7558`.

[237] R. Rapp, "Dilepton Production in Heavy-Ion Collisions", *PoS* **CPOD2013** (2013) 008, `arXiv:1306.6394`.

[238] A. Chaudhuri, "Direct photon production and interferometry in $\sqrt{s_{\mathrm{NN}}} = 200$ GeV Au+Au and in $\sqrt{s_{\mathrm{NN}}} = 2.76$ TeV Pb+Pb collisions", `arXiv:1305.6121`.

[239] J. K. Nayak and B. Sinha, "Electromagnetic signals from Au+Au collisions at RHIC energy, $\sqrt{s_{\mathrm{NN}}} = 200$ GeV and Pb+Pb collisions at LHC energy, $\sqrt{s_{\mathrm{NN}}} = 2.76$ TeV", *Phys. Lett. B* **719** (2013) 110–115, `arXiv:1210.3993`.

[240] P. B. Arnold, G. D. Moore, and L. G. Yaffe, "Photon emission from quark gluon plasma: Complete leading order results", *JHEP* **0112** (2001) 009, `arXiv:hep-ph/0111107`.

[241] **ALICE**, D. Lohner, "Measurement of Direct-Photon Elliptic Flow in Pb–Pb Collisions at $\sqrt{s_{\mathrm{NN}}} = 2.76$ TeV", *J. Phys. Conf. Ser.* **446** (2013) 012028, `arXiv:1212.3995`.

[242] **PHENIX Collaboration**, A. Adare *et al.*, "Observation of direct-photon collective flow in $\sqrt{s_{\mathrm{NN}}} = 200$ GeV Au+Au collisions", *Phys. Rev. Lett.* **109** (2012) 122302, `arXiv:1105.4126`.

[243] R. Chatterjee, H. Holopainen, I. Helenius, T. Renk, and K. J. Eskola, "Elliptic flow of thermal photons from event-by-event hydrodynamic model", *Phys. Rev. C* **88** (2013) 034901, `arXiv:1305.6443`.

[244] D. Lohner, "Anisotropic flow of direct photons in Pb–Pb collisions at $\sqrt{s_{\mathrm{NN}}} = 2.76$ TeV", PhD thesis, University of Heidelberg, October 2013. `http://www.physi.uni-heidelberg.de//Publications/lohner_doktorarbeit.pdf`

[245] C. Shen, U. W. Heinz, J.-F. Paquet, and C. Gale, "Thermal photons as a quark-gluon plasma thermometer reexamined", *Phys. Rev. C* **89** (2014), no. 4, 044910, `arXiv:1308.2440`.

Danksagung

Ich möchte mich zunächst bei Professor Johannes P. Wessels für die Gelegenheit an diesem außerordentlich interessanten Thema arbeiten zu dürfen bedanken. Bedanken möchte ich mich auch bei Dr. Christian Klein-Bösing für dessen hervorragende Betreuung und die jederzeit interessanten Anregungen. Auch dafür, dass er die Zeit gefunden hat die Arbeit vor der Abgabe durchzusehen, möchte ich mich bedanken. Darüber hinaus gilt mein Dank allen Mitgliedern der Photon Conversion Group. Besonders möchte ich mich hier jedoch bei Dr. Klaus Reygers bedanken, dessen Expertise auf dem Gebiet der direkten Photonen viel zum gelingen dieser Arbeit beigetragen hat. Als einem weiteren Mitglied der Photon Conversion Group möchte ich mich ganz herzlich bei Friederike Bock bedanken. Mir haben die intensiven Gespräche über Photon, Physik und auch darüber hinaus immer viel Freude gemacht.

Ich möchte mich auch bei meinem Büro, Linus Feldkamp, Dr. Markus Heide, Daniel Mühlheim, Annika Passfeld sowie Uwe Westerhoff bedanken. Wir haben auch neben der Physik immer interessante Gesprächsthemen gefunden und so herrschte für mich immer eine angenehme und produktive Arbeitsatomsphäre. Allen weiteren Mitarbeitern der Arbeitsgruppe Wessels, Dr. Anton Andronic, Jonas Anielski, Dr. Christoph Baumann, Dr. Cyrano Bergmann, Jennifer Bersch, Dr. Tom Dietel, Stephan Dyba, Dr. David Emschermann, Henriette Gatz, Norbert Heine, Philipp Kähler, Thomas Keuter, Sebastian Klamor, Martin Kohn, Friederike Poppenborg, Henrik Poppenborg, Markus Rammler, Dr. Baldo Sahlmüller, Dr. Eva Sicking, Markus Tegeder, Wolfgang Verhoeven, Dr. Don Vernekohl, und Markus Zimmermann, danke ich für die schöne gemeinsame Zeit.

Am Ende möchte ich mich noch bei all den Menschen bedanken, die mich in der Zeit der Promotion neben der Arbeit begleitet haben. Ich bedanke mich ganz herzlich bei meinen Eltern, Veronika Bill und Dr. Hans-Rudolf Wilde für das Vertrauen und die mentale Unterstützung. Ein ganz besonders herzliches Dankeschön gilt auch meiner Freundin Anja Schöbel, die mich auch in den schwierigen Phasen, vor allem am Ende der Promotion, immer unterstützt und ermutigt hat.

Lebenslauf und Bildungsgang

Persönliche Daten

Name:	Martin Rudolf Wilde
Geburtsdatum:	20.09.1982
Geburtsort:	Herten
Staatsangehörigkeit:	deutsch
Eltern:	Hans-Rudolf Wilde Veronika Bill, geb. Jander
Familienstand:	ledig

Schulbildung

1989 – 1993	Grundschule St. Urbanus Gelsenkirchen
1993 – 2002	Leibniz-Gymnasium Gelsenkirchen
28.06.2002	Allgemeine Hochschulreife

Zivildienst

2002 – 2003	Gelsenkirchener Werkstätten für angepasste Arbeit GmbH

Studium

10.2003 — 09.2009	Physik an der Westfälischen Wilhelms-Universität Münster Diplom am 10.09.2009

Promotionsstudium

Ab 10.2009	Beginn der Dissertation am Institut für Kernphysik bei Prof. Dr. J. P. Wessels

Münster, 25. März 2015